UNIVERSITY OF CALIFORNIA, SAN DIEGO

Turbulence and Internal Waves in Numerical Models of the Equatorial Undercurrents System

A dissertation submitted in partial satisfaction of the
requirements for the degree Doctor of Philosophy

in

Engineering Sciences (Mechanical Engineering)

by

Hieu T. Pham

Committee in charge:

Professor Sutanu Sarkar, Chair
Professor Paul F. Linden
Professor Daniel L. Rudnick
Professor Daniel M. Tartakovsky
Professor Kraig B. Winters

2010

The dissertation of Hieu T. Pham is approved, and it is acceptable in quality and form for publication on microfilm:

Chair

University of California, San Diego

2010

DEDICATION

With all my love...

to my mother and father, Phuong & Chinh

EPIGRAPH

"In every job, relationship, or life situation there is inevitably some turbulence. Learn to laugh at it. It is part of what you do and who you are."

Allen Klein

TABLE OF CONTENTS

Signature Page iii

Dedication iv

Epigraph v

Table of Contents vi

List of Figures viii

List of Tables xvi

Acknowledgements xvii

Vita xix

Abstract xx

Chapter I Introduction 1
A. Background conditions 2
B. Deep-cycle Turbulence 5
C. Internal Gravity Waves in a Stratified Shear Flow: Linear theory 9
D. Observations of Internal Gravity Waves in the EUC 12
E. Numerical models of small-scale processes in the EUC 18
F. Approaches and model problems 23

Chapter II Numerical Method 25
A. Governing Equations 25
B. Boundary conditions 26
C. Numerical Implementation 26

Chapter III Dynamics of a stratified shear layer above a region of uniform stratification 28
A. Objectives 28
B. Problem Formulation 33
C. Evolution of the Shear Layer 36
D. Visualization of the Shear Layer Evolution 41
E. Internal Wave Field 48
F. Mass Transport 55
G. Momentum Transport 58
H. Energy Transport 61
I. Implications 67

Chapter IV Transport and mixing of density in a continuously stratified shear layer . . . 70
A. Objectives . . . 70
B. Problem Formulation . . . 73
C. Evolution of the Shear Layers . . . 77
D. Turbulence Evolution . . . 79
1. Visualization of the turbulent fields . . . 79
2. Turbulence Budgets . . . 84
3. Length Scales . . . 88
4. Non-dimensional Turbulent Parameters . . . 90
E. Eddy Diffusivity . . . 92
F. Eddy Diffusivity Estimated Using Irreversible Mixing . . . 95
G. Implications . . . 98

Chapter V Internal Waves and Turbulence in a Stratified Jet . . . 100
A. Objectives . . . 100
B. Problem Formulation . . . 103
C. Far Jet . . . 106
1. Internal Wave Field . . . 109
2. Turbulent Kinetic Energy Budget . . . 111
D. Near Jet . . . 116
1. Internal Wave Field . . . 116
2. 'Hot Pockets' . . . 120
3. Induced Dissipation . . . 121
4. Turbulent Kinetic Energy Budget . . . 125
E. Implications . . . 134

Chapter VI Mixing events in a stratified jet subject to surface wind and buoyancy forcing . . . 137
A. Objectives . . . 137
B. Problem Formulation . . . 140
C. Evolution of the mean flow . . . 145
D. Internal Waves . . . 150
E. Mixing and generation of intermittent turbulence . . . 157
F. Momentum budget . . . 165
G. Kinetic Energy Budgets . . . 168
H. Implications . . . 174

Chapter VII Conclusions . . . 177

Bibliography . . . 181

LIST OF FIGURES

Figure I.1: Profiles of potential temperature and zonal velocities measured at the equator. Profiles 140W-1984 are taken at 0230 UTC 28 November 1984 at 140°W. Profiles 134W-1987 are taken at 0630 UTC 17 April 1987 at 134°W. Profiles 140W-1987 are averaged data from 12 May - 11 June 1987 at 140°W. Profiles are determined by linearly interpolating from the observed data. Adapted from Skyllingstad & Denbo (1994) 3

Figure I.2: Profiles of zonal velocities, meridional velocities and temperature, averaged over the period from 12 May to 11 June from 1983 to 1987, at a surface mooring. Adapted from McPhaden & Peters (1992). . 4

Figure I.3: Observations taken during April 14-28, 1987. Hourly-averages of: surface buoyancy flux; mixed-layer depth, MLD; squared shear, S^2 and squared buoyancy frequency, N^2; gradient Richardson number, Ri_g; turbulent dissipation, ϵ; and isotherm displacement, η. MLD is estimated as the depth at which the density exceeds the surface value by 1%. Ri_g, ϵ and η are at 28 m depth. Adapted from Moum *et al.* (1992) 5

Figure I.4: (a) Gradient Richardson numbers, Ri_g and (b) turbulent dissipation, ϵ, in log scale. Adapted from Peters *et al.* (1988) 6

Figure I.5: (Top) Temperature field exhibits an internal wave packet. Region within the dotted box is expanded in the bottom figure showing wave overturning event. Adapted from Hebert *et al.* (1992) 13

Figure I.6: (Left) Gradient Richardson number computed by using hourly-average zonal velocity profile and the average of the density profiles before and after the wave packet. (Right) Turbulent dissipation profiles before, during and after the wave packet offset by four decades. Values $> 10^{-7}$ are hatched, those $> 10^{-6}$ are cross-hatched, and those $> 10^{-5}$ are black. Adapted from Hebert *et al.* (1992) 14

Figure I.7: Time series of temperature measured at various depth. The nighttime mixed-layer depth is 30-34 m. High-frequency fluctuations are observed at sunrise. Adapted from McPhaden & Peters (1992) . . 15

Figure I.8: Time series of velocities and momentum fluxes with a wave packet. The wave packet is recorded on 8 November 1991. The vertical dotted lines in (c) enclose the period of the wave packet. Adapted from Lien *et al.* (1996) 16

Figure III.1: (a) *Initial* mean profiles. Each case has a temporally evolving shear layer between two streams with velocity $-\Delta U/2$ and $\Delta U/2$, and initial vorticity thickness, $\delta_{\omega,0}$. The maximum shear is at $z = 0$. The 2-layer density variation corresponds to a tangent-hyperbolic profile with $J(0) = 0.1$. The other density profiles correspond to a moderate linear stratification, $J_s = 0.05$, in the shear layer above a bottom region, $z < -2.5\delta_{\omega,0}$, with uniform deep stratification that takes the values: $J_d = 0.1$, 0.25 and 1.0. The initial value of bulk Richardson number, $Ri_{b,0} = 0.1$, is the same for all cases. (b) Cartoon of internal wave excitation by shear layer instabilities. The indicated group and phase velocity are relative to the lower free-stream. 32
Figure III.2: (a) Vorticity thickness, δ_ω. (b) Bulk Richardson number, Ri_b, (c) Momentum thickness, δ_θ. (d) Bulk Richardson number, $Ri_{b,\theta}$. . . . 36
Figure III.3: Profiles of squared buoyancy frequency N^2 for $J_d = 0.25$ (a) in KH regime, (b) in turbulence regime. 39
Figure III.4: Mean shear profiles in case $J_d = 0.25$ (a) in KH regime, (b) in turbulence regime. 40
Figure III.5: Gradient Richardson number, Ri_g, profiles in case $J_d = 0.25$. . . . 40
Figure III.6: Spanwise vorticity, ω_2, in x-z plane at $y = 8.5$ in two-layer case. . 42
Figure III.7: Spanwise vorticity, ω_2, in x-z plane at $y = 8.5$ in case $J_d = 0.25$. . 43
Figure III.8: Density field, ρ, in x-z plane at $y = 8.5$ in two-layer case. 44
Figure III.9: Density field, ρ, in x-z plane at $y = 8.5$ in case $J_d = 0.25$. 45
Figure III.10: Slices of $\partial w'/\partial z$ in the x-z plane at $y = 8.5$. Strong waves are observed in case $J_d = 0.25$ (c,d) and $J_d = 1.0$ (e,f). The left panels correspond to time in the KH regime; the right panels correspond to time in the turbulence regime. In the case of $J_d = 0.1$, the internal wave field is negligible in the KH regime, (a), but noticeable in the turbulence regime, (b). The dashed lines in (c,e) shows the propagating angles predicted by linear wave theory. The scale ranges from -0.01 (black) to 0.01 (white). 47
Figure III.11: Spanwise-averaged power spectra of the vertical velocity on the horizontal center-plane, $z = 0$, and at the bottom edge of the shear layer, $z = -2.5\delta_{\omega,0}$, in case $J_d = 0.25$. Two different times are shown. 48
Figure III.12: Case $J_d = 0.25$: (a) Time series of $\partial w/\partial z$ at a streamwise probe, $z = -10$, $y = 8.5$, in the stationary frame; (b) the wave field in (a) limited to the KH regime and mapped to a frame moving with the bottom free-stream velocity; (c) power spectrum of the field in (b); (d) similar to wave field in (b) but in the turbulence regime; (e) power spectrum of the field in (d). The scale in (a,b,d) is from -0.01 (black) to 0.01 (white). The contours in (c,e) are in log scale. The dashed lines in (c,e) indicate the buoyancy frequency; the diagonal lines show the relation $\Omega = (\Delta U/2)\, k$. 49
Figure III.13: Case $J_d = 1.0$: see caption in Fig. III.12. 50

Figure III.14: Case $J_d = 0.1$: see caption in Fig. III.12. 51
Figure III.15: Density variation, $\Delta_t\rho$ defined in Eq.(III.13), in two-layer case. . . 55
Figure III.16: Density variation, $\Delta_t\rho$ defined in Eq.(III.13), in case $J_d = 0.25$ (a) in KH regime, (b) in turbulence regime. 56
Figure III.17: (a) Vertical mass fluxes at $z = -5$. (b) Net mass gain inside the shear layer in case $J_d = 0.25$. The dots show the net mass gain in the shear layer. The dash line denotes the diffusive contribution. . 57
Figure III.18: Momentum thickness: (a) upper portion, $\delta_{\theta,u}$, (b) lower portion, $\delta_{\theta,l}$. 58
Figure III.19: (a) Reynolds stress $\langle u'w' \rangle$ at depth $z_l = -5$. (b) Variation in the mean velocity profile, $\Delta_t u$, in case $J_d = 0.25$. 59
Figure III.20: Integrated turbulent kinetic energy (a)$J_d = 0.25$ (b)$J_d = 1.0$ —, over test domain; − − −, over the shear layer. 62
Figure III.21: Vertical profiles of *tke* budget in case $J_d = 0.25$ at (a) t = 83, (b) t = 160. 63
Figure III.22: (a) Balance of *tke* budget for $J_d = 0.25$. The production, dissipation and buoyancy flux are integrated from z_{max} to $z = -5$. $\langle p'w' \rangle$ is at $z = -5$. (b) Internal wave flux, $\langle p'w' \rangle$, at $z = -5$ compared among different cases. 63

Figure IV.1: (a) Schematics of *initial* mean velocity and density profiles. (b) *Initial* gradient Richardson number Ri_g. The dashed line indicates the marginal value, $Ri_g = 0.25$, for shear instability. 73
Figure IV.2: Evolution of (a) the momentum thickness δ_θ and (b) the gradient Richardson number Ri_g at the centerline of the shear layer $z = 0$. The dash line indicates the critical value of $Ri_g = 0.25$ for shear instability. 77
Figure IV.3: Density field on a vertical xz plane at y = 3.9. 79
Figure IV.4: Turbulent kinetic energy dissipation rate ε on a vertical xz plane at y = 3.9. 81
Figure IV.5: Density variance dissipation rate χ_ρ on a vertical xz plane at y = 3.9. 82
Figure IV.6: Streamwise vorticity ω_1 on a vertical transverse plane at x = 15.4. 83
Figure IV.7: J_d cases: (a) Internal wave field shown in the xz cross section at y = 3.9 of the fluctuating vertical velocity w' field at t = 80; (b) Wave energy flux $\langle p'w' \rangle$ across the horizontal plane $z = -5$. 84
Figure IV.8: TKE budgets in the vertical direction z: (a) in the two-layer case at t = 102, and (b) in the J_d case at t = 100. 85
Figure IV.9: Evolution of TKE production, dissipation and buoyancy flux measured at center of the shear layer $z = 0$ in time: (a) in the two-layer case; (b) in the J_d case. 86
Figure IV.10: Density variance budgets in the vertical direction z (a) in the two-layer case at t = 102, and (b) in the J_d case at t = 100. 87
Figure IV.11: Evolution of production and dissipation of density variance measured at center of the shear layer $z = 0$ in time:(a) in the two-layer case; (b) in the J_d case. 88

Figure IV.12: Evolution of length scales (a) in the two-layer case and (b) in the J_d case. 89

Figure IV.13: Evolution of (a) buoyancy Reynolds number, $Re_b = \epsilon/\nu N^2$, and (b) local turbulent Reynolds number $Re_T = qL_E/\nu$. Both are at the shear center. 90

Figure IV.14: Evolution of (a) eddy diffusivity K_ρ and (b) mixing efficiency Γ at the center of the shear layer. 92

Figure IV.15: (a) $K_\rho \, vs \, Re_b$; (b) same as in (a) zoomed on to the intermediate mixing regime during the decay of the flow. Arrows indicate progress in time. Note the abscissa is given in logarithmic scale in (a) and linear scale in (b). 93

Figure IV.16: (a) $K_\rho \, vs \, Re_T$; (b) same as (a) zoomed on to the intermediate mixing regime during the decay of the flow. Arrows indicate progress in time. Note the abscissa is given in logarithmic scale in (a) and linear scale in (b). 94

Figure IV.17: (a) $K_\rho \, vs \, Re_T/Ri_g$; (b) same as (a) zoomed on to the intermediate mixing regime during the decay of the flow. Arrows indicate progress in time. Note the abscissa is given in logarithmic scale in (a) and linear scale in (b). 95

Figure IV.18: Evolution of (a) estimated eddy diffusivity $\tilde{K}_\rho$ and (b) irreversible mixing efficiency Γ^d (b). Arrow indicates progress in time. Note the abscissa is given in logarithmic scale in (a) and linear scale in (b). 96

Figure IV.19: (a) $\tilde{K}_\rho \, vs \, Re_b$, (b) same as (a) zoomed on to the intermediate mixing regime during the decay of the flow. Arrows indicate progress in time. Note the abscissa is given in logarithmic scale in (a) and linear scale in (b). 97

Figure IV.20: (a) $\tilde{K}_\rho \, vs \, Re_T$, (b) same as (a) zoomed on to the intermediate mixing regime during the decay of the flow. Arrows indicate progress in time. Note the abscissa is given in logarithmic scale in (a) and linear scale in (b). 97

Figure IV.21: (a) $\tilde{K}_\rho \, vs \, Re_T/Ri_g$, (b) same as (a) zoomed on to the intermediate mixing regime during the decay of the flow. Arrows indicate progress in time. Note the abscissa is given in logarithmic scale in (a) and linear scale in (b). 98

Figure V.1: Typical temperature profile and zonal currents in the EUC system (Skyllingstad & Denbo, 1994). 101

Figure V.2: (a) *Initial* mean profiles. The velocity profile corresponds to a shear layer on top of a jet. The jet center is at depth z = -15 $\delta_{\omega,0}$ in the *far jet* and at depth z = -6.5 $\delta_{\omega,0}$ in the *near jet*. (b) *Initial* stratification profiles J(z) used in both cases. (c) *Initial* $1/Ri_g(z)$ profiles. 103

Figure V.3: Far jet. Instantaneous wave field in the x-z plane at $y = 8.4\delta_{\omega,0}$: (a) $\partial w'/\partial z$ at t = 100; (b) $\partial w'/\partial z$ at t = 150; (c) $\partial w'/\partial z$ at t = 200; (d) ε at t = 100; (e) ε at t = 150; (f) ε at t = 200. Dashed lines in (a) indicate propagation angle predicted by linear wave theory. . 107
Figure V.4: Far jet. (a) Horizontally-averaged power spectra of the vertical velocity w on the horizontal plane $z = -10\delta_{\omega,0}$ at various times. (b) Squared vertical wavenumber m^2 at t = 100 computed using $k\delta_{\omega,0} = 0.87$ and $c_a = 0$. 108
Figure V.5: Far jet. Instantaneous w field in the x-t plane at $y = 8.4\delta_{\omega,0}$ and $z = -6\delta_{\omega,0}$ 108
Figure V.6: Far jet. Instantaneous w field in the z-t plane at $x = 25.2\delta_{\omega,0}$ and $y = 8.4\delta_{\omega,0}$. 109
Figure V.7: Far jet. TKE budget at (a) t = 118 and (b) t = 183. 112
Figure V.8: Far jet. Components of transport T_3 at (a) t = 118 and (b) t = 183.114
Figure V.9: Far jet. (a) Dashed line: Integrated TKE from $z^\star = -5\delta_{\omega,0}$ to z_{max}; solid line: Integrated TKE across the test domain. (b) Terms in the TKE budget integrated from $z^\star$ to z_{max}. 115
Figure V.10: Near jet. Internal wave field is visualized through a slice of $\partial w'/\partial z$ in the x-z plane at $y = 8.4\delta_{\omega,0}$ at time (a) t = 125 and (b) t = 150 117
Figure V.11: Near jet. (a) Horizontally-averaged power spectra of the vertical velocity w on the horizontal plane $z = -4\delta_{\omega,0}$ at various times. (b) Squared vertical wavenumber m^2 at t = 150 computed using $c_a = 0$ and two values of horizontal wavenumber: $k\delta_{\omega,0} = 0.25$ based on the peak of energy spectrum at $t = 145$ in (a) and $k\delta_{\omega,0} = 0.87$ based on the KH mode. 117
Figure V.12: Near jet. (a) Instantaneous vertical velocity field w in the x-t plane at $y = 8.4\delta_{\omega,0}$ and $z = -4\delta_{\omega,0}$. (b) Instantaneous dissipation field ε on the same plane. The white dashed lines denotes $\langle u \rangle = dx/dt \approx 1.7\Delta U$. 118
Figure V.13: Near jet. Isocontours in the density field in the x-z plane at $y = 8.4\delta_{\omega,0}$. (a-c) corresponds to t = 150, 170 and 185, respectively. Arrow indicates 'hot pocket'. 120
Figure V.14: Near jet. (a) Isopycnal surfaces at t = 162: the darker isopycnal is of $\rho = 1.0$ corresponding to the initial mean density at $z = 0$; the lighter isopycnal is of $\rho = 1.07$ corresponding to the initial mean density at $z = -4.7\delta_{\omega,0}$. HS indicates horseshoe-like density intrusions. The lighter isopycnal is blanked in the range $0 < y < 5\delta_{\omega,0}$. (b) Isosurface of $\Delta = 5$ at t = 162 shows the horseshoe vortices. In this figure, positive z direction points downward. . . . 122
Figure V.15: Near jet. Isocontours in the dissipation field in the x-z plane at $y = 8.4\delta_{\omega,0}$. (a-c) corresponds to t = 150, 170 and 185, respectively. Arrow indicates 'hot pocket'. 123
Figure V.16: Near jet. Instantaneous dissipation field ϵ field in the z-t plane at $x = 25.2\delta_{\omega,0}$ and $y = 8.4\delta_{\omega,0}$. Solid lines are isopycnals. 124

Figure V.17: Near Jet. TKE budget at (a) t = 143 and (b) t = 171. 125
Figure V.18: Near Jet. Components of TKE transport T_3 at (a) t = 143 and (b) t = 171. 126
Figure V.19: Near Jet. Dashed line indicates integrated TKE in the region $-2.5 < z < z_{max}$. Solid line indicates integrated TKE over entire test domain. The difference between the two lines is the TKE outside the shear layer and in the jet. 127
Figure V.20: Near Jet. Integrated TKE budget. The terms are spatially integrated in the jet upper-flank $-6.5 < z < -2.5\delta_{\omega,0}$. 128
Figure V.21: Near Jet. Horizontally averaged power co-spectra of Reynolds stress $u'w'$ at $z = -4\delta_{\omega,0}$. 129
Figure V.22: Near Jet. Ri_g profiles. 129
Figure V.23: Near jet. Local gradient Richardson number $\hat{Ri}_g$ field at y = $8.4\delta_{\omega,0}$ and t = 100, 145 and 175. 130
Figure V.24: Near jet. Expanded-view of the density fields with the aspect ratio L_z:L_x = 1:35. 132
Figure V.25: Near Jet. Mixing efficiency. (a) Γ. (b) Γ_d. The dotted line shows the value $\Gamma = \Gamma_d = 0.2$. 133

Figure VI.1: (a) *Initial* mean profiles. The velocity profile consists of a stratified jet below a wind-driven mixed layer. The jet center is at depth z = -5/3 δ_0. (b) *Initial* squared shear profile S^2, squared buoyancy frequency profile N^2 normalized by U_j^2/δ_0^2, and gradient Richardson number profile Ri_g. The vertical dotted line indicates the critical value $Ri_g = 0.25$ for shear instability. Thus, only the thin surface region, $-0.33 < z < 0$, has linearly unstable shear. 140
Figure VI.2: Time evolution of (a) surface velocity $\langle u_s \rangle$ at $z = 0$, and (b) stirring depth δ_s and the corresponding $Ri_{g,s}$. The dotted lines indicate the critical value of $Ri_g = 0.25$ 145
Figure VI.3: Vertical mean profiles at various time: (a) streamwise velocity $\langle u \rangle$, (b) shear rate $d\langle u \rangle / dz$. 147
Figure VI.4: Vertical mean profiles at various time: (a) density $\langle \rho \rangle$ and (b) squared buoyancy frequency N^2. 148
Figure VI.5: Vertical profiles of the vertical gradient Richardson number Ri_g at various time. 149
Figure VI.6: Internal wave fields are shown with the vertical fluctuating velocity field w' in the x-z plane at $y = 1.1$. 150
Figure VI.7: Internal waves are shown with 3D isocontours in the density field at (a) $t = 5$ and (b) $t = 10$. The lighter isosurface denotes $\rho = 0.048$ while the darker denotes $\rho = 0.144$. 152
Figure VI.8: Horizontally-averaged k_x spectra of the vertical fluctuating velocity field w' at various time: (a) at $z = -0.33$ and (b) at $z = -1$. . . . 153

Figure VI.9: Horizontally-averaged profiles of the fluctuating fields at various time: (a) streamwise velocity u_{rms}, (b) spanwise velocity v_{rms}, (c) vertical velocity w_{rms}, (d) density ρ_{rms}, (e) Reynolds stress $\langle u'w' \rangle$ and (f) wave energy flux $\langle p'w' \rangle$. The horizontal dotted lines indicates the center of the jet. The upper zero-velocity point of the jet is at approximately $z = -0.4$ after t = 10. 155
Figure VI.10: Contributions to the transport at (a) t = 10 and (b) t = 20. The dotted lines indicate center of the jet. 156
Figure VI.11: Downward ejection in the circled region is shown in the vertical x-z slices of the density field at $y = 1.1$. 157
Figure VI.12: Upward ejection in the circled region and isopycnal overturn in the rectanglular region are shown in the vertical x-z slices of the density field at $y = 1.1$. 159
Figure VI.13: Upward ejection in the circled region, downward ejection in the rectangular region, and isopycnal overturning in the oval region are observed in the vertical x-z slices of the density field at $y = 1.1$. . . 160
Figure VI.14: Ejections of light fluid are shown with 3D isocontours in the density field. Up in this figure corresponds to down in physical space. Horseshoe-like vortex tube ejecting fluid from the stirring surface downward in physical space at $t = 18$. The darker isosurface denotes $\rho = 0.144$ while the lighter one corresponds to $\rho = 0.197$. The negative z direction points upward in this figure. 161
Figure VI.15: Ejections of heavy fluid are shown with 3D isocontours in the density field. Breaking horseshoe-like vortex tube denoted by circle A and single vortex tube denoted by circle B show ejections from the stirring surface upward toward the free surface at $t = 45$. The isosurface corresponds to $\rho = 0.048$. 162
Figure VI.16: z-t diagrams of (a) the density field and (b) dissipation field measured at $x = 1.3$ and $y = 1.1$. Arrows indicate the effect of downward ejections. 164
Figure VI.17: In the surface layer $-0.33 < z < 0$: (a) the initial and final mean streamwise velocity $\langle u \rangle$; (b) Viscous drag, M_2 at z = 0 and M_3 at z = -0.33, and turbulence/wave drag, M_4 at z = 0 and M_5 at z = -0.33, as a function of time. 166
Figure VI.18: In the jet upper-flank $-1.67 < z < -0.33$: (a) the initial and final mean streamwise velocity $\langle u \rangle$; (b) Viscous drag, M_2 at z = -0.33 and M_3 at z = -1.67, and turbulence/wave drag, M_4 at z = -0.33 and M_5 at z = -1.67, as a function of time. 167
Figure VI.19: (a) Mean kinetic energy at $t = 0$ and 45; (b) Energy input by the wind stress, $\langle u_s \rangle \tau_w$, and energy converted to turbulent kinetic energy P integrated over the region $-1.67 < z < 0$. 169
Figure VI.20: TKE budgets at (a) t = 5 and (b) t = 20. 170
Figure VI.21: (a) Vertical profiles of the buoyancy flux B at various time; (b) The time evolution of B at different depth. 171

Figure VI.22: Integrated TKE budget over the upper-flank of the jet $-1.67 \leqslant z \leqslant -0.33$. 172
Figure VI.23: Amount of turbulent kinetic energy carried by the pressure transport T_p, turbulent transport T_t and viscous transport T_v across depth: (a) $z = -0.33$ and (b) $z = -1.67$. 173

LIST OF TABLES

Table III.1: Energy flux efficiency, energy partition and mixing efficiency. The terms in the tke budget are integrated in both time and space (from $z = -5$ to z^t_{max}) to calculate the tabulated values. 66

Table VI.1: Comparison of parameters between simulations and observations. Observational data in the first column is taken from Moum *et al.* (1992) in which the jet center velocity is U_j, the jet thickness is δ_0 and mixed layer depth is δ_m. Values of N^2, S^2, and Ri_g are measured at depth $z = 28\,m$ in the observational data while they are computed at $z = -0.5$ in the current study. 144

Table VI.2: Momentum budget: Equation VI.7 integrated over the time of simulation. 166

ACKNOWLEDGEMENTS

I would like to acknowledge my advisor, Professor Sutanu Sarkar, for the opportunity to pursue doctoral research. Four years ago I walked into his office asking for a letter of recommendation and now he is giving me a degree. His guidance, support and encouragement has been invaluable. I thank the members of my thesis committee for many helpful suggestions. Professors Paul Linden, Jim Rottman and Kraig Winters have been inspirational through their excellent teaching and research in the field of environmental fluid mechanics.

I am indebted to Sankar Basak and Kyle Brucker whose codes are used for the simulations in the thesis. Special thanks to Kyle for the endless assistance during my first year in the lab. Matt and Eric are appreciated for proofreading my papers as well as for the pleasant political discussions. Thanks to Bishak for the late night chats about research, life and curry chicken. All other members of the CFD labs are acknowledged for their support and humor. Conference meetings would not have been as enjoyable without you.

The support provided by ONR grant N000140810504, program monitor Scott Harper, and by ONR grant N000140710133, program monitor Ron Joslin, is greatly appreciated. This work was supported in part by a grant of computer time from the DOD High Performance Computing Modernization Program. The numerical simulations have been performed on the Cray XT4 (Jade) at the Engineering Research and Development Center and on the Cray XT5 (Pingo) at the Arctic Region Supercomputing Center.

The contents of chapter III appear in *Journal of Fluid Mechanics*: Pham, H. T., Sarkar, S. and Brucker, K. A., "Dynamics of a Stratified Shear Layer Above a Region of Uniform Stratification", *J. Fluid Mech.*, **630**, 191-223 (2009). The dissertation author is the primary researcher and the research supervisor and Kyle A. Brucker are the co-authors of the paper.

The contents of chapter IV appear in *Journal of Turbulence*: Pham, H. T., and Sarkar, S., "Transport and mixing of density in a continuously stratified shear layer", *J.*

Turbulence, **11**, No. 24, 1-23 (2010). The dissertation author is the primary researcher and the research supervisor is the co-author of the paper.

The contents of chapter V appear in *Journal of Fluid Mechanics*: Pham, H. T., and Sarkar, S., "Turbulence and internal waves in a stable stratified jet", *J. Fluid Mech.*, **648**, 297-323 (2010). The dissertation author is the primary researcher and the research supervisor is the co-author of the paper.

The contents of chapter VI are under review for publication in *The Journal of Fluid Mechanics*: Pham, H. T., and Sarkar, S., "Mixing events in a stratified jet subject to surface wind and buoyancy forcing", *J. Fluid Mech.*, *submitted* (2010). The dissertation author is the primary researcher and the research supervisor is the co-author of the paper.

VITA

Education:

2003 B.S., Bioengineering: Pre-medical,
University of California, San Diego.

2007 M.S., Mechanical Engineering,
University of California, San Diego.

2010 Ph.D., Engineering Sciences (Mechanical Engineering),
University of California, San Diego.

Publications:

Pham, H. T., and Sarkar, S., "Mixing events in a stratified jet subject to surface wind and buoyancy forcing", *J. Fluid Mech.*, *submitted* (2010).

Pham, H. T., and Sarkar, S., "Transport and mixing of density in a continuously stratified shear layer", *J. Turbulence*, **11**, No. 24, 1-23 (2010).

Pham, H. T., and Sarkar, S., "Turbulence and internal waves in a stable stratified jet", *J. Fluid Mech.*, **648**, 297-323 (2010).

Pham, H. T., Sarkar, S. and Brucker, K. A., "The evolution of a sheared region between two continuously stratified layers", *Turbulence and Shear Flow Phenomena - VI* , Seoul, Korea (2009).

Pham, H. T., Sarkar, S. and Brucker, K. A., "Dynamics of a Stratified Shear Layer Above a Region of Uniform Stratification", *J. Fluid Mech.*, **630**, 191-223 (2009).

ABSTRACT OF THE DISSERTATION

Turbulence and Internal Waves in Numerical Models of the Equatorial Undercurrents System

by

Hieu T. Pham

Doctor of Philosophy in Engineering Sciences (Mechanical Engineering)

University of California, San Diego, 2010

Professor Sutanu Sarkar, Chair

Direct Numerical Simulation (DNS) of simplified model problems is used to investigate the role of turbulence and internal waves in the Equatorial Undercurrents (EUC) system. Prior observational studies of the Pacific EUC have established a strong correlation between deep-cycle turbulence in the thermocline and internal waves. The object of the thesis is to understand and quantify the dynamical processes underlying turbulence and internal waves in the EUC. The investigation has three phases. In the first phase, an idealized problem of a weakly-stratified shear layer located above a thermocline is simulated to investigate internal waves excited by unstable shear. The evolution of the shear layer consists of coherent Kelvin-Helmholtz (KH) rollers and small-scale turbulence. Internal waves excited by the KH rollers are narrow-band and of stronger amplitude that that of the broadband wave field generated by turbulence. Internal waves are shown to carry significant amount of momentum and energy away from the shear layer. In the second phase, the EUC is represented by a weakly stratified shear layer on top of a stable stratified jet. The objective is to investigate the interaction between the jet and the waves excited by the adjacent shear layer. Two simulations are performed: one with the jet located far from the shear layer (far jet) and the other with the shear layer on top of the jet (near jet). In the far jet, waves excited by the KH rollers are reflected and trapped in the region between the shear

layer and jet and lead to little dissipation. In the near jet, more representative of the EUC configuration, waves with wavelength larger than that of the KH rollers are found in and below the jet. Pockets of hot fluid associated with horseshoe vortices that originate from the shear layer penetrate into the jet region, initiate turbulence and disrupt the internal wave field. In the third final phase of the thesis, a stratified jet situated below a well-mixed surface layer driven by a constant wind stress and a surface buoyancy flux is considered. Turbulence is generated in the surface layer and deepens into the jet upper-flank. Waves generated by the turbulent surface layer propagate downward across the jet. The momentum flux and energy flux carried by the waves are significantly weaker than the waves generated by the unstable shear in the problem studied during the first phase. Intermittent patches of intense dissipation inside the jet upper-flank are the result of ejections of fluid parcels.

Chapter I

Introduction

Equatorial Undercurrents (EUC), eastward flows below westward surface currents at the equator, constitute a major component of the current systems in the tropical ocean. The EUCs are permanent in the Pacific and Atlantic oceans but seasonal in the Indian ocean. The Pacific EUC has been described to be a "ribbon" (Stewart, 2004) with a length of 13000 km, width of 300 km and depth of 200 m. The prevailing trade winds drive a westward surface current which leads to an elevation of the sea surface at the western boundary of the Pacific ocean basin. The resultant eastward horizontal pressure gradient at the equator (Coriolis parameter, $f = 0$) is balanced in the surface water by the westward wind stress but is unbalanced in subsurface waters where the wind-generated stress decreases, leading to an eastward subsurface flow, the EUC. The seasonal thermocline is deep in the western waters and shallow in the eastern waters of the Pacific basin. The EUC plays a crucial role in the balance of the equatorial heat budget and in the characteristics of the cold water tongue present off the equatorial coast of South America. It is believed that variability in the EUC can affect the surface temperature, modulate air/sea coupling, and thereby affect weather patterns (Philander, 1980). Since vertical transport of momentum and heat by turbulence is an important determinant of the upper ocean stratification and currents in response to wind forcing, there have been sustained efforts since the 1980s into the description and parameterization of the fine-scale structure of the EUC. The Tropic Heat experiments, TH1 in November 1984 and TH2 in April 1987, and the Tropical Instability Wave

Experiment (TIWE) in winter 1991 have provided data indicating a complex regime of turbulence and internal waves in the Central Pacific, vicinity of 140°W on the equator. An observational campaign by investigators from Oregon and Washington was initiated in 2008.

With recent advances in computational methods and infrastructure, numerical models have emerged as powerful tools to complement and help interpret observational data. The objectives of the present study are to use numerical approaches of high accuracy to further characterize and understand small-scale processes in the EUC. Model problems based on observations of oceanic background conditions are simulated with focus on assessing the dynamics of turbulence and internal waves in the EUC system. In the remainder of this chapter, a survey of prior relevant literature on the EUC is given.

I.A Background conditions

During TH1 (November 1984) and TH2 (April 1987), intensive measurements of velocities and temperature in the EUC were obtained at 0°, 140°W as reported by Gregg *et al.* (1985), Peters *et al.* (1988), and Moum *et al.* (1989). Fig. I.1 shows a typical vertical structure of the undercurrent zonal velocity and temperature. The EUC system occupies approximately the upper 300 m of the ocean. The surface current is usually westward (negative zonal velocity) with magnitude that depends on wind speed. The eastward surface velocity, as in the 140W-1987 profile is atypical. At about 25-30 m depth, there is eastward flow, denoted by positive velocity, that intensifies with depth as it reaches the maximum speed at a depth of about 110 m. The speed of the EUC core can be as large as 1.5 m/s in the Pacific, while smaller values are observed in the Atlantic and Indian oceans (Philander, 1980). Below the core, the undercurrents relax down to near-zero velocity. The temperature profiles indicate three distinct regions in the EUC system: the mixed/weakly-stratified region occupying the upper 25-30 m, the thermocline located between depths of 30-100 m, and the strongly-stratified deep region. In terms of stability, the profiles imply an upper region which is unstable with

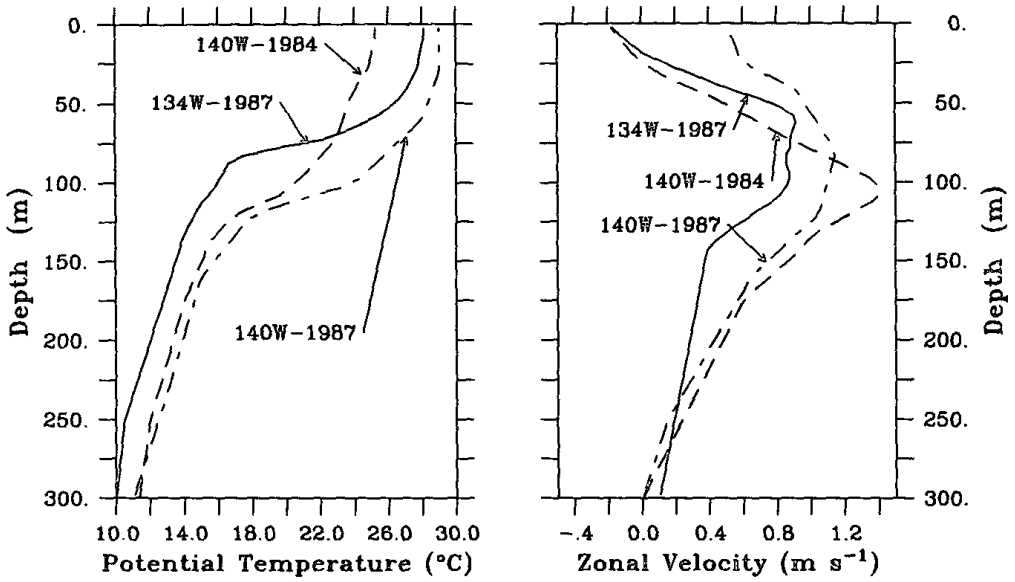

Figure I.1: Profiles of potential temperature and zonal velocities measured at the equator. Profiles 140W-1984 are taken at 0230 UTC 28 November 1984 at 140°W. Profiles 134W-1987 are taken at 0630 UTC 17 April 1987 at 134°W. Profiles 140W-1987 are averaged data from 12 May - 11 June 1987 at 140°W. Profiles are determined by linearly interpolating from the observed data. Adapted from Skyllingstad & Denbo (1994)

.

gradient Richardson number, $Ri_g = N^2/S^2$, less than 0.25, where S is the shear and $N^2 = -(g/\rho_0)d\rho/dz$ is the squared buoyancy frequency. The deep region is stable with $Ri_g > 2$ while, in the thermocline, the stability is marginal (Peters *et al.*, 1988) with Ri_g between 0.25 and 0.35.

As shown in Fig. I.2, the background conditions of the EUC system show significant inter-annual variability. The EUC core velocity decreases from 1.5 m/s in 1984 to 1 m/s in 1987 resulting in a reduction of shear in the thermocline region. In 1987, shortly after the peak of El Niño, the surface water was warmer and the stratification in the thermocline was larger. Variation in both mean velocity and mean temperature profiles leads to variation in the Richardson number profile, with potentially strong effect on the the mixing dynamics. Presumably, factors such as wind direction and speed, surface heat flux, and zonal pressure gradient lead to seasonal and annual vari-

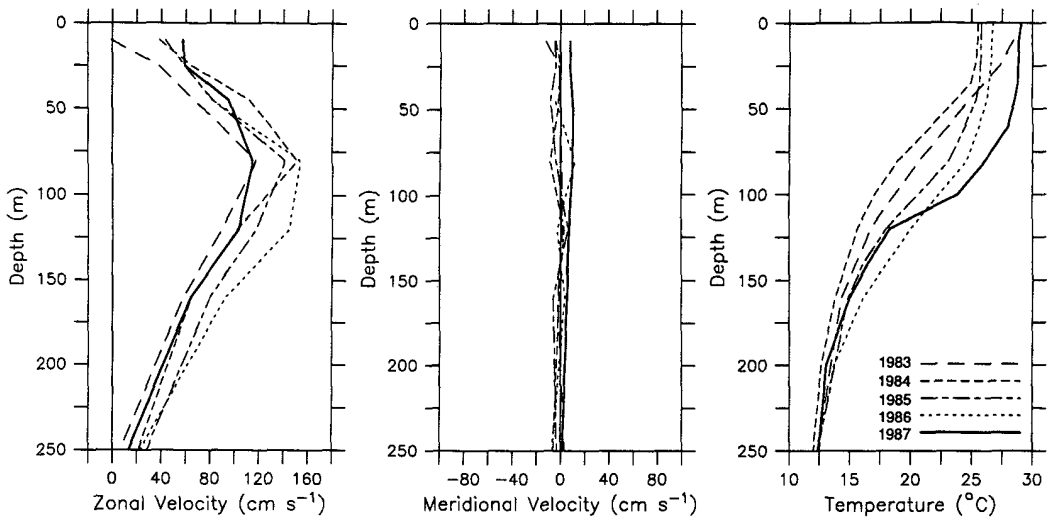

Figure I.2: Profiles of zonal velocities, meridional velocities and temperature, averaged over the period from 12 May to 11 June from 1983 to 1987, at a surface mooring. Adapted from McPhaden & Peters (1992).

ability of the EUC. The change in background conditions makes the EUC system hard to typify; however, its complexity leads to different scenarios, rich with interesting fluid dynamics.

Despite the variability in the vertical structure, the EUC system in the central Pacific does exhibit common characteristics such as the velocity profile of a jet and a shallow seasonal thermocline. Because of the diurnal cycle of the surface heat flux, the mixed-layer depth (MLD) also shows diurnal behavior as shown in Fig. I.3. The largest MLD is only 25 m. Other observations record greater depth such as in Lien *et al.* (1996) and Moum *et al.* (1989) but still limited to the upper 40 m. The Richardson number also shows diurnal modification as reported by Peters *et al.* (1988) and so does the turbulent dissipation. The microstructure profiles in both TH1 and TH2 revealed an intriguing aspect, new to the oceanographic community at the time, that large dissipation rates extend beyond the mixed-layer depth and into the stable region during the night. This phenomenon is known as *deep-cycle turbulence*, further discussed in the next section, whose understanding and parameterization is one of the objectives of this study.

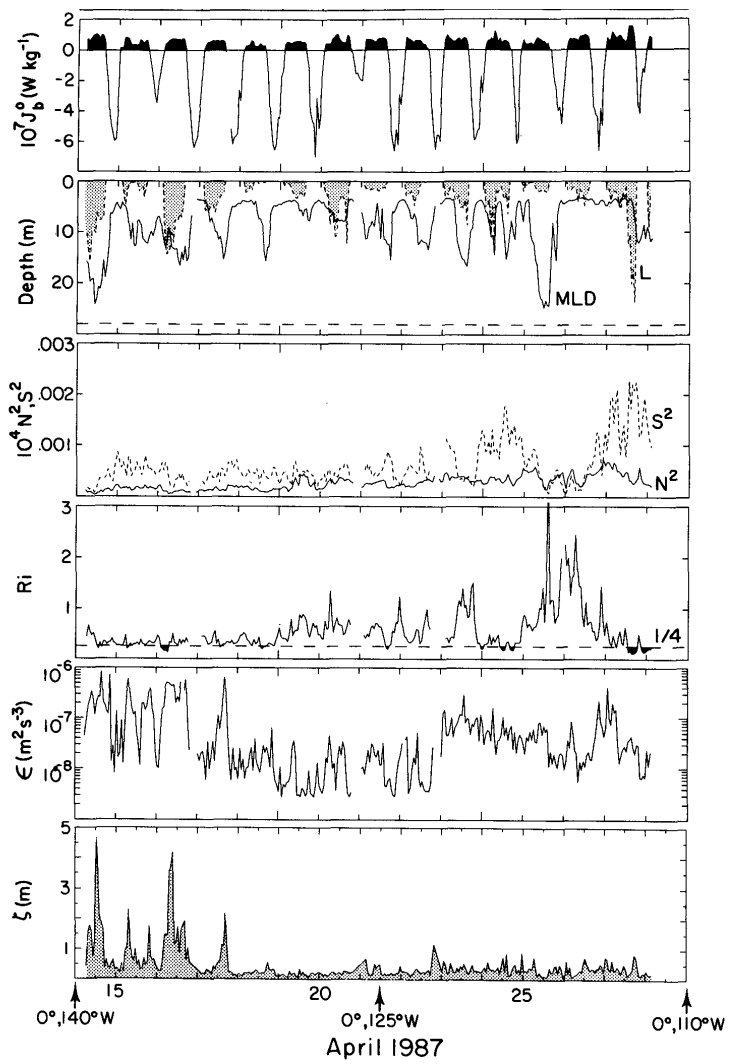

Figure I.3: Observations taken during April 14-28, 1987. Hourly-averages of: surface buoyancy flux; mixed-layer depth, MLD; squared shear, S^2 and squared buoyancy frequency, N^2; gradient Richardson number, Ri_g; turbulent dissipation, ϵ; and isotherm displacement, η. MLD is estimated as the depth at which the density exceeds the surface value by 1%. Ri_g, ϵ and η are at 28 m depth. Adapted from Moum *et al.* (1992)

I.B Deep-cycle Turbulence

One of the most important observations in the EUC system is the induced dissipation rate in the upper flank of the EUC core at night time. The peak nighttime dissipation rate of the turbulent kinetic energy in the marginally-stable region exceeds

(a)

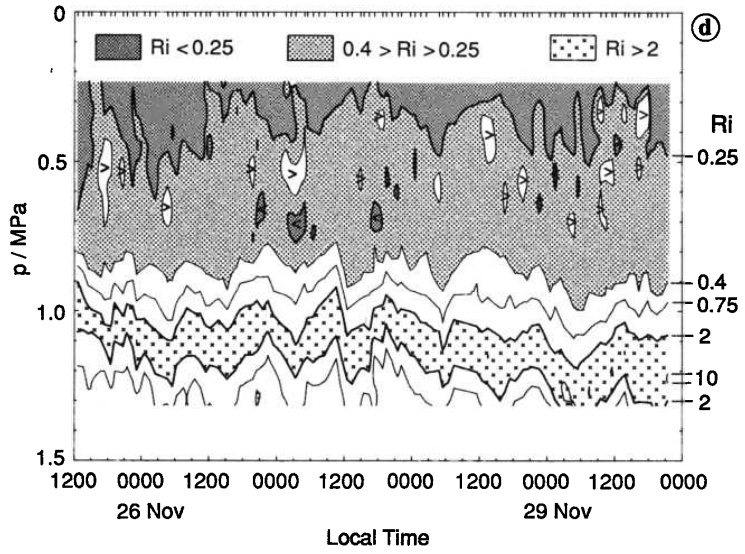

(b)

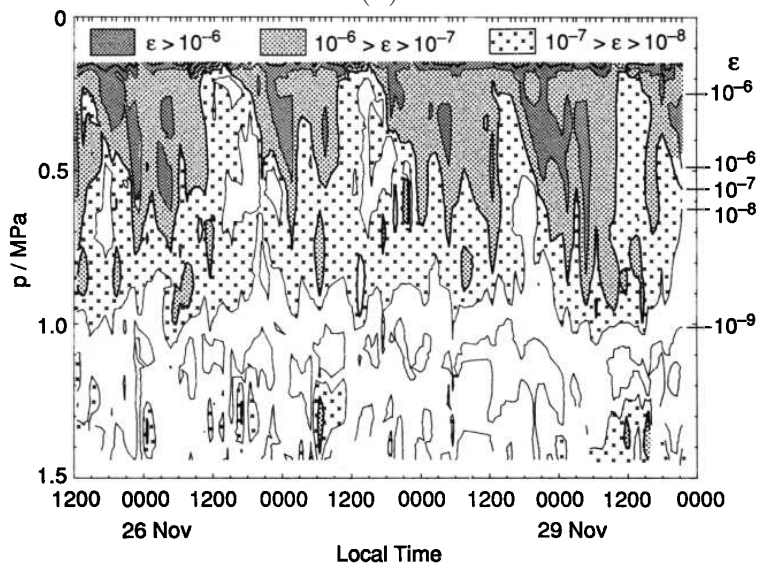

Figure I.4: (a) Gradient Richardson numbers, Ri_g and (b) turbulent dissipation, ϵ, in log scale. Adapted from Peters *et al.* (1988)

the corresponding daytime value by at least a factor of 10 as described by Lien *et al.* (1996), Moum *et al.* (1989), and Peters *et al.* (1994), the so-called deep-cycle turbulence. Fig. I.4 shows the deep-cycle turbulence observed by Peters *et al.* (1988) during TH1. The figure shows bursts of turbulence from the upper weakly-stratified region into the thermocline above the EUC core during night time.

During TH1, Gregg *et al.* (1985) identify five zones within the EUC system with respect to dissipation rate, ϵ: (1) the diurnal mixed layer, upper 10 to 30 m, has high dissipation rate which is correlated with the surface heat flux; (2) the upper high-shear zone, 30 to 90 m below the surface, has dissipation rate and turbulent flux that are high although less than mixed layer values and decreases with depth as Ri_g increases. In this zone, the dissipation rates vary by at least a factor of 10 during a diurnal cycle; (3) the EUC core region, 90 to 120 m, where the zonal velocity peak lies, has low dissipation rates; (4) the lower high-shear zone, 125 m to 150 m, has high dissipation rate which the authors suggest to be due to the intrusions of the salinity maximum. The high dissipation rate in the upper high-shear zone is suggested to correlate to enhanced internal wave activity. It is suspected that internal waves, generated when the turbulence is strong in the mixed layer, propagate down and "break" in the high shear region leading to high nighttime dissipation rates in the upper shear zone. During the day, the mixed zone is restratified, turbulence is suppressed resulting in little wave activity in the shear zone.

Peters *et al.* (1988) further examine data from TH1 and attempt to parameterize turbulence in the EUC system in terms of gradient Richardson number, Ri_g. They define three vertical regions of the EUC: (1) the upper shear zone, from 23 m to 100 m below the surface, has low Ri_g, average of 0.35; (2) the EUC core, between 100 m to 130 m, has Ri_g greater than 2.0; (3) the lower shear zone, below 130 m, has low Ri_g, about 0.5. In region 1, athough the average over a 4.5 day period is $Ri_g = 0.35$, about 40% of the data set shows values of Ri_g below the critical value 0.25. The value of Ri_g exhibits a diurnal cycle only in the region above a depth of 50 m. A transition dissipation rate, $\epsilon_{tr} = 25\nu N^2$, is used as a reference value to signify turbulence activity. The dissipation rate in this upper-shear zone is as high as 1000 times the transition value and varies diurnally by a factor of 100 between daytime and nighttime values. The turbulent dissipation rate is low in regions 2 and 3.

The dataset of Moum *et al.* (1989), also taken during TH1, exhibits deep-cycle turbulence too. The diurnal surface layer is weakly-stratified rather than truly well-mixed. This layer is defined by the density step at its base which cycles between 10 m

during daytime and 35 m during nighttime. The average dissipation is approximately twice the surface buoyancy production of turbulent kinetic energy, and 3 times larger than the expected value in a purely convective mixed layer suggesting that this layer is not driven mainly by convective forcing. In the well-stratified thermocline, turbulent "bursts" of 2 to 3 hours at night separated by several hours are observed. Although the dissipation is intermittent at night, the rates are 100 to 1000 times larger than during the day. The day-night cycle is stronger in the thermocline than in the surface layer. The bursts are suspected to relate to internal waves generated at the mixed layer base. One example of breaking internal waves is noted in the towed thermistor chain measurement. The data shows induced dissipation when a wave packet, 15 m in vertical displacement and 500 m in horizontal wavelength, breaks at night. Nearly 70% of the surface heat flux is transported vertically below 30 m by turbulent mixing, and an insignificant amount penetrates the EUC core.

Wijesekera & Dillon (1991) use a wave dissipation model based on the observed turbulent kinetic energy dissipation rate from TH1 to investigate the momentum budget of the upper equatorial ocean. From the model's results, they conclude that, after sunset, internal waves are generated at the base of the mixed-layer as a result of convective overturns. As the waves propagate downward, they become unstable and generate turbulent eddies above the EUC core where the local Ri_g is driven to be less than 0.25 due to the overlap of internal waves and EUC shear. The dissipation rate at the EUC core is small because of the small shear. The model shows that the vertical length scales of the wave field are greater than 100 m. The wave radiation stress is estimated to be as large as the observed average wind stress and an order of magnitude larger than the turbulent shear stress suggesting a higher efficiency of wave transport relative to turbulent transport. The model also predicts that most of the wave stress at the base of the mixed-layer penetrates below the EUC core. The prediction is not nullified by results of TH1 because measurements are not available below the EUC core. Moum *et al.* (1992) and later observations during TIWE by Lien *et al.* (1996) report that there is low wave activity below the core. This is possibly the reason why Wijesekera & Dillon (1991) cannot close the equatorial momentum budget. The authors indeed

suggest that the internal wave must somehow deposit momentum in the region above the EUC core in order to balance the zonal pressure gradient. Results from later observations of Hebert *et al.* (1992) show breaking of the internal waves into small-scale turbulence.

I.C Internal Gravity Waves in a Stratified Shear Flow: Linear theory

Since the present study involves internal gravity waves, it is necessary to introduce the basic theory governing wave motion. A more detailed discussion can be found in Nappo (2002) and Pedlosky (2003) . The two-dimensional Euler equations for irrotational and inviscid flow in a non-rotating frame under the Boussinesq approximation can be written as follows:

$$\begin{aligned} \frac{\partial u}{\partial t} + u\frac{\partial u}{\partial x} + w\frac{\partial u}{\partial z} &= -\frac{1}{\rho}\frac{\partial p}{\partial x}, \\ \frac{\partial w}{\partial t} + u\frac{\partial w}{\partial x} + w\frac{\partial w}{\partial z} &= -\frac{1}{\rho}\frac{\partial p}{\partial z} - g, \\ \frac{\partial u}{\partial x} + \frac{\partial w}{\partial z} &= 0, \\ \frac{\partial \rho}{\partial t} + u\frac{\partial \rho}{\partial x} + w\frac{\partial \rho}{\partial z} &= 0. \end{aligned} \tag{I.1}$$

The above equations can be linearized as follows:

$$q\left(x,z,t\right) = q_0\left(z\right) + q_1\left(x,z,t\right), \tag{I.2}$$

where $q_0\left(z\right)$ is the background field corresponding to horizontally uniform quantities and $q_1\left(x,z,t\right)$ denotes perturbations. Eqs. I.1 can be solved by assuming wave-like solutions of the form

$$q_1\left(x,z,t\right) = \hat{q}_1\left(z\right)e^{i(kx-\omega t)}, \tag{I.3}$$

where k is the horizontal wavenumber and ω is apparent frequency of the waves in a fixed coordinate system. Solving for $\hat{w}$, the result yields the Taylor-Goldstein equation:

$$\frac{d^2\hat{w}}{dz^2} + \left[\frac{N^2}{(c-u_0)^2} + \frac{u_0''}{(c-u_0)} - k^2\right]\hat{w} = 0, \tag{I.4}$$

where $N^2 = -(g/\rho_0)d\rho_0/dz$ is the squared buoyancy frequency and $c = \omega/k$ is the apparent horizontal phase speed. The terms inside the bracket are crucial in determining the wave solution. When the bracket is positive, the solution consists of propagating modes. In constrast, the waves are evanescent when the bracket is negative.

When the Taylor-Goldstein equation is interpreted in a reference frame moving with speed u_0, the frequency is Doppler-shifted,

$$\omega = \Omega + u_0 k, \tag{I.5}$$

where Ω is the intrinsic frequency measured in the moving frame. Similarly, the intrinsic horizontal phase speed is

$$c_I = \frac{\Omega}{k} = c - u_0. \tag{I.6}$$

An important property of an internal wave field is its group velocity defined as

$$u_g = \frac{\partial\omega}{\partial k}, \quad w_g = \frac{\partial\omega}{\partial m}, \tag{I.7}$$

where k, m denote the horizontal and vertical wavenumbers, respectively. The group velocity quantifies the flux of energy carried by the internal waves. The direction of the group velocity is perpendicular to the wavenumber vector, (k, m).

When there is no background velocity, $u_0 = 0$, Eq. I.4 becomes

$$\frac{d^2\hat{w}}{dz^2} + \left[\frac{k^2N^2}{\omega^2} - k^2\right]\hat{w} = 0. \tag{I.8}$$

Solving the above equation yields the dispersion relation

$$\omega = \frac{kN}{(k^2+m^2)^{1/2}} = Ncos\theta, \tag{I.9}$$

where θ is the angle that the group velocity makes with the vertical or the wavenumber vector makes with the horizontal. It can be seen that, for a propagating mode, the intrinsic wave frequency cannot be larger than the buoyancy frequency of the ambient.

Since the stratification varies in the ocean, it is important to know how the change affects wave propagation. Consider a two-layer problem with the lower layer stratified with N_1, the upper with N_2, and no background flow. A monochromatic wave with frequency ω propagates upward from region 1 to 2. At the interface, the wave can transmit or reflect depending on the background stratification. The reflection coefficient, r, is defined as the ratio of the amplitude of the reflected downward wave to the incident upward wave. According to linear analysis,

$$r = \frac{m_1 - m_2}{m_1 + m_2}, \tag{I.10}$$

where m_1 and m_2 are the corresponding vertical wavenumbers. When $r = 0$, the wave is totally transmitted. When $|r| = 1$, there is complete reflection and the wave is trapped in region 1. In the case $N_2 < \omega < N_1$, the wave propagates in region 1, is evanescent in region 2, and suffers complete reflection at the interface. In contrast, in the case $N_1 < \omega < N_2$, a wave which is evanescent in region 1 can propagate in region 2 and the associated Reynolds shear stress can still transport momentum vertically from region 1 into region 2. As shown by the Taylor-Goldstein equation, the ambient velocity u_0 can also change the sign of the bracket term thus affecting the wave modes. At a velocity interface where u_0 abruptly changes, wave reflection may occur, similar to that at the interface between two levels of stratification.

An interesting scenario occurs when the bracket term in the Taylor-Goldstein equation becomes undefined with the wave phase speed c equal to the ambient velocity u_0. A layer at which such a condition prevails is called a critical layer. When internal waves pass through the critical level, the wave stress is reduced significantly. Booker & Bretherton (1967) show that the coefficient of reduction is $e^{-2\pi\sqrt{R_c - 0.25}}$ where R_c is the Richardson number at the critical level. When $R_c > 0.25$, the wave is absorbed by the mean flow. With $R_c = 0.5$, which is typical in the EUC core, less than 4% of the wave stress can pass through the critical layer. When $R_c < 0.25$, the waves becomes unstable and break into turbulence.

I.D Observations of Internal Gravity Waves in the EUC

To understand the physics of the deep-cycle turbulence, Moum *et al.* (1992) return to the Pacific EUC in TH2. The temperature time record taken by a towed thermistor shows intermittent occurrence in the thermocline of high-frequency narrowband bursts whose characteristic frequency, upon conversion using $\lambda = U_{ship}/f$, gives a wavelength of $150-250\,m$. The results illustrate a strong correlation between turbulent dissipation and internal waves in the thermocline below the mixed layer and above the EUC core. In this region, both turbulence and internal waves display diurnal behavior with nighttime values of the dissipation rates and wave potential energy 100 times larger than at daytime. The authors conclude from the data that, in the low-Ri region of the thermocline, breaking of internal wave packets is the main source of turbulence. (However, we note that the shear was lower and stratification higher in TH2 relative to TH1). The internal waves are generated locally and dissipated quickly. The timescale for dissipation of the internal wave energy by turbulence is less than 1.0 hour indicating that the waves cannot travel far in the horizontal direction and the absorption of wave energy by the mean flow is as important as the dissipation of waves by turbulence. One possible wave generation mechanism is suggested to be the "obstacle effect". Waves are generated by large-scale mixed-layer eddies impinging on the mixed-layer base. In the presence of the EUC current, internal waves are excited as in the case of lee waves by flow past hills in the atmosphere. These waves are anisotropic with a phase speed of about the average velocity of the mixed-layer and unstable to both advective and shear instabilities. Another source of waves is the Kelvin-Helmholtz shear instability since the gradient Richardson number, Ri_g, is marginally critical in this region. The presence of finite-amplitude internal waves in a stratified shear flow results in a reduction of critical wave slope for which advective instabilities occur (Thorpe, 1978). Munk (1981) in his review notes that region with $Ri > 0.25$ can be unstable to advective instability (Thorpe, 1978) if the wave slope is sufficiently large. It is possible that the internal waves are due to both the "obstacle effect" and shear instabilities; the observations are

unable to distinguish between them.

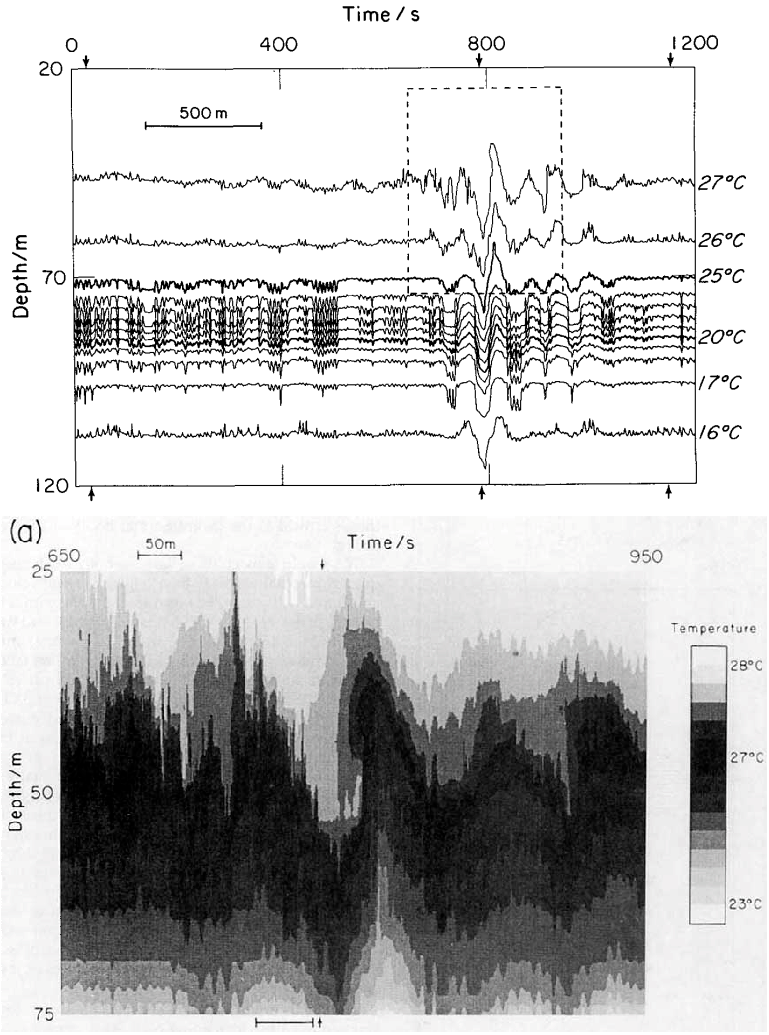

Figure I.5: (Top) Temperature field exhibits an internal wave packet. Region within the dotted box is expanded in the bottom figure showing wave overturning event. Adapted from Hebert *et al.* (1992)

.

Also in the Tropic Heat II experiment, Hebert *et al.* (1992) report the details of a single internal wave packet in which one of the waves exhibits an overturning event. Figs. I.5, taken from their paper, shows the wave packet in the temperature field. The packet consists of five distinct wave crests and six troughs, coherent over the thermocline. The wave has horizontal wavelength of approximately 100 m, maximum

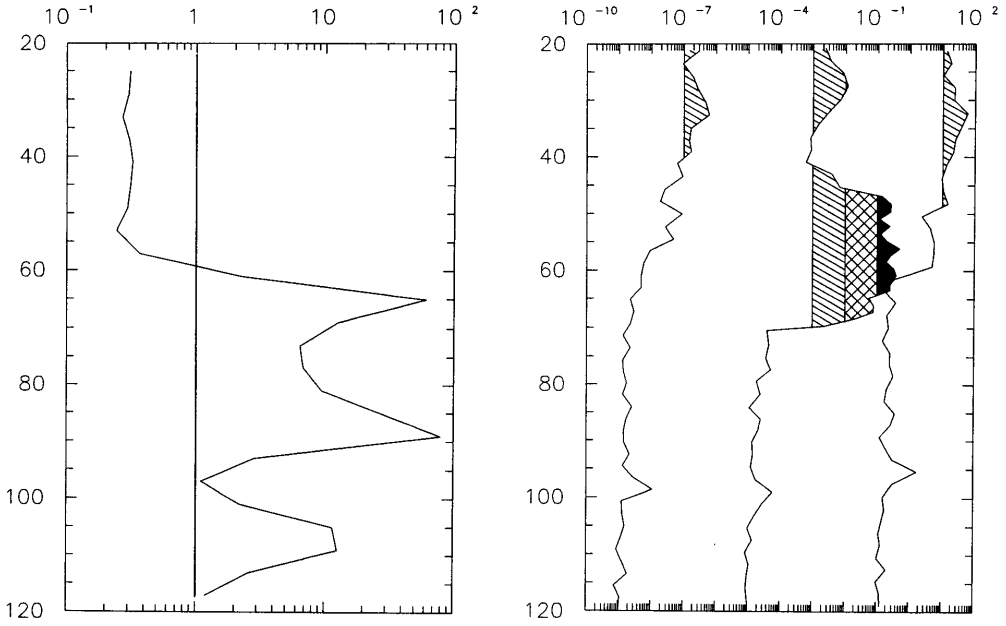

Figure I.6: (Left) Gradient Richardson number computed by using hourly-average zonal velocity profile and the average of the density profiles before and after the wave packet. (Right) Turbulent dissipation profiles before, during and after the wave packet offset by four decades. Values $> 10^{-7}$ are hatched, those $> 10^{-6}$ are cross-hatched, and those $> 10^{-5}$ are black. Adapted from Hebert *et al.* (1992)

.

peak-to-peak amplitude of 20 m at depth 50 m. The frequency is expected to be near the buoyancy frequency ($N \simeq 0.01 s^{-1}$ with corresponding time period of about 10 min). The middle wave crest of the packet is gravitationally unstable resulting in overturning. Although $Ri \approx 0.3$, according to Thorpe (1978), instability is still inflicted because the middle wave has a larger wave slope relative to other waves in the packet. Both advection and shear can be possible sources for intability. The two wave crests and troughs to the left have high-frequency fluctuations suggesting that turbulent mixing does occur. The two waves to the right shows no sign of mixing. The dissipation rates within the patch of the overturning wave is at least three orders of magnitude larger than outside the patch as shown in Fig. I.6. The wave signature is coherent in both low and high-Ri_g regions, with the induced dissipation extending

well into the high-Ri_g region. The Thorpe overturning scale is of the order of Ozmidov buoyancy length scale, $L_O = (\epsilon/N^3)^{1/2}$, implying that the breaking wave energy can be quickly dissipated within one buoyancy period.

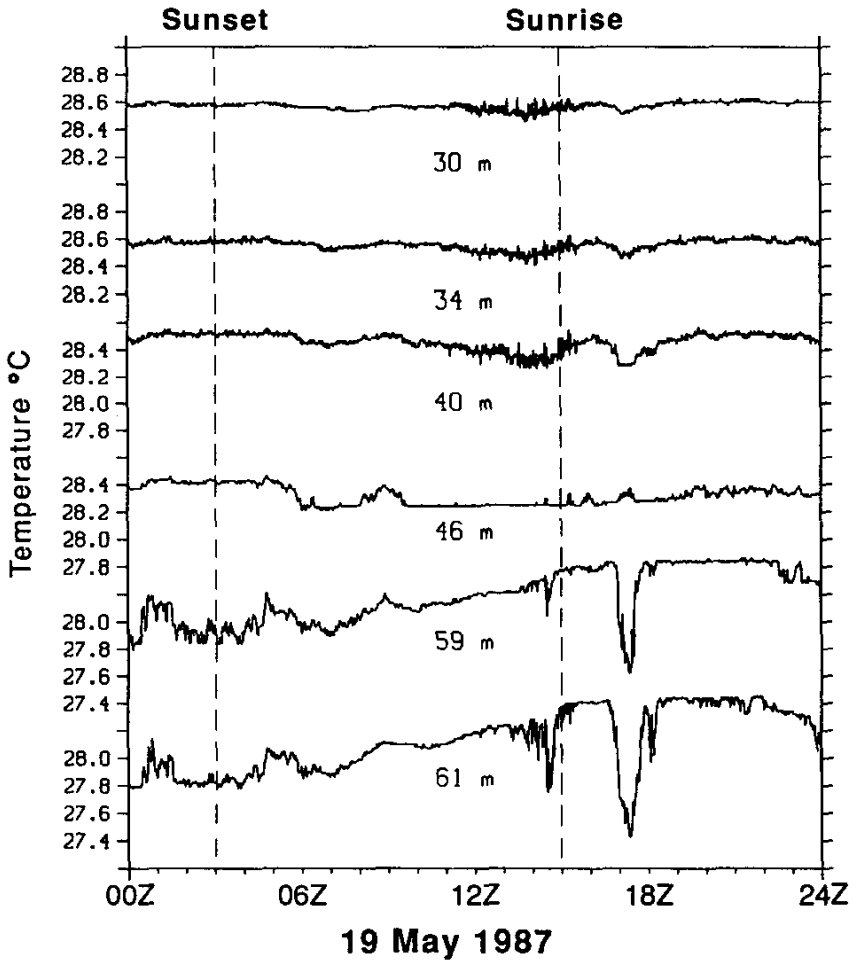

Figure I.7: Time series of temperature measured at various depth. The nighttime mixed-layer depth is 30-34 m. High-frequency fluctuations are observed at sunrise. Adapted from McPhaden & Peters (1992)

.

McPhaden & Peters (1992) analyze temperature time series taken at an equatorial surface mooring, 140°W, including a special dataset with 1 min temporal resolution. As shown in Fig. I.7 a strong diurnal cycle in temperature variance at frequencies of 10-30 cycles per hour and coherent over a 31 m extending into the thermocline is evident and attributed to an internal wave field. The local buoyancy frequency is 6-10

cycles per hour. The authors suggest the following scenario for deep-cycle turbulence: Internal waves are excited at the base of the nighttime mixed layer. As they propagate downward, they are Doppler-shifted to frequencies higher than the local buoyancy frequency by the EUC. In the thermocline, the vertical wave shear superimposed by marginally-stable shear of the EUC triggers local shear instability. The local instability grows and break down into small-scale turbulence. We note that, although plausible, this scenario is not directly validated by the observations.

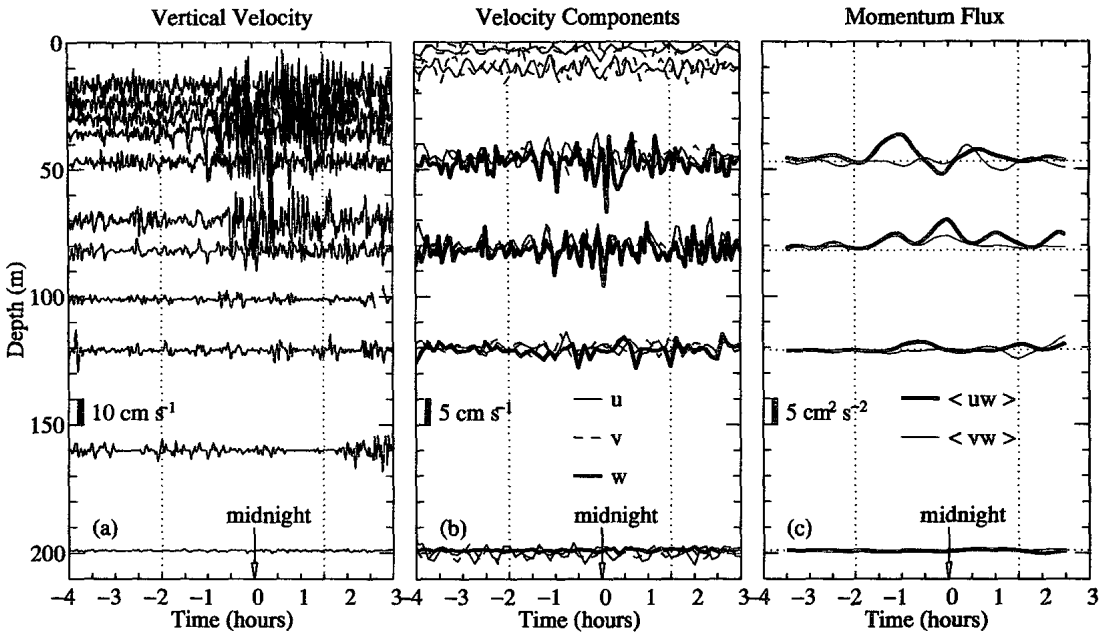

Figure I.8: Time series of velocities and momentum fluxes with a wave packet. The wave packet is recorded on 8 November 1991. The vertical dotted lines in (c) enclose the period of the wave packet. Adapted from Lien *et al.* (1996)

Lien *et al.* (1996) further confirm the correlation between internal waves and deep-cyle turbulence by revisiting the Pacific EUC during the Tropical Instability Wave Experiment (TIWE) in winter 1991. Moored measurements of horizontal velocities and temperature shows nighttime enhancements of high-frequency temperature variance, vertical isotherm displacement variance and zonal velocity variance in the region below the mixed-layer and above the EUC core. (The vertical isotherm displacement is defined as $\eta = -(T - \langle T \rangle)/\partial_z T$ where the bracket denotes the low-pass filtered temper-

ature field.) The enhancements occur at frequencies close to and above the background buoyancy frequency. Internal waves can have higher-than-N frequency when they are Doppler-shifted by the EUC. Analysis of the energetics at 45 m depth shows the average ratio between the hourly-average potential energy, $\frac{1}{2}N^2\eta^2$, and the horizontal kinetic energy, $\frac{1}{2}(u^2+v^2)$, to be 0.76. The ratio between the dissipation rate and the shear production is about 0.5. The buoyancy flux is estimated to be 2%-15% of the shear production, leaving 35%-48% for transport, either through short-range turbulence processes or through long-range internal wave radiation. The evolution of an internal wave packet during the experiment is shown in Fig. I.8. The waves are found to propagate downward and westward with wavelength larger than 200 m. The wave period is about 20 min comparable to the value of the local buoyancy period which varies between 8.5 min and 30 min at a depth of 45 m. The vertical coherence is at least 10 m, much larger than the overturning scale of about 1 m at the mixed layer base, so that the variability is associated with an internal wave and not overturning turbulence. The wave signature is clear in the upper 45 m, becomes less obvious between 45 m and 80 m and disappear below the EUC core. In the presence of the wave packet, the momentum fluxes are enhanced in the upper 80 m and negligible below the EUC core. The shear production is estimated to be of the same order as the dissipation rate.

Lien *et al.* (2002) revisit the Pacific EUC in 1998 to further strengthen the correlation between internal waves and turbulence. Measurements are done in both Lagrangian and Eularian frames. The Lagrangian data are collected by neutrally-buoyant floats moving with water motions. Mooring at 0°, 140° W provides Eularian data. The two data sets agree well when the Doppler-shift is used to relate the two reference frames. The frequency spectra of vertical velocity, vertical acceleration and the time rate of change of temperature computed from the data collected from the float deployed at 45 m depth (surface mixed layer is shallower than 25 m) shows the presence of near-N internal waves. These waves are found to propagate westward with a zonal wavelength of approximately 360 m and a phase speed of 0.5 m/s. During deployment, the float also encounters a shear instability event in which a strong turbulence burst is recorded. The heat flux during the burst is more than 4000 W/m^2 which is two

orders of magnitude larger than the average values before and after the event. The authors believe that the near-N internal waves are generated locally in the deep-cycle layer through shear instability. The background condition is favorable with Richardson number Ri of 0.19. Some of these waves break suppling energy to the turbulence. Some radiate away forming the background near-N waves.

I.E Numerical models of small-scale processes in the EUC

Both, two- and three-dimensional numerical investigations, are reviewed. However, it is worth noting that the nonlinear evolution of the disturbances and the turbulent dissipation rates are not expected to be accurate in the two-dimensional simulations.

Two-dimensional simulations

Skyllingstad & Denbo (1994) perform two-dimensional nonhydrostatic simulations with background conditions taken from the data of Tropic Heat experiments to investigate the role of internal waves in the EUC system. The domain size was $1280\,m \times 300\,m$ discretized with a 256×60 grid with a uniform grid spacing of $5\,m$. An eddy viscosity model with a Ri_g-based stability function was employed. The model was forced with a wind stress and a heat flux that corresponds to daytime heating and nighttime cooling and, during an initial period of a day, random fluctuations of the heat flux were imposed to facilitate spinup. Internal wave packets are observed to propagate downward and always westward or upstream *relative* to the jet velocity. For the profile 134W-1987 in Fig. I.1, the peak wavelength is about 250 m and the frequency is about 0.5 cph. Kelvin-Helmholtz (KH) instabilities are observed in the high-shear, low Ri_g region and it is hypothesized (but not demonstrated) that the internal wave packets are associated with the KH instabilities. For the profile 140W-1987 in Fig. I.1, the horizontal wavelength of the internal wave packets is smaller, approximately 100 m and the frequency is higher. Furthermore, there is the possibility of critical layer

dynamics associated with the wave phase velocity becoming equal to the local flow velocity, since the surface velocity (assumed to be the phase velocity of the internal waves) is eastward in this profile. The existence of critical layers in the EUC system has not been confirmed by observations. A later study of Lien *et al.* (1996) shows wave activity in the lower flank of the EUC; however, the possibility of a critical layer is not discussed.

Sutherland (1996) solves the two-dimensional nonlinear equation of motions for incompressible Boussinesq flow to investigate if shear instability of the upper-flank of the EUC can excite downward propagating internal waves of large amplitude. The velocity profile $U(z)$ and the squared buoyancy $N^2(z)$ profile are approximated by hyperbolic tangent functions. The inflectional points of the profiles are offset by a vertical distance such that the shear layer resides above the thermocline. The stratification in the shear layer is quantified by the parameter $J_0 = N_0^2/S^2$ where $S = max(|dU/dz|)$. Similarly, the stratification in the deep region is measured with a parameter J_d defined with the deep value of N^2. Two sets of simulations are interrogated: $J_0 = 0$ (unstratified shear layer) and 0.05 (weakly-stratified shear layer). In each set, values of J_d vary between 0.2 to 0.4. In both sets, strong internal excitation are observed in cases with $J_d = 0.4$, and there is no excitation when $J_d = 0.2$. Internal waves are excited directly by the growth of the most unstable normal mode of linear theory. The effect of the stratification in the shear layer is to enhance the interaction between the wave and mean flow by allowing the transfer of eddy energy between the forms of available potential and kinetic energy. The author concludes that strong internal waves are excited when $J_0 < 0.25$ and $J_d > 0.25$. The momentum extracted from the mixing region causes the mean flow to decelerate significantly. The author also speculates that internal waves can travel to great depth where they become a source of momentum driving the zonal countercurrent.

Sun *et al.* (1998) numerically solve the Taylor-Goldstein equation using the hourly-averaged currents and stratification observed in TIWE experiment to investigate the role of shear instability in maintaining deep-cycle turbulence. The results suggest four regimes of instability based on the zonal current structure. The first regime

consists of westward surface flow, and therefore, has phase velocity directed to the west. The gradient Richardson number in this regime drops to nearly zero, suggesting strong instability. However, the authors indicate that the instability can be damped by boundary proximity effects. Smallest growth rate is observed here. The second regime lies at the boundary between the surface westward current and the eastward flow of the EUC where the local velocity is near zero. In this regime, the instabilities are most energetic with the largest growth rate. The third regime resides on the upper flank of the EUC with the instabilities having eastward phase velocity. This regime is intermittently unstable with very small growth rate. The fourth regime is associated with a thin shear layer at the bottom of the EUC near 180 m depth. Like the third regime, the instability here is weak and intermittent. In terms of the entire EUC system, the frequencies of the unstable modes with the largest growth rate are a few cycles per hour. These modes have phase speed ranging from 0.3 m/s westward to 0.4 m/s eastward with wavelengths between 100 to 400 m. The analysis of the kinetic energy equation indicates that instabilites are capable of transporting energy vertically. The authors find the temporal and spatial characteristics of the unstable modes in this study to be consistent with the parameters of the observed internal waves and, therefore, conclude that shear instability is responsible for the deep-cycle turbulence.

Smyth & Moum (2002) perform stability analysis and nonlinear two-dimensional simulations of an asymmetrically-stratified Bickley jet to study the possible instability mechanism and wave propagation characteristics of internal waves in the EUC system. The jet is stratified with the N^2 profile having a step function. The stratification in the upper and lower flanks of the jet is defined by J_U and J_L, respectively. Although the jet with such a density profile is a highly idealized model flow relative to the undercurrent, the study reveals important characteristics. In the case where the jet has a constant value of N across its entire extent, there is no instability when $J_U = J_L > 0.13$. In the cases with asymmetric stratification, the marginal stability curves show a range of J between 0.17 and 0.22 so that if one of the J value falls below this range, the jet becomes unstable. In the case of $J_U = 0.0$ and $J_L = .09$, three classes of unstable normal modes

are found: the extended sinuous (S) and varicose (V) modes similar to ones seen in the classical unstratified jet and a newly discovered mode, namely the R mode. When J_L increases to 0.25, the V mode is damped out but the R mode persists. The R mode can grow despite the strong stratification in the lower-flank since it extracts energy from the upper-flank where the stratification is weak. Nonlinear simulations of cases with $J_U = 0.0$ and 0.05, and the deep value of $J_L = 0.25$ shows internal waves propagating downward, away from the jet. Internal waves are not observed in the case $J_U = 0.0$, $J_L = 0.14$. The internal waves excited by the R mode have larger wavelength and phase speed compared to the observed values in the EUC. Strong 'turbulence' is observed in the lower-flanks where strong stratification is present. The authors suggest that waves are generated by weakly-stratifed shear in the upper-flank, propagate downward, and break when they encounter the more strongly-stratified lower-flank.

Three-dimensional simulations

Wang *et al.* (1998) investigate the deep-cycle turbulence of the EUC using a three-dimensional LES model. The model includes many large-scale flow terms: the EUC currents, zonal pressure gradient, upwelling, horizontal divergence, zonal temperature gradient and mesoscale eddy forcing. The model is forced with a constant easterly stress and a surface heat flux with diurnal heating/cooling, and the subsequent evolution of the flow variables is obtained. The subgrid model is an eddy viscosity model with a equation for subgrid turbulent kinetic energy and Ri_g-based stability functions for the vertical transport (Moeng, 1984; Sullivan *et al.*, 1996). The domain size is $160\,m \times 160\,m \times 270\,m$ with a grid of $32 \times 32 \times 270$ points. The mixed layer depth (defined by the z location where the density differs from the surface density by $0.01\,kg/m^3$) shows a clear diurnal cycle between a minimum daytime value of approximately $5\,m$ to a nighttime peak of $30\,m$. During the night, the turbulence dissipation rate is observed to penetrate to a depth of $80\,m$, as much as 50 m below the mixed layer base. The gradient Richardson number in the mixed layer and region right below can be lower than 0.25. About 40 m below the mixed-layer base, the gradient Richardson number is always greater than 0.25 but the flow is still turbulent. It is suggested that the deep-

cycle turbulence is related to local shear instability. Nonetheless, the model does *not* show propagating internal waves. The horizontal domain of the model is 160 m which is comparable to only one wavelength of internal waves observed in previous studies.

In a subsequent study, Wang & Muller (2002) increase the domain size to $960\,m \times 320\,m \times 270\,m$ to allow internal waves, and employ a $192 \times 64 \times 270$ grid. The authors examine the effects of the EUC mean velocity profile upon the mixed layer turbulence and the internal wave field. The important conclusion of Wang & Muller (2002) is that the inclusion of the *full* EUC current profile is crucial to obtain deep-cyle turbulence whose characteristics are consistent with observations. There is no wind stress in the model; a *constant* surface cooling is the only forcing term so that it is convective turbulence that is generated in the surface layer. The ambient flow is divided into two regions: (1) The unstable upper mixed region from the surface to 30 m below ($Ri_g < 0.25$); (2) the stably-stratified EUC region below 30 m ($Ri_g > 0.25$). A simulation with the full EUC velocity profile showed internal wave packets with a broad spectral peak at about $320\,m$ and a frequency of about 1.2 cph. However, the disturbance field was not directly interrogated to examine linear theory results for dispersion and polarization of freely propagating internal waves. Turbulence penetrates up to 55 m where the mean value of Ri_g is as large as 0.4. A simulation with the shear in region 1 removed shows that, relative to the full shear case, turbulence penetration is weaker, the internal wave wavelength is larger and its amplitude smaller. Simulation with the shear in region 2 removed also results in weak penetration of turbulence into the mixed layer. However, the internal waves have a larger energy flux and their wavelength, approximately 80 m, is smaller relative to the numerical experiment with the full velocity profile. The thermal plumes in the surface layer, although necessary, are not the primary mechanism for the generation of internal waves. Instead, the plumes trigger shear instability resulting in the impingement of large-scale overturns at the mixed-layer base. The internal waves are primarily excited by shear instability in the mixed region and extend into the stable EUC region. The authors find that local shear instability in the region below the mixed layer can occur when the mean Richardson number is below 0.4.

I.F Approaches and model problems

From the above observations and numerical studies, it is clear that deep-cycle turbulence strongly correlates with intermittent internal waves with coherent phase propagation is more complex than classical shear-driven turbulence. At the same time, the propagating internal waves do not fit the simple picture of linearly evolving disturbances and a number of outstanding issues remain as discussed below. In the thesis, the EUC problem will be revisited using DNS techniques. DNS will allow the investigation of internal wave transport and turbulence dissipation rates without recourse to any subgrid model, albeit at modest values for the dimensional length scales and nondimensional Reynolds number.

The literature survey shows that the mechanism underlying internal wave generation is unclear. The first hypothesis is that the waves are associated with linear instability of the zonal current in the thermocline. Locally, a combination of increased shear and decreased stratification leads to an instability of the mean profile that is manifested as an internal wave packet. The local shear instabilites grow, evolve nonlinearly and eventually result in deep-cycle turbulence. This hypothesis is supported by the studies of Lien *et al.* (1996) and Lien *et al.* (2002). Additional support is provided by the stability analysis and 2-dimensional calculations of Sutherland (1996) and Smyth & Moum (2002) showing that a region with low Ri_g supports a linear instability that propagates into the deeper region with high Ri_g. The second hypothesis suggests that internal waves are generated by flow of the EUC jet relative to the corrugated base of the mixed layer, analogous to internal wave generation by stratified flow over rough topography. The corrugations are presumably caused by surface layer instabilities, instabilities at the sheared interface, or by mixed layer turbulence. The downward-propagating internal waves break down when they encounter strong shear in the upper flank of the EUC leading to enhanced dissipation. Unlike the first hypothesis, the local value of Ri_g in the thermocline does not have to become less than 0.25 to generate internal waves. The studies of Peters *et al.* (1988), Moum *et al.* (1989), Wijesekera & Dillon (1991), Skyllingstad & Denbo (1994), and Wang & Muller (2002) support this

hypothesis. We note that the recent LES study of a stratified bottom boundary layer by Taylor & Sarkar (2007) and Taylor & Sarkar (2008) show internal waves generated by broadband turbulence that develop a peak near $N/\sqrt{2}$ in the propagation region. There is no external shear in the model problem preventing any subsequent nonlinear evolution of the internal wave packets. The contribution of the internal wave field to momentum transport into the interior and to local dissipation is not clear. The thesis research will help quantify these quantities as a function of environmental parameters. The study consists of the following subproblems:

1. DNS of a weakly-stratified shear layer above a thermocline. Results of this study presented in Chapter III characterize the internal waves and turbulence associated with shear instabilities at the base of a weakly-stratified region.

2. The simulations in problem 1 are re-examined to investigate the wave fluxes at higher Reynolds number. Results of this study presented in Chapter IV also provide details of turbulence and mixing inside the shear layer as well as their parameterizations.

3. DNS of a stratified jet patterned on the EUC profile with an upper weakly stratified sheared region. Results of this simulation presented in Chapter V shed light on the interaction of internal waves (generated by shear instabilities as in problem 1) with the external shear present in a jet to result in turbulence.

4. DNS of a stratified jet subject to surface windstress and buoyancy forcing. Results of this study presented in Chapter VI highlight the roles of the surface forcing as well as the fine-scale response of the jet.

Chapter II

Numerical Method

II.A Governing Equations

The conservation equations for mass, momentum and density for an unsteady, incompressible flow under the Boussinesq approximation are solved numerically. These equations are:

Mass:

$$\frac{\partial u_j}{\partial x_j} = 0, \tag{II.1}$$

Momentum:

$$\frac{\partial u_i}{\partial t} + \frac{\partial \left(u_j u_i\right)}{\partial x_j} = -\frac{1}{\rho}\frac{\partial p}{\partial x_i} + \nu \frac{\partial^2 u_i}{\partial x_j \partial x_j} + F_i, \tag{II.2}$$

Density:

$$\frac{\partial \rho}{\partial t} + \frac{\partial \left(u_j \rho\right)}{\partial x_j} = \kappa \frac{\partial^2 \rho}{\partial x_j \partial x_j}. \tag{II.3}$$

Here, ν is the kinematic viscosity, κ is the molecular diffusivity, and F_i are terms of external forcing such as gravity or horizontal pressure gradient. The asterisks denote dimensional quantities. Since the Boussinesq approximation is employed, the density is decomposed into a constant reference density, ρ_0 and a small departure which is further split into a mean component, $\langle\rho\rangle$, and a fluctuating component, ρ':

$$\rho = \rho_0 + \langle\rho\rangle\left(z\right) + \rho'\left(x_i, t\right). \tag{II.4}$$

The hydrostatic contribution of the reference density, ρ_0, and mean component, $\langle\rho\rangle$, to the pressure is subtracted from the total pressure so that the dynamic pressure is

solved for, and it is only the fluctuating component of the density field that contributes to the buoyancy effect in the momentum equation. Eq. II.2 reduces to

$$\frac{\partial u_i}{\partial t} + \frac{\partial (u_j u_i)}{\partial x_j} = -\frac{\partial p}{\partial x_i} + \nu \frac{\partial^2 u_i}{\partial x_j \partial x_j} + \frac{\rho'}{\rho_0} g_i + F_i. \tag{II.5}$$

II.B Boundary conditions

Specific boundary conditions used in the simulations are given in each following chapters depending on the model setup. In general, periodic boundary conditions are used in the stream-wise (x) and spanwise (y) directions for all variables. In the cross-stream direction (z), a combination of Dirichlet and Neumann boundary conditions coupled with a sponge region are employed.

The sponge region is employed at the top and bottom boundaries for the simulations in Chapter III-V and only at the bottom boundary for the simulation in Chapter VI to control spurious reflections of internal waves propagating out of the domain. The velocities and density in the sponge region are relaxed by adding to the right-hand-side of Eqs.(II.5) and (II.3) a term of the form

$$\begin{aligned} &- \quad \phi(z) \left[u_i(x_i, t) - \langle u \rangle_i (z, t = 0) \right] , \\ &- \quad \phi(z) \left[\rho(x_i, t) - \langle \rho \rangle (z, t = 0) \right] . \end{aligned}$$

, respectively. Here, $U_{i,\infty}$ and ρ_∞ are, respectively, the free stream velocities and density. These are set based on the initial values of the mean velocity and density at $t = 0$. The function $\phi(x_i)$ is constructed such that it increases quadratically from $\phi = 0$ to $\phi = A$ in a region of thickness a. The amplitude A and thickness a are varied in different simulations.

II.C Numerical Implementation

A detailed description of the numerical method can be found in Basak (2005) and Brucker (2009). Briefly, Eqs. II.1, II.5 and II.3 are solved using a second-order central difference scheme for spatial discretization on a staggered grid where vector quantities

are stored at the cell faces and scalar quantities are stored at the cell centers. A multigrid Poisson solver is employed to accelerate the convergence rate for the pressure field. In simulations of free shear flows such as those in Chapter III, IV and V, a low-storage third-order Runga-Kutta method is used for temporal integration. In simulations involving surface forcing in Chapter VI, Crank-Nicolson time marching scheme is used to advance the viscous term in order to achieve time steps larger than the Runga-Kutta method. The code employs a domain decomposition method, implemented using MPI libraries, to handle the memory and CPU requirements for large simulations.

Chapter III

Dynamics of a stratified shear layer above a region of uniform stratification

III.A Objectives

Stratified shear flow away from boundaries has been the subject of many studies, employing both experimental and numerical techniques. Nevertheless, there are only a handful that study the dynamics of a stratified shear layer in the presence of an external stratification where internal waves may be supported. Such a scenario can occur in the natural environment when the stratification extends continuously beyond the shear layer, and will be the focus of the current study.

Laboratory experiments, for example, Thorpe (1973) and Koop & Browand (1979), were the earliest systematic studies of instability and turbulence in a stratified shear layer. In those studies, the shear zone was between two layers of constant density and the mean shear was inflectional. Rohr *et al.* (1988) performed experiments of homogeneous shear flow turbulence (constant value of shear S and stratification N) using a salt-stratified water channel. Piccirillo & VanAtta (1997) studied the same problem using a thermally stratified wind tunnel, and numerical simulations were performed by

Gerz *et al.* (1989); Holt *et al.* (1992); Kaltenbach *et al.* (1994); Jacobitz *et al.* (1997); Jacobitz & Sarkar (2000); Diamessis & Nomura (2004). Numerical simulations of the stratified shear layer (or mixing layer) between two streams with a velocity difference have been performed using small-amplitude initial perturbations to understand the role of stratification by Staquet & Riley (1989); Caulfield & Peltier (1994, 2000); Staquet (2000); Smyth & Moum (2000*a*,*b*); Smyth *et al.* (2001) and, more recently, by Brucker & Sarkar (2007) who examined buoyancy effects when the initial perturbations are turbulent. A stratified shear layer may have horizontal shear in contrast to the vertical shear common to all the aforementioned studies. The constant-shear example of horizontal shear was studied numerically by Jacobitz & Sarkar (1999) while Basak & Sarkar (2006); Deloncle *et al.* (2007) have studied the case of inflectional horizontal shear.

Internal waves generated by unstable velocity shears have been observed in previous atmospheric and oceanic studies. Wind shear is believed to be one of the principal sources of internal waves excitation in the lower atmosphere (Einaudi *et al.*, 1978/79). Internal waves observed in the mesosphere (Holton *et al.*, 1995) and in the upper stratosphere (Rosenlof, 1996) are excited by nonorographic sources, for example the Kelvin-Helmhotz instability, since orographic waves can not reach these altitudes. Below the surface of the equatorial oceans, alternating eastward and westward currents (Luyten & Swallow, 1976; Eriksen, 1982; Firing, 1987) are observed. Eriksen (1982) has observed large-scale structures of the countercurrents persisting for a long period of time. Moum *et al.* (1992) and Sun *et al.* (1998) suggest that internal waves associated with the Equatorial Undercurrent can be the main source of mixing in the thermocline. Since internal waves can transport and redistribute momentum and energy (Eliassen & Palm, 1960; Andrew & McIntyre, 1978; Fritts, 1982), it becomes necessary to examine the transport of the internal waves excited by unstable shears.

A stratified shear layer with weak stratification of value J_0, nondimensionalized with the maximum shear, that overlies an adjacent region with stronger stratification J_d has been investigated using linear theory and 2-dimensional nonlinear simulations by Sutherland (1996). Internal waves are found to radiate downward from the shear layer

and propagate in the deep far-field. It is found that internal waves are generated by the most unstable linear mode and, from the 2-D simulations that track the evolution of a KH billow, it is concluded that strong internal waves are excited when $J_0 < 0.25$ and $J_d > 0.25$. Sutherland (2006) examined the evolution of a shear layer (also a jet) with asymmetric stratification, using linear theory and 2-D simulations. The distance, δ, between the shear layer and the top of the stratified region was varied along with the values of J_d. For small δ, the shear layer instability mode was found to directly couple to the internal wave mode and its subsequent nonlinear evolution was significantly modified. Simulations of a jet with asymmetric stratification have been performed in two dimensions by Skyllingstad & Denbo (1994); Smyth & Moum (2002) to model aspects of the equatorial undercurrent and using three-dimensional DNS by Tse *et al.* (2003) as a model for the jet at the atmospheric tropopause. Skyllingstad & Denbo (1994) in a problem forced with wind stress and buoyancy flux identify local instabilities as well as internal wave packets. Smyth & Moum (2002) consider a Bickley jet with low stratification, J_U, in the upper half and high stratification, J_L, in the lower half. Their simulations of cases with $J_U = 0.0$,0.05, and $J_L = 0.25$ show energetic internal waves directed downward away from the jet. Tse *et al.* (2003) perform three-dimensional simulations where the velocity and temperature profiles of the base flow, constructed to model a jet in the atmospheric tropopause, are forced. A quasi-equilibrium jet results with strong shear-forced turbulence in the core of the jet where the gradient Richardson number, $Ri_g << 0.25$. The edges of the jet, with moderate-to-large values of Ri_g, have patchy turbulence, attributed to nonlinear wave activity. Propagation of internal waves in the jet far field is not significant. It is found that the change of the fluctuations from mechanical turbulence in the core to stratified turbulence at the edges can be effectively characterized through length scales and through budget equations for the velocity and temperature variances.

The effect of internal waves on the deepening of a mixed layer in a stratified fluid was studied by Linden (1975). An oscillating grid was used to generate a turbulent mixed layer on top of a layer with a constant density gradient. As the mixed layer deepened, the density gradient was observed to increase to a maximum in the thermo-

cline. Internal waves were observed to propagate away from the mixed layer. These waves caused a loss of energy available for mixing. The experiment estimated up to 50% reduction in the mixing rate due to the presence of internal waves. A similar study carried out by E & Hopfinger (1986) compared the deepening rate between a two-layer and a constant density gradient system. Internal waves radiating energy away from the interface only occurred in the latter case. The energy radiation was found not to significantly affect the mass entrainment rate, defined by $E = (1/u)dD(t)/dt$ with D the mixed layer depth and u the r.m.s. velocity fluctuation. The coefficients K and n in the entrainment rate relation $E = KRi^{-n}$ were found to be the same in both cases, independent of the presence of internal waves.

Internal wave propagation was also observed in the experiments of Strang & Fernando (2001) designed to study turbulent entrainment and mixing at a sheared density interface. A shear layer separated a light, upper well-mixed turbulent layer from a lower quiescent layer which was either constant density or linearly stratified. Internal waves only appeared in the latter case. When the lower layer was linearly stratified, 'interfacial swelling' in the shear layer was observed and argued to be responsible for internal wave excitation. The buoyancy flux and the entrainment rate were higher when internal waves do not propagate into the lower layer. The mass entrainment rate was reduced by as much as 50% in the presence of internal waves. The ratio of the wave energy flux to the rate of change of potential energy due to mixed-layer deepening was found to be approximately 48%.

Sutherland & Linden (1998) quantified the effects of internal waves in an experimental investigation of stratified fluid with shear that flows over a thin barrier. In the experiment, the upper region was lightly stratified while the lower region had a higher density gradient. Vortices, shed in the wake of the thin barrier, disturbed the base of the sheared, mixing region and internal waves were observed to radiate downward. The propagating waves made angles to the vertical in range of $45 - 60°$. The Reynolds stress was measured and it was found that approximately 7% of the average momentum across the shear depth was lost due to wave transport. A 2-D numerical simulation was also performed. The simulation showed a higher value of the momentum extraction

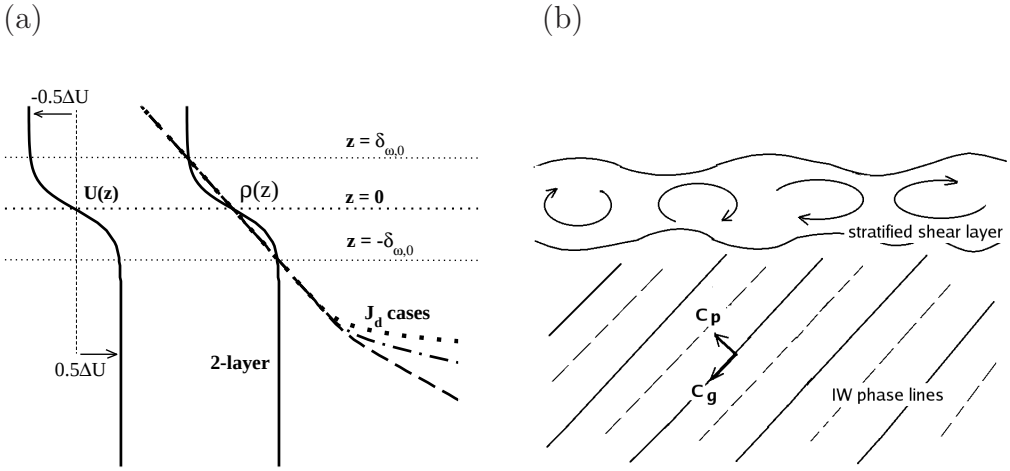

Figure III.1: (a) *Initial* mean profiles. Each case has a temporally evolving shear layer between two streams with velocity $-\Delta U/2$ and $\Delta U/2$, and initial vorticity thickness, $\delta_{\omega,0}$. The maximum shear is at $z = 0$. The 2-layer density variation corresponds to a tangent-hyperbolic profile with $J(0) = 0.1$. The other density profiles correspond to a moderate linear stratification, $J_s = 0.05$, in the shear layer above a bottom region, $z < -2.5\delta_{\omega,0}$, with uniform deep stratification that takes the values: $J_d = 0.1$, 0.25 and 1.0. The initial value of bulk Richardson number, $Ri_{b,0} = 0.1$, is the same for all cases. (b) Cartoon of internal wave excitation by shear layer instabilities. The indicated group and phase velocity are relative to the lower free-stream.

from the mean flow. The authors proposed that internal waves propagating at near 45° angle with the vertical were preferred since, through nonlinear interaction, they were capable of modifying the mean flow in a manner which fostered their continual generation.

In the present study, we use direct numerical simulations (DNS) to investigate the problem of an inhomogeneous stratified shear layer located between a weakly stratified upper layer and strongly stratified lower layer (schematic in Fig. III.1). Unlike previous simulations of this shear layer configuration, the present three-dimensional study allows the examination of internal wave dynamics in the presence of realistic turbulent mixing. The flow is seeded with small-amplitude perturbations. The deep stratification is varied

to elucidate its effect on the evolution of both the sheared region and the internal wave field. We examine the DNS results to help answer the following questions: How does the thickening of the shear layer depend on deep stratification? Does linear theory provide guidance to characterize the internal waves in these fully nonlinear, three-dimensional simulations? What are the relative roles of Kelvin-Helmholtz rollers and small-scale, three-dimensional turbulence insofar as internal waves? Are the mass flux, momentum flux and energy flux carried away by the internal waves significant?

III.B Problem Formulation

Fig. III.1 is a schematic of the simulated shear layer between two layers of fluid moving in opposite directions with a velocity difference ΔU^* and a vertical density stratification owing to a temperature variation. The flow evolves temporally with statistics that are homogeneous in the streamwise (x) and spanwise (y) directions. The horizontal velocity varies continuously in the vertical cross stream direction (z) with a hyperbolic tangent profile,

$$\langle u^* \rangle = -\frac{\Delta U^*}{2} tanh\left(\frac{2z^*}{\delta^*_{\omega,0}}\right),$$

where the initial vorticity thickness is defined by $\delta^*_{\omega,0} = \Delta U^*/(d\langle u^* \rangle/dz^*)_{max}$. Here, the superscript * denotes dimensional quantities. The squared buoyancy frequency is defined by $N^{*2} = -(g^*/\rho^*_0)\, d\langle \rho^* \rangle/dz^*$ and a nondimensional measure of the stratification is the Richardson number, $J(z) = N^*(z^*)^2\delta^{*2}_{\omega,0}/\Delta U^{*2}$. Two types of density profile are considered. A two-layer density variation, corresponding to the classical Thorpe problem, is defined with a tangent-hyperbolic profile obtained by replacing ΔU^* in the mean velocity profile with the density change, $\Delta\rho^*$. The value of $\Delta\rho^*$ is chosen to set $J(z = 0) = 0.1$. The second type of density profile corresponds to a weakly stratified shear layer above a region of deep stratification. The fluid above and inside the shear layer region is linearly stratified with Richardson number, $J_s = 0.05$. At depth $z^* = -2.5\delta^*_{\omega,0}$ the stratification changes to the value of the Richardson number specified in the deep region, J_d. Three simulations are performed with deep stratification,

$J_d = 0.1$, 0.25 and 1. According to linear analysis, the smallest J_d case does not permit propagating internal waves while the other two do. The density profiles are chosen so that the value of the bulk Richardson number, Ri_b, defined by Eq. (III.4) for a shear layer, has the same initial value for all four simulations.

The initial vorticity thickness, $\delta^*_{\omega,0}$, the density jump, $\Delta\rho^*_0$, across twice the initial vorticity thickness, and the velocity difference, ΔU^*, are used for nondimensionalization. Henceforth, u, x, y, z, p, ρ, t will denote nondimensional variables and, with the Boussinesq approximation, the governing equations can be written as follows:

$$\frac{\partial u_k}{\partial x_k} = 0\,, \tag{III.1}$$

$$\frac{\partial u_i}{\partial t} + \frac{\partial\,(u_k u_i)}{\partial x_k} = -\frac{\partial p}{\partial x_i} + \frac{1}{Re_0}\frac{\partial^2 u_i}{\partial x_k \partial x_k} - Ri_{b,0}\rho'\delta_{i3}\,, \tag{III.2}$$

$$\frac{\partial \rho}{\partial t} + \frac{\partial\,(u_k \rho)}{\partial x_k} = \frac{1}{Re_0 Pr}\frac{\partial^2 \rho}{\partial x_k \partial x_k}, \tag{III.3}$$

where

$$Re_0 = \frac{\Delta U^* \delta^*_{\omega,0}}{\nu^*}\,, \quad Ri_{b,0} = \frac{g^* \Delta\rho^*_0 \delta^*_{\omega,0}}{\rho^*_0 \Delta U^{*2}} = g\frac{\Delta\rho^*_0}{\rho^*_0}\,, \quad Pr = \frac{\nu^*}{\kappa^*}\,. \tag{III.4}$$

Here, ν^* is the kinematic viscosity, and κ^* is the molecular diffusivity. The initial bulk Richardson number can be interpreted as a nondimensional reduced gravity. Subscript 0 denotes a value at initial time. All simulations are run with $Re_0 = 1280$, $Pr = 1$ and $Ri_{b,0} = 0.1$. Although thermally stratified water has $Pr = 5 - 10$ depending on water temperature, we choose $Pr = 1$ to avoid the increase in computational resources, necessary at high Pr. The evolution of the shear layer at different values of J_d is examined. Three simulations are performed with $J_d = 0.1$, 0.25 and 1.0. A two-layer stratified shear layer is also simulated at the same initial Re_0, Pr and $Ri_{b,0}$ for comparison.

The domain size is 51.6 x 17.2 x 96.57 and the numbers of gridpoints in x, y, z directions are 384 x 128 x 512, respectively. The grid is uniform in the streamwise and spanwise directions with a spacing of 0.134. In the vertical direction the grid is uniform in the region $-7.5 \leqslant z \leqslant 2.5$ with a spacing of 0.0756. Outside this region the grid is mildly stretched at ratio of 2% giving a maximum spacing of 0.475. A second-order finite difference method on a staggered grid is used for spatial derivatives

and a third-order low storage Runge-Kutta method is used for time advancement. The flow is initialized with low amplitude velocity perturbations. These fluctuations have an initial broadband spectrum given by

$$E(k) \propto k^4 exp\left[-2\left(\frac{k}{k_0}\right)^2\right],$$

where k_0 is set such that the spectrum peaks at 1.7. The initial velocity fluctuations are introduced in the shear layer with the peak values set at 1% (ΔU). The noise is restricted in the shear region with the shape function, $A(z)$, where

$$A(z) = exp\left(-z^2\right).$$

Periodic boundary conditions are used in the streamwise and spanwise directions. Dirichlet boundary conditions are enforced for horizontal velocities and pressure while vertical velocity and density have Neumann conditions:

$$\begin{aligned} u(z_{min}) = \frac{1}{2}, \quad u(z_{max}) &= -\frac{1}{2}, \\ v(z_{min}) = v(z_{max}) &= 0, \\ p(z_{min}) = p(z_{max}) &= 0, \\ \frac{\partial w}{\partial z}(z_{min}) = \frac{\partial w}{\partial z}(z_{max}) &= 0, \\ \frac{\partial \rho}{\partial z}(z_{max}) &= -\frac{J_s}{g}, \\ \frac{\partial \rho}{\partial z}(z_{min}) &= -\frac{J_d}{g}. \end{aligned}$$

A sponge region is employed at the top ($z > z^t_{max} = 15$) and the bottom ($z < z^t_{min} = -50$) boundaries to control spurious reflections of internal waves propagating out of the domain. The test domain of interest, $z^t_{min} < z < z^t_{max}$, excludes the sponge region. The velocities and density in the sponge region are relaxed by adding to the right-hand-side of Eqs. (III.2) and (III.3) a term of the form

$$\begin{aligned} - \quad & \phi(z)\left[u_i(x_i,t) - \langle u\rangle_i(z,t=0)\right], \\ - \quad & \phi(z)\left[\rho(x_i,t) - \langle \rho\rangle(z,t=0)\right]. \end{aligned}$$

The damping function, $\phi(z)$, increases quadratically from $\phi = 0$ to 1.0 in a region of thickness 15 utilizing 30 gridpoints at each boundary. Flow instabilities, notably KH

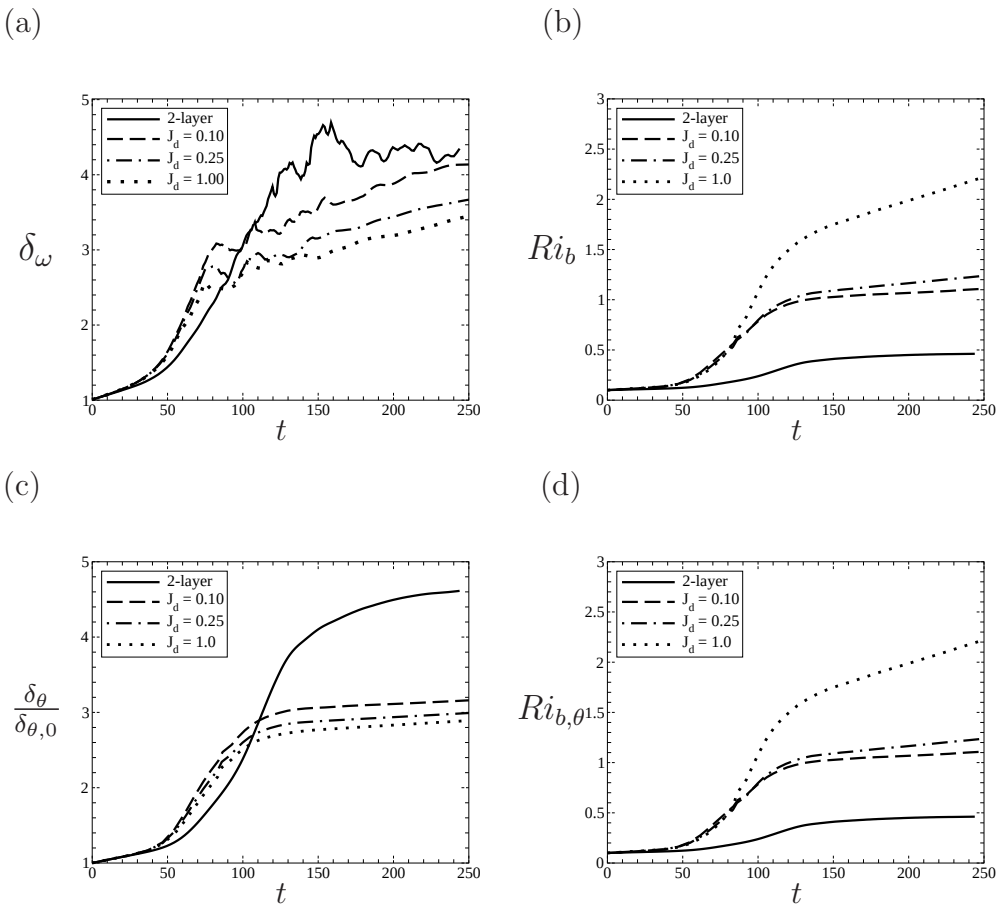

Figure III.2: (a) Vorticity thickness, δ_ω. (b) Bulk Richardson number, Ri_b, (c) Momentum thickness, δ_θ. (d) Bulk Richardson number, $Ri_{b,\theta}$.

rollers, form followed by a transition into small-scale, three-dimensional turbulence. Simulations are continued until most of the fluctuation energy inside the shear layer is dissipated, roughly at $t_f = 250$ time units $(\delta^*_{\omega,0}/\Delta U^*)$. Details of the numerical methods used in this study can be found in Basak & Sarkar (2006) and Brucker & Sarkar (2007).

III.C Evolution of the Shear Layer

The Kelvin-Helmholtz (KH) instability mode is initially amplified, KH rollers develop, secondary instabilities follow and, finally, there is breakdown to three-dimensional turbulence (Thorpe, 1973; Koop & Browand, 1979; Staquet & Riley, 1989; Caulfield

& Peltier, 2000; Smyth & Moum, 2000b). In the following text, we show the strong influence of the deep stratification on the flow statistics starting with overall quantities: the thickness of the shear layer and the bulk Richardson number Ri_b followed by an account of how the mean profiles develop in time.

Fig. III.2(a) shows the evolution of the vorticity thickness $\delta_\omega(t) = 1/(d\langle u\rangle/dz)_{max}$, a typically used measure of the thickness of the sheared region while Fig. III.2(b) shows the evolution of the bulk Richardson number defined by

$$Ri_b(t) = \frac{g^*\Delta\rho^*(t)\delta^*_\omega(t)}{\rho^*_0\Delta U^{*2)}} = \frac{g\Delta\rho^*_0}{\rho^*_0}\Delta\rho(t)\delta_\omega(t)\,, \tag{III.5}$$

where $\Delta\rho(t)$ is the density difference across $z = -\delta_\omega(t)$ and $z = \delta_\omega(t)$. Fig. III.2(a) shows that the thickness growth rate is initially smaller in the two-layer case since the value of centerline Richardson number, $J(0) = 0.1$, is larger than the corresponding value of $J(0) = 0.05$ in the cases with deep stratification. The thickness evolves in three different stages. The stage from $t = 0$ to 30 is not a focus of the discussion since the evolution of the shear layer during this period is identical in all cases. After this initial period, there is a second stage where visualization of the vorticity field shows the the formation of distinct and dominant KH rollers which increase in size by pairing or amalgamation. We denote this period as the KH regime. Later, when rollers break down, the shear layer enters a third regime, turbulence, wherein small-scale, three-dimensional features dominate the vorticity field. The transition time between the second and third regimes is different among cases. In the two-layer case, the transition time occurs late at $t = 130$ while it is earlier, approximately $t = 100$, in J_d cases. To ease the discussion, from this point we indicate $t = 100$ as the transitional time for all J_d cases. This is the time when the vorticity thickness exhibits a small reduction in size before the growth rate increases due to turbulent stirring. In the KH regime, the vorticity thickness δ_ω grows at slightly higher rate in the J_d cases than in the two-layer case. The growth rate, $d\delta_\omega/dt$, is 0.045 in the J_d cases and 0.036 in the two-layer case.

In the turbulent regime, there is a qualitative difference between the two-layer case and the cases with ambient stratification: the shear region in the former approaches an approximately constant thickness while the shear region continues to grow in the

latter, see Fig. III.2(a). The asymptotic thickness in the two-layer case corresponds to $Ri_b \simeq 0.38$, a value within the range measured in previous numerical and experimental studies as reviewed by Smyth & Moum (2000*a*). In the J_d cases, there is a secondary growth that is linear as in the KH regime but at a more moderate rate, approximately $d\delta_\omega/dt = 0.004$, with little variation among the different J_d cases. Viscous growth is not the primary cause since a laminar shear layer whose thickness is proportional to $\sqrt{t/Re}$ does not grow linearly and the numerical value of the viscous growth rate is smaller than the observed value. The secondary growth in the turbulence regime strongly influences the evolution of the bulk Richardson number Ri_b as shown in Fig. III.2(b). Ri_b grows vigorously in case $J_d = 1.0$ showing a strong effect of the deep stratification. In all cases the velocity difference does not vary in time so that, according to Eq. (III.5), a growth in the thickness δ_ω or in $\Delta\rho$ can cause the observed growth in Ri_b. Case $J_d = 0.10$ has a larger thickness than case $J_d = 1.0$; however, it is the *latter* that has the larger value of Ri_b, nearly twice the corresponding value in the former case. The difference is entirely due to a stronger density gradient across the layer. Thus, the small thickness growth at late time, amplified by a strong external density gradient, results in substantial growth in Ri_b.

Another measure of shear layer thickness is the momentum thickness, δ_θ, defined by

$$\delta_\theta = \int_{z_l}^{z_u} \left(\frac{1}{4} - \langle u \rangle^2 \right) \, dz \, . \tag{III.6}$$

Depths z_u and z_l are upper and lower bounds of the shear layer where the turbulence production is approximately zero but the Reynolds shear stress $\langle u'w' \rangle$ is not necessarily zero. Compare Fig. III.2 (a) to (c), the evolution of δ_ω and δ_θ are similar in the two-layer case, but the J_d cases show strong difference. The secondary growth that was exhibited by δ_ω is much smaller in δ_θ. An analog of $Ri_b(t)$ is $Ri_{b,\theta}(t)$ obtained by substituting $\delta_\omega(t)$ on the r.h.s of Eq. (III.5) by $4\delta_\theta(t)$ and letting $\Delta\rho(t)$ be the density change over $4\delta_\theta(t)$. The factor of 4 ensures that Ri_b and $Ri_{b,\theta}$ have the same value for a tangent-hyperbolic velocity profile. Fig. III.2(d) shows the evolution of $Ri_{b,\theta}(t)$. Similarly to Ri_b, the quantity $Ri_{b,\theta}$ continues to grow at late time but at a significantly smaller rate. Here, the small but non-zero secondary growth, barely visible in the

(a) (b)

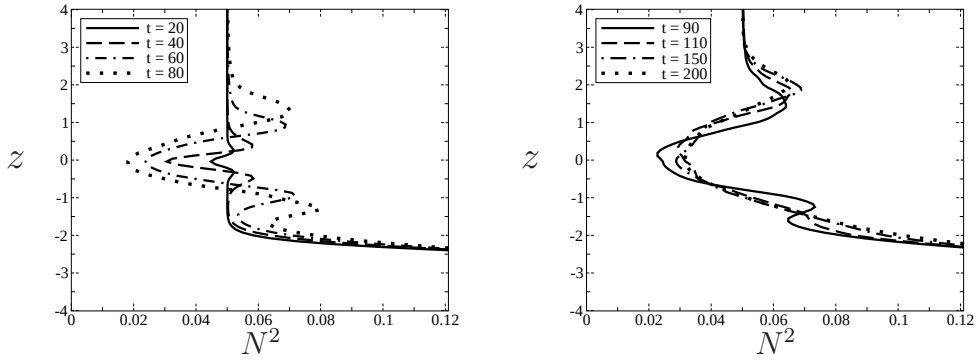

Figure III.3: Profiles of squared buoyancy frequency N^2 for $J_d = 0.25$ (a) in KH regime, (b) in turbulence regime.

evolution of δ_θ, is magnified by the density difference across the shear layer.

As the shear layer evolves in time, pycnoclines (regions with large N) are observed at the edges of the layer. The development of an overshoot in density gradient is shown with profiles of nondimensional squared buoyancy frequency N^2 in Figs. III.3(a,b). The pycnoclines begin to form as soon as the shear layer starts stirring the ambient stratification profile. At first, the formation is similar at both edges. Later, the pycnocline at the bottom edge merges into the strong background density gradient in the bottom region, while the one at the top persists for a long period of time. The density gradient in the pycnocline is unsteady, growing at first, and then decaying due to the buoyancy induced reduction in vertical mixing. The formation of a pycnocline, a result of the mixing of a density gradient by inhomogeneous turbulence, has been observed in previous studies (Linden, 1975; Sutherland & Linden, 1998; Taylor & Sarkar, 2007). The evolution of the mean shear is plotted in Fig. III.4. The evolution during the initial period, $t < 60$, is typical of a shear layer, namely, the profile thickens and the peak shear at $z = 0$ diminishes. However, as shown in Fig. III.4(b), later the mean shear develops local peaks at the upper and lower flanks. The reason is that the enhanced values of N^2 (pycnoclines) at the flanks inhibit the mixing of momentum relative to the center of the shear layer allowing mean shear at the flanks to be larger than at the centerline. The bottom peak of mean shear is reminiscent of the elevated shear seen at

(a) (b)

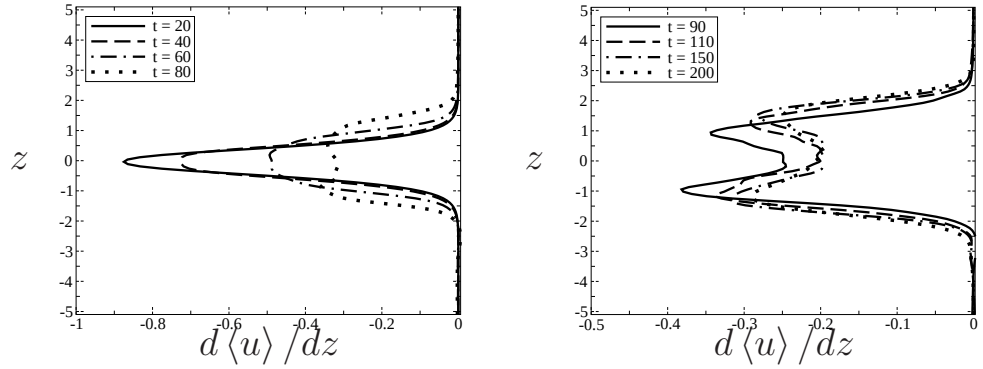

Figure III.4: Mean shear profiles in case $J_d = 0.25$ (a) in KH regime, (b) in turbulence regime.

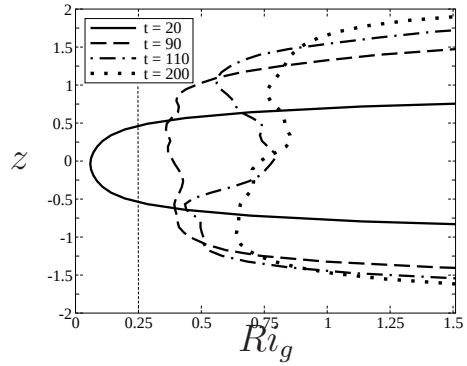

Figure III.5: Gradient Richardson number, Ri_g, profiles in case $J_d = 0.25$.

the base of the mixed layer in observations of the transition layer in the upper ocean (D'Asaro *et al.*, 1995; Weller & Plueddemann, 1996; Johnston & Rudnick, 2009).

The gradient Richardson number, $Ri_g(z) = N^2/(d\langle u\rangle/dz)^2$, is plotted at several times for case $J_d = 0.25$ in Fig. III.5. The profiles of N^2 and $d\langle u\rangle/dz$ were earlier shown in Figs. III.3 and III.4, respectively. The double hump in the velocity gradient profile is also seen in the Ri_g profile at late times. The late time behavior of the gradient Richardson number is governed by the velocity gradients. The downward shift of the shear peak can lead to a reduction in the gradient Richardson number at the edges of the shear layer at late times. In ocean and atmospheric models, the turbulent mass and momentum transport are typically parametrized in terms of the gradient Richardson number. Specifically, the mixing of mass and momentum due to turbulence is set to

zero once the gradient Richardson number reaches a critical value, usually between $0.25 - 1.0$. When this type of parametrization is utilized the shear layer can no longer grow. The spatial profiles of $d\langle u\rangle/dz$ and N^2 and hence Ri_g are fixed. By fixing these spatial profiles the secondary (late-time) growth seen in Ri_b, Fig. III.2(b), would be missed as would be late-time evolution of $Ri_g(z)$.

III.D Visualization of the Shear Layer Evolution

Visualizations of the spanwise vorticity and the full density field for the two-layer and $J_d = 0.25$ cases illustrate the strong effect of deep stratification on the evolution of the shear layer. Comparisons are also made to the stratified two-layer case of Koop & Browand (1979); Smyth & Moum (2000*a*,*b*).

The spanwise vorticity in the two-layer case on the plane $y = 8.5$ at t = 70, 100, 120, and 160 are shown in Figs. III.6(a-d), respectively. At $t = 70$ the roll-up is just beginning, and by $t = 100$ there is evidence of pairing. At $t = 120$ the pairing has completed and the vortices start to break down into small-scale turbulence. Finally, at $t = 160$ there is little evidence of large scale vortical structures, which have been replaced with a largely disordered field of turbulent motion with smaller length scale. The visualizations presented here are qualitatively similar to the computations of Smyth & Moum (2000*a*), and to the spatially evolving shear layer studied by Koop & Browand (1979). The roll-up, pairing, and breakdown phases in the $x - z$ plane look very similar to Koop & Browand (1979). The coherence in the braid region visualized in the $x - y$ plane, not shown, also shows good qualitative agreement with their study.

The evolution of the spanwise vorticity for the $J_d = 0.25$ case is shown in Figs. III.7(a-d) at similar times to those in the two-layer case. In Fig. III.7(a) there is already evidence of smaller scale disorder, $x \approx 38$. Fig. III.7(b) shows no evidence of pairing, but rather a breakdown, not seen until much later in the two-layer case. The vorticity in Fig. III.7(b) looks more similar to Fig. III.6(c) rather than III.6(b). The edges of the layer containing significant vorticity in the $J_d = 0.25$ case remain much flatter, with respect to z, than the two-layer case. Clearly, the presence of the lower strati-

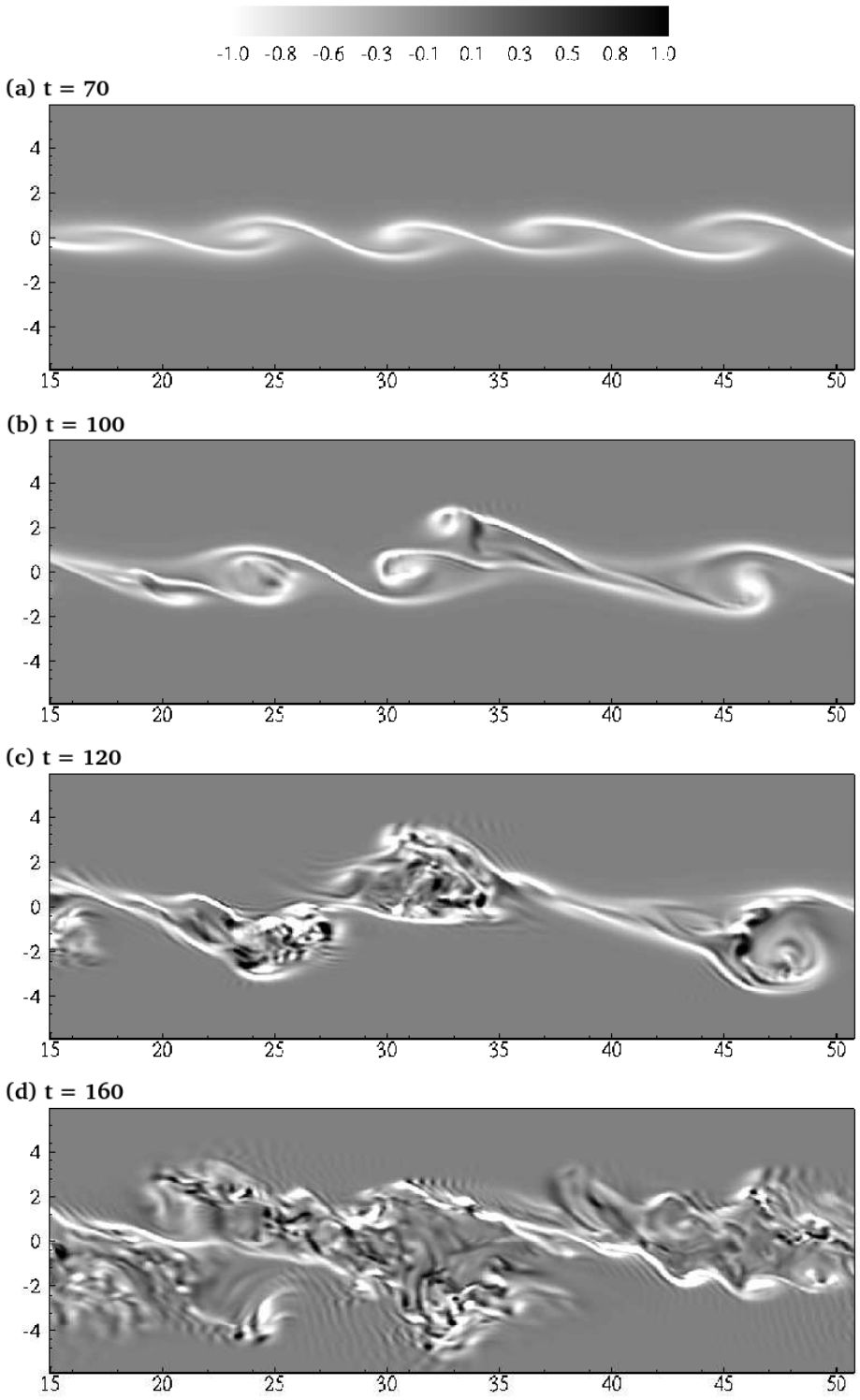

Figure III.6: Spanwise vorticity, ω_2, in x-z plane at $y = 8.5$ in two-layer case.

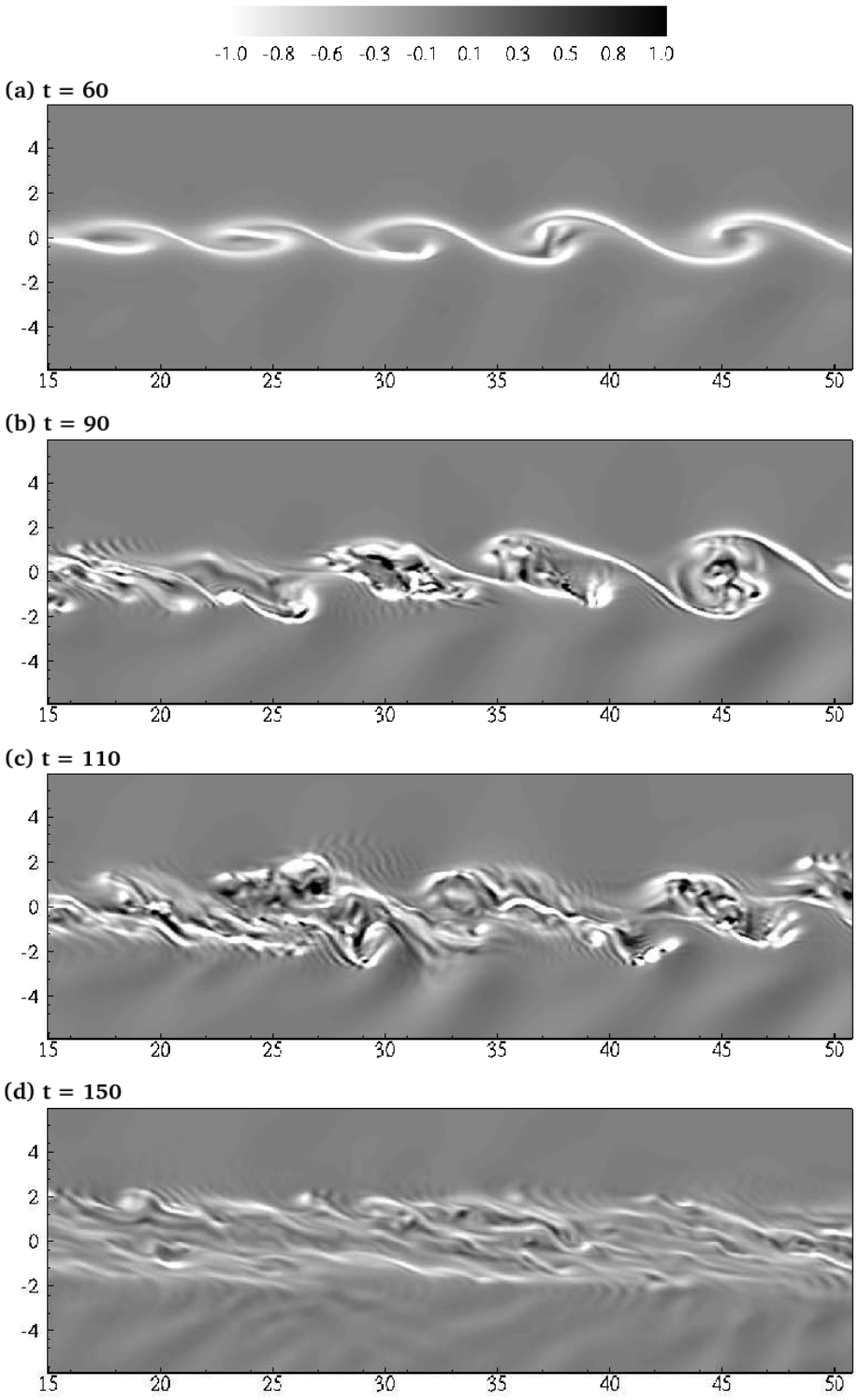

Figure III.7: Spanwise vorticity, ω_2, in x-z plane at $y = 8.5$ in case $J_d = 0.25$.

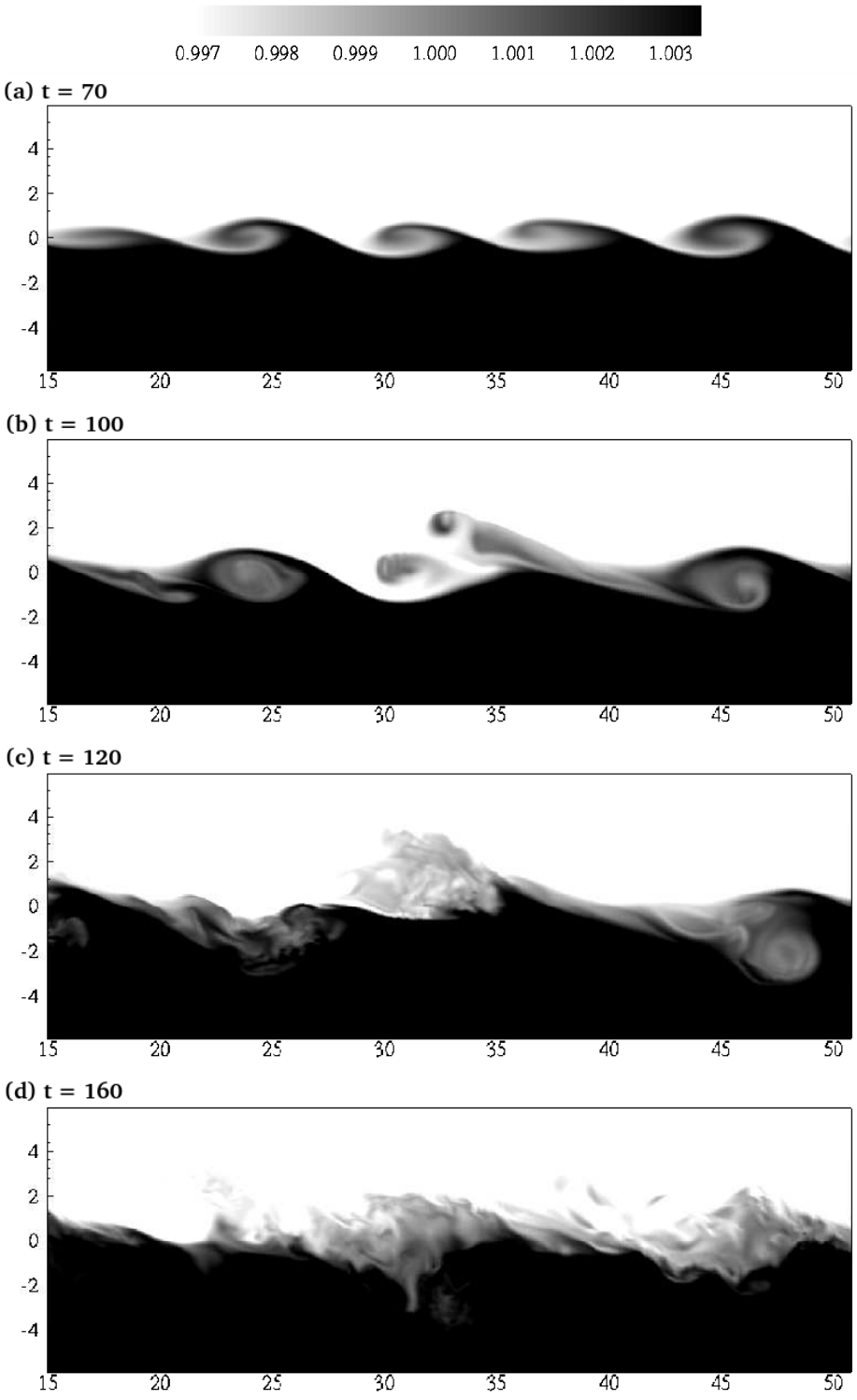

Figure III.8: Density field, ρ, in x-z plane at $y = 8.5$ in two-layer case.

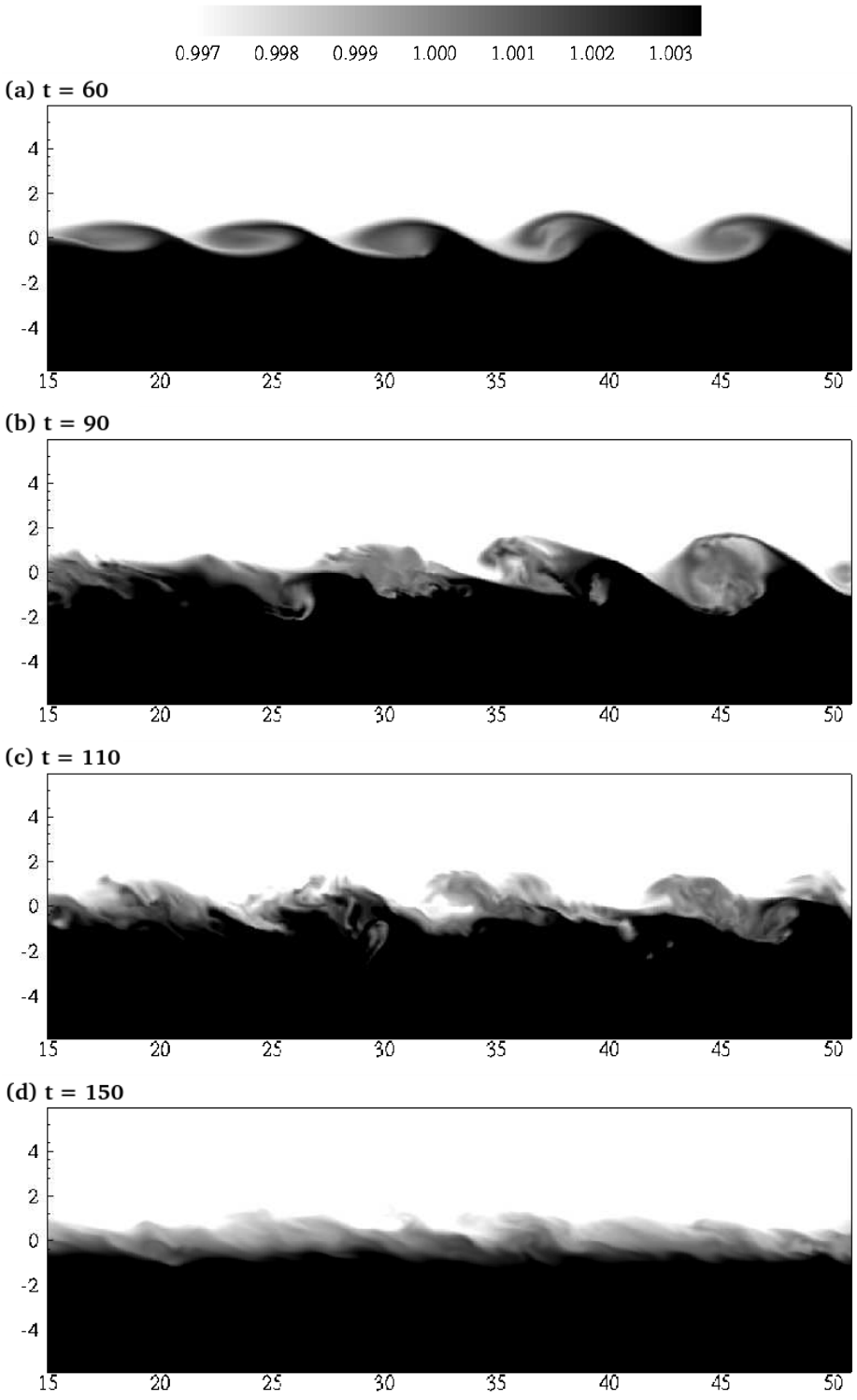

Figure III.9: Density field, ρ, in x-z plane at $y = 8.5$ in case $J_d = 0.25$.

fication leads to significantly different vertical structure than the two-layer case. The explanation is as follows: Since the fundamental frequency of the most unstable mode, by linear theory, is affected little by the presence of the deep stratification (Drazin *et al.*, 1979) the difference must be in the non-linear portion of the evolution. The first non-linear process to occur in the two-layer case is pairing. As noted above pairing is evident in Fig. III.6(b) and has been disrupted in Fig. III.7(b). This lack of pairing was also observed by Strang & Fernando (2001) who were investigating the upper limit of KH formation in terms of the bulk Richardson number. Their stratification was so strong as to eventually suppress the formation of KH rollers. Here, the rollers form but are unable to pair because the lower fluid is too heavy to be displaced above the upper fluid. Like the two-layer case, the thin braid like regions extend throughout the entire spanwise domain until the rollers begin to breakdown at which time the spanwise coherence is lost.

The density field provides a perspective on mixing by the flow instabilities and turbulence. The full density field is visualized for the two-layer and $J_d = 0.25$ cases in Figs. III.8 and III.9, respectively. Figs. III.8(a) and III.9(a) show the density field in the early stage of KH roller formation. As previously mentioned, the deep stratification has little effect on the disturbance wave length. However, breakdown to small-scale mixing occurs earlier in the presence of deep stratification. This breakdown is clearly evident at $x \approx 38$ in III.9(b) where regions of mixed fluid have replaced the pairing that occurs in the two-layer case at similar time, Fig. III.8(b). In Figs. III.8(b-c) there are regions of mixed fluid that have been completely submersed in regions of higher density, this behavior is absent in $J_d = 0.25$ case. The deep stratification prevents the heavy fluid from being lifted above the lighter fluid. At late time the interface between the two fluids is thinner and much smoother in the $J_d = 0.25$ case relative to the two-layer case (compare Fig. III.9(d) to III.8(d)).

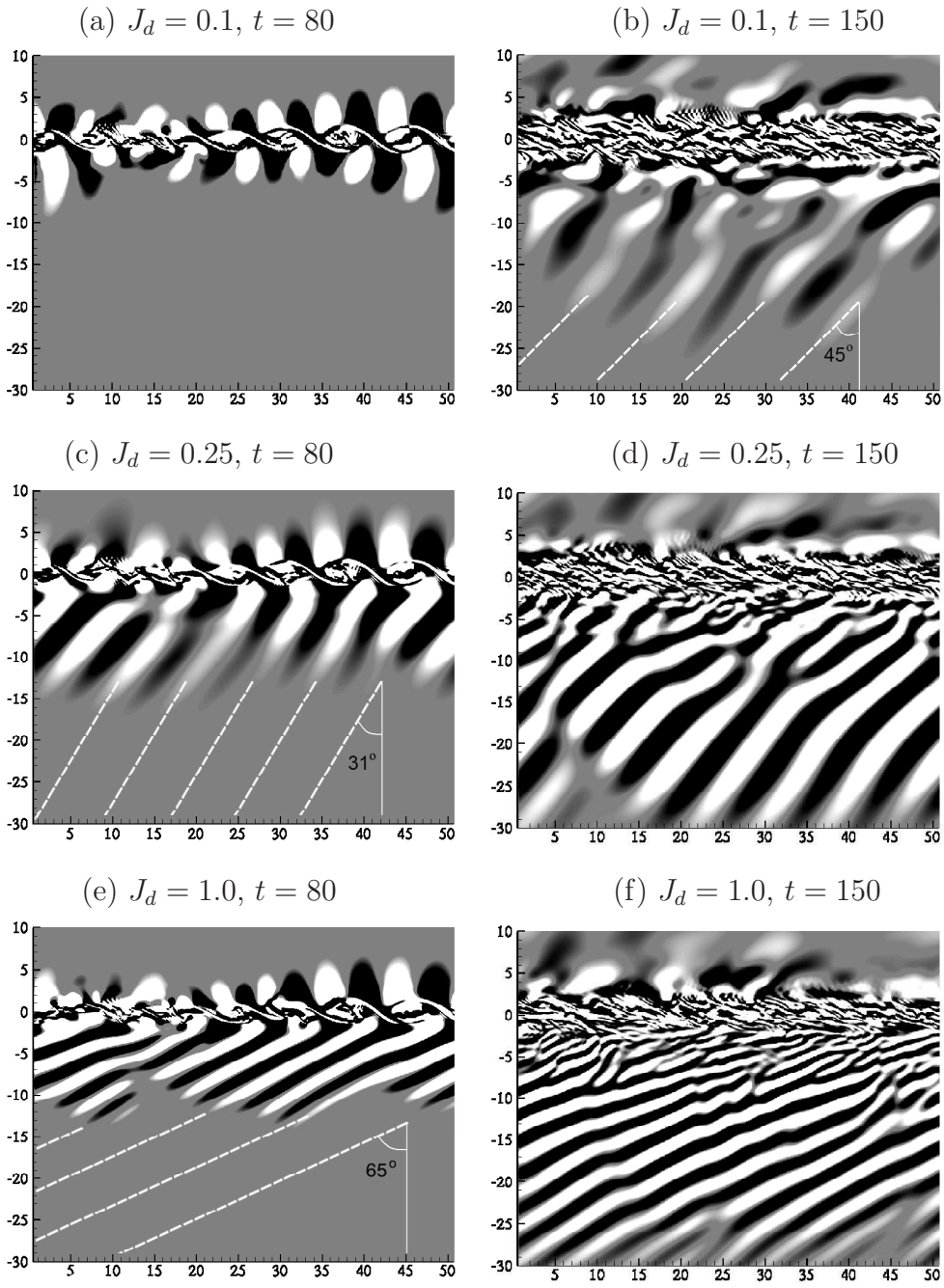

Figure III.10: Slices of $\partial w'/\partial z$ in the x-z plane at $y = 8.5$. Strong waves are observed in case $J_d = 0.25$ (c,d) and $J_d = 1.0$ (e,f). The left panels correspond to time in the KH regime; the right panels correspond to time in the turbulence regime. In the case of $J_d = 0.1$, the internal wave field is negligible in the KH regime, (a), but noticeable in the turbulence regime, (b). The dashed lines in (c,e) shows the propagating angles predicted by linear wave theory. The scale ranges from -0.01 (black) to 0.01 (white).

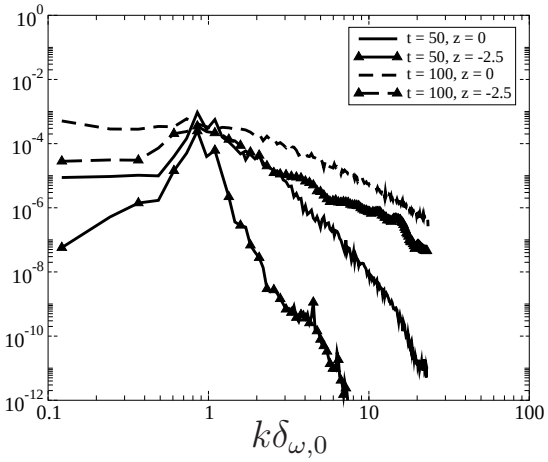

Figure III.11: Spanwise-averaged power spectra of the vertical velocity on the horizontal center-plane, $z = 0$, and at the bottom edge of the shear layer, $z = -2.5\delta_{\omega,0}$, in case $J_d = 0.25$. Two different times are shown.

III.E Internal Wave Field

Internal gravity waves that propagate into the stratified region beneath the shear layer are observed during the KH stage in the two cases with $J_d = 0.25$ and 1.0 and, during the later turbulent stage, internal waves are observed in all three cases. The internal wave field is visualized with instantaneous $x - z$ slices of $\partial w'/\partial z$ at various times in Fig. III.10. Since the top region is weakly stratified, $J_s = 0.05$ in all cases, the propagation of internal waves above the shear layer is insignificant. At the base of the shear layer, the phase lines are directed downward and to the left, thus opposing the free stream. The phase lines move upward and, consistent with internal gravity waves, the wave energy moves downward. Phase lines are parallel to the wave group velocity vector, $\mathbf{c}_g$, relative to the bottom free stream velocity. In the present study, $\mathbf{c}_g$ transports energy away from the shear region into the bottom deep region.

During the KH regime, waves are excited by KH rollers, analogous to waves excited by flow over a surface corrugation of prescribed wavelength. Let θ be the angle made by the phase lines (equivalently, $\mathbf{c}_g$) with the vertical. Figs. III.10(c,e) show that, in the KH regime, there is a preferred value for θ: $32 - 38^\circ$ when $J_d = 0.25$ and $62 - 68^\circ$ when $J_d = 1.0$. In Fig. III.11, the horizontal wavenumber spectrum at early time, $t = 50$, in the center of the shear layer shows a strong peak at $k\delta_{\omega,0} = 0.85 \pm .06$

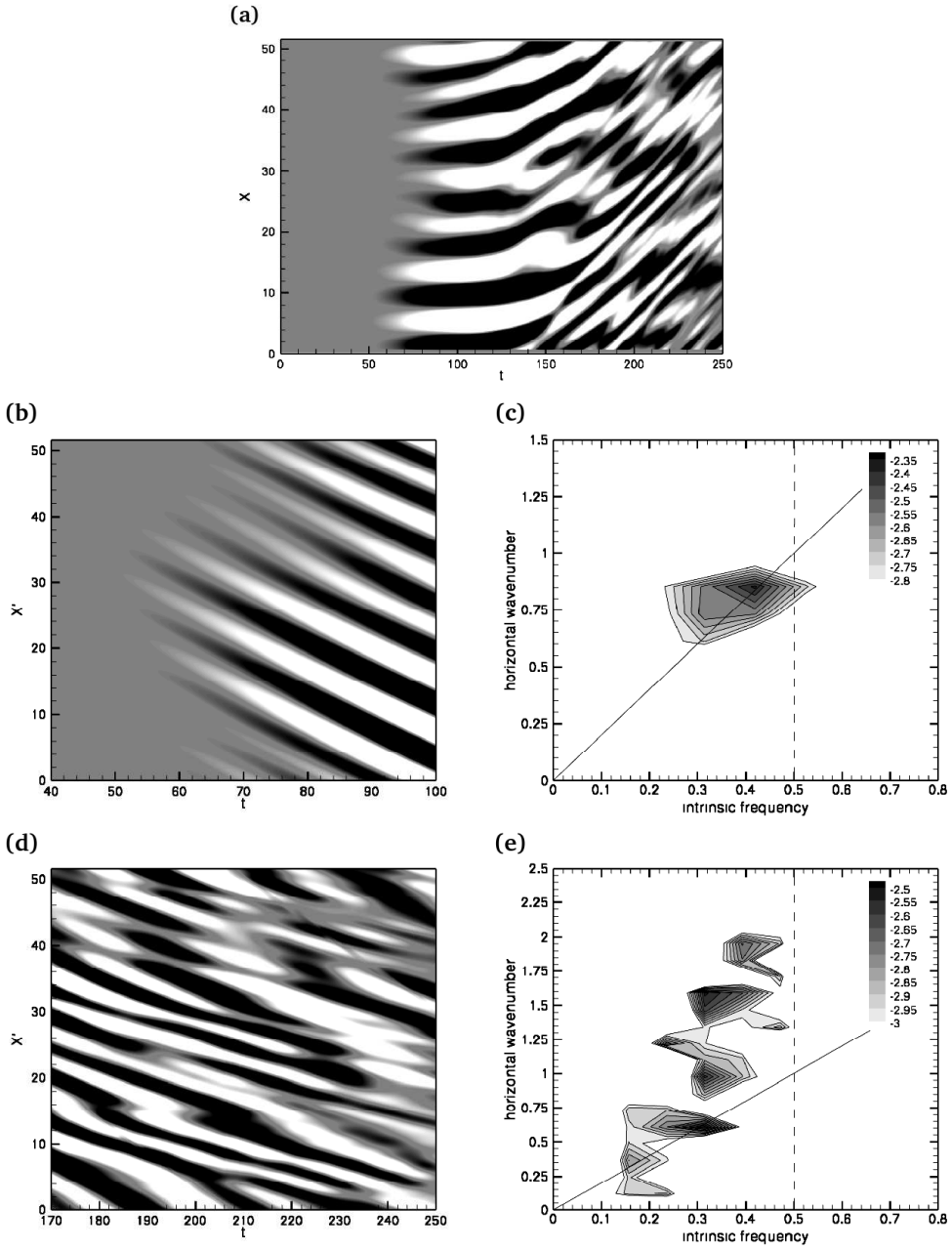

Figure III.12: Case $J_d = 0.25$: (a) Time series of $\partial w/\partial z$ at a streamwise probe, $z = -10$, $y = 8.5$, in the stationary frame; (b) the wave field in (a) limited to the KH regime and mapped to a frame moving with the bottom free-stream velocity; (c) power spectrum of the field in (b); (d) similar to wave field in (b) but in the turbulence regime; (e) power spectrum of the field in (d). The scale in (a,b,d) is from -0.01 (black) to 0.01 (white). The contours in (c,e) are in log scale. The dashed lines in (c,e) indicate the buoyancy frequency; the diagonal lines show the relation $\Omega = (\Delta U/2)\, k$.

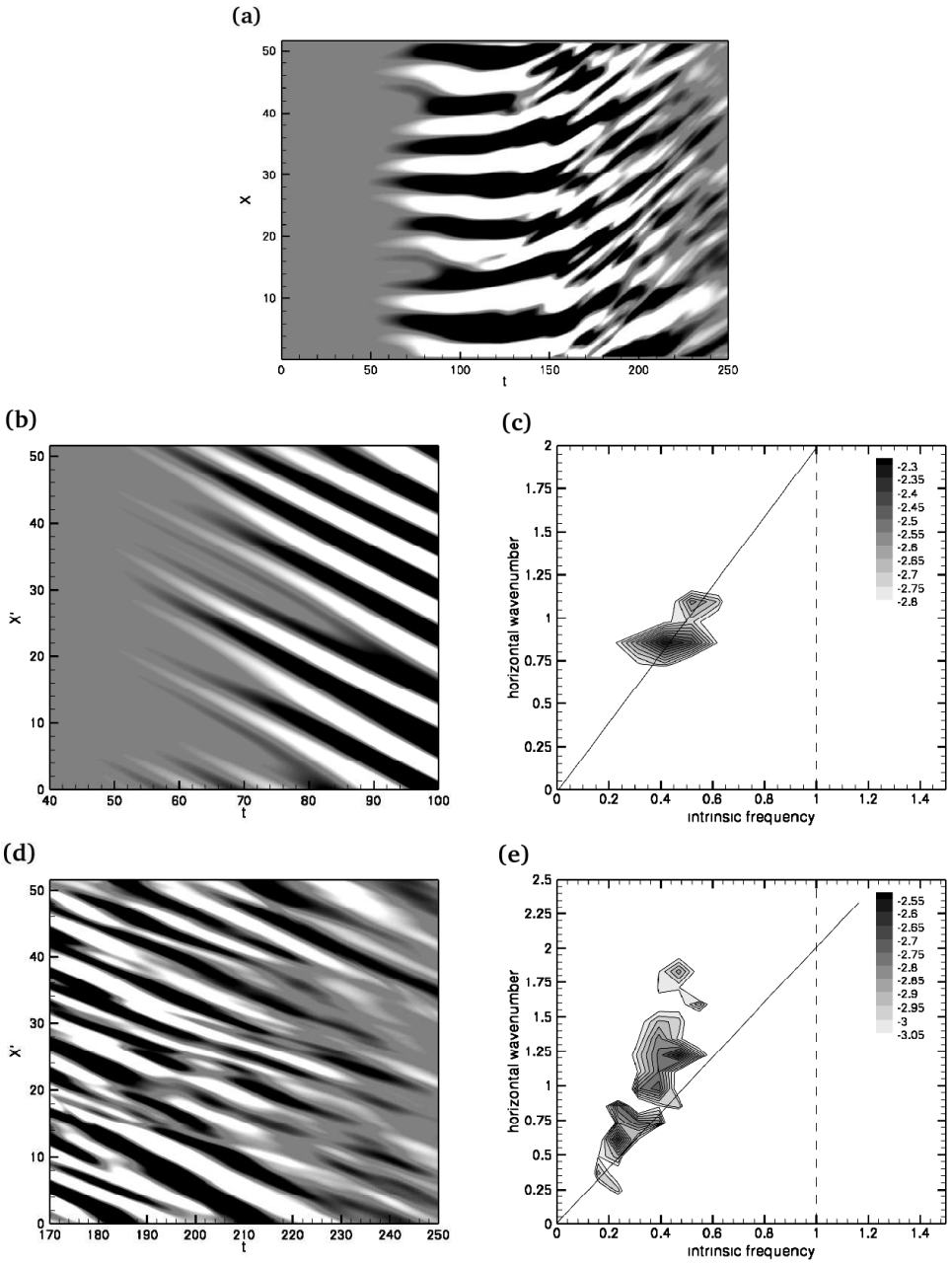

Figure III.13: Case $J_d = 1.0$: see caption in Fig. III.12.

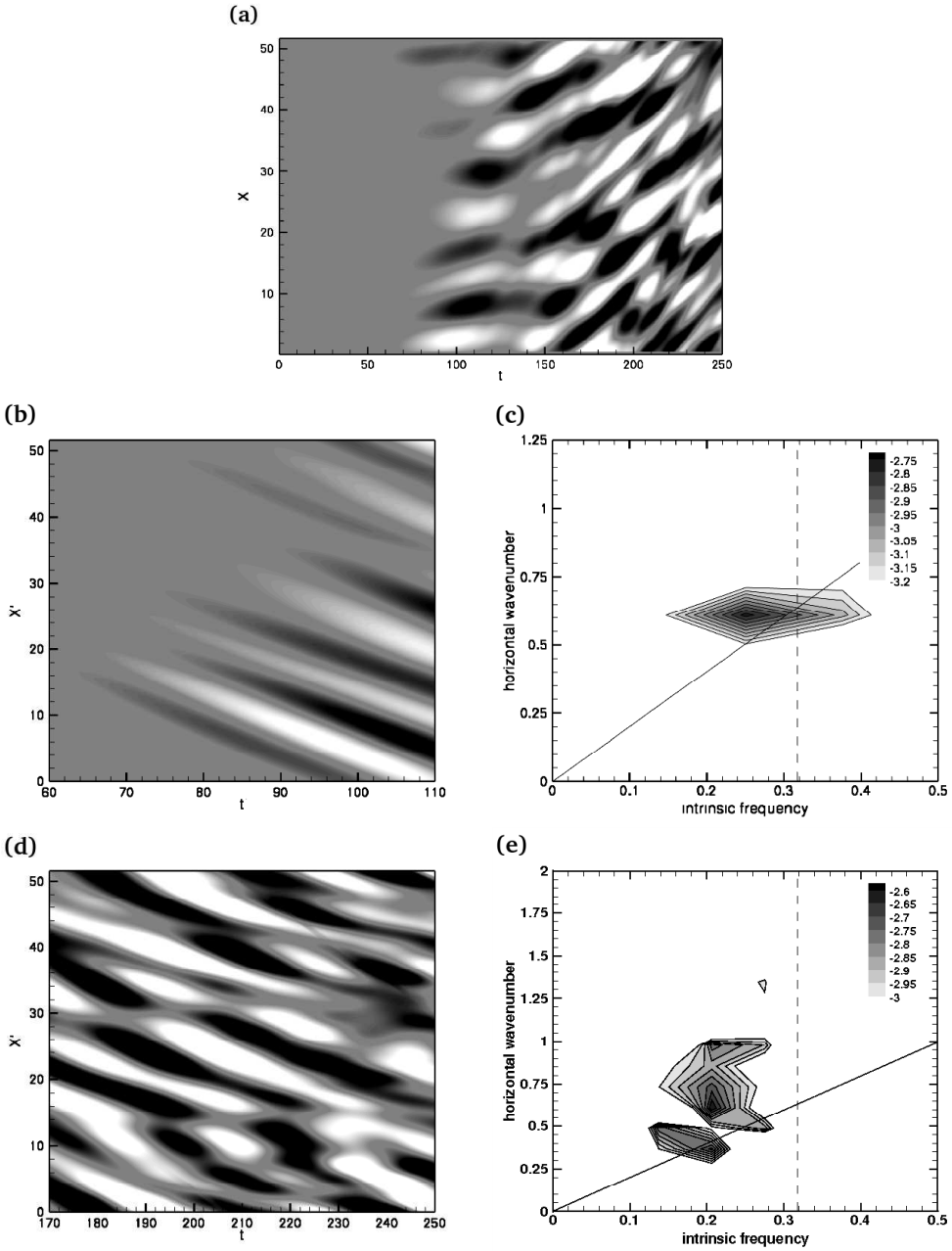

Figure III.14: Case $J_d = 0.1$: see caption in Fig. III.12.

which corresponds to $\lambda_{KH} = 7.4 \pm 0.5\delta_{\omega,0}$, comparable to the wavelength of the most unstable mode $7.2\delta_{\omega,0}$ obtained by linear, inviscid theory (Monkewitz & Huerre, 1982). (The error bar reported in the wavenumber, k, is the ratio of π over the sampling period.) The spectrum at depth $z = -2.5\delta_{\omega,0}$, a location at the edge of the shear layer, and at $t = 50$ also shows a peak at the same wavenumber, showing a strong coupling between the internal waves outside the shear layer and the coherent KH rollers inside the shear layer. Since the rollers are spanwise coherent, the streamwise wavenumber can be considered to represent the horizontal wavenumber for both the rollers and the KH-excited internal waves. The horizontal wave number spectra at later time, $t = 100$, are also shown in Fig. III.11. The late-time spectrum inside the shear layer is broadband *without* a discrete peak at the KH mode. Note that the dependence of the most unstable wavelength on the stratification in the shear layer, J_s, is weak (Hazel, 1972) and on the deep stratification is also weak (Drazin *et al.*, 1979). Therefore, the wavelength $7.4 \pm 0.5\delta_{\omega,0}$ is taken to be representative of all simulated cases.

Linear stability theory that gives the value of the most unstable KH mode in the generation region, combined with linear internal wave theory, can explain the preference for a characteristic angle of the early-time waves shown in Figs. III.10(c,e) as will be demonstrated now. Since the bottom stream moves with a fluid velocity of $0.5\Delta U$, the apparent frequency, ω, measured in the simulation frame (stationary in this study) is related to the intrinsic frequency, Ω, measured in the frame moving with the free-stream fluid in the bottom region by

$$\omega = \Omega + 0.5\Delta U k \,. \tag{III.7}$$

The mean streamwise velocity at $z = 0$ is $\langle u \rangle = 0$ so that the KH rollers can be approximated to be stationary, i.e. $\omega = 0$, then

$$\Omega = -0.5\Delta U k_{KH} = 0.43 \pm 0.03 \frac{\Delta U}{\delta_{\omega,0}} \,, \tag{III.8}$$

where k_{KH} is chosen to be negative corresponding to waves propagating in the negative x direction with respect to the bottom free stream.

According to linear theory, internal gravity waves will propagate in a medium if the magnitude of the intrinsic frequency, Ω, is less than the buoyancy frequency, N, of

that medium. Eq. (III.8) then implies that KH-produced internal waves are possible only if the ambient stratification satisfies the following condition:

$$J_d > 0.18\,. \tag{III.9}$$

Consistent with the above condition, internal waves are not observed during the KH regime in the $J_d = 0.10$ case shown in Fig. III.10(a). In contrast, there is strong excitation of internal waves in cases with $J_d = 0.25$ and 1.0 as shown by Figs. III.10(c,e). In order to calculate the internal wave phase angle, we combine Eq. (III.8) with the linear dispersion relationship for internal gravity waves to obtain,

$$\cos(\theta) = \frac{\Omega}{N} = \frac{0.43 \pm 0.03}{\sqrt{J_d}}\,. \tag{III.10}$$

According to the prediction of linear theory, Eq. (III.10), the angle made by the phase lines with the vertical is $\theta = 31 \pm 7^\circ$ when $J_d = 0.25$ and $\theta = 65 \pm 2^\circ$ when $J_d = 1.0$. Figs. III.10(c,e) shows phase lines with θ in the range of $32 - 38^\circ$ and $62 - 68^\circ$ for cases $J_d = 0.25$ and $J_d = 1.0$, respectively. Evidently, there is very good quantitative agreement between the prediction of linear theory and the internal wave angles observed in the present fully nonlinear simulations.

The temporal frequency and wavenumber content of the observed internal waves is further quantified as follows. Part (a) of Figs. III.12 - III.14 show the time series of $\partial w/\partial z$ measured on a streamwise line located at $y = 8.5\delta_{\omega,0}$ and $z = -10\delta_{\omega,0}$ for cases with $J_d = 0.25$, 1.0 and 0.1, respectively. The time series is recorded in the stationary simulation frame. Clearly, the initial wave field during $40 < t < 100$ due to KH-rollers is stationary and thus the apparent frequency, ω, is zero. In part (b) of these figures, the $\partial w/\partial z$ field is mapped into the frame moving at the free-stream velocity in the bottom region by

$$x' = x - \langle u \rangle \cdot t\,. \tag{III.11}$$

where $\langle u \rangle$ at this location is close to $0.5\Delta U$. The power spectra of the mapped field is computed to obtain the intrinsic frequency, Ω, and the results are shown in part (c) of Figs. III.12-III.14. Both cases $J_d = 0.25$ and 1.0 show a strong peak at $k\delta_{\omega,0} = 0.85 \pm .06$, which is identical to the wavenumber of the most unstable KH mode, k_{KH}.

The temporal frequency peaks at $\Omega = 0.43 \pm 0.05$ and $0.41 \pm 0.05\Delta U/\delta_{\omega,0}$ in case $J_d = 0.25$ and 1.0, respectively. The error bars in the wavenumber and frequency are due to the finite values of spatial length and temporal period in the data that is available to compute the spectra. The diagonal solid line in part (c) of the figures represents the dispersion relation $\Omega = 0.5\Delta U k$. For cases, $J_d = 0.25$ and 1.0, these diagonal lines pass through the (Ω, k) location of peak power spectrum, and are consistent with the shape of the $\Omega - k$ contours. Thus, the computed frequencies agree well with the frequency predicted by linear theory, Eq. (III.8).

Although the KH rollers cannot excite internal waves in case $J_d = 0.1$ as discussed previously, the thickening of rollers by diffusion and during the pairing process generates disturbances at smaller wavenumber, i.e. larger wavelength such that the radiation condition is met. Fig. III.14(a) shows the presence of such internal waves. The power spectrum shown in Fig. III.14(c) shows a peak at $k\delta_{\omega,0} = 0.61 \pm 0.06$ and $\Omega = 0.25 \pm 0.06\Delta U/\delta_{\omega,0}$, resulting in $\theta = 38 \pm 18°$. The dispersion relation also holds in this case. The solid line slightly deviates from the peak location because the wave packets have a small positive x-velocity in the stationary frame as shown in Fig. III.14(a).

At later time, in the turbulence regime, internal waves continue to be generated by the shear layer. However, as shown by the right panels of Fig. III.10, the phase lines in the vicinity of the shear layer become less structured and the amplitudes are smaller compared to those generated by the rollers. Since the turbulence has a broadband spectrum, turbulence-generated waves are excited over a broad range of angles as shown in Figs. III.10(b,d,f) in the region beneath the shear layer. The wavenumber spectrum, earlier shown in Fig. III.11, indicates that late-time fluctuations are broadband without a discrete peak at the fundamental KH mode. Turbulence generated internal waves are often observed to eventually propagate at a narrow band of angles around $\theta = 45°$, although they might span a wide frequency range in the region of generation. The narrow band of propagation angles has been observed in laboratory experiments of a shear layer (Sutherland & Linden, 1998) and grid turbulence (Dohan & Sutherland, 2003), and in a numerical simulation of a turbulent bottom boundary layer by Taylor & Sarkar (2007). The phase lines of the turbulence generated waves observed at later

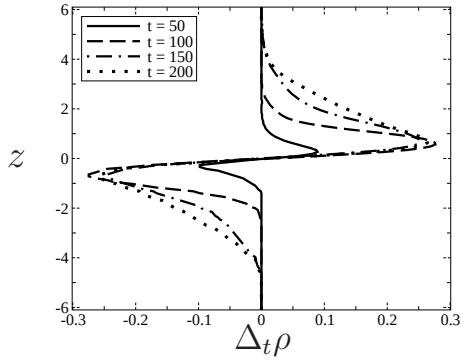

Figure III.15: Density variation, $\Delta_t\rho$ defined in Eq.(III.13), in two-layer case.

time in the $J_d = 0.1$ case also cluster around 45° in the deep region, as shown by Fig. III.10(b). Taylor & Sarkar (2007) offer the following explanation for their boundary layer generated waves that is based on frequency-specific viscous decay: both, high- and low-frequency waves, have low vertical group velocity, larger time of flight to a given vertical level, and large viscous attenuation leaving behind mid-frequency waves clustered around $\theta = 45°$.

Figs. III.12 - III.14(e) give the power spectra of the late-time internal waves in a frame moving with the free-stream velocity. The peak intrinsic frequencies in cases $J_d = 0.1$, 0.25, and 1.0 are 0.21 ± 0.04, 0.31 ± 0.04 and $0.47 \pm 0.04\Delta U^*/\delta^*_{\omega,0}$, which correspond to $\theta = 48 \pm 10°$, $52 \pm 6°$, and $62 \pm 3°$, respectively. The range of wavenumbers in the power spectra is broader than the early-time spectra in part (c) of these figures. Furthermore, the solid diagonal line, $\Omega^* = (\Delta U^*/2)k^*$ is not consistent with the observed power spectrum, showing that the theory that was demonstrated for the KH-generated waves does not work for the late-time turbulence generated waves.

III.F Mass Transport

Linear wave theory predicts that there is no net mass transport by internal waves over a wave period; however, we observe an accumulation of mass in the region near the shear layer. We will show below that the observed mass gain is due to molecular diffusion. The density gradient at the bottom is more negative than at the top surface resulting an accumulation of mass in the shear layer.

(a) (b)

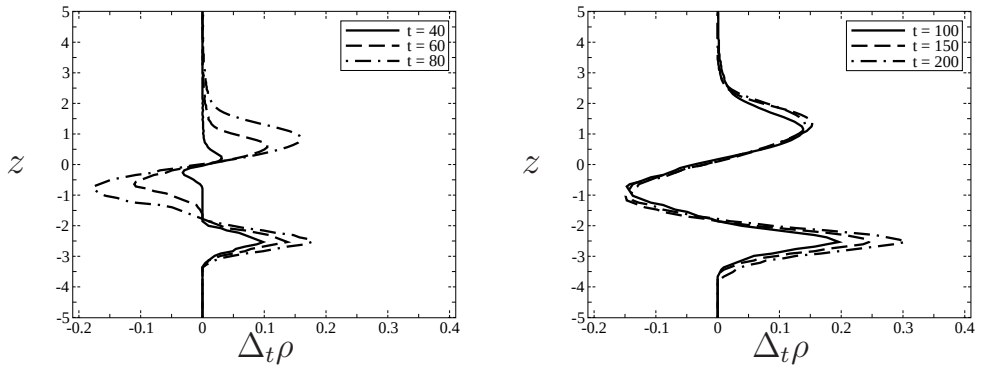

Figure III.16: Density variation, $\Delta_t\rho$ defined in Eq.(III.13), in case $J_d = 0.25$ (a) in KH regime, (b) in turbulence regime.

Take the horizontal average of the density equation, Eq.(III.3),

$$\frac{\partial \langle\rho\rangle}{\partial t} = -\frac{\partial \langle\rho' w'\rangle}{\partial z} + \frac{1}{Re_0 Pr}\frac{\partial^2 \langle\rho\rangle}{\partial z^2}, \tag{III.12}$$

where $\langle\cdot\rangle$ denotes average quantity. The density change in time, $\Delta_t\rho$, can be defined by

$$\Delta_t\rho = \langle\rho\rangle(z,t) - \langle\rho\rangle(z,t=0)\ , \tag{III.13}$$

and the net mass accumulation, $\Delta_t m$, is the spatial integral of $\Delta_t\rho$ from $z = z_l$ to z_u. The depths z_l and z_u are chosen away from the shear layer where the mean density gradient does not vary in time. Integration of Eq.(III.12) in space and time results in

$$\Delta_t m = \int_{z_l}^{z_u} \Delta_t\rho\, dz = \int_0^t \langle\rho' w'\rangle(z_l)\ dt + \frac{1}{Re_0 Pr}\frac{\Delta U^2}{g\delta_{\omega,0}}(J_d - J_s)\, t\,, \tag{III.14}$$

where the vertical mass flux, $\langle\rho' w'\rangle$, at z_u is negligible. The left-hand-side of Eq.(III.14) gives the net mass gain, $\Delta_t m$, in the shear layer. Fig. III.15 shows profiles of $\Delta_t\rho$ at various times in the two-layer case. As the shear layer evolves, the upper portion gets heavier while the lower portion gets lighter as result of mixing. The spatial integration of any of the profiles in this figure, i.e. the left-hand-side of Eq.(III.14), yields zero mass gain. This agrees with the right-hand-side since there is neither mass flux, $\langle\rho' w'\rangle$, nor density gradient outside the shear layer.

In the J_d cases, the mixing in the shear layer is similar but there is an accumulation of mass in the transition region where J_s merges with J_d. Fig. III.16(a) shows the

(a) (b)

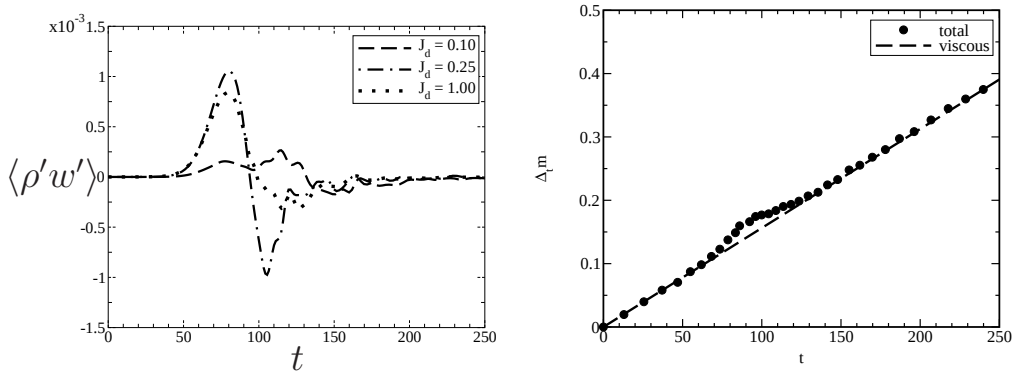

Figure III.17: (a) Vertical mass fluxes at $z = -5$. (b) Net mass gain inside the shear layer in case $J_d = 0.25$. The dots show the net mass gain in the shear layer. The dash line denotes the diffusive contribution.

density variation profiles in case $J_d = 0.25$ during the KH regime. The figure shows mass change, $\Delta_t\rho$, due to shear mixing around the shear center, $z = 0$, accompanied by mass change due to viscous diffusion in the transition region around $z = -2.5$. At $t = 40$, the variation due to diffusion is larger than that due to shear mixing. As the shear layer evolves, the mixing region thickens until it reaches the transition region. The growth of the mixing region is restrained by the presence of the transition region when compared to the 2-layer case. The transition region exhibits insignificant thickness growth in time. In the turbulence regime, as shown in Fig. III.16(b), the mixing due to shear becomes steady but the viscous mass diffusion into the transition region continues. The density variation due to diffusion outgrows the effect of mixing at late time. It is noted that, according to the diffusive term in Eq.(III.14), the region of maximum accumulation has the largest difference in density gradient across the region. Thus, the transition region indeed shows the maximum density variation.

According to linear wave theory, internal waves do not transport mass, i.e. the integration of vertical mass flux, $\langle\rho'w'\rangle$, over a wave period is zero. Fig. III.17(a) shows the time evolution of the mass flux across depth $z = -5$ in the J_d cases. The profiles show an upward flux trailed by a downward flux. However, the upward flux is stronger than the downward resulting a net upward flux. The imbalance is due to

(a) (b)

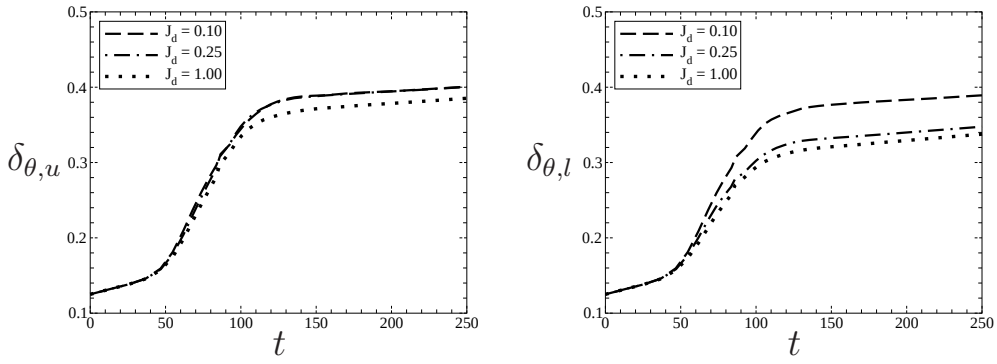

Figure III.18: Momentum thickness: (a) upper portion, $\delta_{\theta,u}$, (b) lower portion, $\delta_{\theta,l}$.

the unsteady decaying source in the shear layer. Although there is a mass transport due to internal waves, the gain is small relative to the diffusive mass accumulation as shown in Fig. III.17(b). In the figure, the dots represent the net mass gain in the shear layer, $\Delta_t m$, calculated using the left-hand-side of Eq.(III.14). The dashed line shows the gain due to the diffusive term on the right-hand-side. In the computation, we take $z_l = -5$ and $z_u = 5$ where the density gradient does not vary in time. It is obvious that the mass accumulation inside the shear layer is mainly contributed by diffusion. The effect from the internal waves during the period $t = 60$ to 130 when the wave flux, $\langle \rho' w' \rangle$, is strong leads to no net mass gain.

III.G Momentum Transport

Internal waves provide a viable route for momentum transport from a region with instabilities and turbulence to an external, quiescent region. In order to quantify the momentum loss due to wave excitation, we examine the evolution of the momentum thickness of the shear layer. The momentum thickness, δ_θ, was defined previously by Eq. (III.6). Since the stratification in the top and bottom regions is different, Eq. (III.6) is split into upper and lower portions,

$$\delta_\theta = \delta_{\theta,u} + \delta_{\theta,l} = \int_{z_l}^{z_0} \left(\frac{1}{4} - \langle u \rangle^2 \right) \, dz + \int_{z_0}^{z_u} \left(\frac{1}{4} - \langle u \rangle^2 \right) \, dz \,, \tag{III.15}$$

(a) (b)

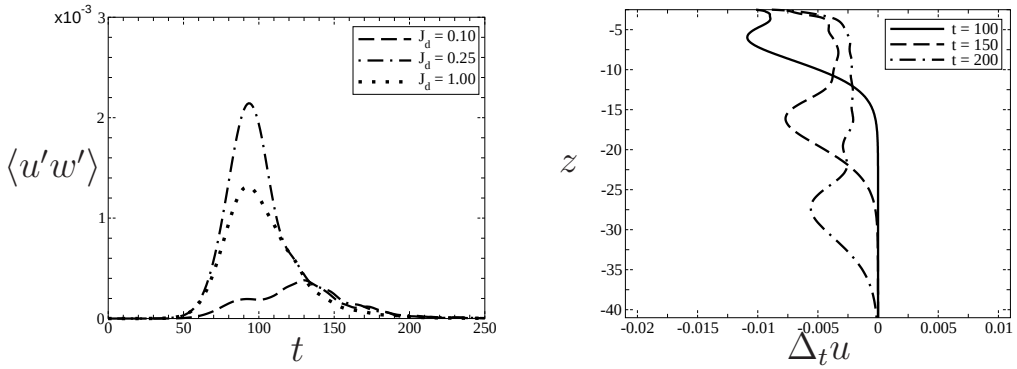

Figure III.19: (a) Reynolds stress $\langle u'w' \rangle$ at depth $z_l = -5$. (b) Variation in the mean velocity profile, $\Delta_t u$, in case $J_d = 0.25$.

where z_0 is the location of zero velocity. Figs. III.18(a,b) show the time evolution of the momentum thickness in the upper and lower portions, respectively. It is evident that the shear layer grows asymmetrically. The asymmetry is related to the stratification intensity in the deep layer. In case $J_d = 0.10$, the upper and lower portions grow similarly. When J_d increases, the lower portion grows significantly less. In case $J_d = 0.25$ where strong internal waves are observed in the bottom region, the top portion grows *exactly* as in case $J_d = 0.10$. However, the bottom portion is nearly 15% smaller. Comparing case $J_d = 1.0$ to case $J_d = 0.25$, it is observed that the thickness growth is less in both upper and lower portions. Stratification decreases overall turbulence production in the core of the shear layer but enhances Reynolds shear stress at the boundaries by allowing internal waves. In order to distinguish between these two features, it is necessary to make precise the quantities that contribute to the thickness growth. Differentiating each portion of (III.15) in time yields

$$\begin{aligned} \frac{d\delta_{\theta,u}}{dt} &= -\int_{z_0}^{z_u} \frac{d\,\langle u \rangle^2}{dt}\, dz\,, \\ \frac{d\delta_{\theta,l}}{dt} &= -\int_{z_l}^{z_0} \frac{d\,\langle u \rangle^2}{dt}\, dz\,. \end{aligned} \tag{III.16}$$

When the x-component of the momentum equation is averaged in the horizontal directions and the result is multiplied with the mean velocity $\langle u\rangle$, we obtain

$$\frac{1}{2}\frac{d\langle u\rangle^2}{dt} = \langle u'w'\rangle \frac{d\langle u\rangle}{dz} - \frac{d}{dz}\left[\langle u\rangle \langle u'w'\rangle\right] - \frac{1}{Re_0}\left(\frac{d\langle u\rangle}{dz}\right)^2 + \frac{1}{Re_0}\frac{d}{dz}\left[\langle u\rangle \frac{d\langle u\rangle}{dz}\right]. \quad \text{(III.17)}$$

Substitution of the above result into Eq.(III.16) leads to the following expression for the temporal rate of change of momentum thickness:

$$\begin{aligned}
\frac{d\delta_{\theta,u}}{dt} &= 2\int_{z_0}^{z_u}\left[P + \frac{1}{Re}\left(\frac{d\langle u\rangle}{dz}\right)^2\right] dz - \langle u'w'\rangle (z = z_u)\ , \\
\frac{d\delta_{\theta,l}}{dt} &= 2\int_{z_l}^{z_0}\left[P + \frac{1}{Re}\left(\frac{d\langle u\rangle}{dz}\right)^2\right] dz - \langle u'w'\rangle (z = z_l)\ .
\end{aligned} \quad \text{(III.18)}$$

Here, $P = -\langle u'w'\rangle (d\langle u\rangle/dz)$ is the turbulence production. We have used the conditions that $\langle u\rangle = -1/2, 0, 1/2$ at $z = z_u, 0, z_l$, respectively. The last terms in Eq. (III.17) can be ignored since the velocity gradient at depths z_u and z_l is relatively small. Integrating (III.18) from time t_0 to t, the expression for momentum thickness as a function of time takes the form

$$\begin{aligned}
\delta_{\theta,u}(t) &= \delta_\theta(t_0) + 2\int_{t_0}^{t}\int_{z_0}^{z_u}\left[P + \frac{1}{Re_0}\left(\frac{d\langle u\rangle}{dz}\right)^2\right] dz\, dt - \int_{t_0}^{t}\langle u'w'\rangle (z = z_u)\ dt\,, \\
\delta_{\theta,l}(t) &= \delta_\theta(t_0) + 2\int_{t_0}^{t}\int_{z_l}^{z_0}\left[P + \frac{1}{Re_0}\left(\frac{d\langle u\rangle}{dz}\right)^2\right] dz\, dt - \int_{t_0}^{t}\langle u'w'\rangle (z = z_l)\ dt\,.
\end{aligned} \quad \text{(III.19)}$$

The growth of momentum thickness is the result of a positive contribution from the turbulence production in the shear layer and a negative contribution from the momentum flux $\langle u'w'\rangle$ at the edges of the shear layer. The viscous contribution can be neglected at high Reynolds number. Since the stratification is weak in the top region, we focus our discussion on the bottom region where the fluid is strongly stratified. Fig. III.19(a) shows the time evolution of the momentum flux $\langle u'w'\rangle$ at depth $z_l = -5$ for the three cases. The flux is strongest in case $J_d = 0.25$, and weakest in case $J_d = 0.10$. Although, less momentum is transported away in case $J_d = 1.0$ relative to case $J_d = 0.25$, δ_θ is *smaller* in the former. This is a result of the reduction in turbulence production owing to buoyancy. It is of interest to compare the radiated momentum flux in the shear layer

with other configurations. The peak value of $\langle u'w' \rangle \simeq 2 \times 10^{-3}$ in Fig. III.19(a) for the internal wave momentum flux is larger than the corresponding value of $\langle u'w' \rangle \leq 10^{-4}$ observed in a jet by Smyth & Moum (2002).

In order to estimate the efficiency of momentum transport by internal waves, we compare the time integrated momentum flux in Eq.(III.19) to the initial momentum in the shear layer, which is 1 ($\Delta U^* \delta^*_{\omega,0}$, dimensionally). The time integration from $t = 0$ to 250 indicates approximately 10% ($J_d = 0.25$), 7% ($J_d = 1.0$), and 3% ($J_d = 0.10$) of the initial momentum can be extracted by the internal waves. In their study of a shear layer formed by flow over a vertical barrier, Sutherland & Linden (1998) report slightly higher values from their two-dimensional simulations. This is typical since velocity fluctuations are more correlated in two-dimensional flows. In their laboratory experiments, 7% is the maximum value that is observed for the momentum propagated away by the internal waves. As the internal waves propagate downward with significant amount of momentum, the mean flow decelerates as noted by Fritts (1982). Fig. III.19(b) shows the variation in the mean velocity profile, $\Delta_t u\,(z,t) = \langle u \rangle\,(z,t) - \langle u \rangle\,(z, t = 0)$. The deceleration magnitude can be 1% near the shear layer and reduces to a smaller value as the waves travel away owing to local viscous diffusion.

III.H Energy Transport

The amount of fluctuation energy transported away from the shear layer by internal waves is quantified and found to be substantial. The shearing event generates fluctuation kinetic energy and waves carry the energy into the deep layer. Therefore, velocity fluctuations measured by the turbulent kinetic energy, *tke*, denoted by $K = 1/2\,\langle u_i' u_i' \rangle$, accumulate outside the shear layer. (Although we use the terms turbulent kinetic energy and fluctuation kinetic energy interchangeably, nonzero K well outside the shear layer is wave energy and not turbulence.) The amount of energy transported is obtained by subtracting the amount of energy inside the shear zone from the total amount present in the simulated domain. Integration of K from $z = -\delta_\omega$ to δ_ω provides a good measure of the *tke* inside the shear zone. Figs. III.20(a,b) show the spatially integrated

(a) (b)

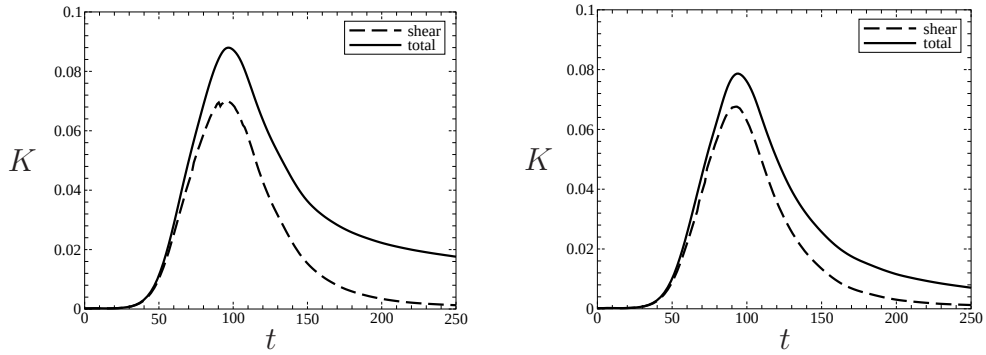

Figure III.20: Integrated turbulent kinetic energy (a)$J_d = 0.25$ (b)$J_d = 1.0$ —, over test domain; − − −, over the shear layer.

K as a function of time for cases $J_d = 0.25$ and 1.0, respectively. The dashed lines indicate the energy inside the shear layer and the solid lines shows the energy in the test domain that excludes the sponge regions. The difference between the two curves yields the amount of energy transported outside the layer by the internal waves. Transport to the exterior starts at $t = 50$, shortly after the KH rollers begin to develop. Fluctuation energy associated with instabilities and turbulence progressively builds up inside the shear layer and, correspondingly, more energy is pumped into the deep region below the shear layer. At late time, the energy inside the shear layer vanishes owing to the dissipative nature of turbulence, but energy remains present outside where the viscous dissipation is relatively weak. Outside the shear layer, the energy resides mainly in the bottom region where the ambient stratification supports internal waves. From Fig. III.20(a), approximately 0.02 ΔU^2 has been transported (the difference between the two lines at late time). Relative to the initial mean kinetic energy inside the shear layer, the transported energy is roughly 15% in case $J_d = 0.25$, 7% in case $J_d = 1.0$, and 3% in case $J_d = 0.10$. The initial mean kinetic energy is calculated by integrating $1/2 \langle u \rangle^2$ at time $t = 0$ from $z = -\delta_{\omega,0}$ to $\delta_{\omega,0}$.

It is desirable to describe the "efficiency" of energy transport in light of the *tke* budget. The evolution equation for the turbulent kinetic energy is

$$\frac{dK}{dt} = P - \varepsilon + B - \frac{\partial T_i}{\partial x_i} \, . \tag{III.20}$$

(a) (b)

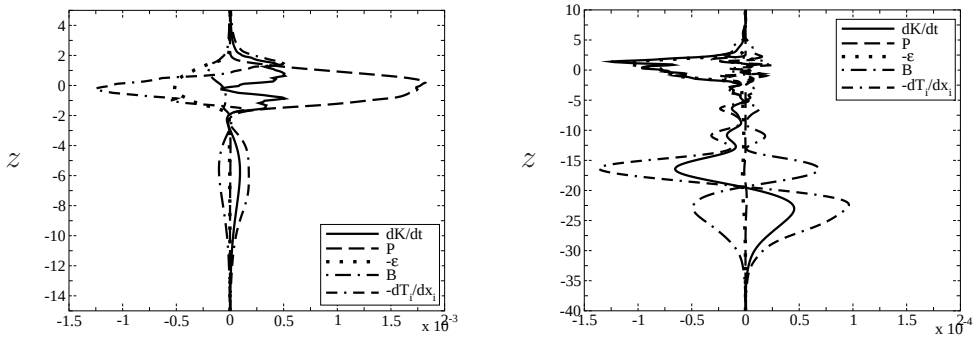

Figure III.21: Vertical profiles of *tke* budget in case $J_d = 0.25$ at (a) t = 83, (b) t = 160.

(a) (b)

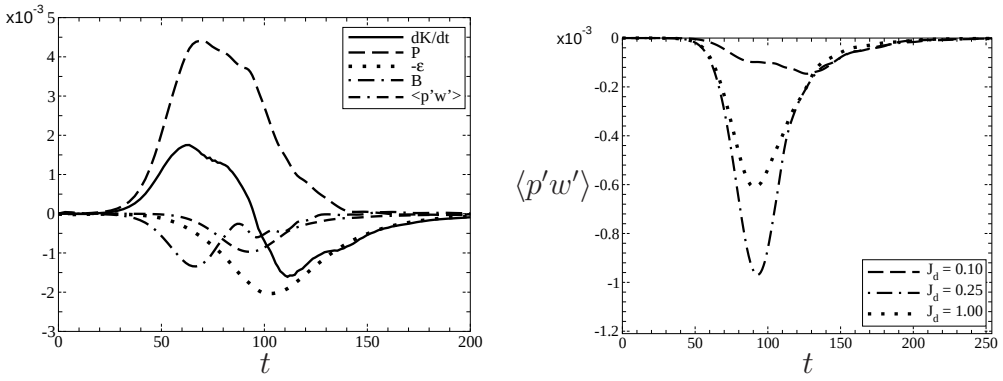

Figure III.22: (a) Balance of *tke* budget for $J_d = 0.25$. The production, dissipation and buoyancy flux are integrated from z_{max} to $z = -5$. $\langle p'w' \rangle$ is at $z = -5$. (b) Internal wave flux, $\langle p'w' \rangle$, at $z = -5$ compared among different cases.

Here, K is the turbulent kinetic energy defined previously, P is the production rate, defined as

$$P \equiv -\left\langle u_i' u_j' \right\rangle \frac{\partial \left\langle u_i \right\rangle}{\partial x_j} = -\left\langle u' w' \right\rangle \frac{d \left\langle u \right\rangle}{dz} \ ,$$

ε is the dissipation rate, defined as

$$\varepsilon \equiv \frac{2}{Re_0} \left\langle s_{ij}' s_{ij}' \right\rangle ; s_{ij}' = \frac{1}{2} \left(\frac{\partial u_i'}{\partial x_j} + \frac{\partial u_j'}{\partial x_i} \right) \ ,$$

B is the buoyancy flux, defined as

$$B \equiv -Ri_{b,0} \left\langle \rho' w' \right\rangle \ ,$$

$\partial T_i / \partial x_i$ is the transport of tke, defined by

$$T_i \equiv \frac{1}{2} \left\langle u_i' u_j' u_j' \right\rangle + \left\langle u_i' p' \right\rangle - \frac{2}{Re_0} \left\langle u_j' s_{ij}' \right\rangle \ .$$

For the present flow, the transport term simplifies to $\partial T_3 / \partial z$ with

$$T_3 = \frac{1}{2} \left[\left\langle w' u' u' \right\rangle + \left\langle w' v' v' \right\rangle + \left\langle w' w' w' \right\rangle \right] + \left\langle p' w' \right\rangle - \frac{2}{Re_0} \left[\left\langle u' s_{31}' \right\rangle + \left\langle v' s_{32}' \right\rangle + \left\langle w' s_{33}' \right\rangle \right] .$$

Figs. III.21 (a,b) show the profile of each term in the tke budget in case $J_d = 0.25$ at time $t = 83$ and 160, respectively. At $t = 83$, the production and dissipation are large but restricted to the shear region. The presence of propagating internal waves external to the shear layer is shown by the extension of profiles of the buoyancy flux, transport (essentially $d \left\langle p' w' \right\rangle / dz$) and dK/dt into the deep region. At time t = 160, the production is negligible and, in the shear region, the dissipation rate is balanced by dK/dt. The internal gravity waves continue to transport energy into the deep region. The profiles at $t = 160$ show that, in the deep region, approximately half of the transport goes into changing the fluctuation kinetic energy and half into the buoyancy flux, i.e. changing the fluctuation potential energy.

We now characterize the energetics of the fluctuations during the entire evolution rather than at the two specific times of Fig. III.21. Integrating Eq. (III.20) from depth $z^\star$ to the top boundary z_{max}^t of the test region yields

$$\int_{z^\star}^{z_{max}^t} \frac{dK}{dt} \, dz = \int_{z^\star}^{z_{max}^t} P \, dz - \int_{z^\star}^{z_{max}^t} \epsilon \, dz + \int_{z^\star}^{z_{max}^t} B \, dz \ + \left\langle p' w' \right\rangle (z^\star) \ . \qquad \text{(III.21)}$$

Fig. III.22(a) shows the time evolution of terms in Eq. (III.21) for case $J_d = 0.25$. The spatial integration includes the upper region excluding the sponge region, the shear layer and the bottom region down to depth $z^\star = -5$. As the vortices roll up, there is significant energy extraction from mean shear by fluctuations through the turbulent production, some of which is used to increase turbulent kinetic energy. Also in the presence of the rollers, the buoyancy flux reaches its maximum value since larger eddies have the capability to lift up heavy fluid. The peak dissipation rate occurs at later time when the flow turns turbulent. The term $\langle p'w' \rangle$, called the pressure transport term in the turbulence literature and the internal wave flux in the literature on waves, is significant and occurs at a time between the occurrence of peak production and peak dissipation. When $z^\star$ is far away from the shear layer, the internal wave (IW) flux, $\langle p'w' \rangle$, dominates the other transport terms. Fig. III.22(b) shows the energy flux $\langle p'w' \rangle$ at $z = -5$ for the three simulated cases. Similar to the momentum flux, the IW flux depends strongly on the stratification in the deep region. For weak stratification ($J_d = 0.1$) the wave excitation is negligible and so is the IW flux. Case $J_d = 0.25$ has the strongest IW flux, not $J_d = 1.0$. The dependence of internal wave flux on J_d is non-monotone because increasing the stratification, on one hand, increases the flux for a given amplitude of vertical velocity fluctuation but, on the other hand, decreases the vertical velocity fluctuations in the generation region. In the shear layers simulated here, the net IW flux due to the rollers is significantly higher than the flux due to small-scale turbulence.

An overall quantification of the efficiency of IW flux is obtained by integration of Eq. (III.21) from time $t = 0$ to late time t_f when turbulent kinetic energy inside the shear layer vanishes. This procedure is convenient since the temporal peak values of the various terms in the *tke* balance occur at different times. Table III.1 shows the efficiency of energy transport by waves relative to other terms in the energy budget. Strang & Fernando (2001) estimate the ratio of IW flux to the rate of change of potential energy as approximately 48%, slightly smaller than the values of 75% and 57% for $IW/(-B)$ in Table III.1. The production, P, measures the extraction of *tke* from the mean shear flow by the Reynolds shear stress of the fluctuations. It is useful to

Table III.1: Energy flux efficiency, energy partition and mixing efficiency. The terms in the tke budget are integrated in both time and space (from $z = -5$ to z^t_{max}) to calculate the tabulated values.

J_d	IW/P	IW/ϵ	$IW/(-B)$	ϵ/P	$(-B)/P$	Γ	Γ_d
0.1	0.05	0.08	0.18	0.6	0.28	0.46	0.46
0.25	0.17	0.33	0.75	0.53	0.23	0.44	0.44
1.0	0.14	0.25	0.57	0.55	0.24	0.44	0.43

quantify the partition of the extracted energy into the various sinks of the *tke* balance as done in columns 2, 5 and 6 of Table III.1. In case $J_d = 0.25$, 53% of the production is dissipated, 23% used for stirring the density field, and 17% is transported away by internal waves. In the same order, the values are 55%, 24%, 14% for case $J_d = 1.0$ and 60%, 28%, 5% for case $J_d = 0.1$. As the numbers show, internal waves can considerably alter the energetics inside the shear layer.

The quantity, $\Gamma = -B/\epsilon$, the so-called mixing efficiency is an important quantity that is often used by oceanographers to infer the eddy diffusivity of mass, K_ρ, from the dissipation rate obtained by microstructure measurements or estimated by measurement of the Thorpe scale. If Γ is known, the expression $K_\rho = \Gamma\epsilon/N^2$ can be used without further approximation to obtain the eddy diffusivity (Osborn, 1980). The quantity, $\Gamma_d = \epsilon_\rho/\epsilon$, can be measured directly in the ocean from temperature gradient and velocity shear data, and is used as a surrogate for the mixing efficiency (Oakey, 1985). Here, ϵ_ρ is defined by

$$\epsilon_\rho = \frac{1}{PrRe_0}\frac{g}{\rho_0|d\bar{\rho}/dz|}\overline{\frac{\partial\rho'}{\partial x_k}\frac{\partial\rho'}{\partial x_k}}. \tag{III.22}$$

The quantity, ϵ_ρ, signifies irreversible loss of turbulent potential energy to the background density field. The last two columns of Table III.1 give the overall mixing efficiency where the buoyancy, viscous and scalar dissipation are integrated in time before the ratios are taken. Although, $\Gamma = \Gamma_d = 0.2$ is often employed, the value can depend on the type of flow, the age of the flow in non-stationary examples, as well as

other parameters such as Reynolds number, Richardson number, and Prandtl number. Here, both Γ and Γ_d are approximately 0.44 for all J_d cases, somewhat smaller than the value of 0.6 reported by Smyth *et al.* (2001) where they simulate a two-layer case at Re = 1965 and $Ri_b = 0.08$.

III.I Implications

The direct numerical simulations conducted here show that the presence of an ambient region with uniform stratification substantially changes the evolution of a stratified shear layer from the typically studied situation of shear between two layers, each with constant density that differ. Three cases with different strengths of stratification in the deep region ($J_d = 0.10$, 0.25, and 1.0) and with uniform stratification, $J_s = 0.05$, in the shear zone were compared with a two-layer case. All four cases have the same overall bulk Richardson number, $Ri_b = 0.10$.

The thickness of the shear zone measured with the vorticity thickness, δ_ω, increases with increasing time. The thickness, δ_ω, is smallest in the case with strongest stratification, $J_d = 1.0$. Unlike the 2-layer case where the thickness asymptotes at late time, δ_ω has a secondary growth stage at late time with a moderate but noticeable growth rate. This secondary growth leads to a vigorous growth in bulk Richardson number, Ri_b because the shear layer entrains heavier fluid at the bottom edge. At the end of the $J_d = 1.0$ simulation, $Ri_b \simeq 4$, an order of magnitude larger than the asymptotic value of $Ri_b = 0.32 \pm 0.06$ observed in the two-layer problem. Another measure of shear layer thickness is the momentum thickness, δ_θ. The J_d cases have significantly smaller δ_θ with respect to the two-layer situation. Furthermore, the secondary growth of δ_θ in the J_d cases is much smaller than that of δ_ω. The shear layer stirs and mixes up the density field and, consequently, pycnoclines (regions with a strong change in density gradient) are formed at the edges of the layer. At the bottom edge, the pycnocline grows and then merges into the strong background stratification. The pycnocline at the top edge grows and then depletes in time. The deep stratification leads to an important qualitative difference in the profile of mean shear with respect to the two-layer

case. The position of maximum shear shifts from its initial position at the center of the shear layer downward toward the center of the thermocline in contrast to the two-layer case where the maximum shear remains at the center. Lower-momentum fluid that is transported to the pycnocline by stirring is unable to exchange its momentum with the higher-momentum fluid because of the large stable stratification in the pycnocline and, as a result, the shear in enhanced. Even with the enhanced shear, the gradient Richardson number is much larger than the critical value of 0.25 in the pycnocline and, consequently, shear instabilities are prohibited. In the presence of a deep stratification the coherent structures break down shortly after their formation because the non-linear pairing process, observed in the two-layer case, is inhibited.

The shear layer excites strong internal waves in the cases with $J_d = 0.25$ and 1.0. Waves are excited during both the early-time stage of Kelvin-Helmholtz (KH) instability and the late-time stage of three-dimensional turbulence. The early-time generation of internal waves is especially strong and their characteristics can be explained by linear theory: the horizontal wave number is given by the most unstable wavelength i.e. the KH mode, the temporal frequency is that due to the bottom free-stream moving over the approximately stationary KH rollers, and the linear dispersion relationship for internal gravity waves predicts the observed angle of the phase lines (equivalently group velocity). In particular, the phase lines are observed to tilt at approximately θ =32-38° ($J_d = 0.25$) and 62-68° ($J_d = 1.0$) to the vertical. The power spectrum of the early-time internal waves as function of temporal frequency and wave number is also found to be consistent with linear theory. $J_d > 0.18$ is the condition for the KH instability to excite propagating internal waves. Consequently, KH-generated internal waves are not observed when $J_d = 0.10$. However, the late-time turbulent stage does permit internal waves that are observed to span a wide range of wave numbers, frequencies and phase angles in the generation region. The linear theory that was found to work well at early time does not explain the characteristics of the late-time waves. In agreement with previous laboratory and numerical studies of turbulence-generated waves, the phase lines in the deep propagation region cluster in a narrow band, approximately around 45°.

Internal waves, observed here to propagate in the bottom interior region, do not transport mass away or into the shear layer, consistent with linear wave theory, but are shown to constitute a significant pathway for energy transfer into the interior. The net mass gain, observed here, is the result of the molecular diffusive flux associated with the density gradient external to the shear layer. Nonetheless, internal waves extract momentum from the shear layer. Therefore, the evolution of the momentum thickness δ_θ shows asymmetry: the thickness grows less in the bottom portion where strong internal waves are generated. The extraction is most efficient in the case with $J_d = 0.25$. Measures of Reynolds stress in the deep region shows that internal wave can carry up to 10% of the initial momentum inside the shear layer. The significant drag causes the bottom part of the shear layer to decelerate. Along with momentum, waves also transport energy to the ambient. The internal wave energy flux is examined by comparing the terms in the vertically integrated turbulent kinetic energy equation. Case $J_d = 0.25$ shows the strongest energy flux and not $J_d = 1.0$ implying that there is a buoyancy frequency which is optimal with respect to wave energy flux. Integration of the kinetic energy budget over the simulated time shows that the internal waves are important to the energetics of the shear layer. The contribution of the wave energy flux can be up to 17% of the production, 33% of the dissipation and 75% of the buoyancy flux. Therefore, internal waves provide an important route for transport of fluctuation energy from shear flow instabilities into the stratified interior with potentially important implications for energy pathways in the ocean and in the atmosphere.

The contents of this chapter have been published in the Journal of Fluid Mechanics: Pham, H. T., Sarkar, S. and Brucker, K. A., "Dynamics of a Stratified Shear Layer Above a Region of Uniform Stratification", J. Fluid Mech.*,* ***630****, 191-223 (2009). The dissertation author is the primary researcher and the research supervisor and Kyle A. Brucker are the co-author of the paper.*

Chapter IV

Transport and mixing of density in a continuously stratified shear layer

IV.A Objectives

In the past decades, turbulent mixing in a stratified fluid driven by a background shear has been one of the focal research topics in terms of understanding the mechanism of mixing as well as its parametrization in models of large-scale environmental flows. Although there has been much progress (Fernando., 1991; Peltier & Caulfield, 2003; Ivey *et al.*, 2008), a number of unresolved questions remain including the following: (i) The interaction of internal gravity waves, that can transport significant amount of momentum and energy to the ambient, with local mixing, and (ii) the influence of Reynolds number. These issues are addressed by the current study that utilizes three-dimensional Direct Numerical Simulation (DNS) to investigate turbulent mixing in a high Re shear layer in a continuously stratified ambient where internal waves are supported.

Turbulent mixing in homogeneous flows has been thoroughly investigated including parametrization schemes for mixing. Jacobitz *et al.* (1997) use 3D-DNS to study turbulence mixing in a periodic box with constant vertical shear S in a linearly strat-

ified ambient where stratification is measured by squared buoyancy frequency $N^2 = (-g/\rho_0)\, d\langle\rho\rangle/dz$. The turbulence evolution is found to strongly depend on the gradient Richardson number $Ri_g = N^2/S^2$, the Reynolds numbers defined using the Taylor micro-scale, and the shear number SK/ε where K is the turbulent kinetic energy (TKE) and ε is the dissipation rate. Riley & deBruynKops (2003) investigate the properties of turbulent mixing driven by Taylor-Green vortices. The mixing efficiency is large initially and settles down to the value of approximately 0.4 during the turbulence decay period. Shih *et al.* (2005) investigate the parametrization of eddy viscosity and eddy diffusivity using simulations of homogeneous shear flow with stratification. The evolution of the eddy diffusivity is found to consist of three regimes: energetic, intermediate and diffusive mixing. There is a strong dependence of eddy diffusivity on the turbulence activity $\varepsilon/\nu N^2$, also known as buoyancy Reynolds number Re_b. Other parametrization using the parameters $ReFr_k^2$ and Re/Ri_g are also shown to describe the evolution of eddy diffusivity. Here, $Re = q\Lambda/\nu$ where $q = \sqrt{(}2K)$, Λ is the integral length-scale, and $Fr_k = \varepsilon/(NK)$ is the local Froude number.

Turbulent mixing a two-layer shear flow with hyperbolic tangent density and velocity profiles has received significant attention. Caulfield & Peltier (2000) use stability analysis and 3D-DNS to identify, in addition to the primary Kelvin-Helmholtz (K-H) shear instability, a secondary instability wherein streamwise vortices are formed at the braids, interact with each other, and thus drive the mixing. The secondary instability is also observed in the 3D-DNS of Werne *et al.* (June 2005). Staquet (2000) from 3D-DNS studies describes three stages of mixing: the first stage of primarily 2-D K-H instability with high mixing efficiency, the second stage of small-scale three-dimensional instability as in the work of Caulfield & Peltier (2000), and the final stage of turbulence generation and decay in which the flux Richardson number approaches the value approximately 0.25. In the final stage, the eddy diffusivity exhibits an inverse dependence on the gradient Richardson number Ri_g defined using the sorted background density profile as introduced by Winters *et al.* (1995). Smyth & Moum (2000*b*,*a*); Smyth *et al.* (2001) investigate the effect of Reynolds number Re and Prandtl number Pr upon the evolution of the mixing event and further contrast their 3D-DNS results

to the observed mixing data in the Equatorial Undercurrents. Upon comparison, they conclude that the DNS results agree well with data from field observations. They further state that the age of an turbulent mixing event can be described by the ratio $R_{OT} = L_O/(L_E^{3/4} L_T^{1/4})$, where L_0, L_E, and L_T are the Ozmidov, Ellison, and Thorpe scales, respectively. The mixing efficiency is found to be in the range of $0.2 - 0.6$.

Turbulent mixing with a background shear and a density profile different from the two-layer problem has been studied. Strang & Fernando (2001) perform a laboratory experiment to investigate the turbulent entrainment at a sheared density interface. The background condition is a stratified shear layer situated between a well-mixed turbulent upper layer and a quiescent linearly stratified lower layer. The flow evolution includes K-H instability and a secondary *Hölmböe* wave instability whose interactions with each other can cause breaking and intense mixing. Internal waves are observed to propagate into the lower region. The ratio of the wave energy flux to the rate of change of potential energy due to mixed-layer deepening is approximately 48%. Tse *et al.* (2003) uses 3D-DNS to study the evolution of stratified turbulence in a forced jet, a model for the atmospheric tropopause. The jet is maintained at quasi-equilibrium state with strong turbulence in the core, patchy turbulence and nonlinear internal waves at the edges. It is found that spatial variation in turbulence activity across the jet can be characterized through length scales and budget equations for the velocity and density variances.

Internal waves excited by an unstable shear layer have been observed to carry significant momentum flux. Sutherland & Linden (1998) perform a laboratory experiment in which a thin vertical barrier is put inside a water channel and partially obstructs the incoming flow. The fluid is lightly stratified in the upper region while the lower region is strongly stratified. Vortices, shed in the wake of the barrier, excite internal waves. The waves propagating into the lower region are found to carry approximately 7% of the average momentum across the shear depth. Pham *et al.* (2009) investigate the properties of the internal waves through 3D-DNS of a stratified shear layer at $Re = 1280$. The internal waves are excited by an unstable shear layer located between a weakly stratified region and a region with stronger stratification. The internal waves are found to carry up to 10% of the initial momentum in the shear layer. Integration

of the TKE budget over the shear layer and time shows that the wave energy flux can be up to 17% of the turbulent production, 33% of the dissipation rate and 75% of the buoyancy flux. The mixing efficiency is approximately 0.4.

Different from the work of Pham *et al.* (2009) whose focus is on the properties of the large-scale internal waves radiated by the shear layer, the current investigation focuses on turbulent mixing inside the shear layer. The Reynolds number, $Re = 5000$ is nearly 4 times larger relative to Pham *et al.* (2009). Furthermore, in the current work, the largest turbulent activity $\varepsilon/\nu N^2$ is as large as 200 so that the turbulent mixing spans the entire three regimes according to Shih *et al.* (2005). Specifically, we aim to answer the following questions: (1) How does the presence of the external stratification and the excitation of internal gravity waves affect transport and mixing inside the shear layer ? (2) How well can parametrization schemes in homogeneous stratified flows be applied toward parametrizing inhomogeneous stratified turbulence ?

IV.B Problem Formulation

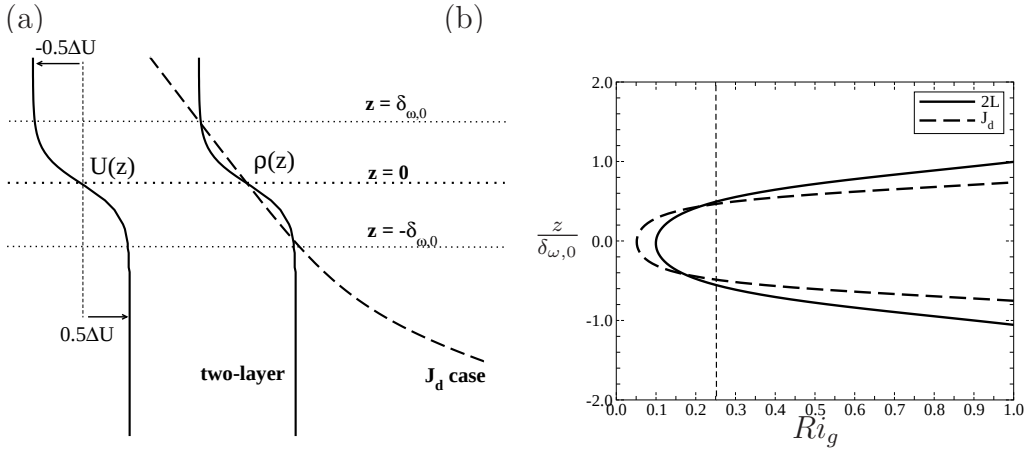

Figure IV.1: (a) Schematics of *initial* mean velocity and density profiles. (b) *Initial* gradient Richardson number Ri_g. The dashed line indicates the marginal value, $Ri_g = 0.25$, for shear instability.

Three-dimensional Direct Numerical Simulations are employed to describe the evo-

lution of inhomogeneous stratified turbulence that originates from shear instability. The flow is a temporally-evolving shear layer with the initial velocity having the following profile at $t = 0$:

$$\langle u^* \rangle (z, t = 0) = \frac{-\Delta U^*}{2} tanh \left(\frac{z^*}{0.5\delta^*_{\omega,0}} \right),$$

where ΔU^* is the velocity difference across the shear layer and $\delta^*_{\omega,0}$ is the initial vorticity thickness defined as $\delta^*_{\omega,0} = \Delta U^* / \left(d \langle u^* \rangle / dz^* \right)_{max}$. Subscript 0 indicates quantities at initial state, superscript $*$ denotes dimensional quantities and the bracket $\langle \cdot \rangle$ indicates horizontal x-y average. Two types of initial density profiles are targeted. The first, namely the two-layer (2L) case, corresponds to the classical Thorpe experiments with the following profile at $t = 0$,

$$\langle \rho^* \rangle = \langle \rho^*_0 \rangle - \frac{\Delta \rho^*}{2} tanh \left(\frac{z^*}{0.5\delta^*_{\omega,0}} \right),$$

where $\Delta \rho^*$ is the density difference across twice the initial vorticity thickness $\delta^*_{\omega,0}$. The second, namely the J_d case, is continuously stratified with the following stratification profile at $t = 0$:

$$J(z) = \frac{J_s + J_d}{2} + \frac{J_s - J_d}{2} tanh \left(\frac{z^* + 2.5\delta^*_{\omega,0}}{\delta^*_{\omega,0}} \right).$$

Here, $J(z) = N(z)^{*2} \delta^{*2}_{\omega,0} / \Delta U^{*2}$ is the non-dimensional Richardson number with the buoyancy frequency $N^{*2} = -\left(g^* / \rho^*_0 \right) d \langle \rho^* \rangle / dz^*$. J_s is chosen such that the density difference, $\Delta \rho^*_0$, across $2\delta_{\omega,0}$ is the same for both cases and J_d is equal to $5J_s$. The initial velocity and density profiles are shown in figure IV.1(a). The two-layer profile has been studied previously (Smyth & Moum, 2000*b*,*a*; Caulfield & Peltier, 2000; Staquet, 2000) and the corresponding mixing efficiency has been discussed at length (Smyth *et al.*, 2001) and will be used as a base case for comparison in the current study. The J_d profile is typical to numerous observations in the ocean pycnocline as well as in the atmospheric inversion in which the background density stratification varies with depth/height.

The governing equations are the incompressible Navier-Stokes equation with Boussinesq approximation with dependent variables: velocity u, v, w, pressure p and density

ρ in a non-rotating Cartesian coordinates with independent variables: x, y and z. The variable p denotes deviations from the mean hydrostatic pressure. The density is decomposed into a reference density ρ_0 and a departure which is composed of a mean and fluctuation as follows:

$$\rho = \rho_0 + \langle\rho\rangle(z) + \rho'(x, y, z, t).$$

The apostrophe indicates the fluctuation from the planar mean value. In the current study, fluctuations can represent both waves and turbulence. The Boussinesq approximation supposes that the variations in density are ignored in the inertial terms in the momentum equations but they contribute to the gravitational force. Using $\delta^*_{\omega,0}$, ΔU^*, ρ^*_0, and $\Delta\rho^*_0$ as the characteristic scales for length, velocity, density, and density difference in the momentum equation, respectively, the non-dimensional governing equations take the following form:

$$\nabla \cdot \mathbf{u} = 0, \tag{IV.1}$$

$$\frac{\partial \mathbf{u}}{\partial t} + (\mathbf{u} \cdot \nabla)\mathbf{u} = -\nabla p + \frac{1}{Re_0}\nabla^2\mathbf{u} - Ri_{b,0}\rho'\delta_{i3}, \tag{IV.2}$$

$$\frac{\partial \rho}{\partial t} + (\mathbf{u} \cdot \nabla)\rho = \frac{1}{Re_0 Pr}\nabla^2\rho, \tag{IV.3}$$

where

$$Re_0 = \frac{\Delta U^* \delta^*_{\omega,0}}{\nu^*}, \quad Ri_{b,0} = \frac{g^* \Delta\rho^*_0 \delta^*_{\omega,0}}{\rho^*_0 \Delta U^{*2}}, \quad Pr = \frac{\nu^*}{\kappa^*}. \tag{IV.4}$$

Here, ν^* and κ^* are the kinematic viscosity and molecular diffusivity, respectively. Both datasets are generated with $Re = 5000$, $Pr = 1$ and $Ri_{b,0} = 0.1$. It is noted that although the bulk Richardson number $Ri_{b,0}$ are the same, the gradient Richardson number $Ri_g(z) = N^2(z) / (d\langle u\rangle/dz)^2$ at the centerline in the two-layer case is twice larger than that in the J_d case as shown in figure IV.1(b).

The initial value of Re is sufficiently large such that the initial instability is nearly inviscid and the separation between the largest and smallest length scales is approximately three orders of magnitude assuming the separation scales as $Re^{-3/4}$. The initial Ri_b is chosen to be less than the critical value of 0.25 for shear instability (Hazel, 1972). The parameters used in this study are relatively low for environmental applications.

Nonetheless, Smyth *et al.* (2001) has simulated a 3D-DNS of a mixing layer with the two-layer profile with $Re = 4978$, $Pr = 1$ and $Ri_b = 0.08$ and compared the computed mixing efficiency to the values from measurements in turbulent patches observed off the California coast and at the equator. They concluded that the parameters in their DNS is high enough to approximate a high Reynolds number limit and further increase in Re would not significantly alter their DNS results.

The numerical method is similar to that in our previous work (Basak & Sarkar, 2006; Brucker & Sarkar, 2007). Briefly, a second-order finite difference method on a staggered grid is used for spatial discretization and the simulation is marched in time with third-order low-storage Runga-Kutta. The current DNS utilizes parallel computing with MPI to handle the computational needs of simulating high Reynolds number flows. The domain size is $30.75 \times 15.39 \times 93.6$ and the grid has $1024 \times 512 \times 768$ points in the x, y, z directions, respectively, for a total of 402 million gridpoints. The domain length L_x is chosen to accommodate approximately four wavelengths of the primary K-H instability. The grid is uniform in the streamwise (x) and spanwise (y) directions with a spacing of 0.03. In the vertical direction, the grid is uniform in the region $-4.5 < z < 3$ with a spacing of 0.03 while the grid is stretched at the rate of 1% outside. Low amplitude velocity perturbations with a broadband spectrum,

$$E(k) \propto \left(\frac{k}{k_0}\right)^4 exp\left[-2\left(\frac{k}{k_0}\right)^2\right],$$

are added to initialize the flow. Here, k_0 is set such that the spectrum peaks at 1.7. Fluctuations are introduced only in the shear layer with the shape function,

$$A(z) = exp\left(-z^2\right).$$

and with a maximum amplitude of 1% ΔU.

Periodic boundary conditions are used in the streamwise and spanwise directions.

In the J_d case, the top and bottom faces of the domain have the following conditions:

$$\begin{aligned} u\left(z_{min}\right) = \frac{1}{2}\,, \quad u\left(z_{max}\right) = -\frac{1}{2}\,, \\ v\left(z_{min}\right) = v\left(z_{max}\right) = 0\,, \\ p\left(z_{min}\right) = p\left(z_{max}\right) = 0\,, \\ \frac{\partial w}{\partial z}\left(z_{min}\right) = \frac{\partial w}{\partial z}\left(z_{max}\right) = 0\,, \\ \frac{\partial \rho}{\partial z}\left(z_{max}\right) = \frac{-J_s}{Ri_{b,0}}\,, \\ \frac{\partial \rho}{\partial z}\left(z_{min}\right) = \frac{-J_d}{Ri_{b,0}}\,. \end{aligned}$$

In the two-layer case, the velocity boundary conditions are the same but the density ρ has a no-flux condition. Since internal waves can propagate far away from the shear layer, a sponge region is added at the top ($z > 15$) and the bottom ($z < -50$) boundaries to control spurious reflections of internal waves. More details about the numerical methods can be found in Basak & Sarkar (2006); Brucker & Sarkar (2007); Pham *et al.* (2009).

IV.C Evolution of the Shear Layers

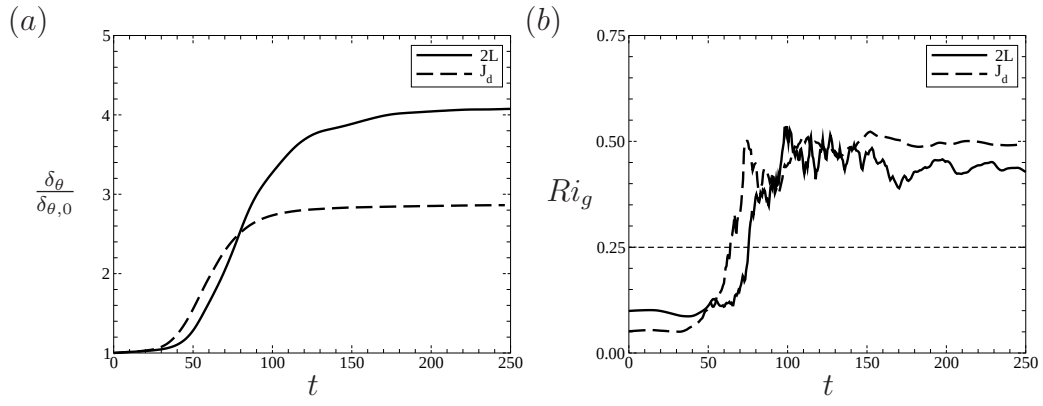

Figure IV.2: Evolution of (a) the momentum thickness δ_θ and (b) the gradient Richardson number Ri_g at the centerline of the shear layer $z = 0$. The dash line indicates the critical value of $Ri_g = 0.25$ for shear instability.

The evolution of the shear layer which consists of shear instability, formation of K-H rollers, their breakdown into three-dimensional turbulence and finally the decay of turbulence can be described with the growth of the momentum thickness δ_θ defined as

$$\delta_\theta = \int_{z_l}^{z_u} \left(\frac{1}{4} - \frac{\langle u \rangle^2}{\Delta U^2} \right) \, dz$$

where the depths z_u and z_l are taken to be 5 and -5, respectively. The depths are locations at which the background shear $d\langle u \rangle / dz$ is approximately zero over time although the momentum flux $\langle u'w' \rangle$ due to internal waves can be large due to internal waves. The growth of δ_θ shown in figure IV.2(a) indicates three evolutionary regimes for both cases. During the early stage approximately $0 < t < 25$, the shear layer adjusts to the initial conditions and the growth is similar between the cases. The second regime is the shear instability regime in which the instability develops into the KH rollers and the shear layers thicken at strong linear rate. The linear growth rate is similar between the two cases although it starts and ends earlier in the J_d case. As the results, δ_θ in the J_d case is significantly smaller at end of the second regime when the K-H rollers can no longer grow and small-scale turbulence dominates the shear layer. The transition from the second regime to the third regime in which the shear layer is dominated by decay of turbulence is sharper in the J_d case. In the two-layer case, during the transition the turbulent shear layer thickens although at significantly smaller rate compared to the growth observed in the second regime. In the third regime as the turbulence decays the growth of δ_θ becomes asymptotic at a value which is more than 25% larger in the two-layer case.

The evolution of Ri_g computed at the center of the shear layer $z = 0$ is shown in figure IV.2(b). In both cases, Ri_g grows at similar rate during the formation of the K-H rollers and exhibits strong fluctuations during the transition to turbulence. After that, Ri_g asymptotes to a constant value. Although the initial value of Ri_g is half of that in the two-layer case, the value during the turbulence decaying stage is larger in the J_d case. The asymptotic value is approximately 0.45 in the two-layer case and 0.5 in the J_d case.

IV.D Turbulence Evolution

In the previous section we have described the evolution of the mean flow, in the section we focus on the evolution of turbulence in the shear zone which consists of two stages: the generation of turbulence through shear instability and the decay of turbulence through molecular mixing and spatial transport to the ambient. Although the stages are the same between the two cases, there are differences which affect the turbulent mixing rate. We elaborate on the differences with the visualization of the shear layer, the TKE budget, the budget of density variance, and the evolution of relevant length scales as well as some non-dimensional turbulence parameters.

IV.D.1 Visualization of the turbulent fields

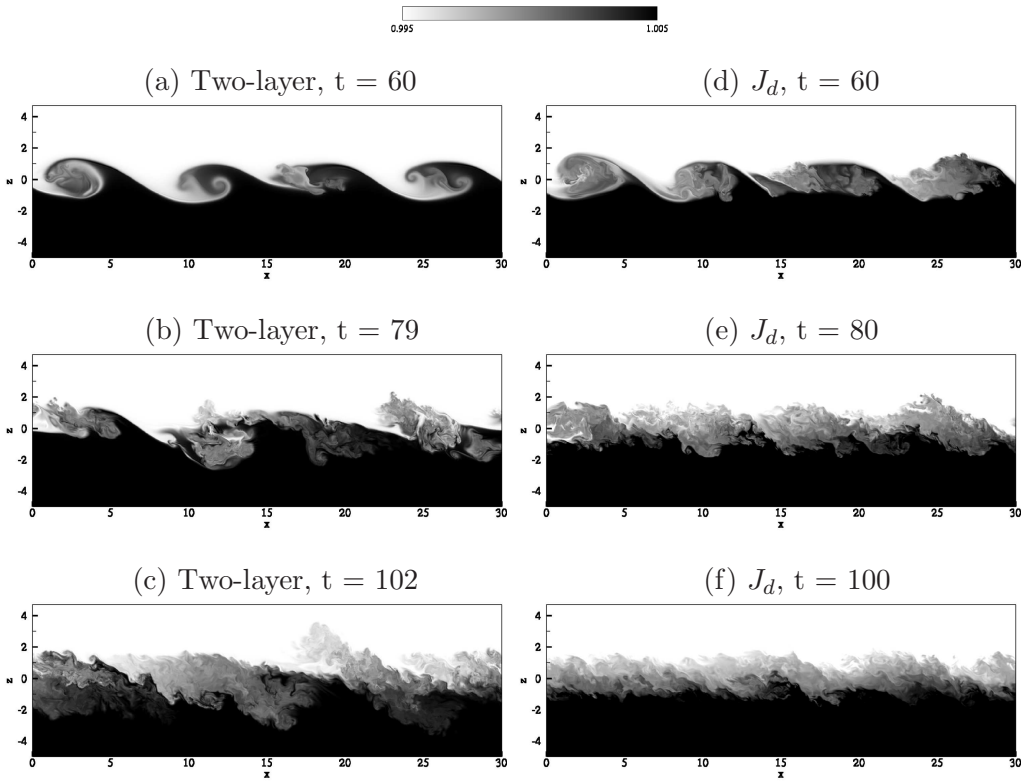

Figure IV.3: Density field on a vertical xz plane at y = 3.9.

Cross sections of the density fields in the simulated flows are shown in figure IV.3. Figures IV.3(a-c) correspond to the two-layer case while figures IV.3(d-f) correspond to

the J_d case. In both cases, the primary shear instability is the same as shown in figures IV.3(a,d) with the horizontal domain consisting of four K-H rollers. The vertical extent of the largest rollers, located at the far left, is also similar. The pairing of K-H rollers is absent in both cases. The presence/absence of pairing influences the evolution of the vertical length scales and consequently affects the amount of potential energy available for mixing. In the two-layer case, the two rollers to the right are breaking in figure IV.3(a). Four isolated patches of small-scale turbulence in figure IV.3(b) corresponding to the four rollers in figure IV.3(a) indicates evidence of breaking without pairing. The braid between the first and second rollers as well as one between the third and the fourth rollers in figure IV.3(b) are still coherent even though the cores of the rollers show significant disintegration. In the J_d case, all four rollers in figure IV.3(d) exhibit high frequency fluctuations in the roller cores. Figure IV.3(e) shows the shear layer at $t = 80$ already consists of small-scale turbulence. Pham *et al.* (2009) observed pairing in the two-layer case but not in the J_d case. Their physical explanation is that, in the J_d case, strong internal waves carry a significant amount of energy outside the shear layer and thus the rollers in the shear layer become too weak to pair. In the current study in which the Reynolds number is approximately four times larger, low viscosity allows for small-scale growth; therefore, the K-H rollers, even in the 2-layer case, tend to break down before they can pair. At approximately $t = 102$, the turbulence in the shear layer in the two-layer case shown in figure IV.3(c) becomes more homogeneous in the horizontal extent compared to that in figure IV.3(b). The braids between the turbulent patches in figure IV.3(b) can no longer be identified in figure IV.3(c). In the J_d case, at $t = 100$, the turbulence in the shear layer in figure IV.3(f) is already decaying. Comparison of the shear layer in figure IV.3(e) to that in figure IV.3(f) shows that the former has stronger fluctuations and larger vertical extent. Between the two cases, the turbulence in the two-layer case in figure IV.3(c) spreads to a greater vertical extent than that in the J_d case in figure IV.3(e).

Figure IV.4 illustrates the TKE dissipation field, $\varepsilon = (2/Re_0)\left\langle s'_{ij}s'_{ij}\right\rangle$ where s'_{ij} is the fluctuating strain rate, corresponding to the density fields shown in figure IV.3. Here, the fluctuations from the planar mean can represent both internal waves and

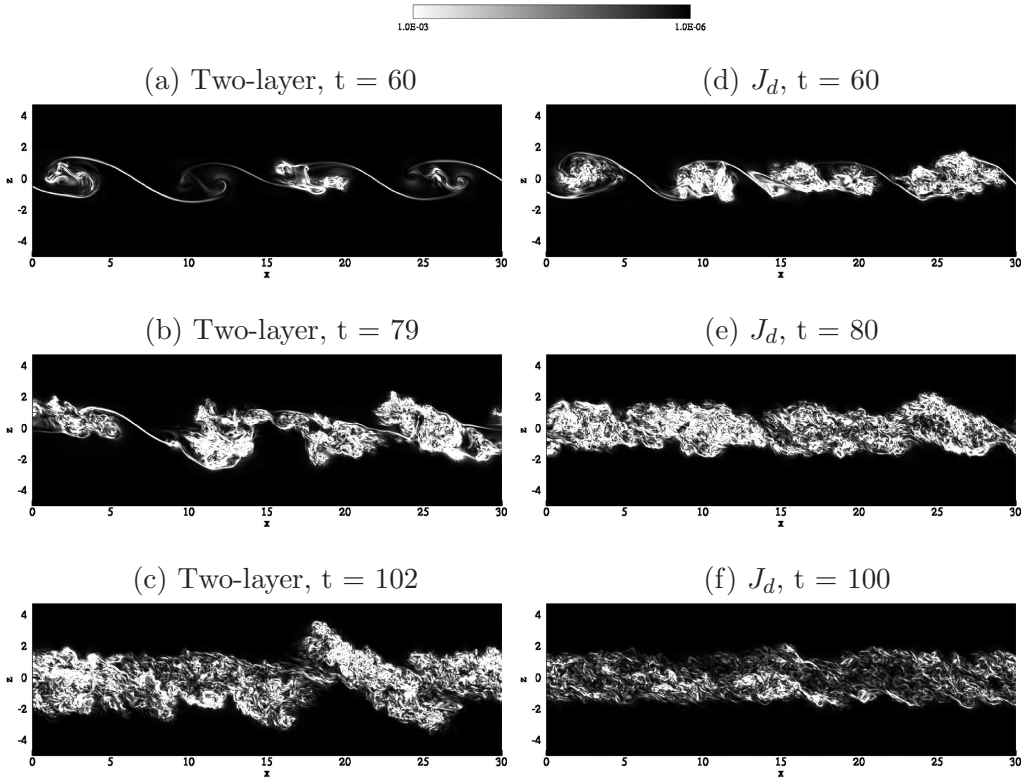

Figure IV.4: Turbulent kinetic energy dissipation rate ε on a vertical xz plane at y = 3.9.

turbulence although the latter has broader energy spectra and larger dissipation rate (Pham *et al.*, 2009). During the generation period of the KH-rollers, intense dissipation occurs in the braid regions where the strain is large. As the flows transitions into turbulence, small-scale fluctuations raise the dissipation rate inside the roller cores as in figure IV.4(b,d). The breaking rollers transform into localized patches of dissipation. In figures IV.4(c,e) the shear layers are fully turbulent. The dissipation patches observed at earlier time merge with each other. The fluctuations at the center of the shear layers become homogeneous in the horizontal extent in figures IV.4 (c,e,f).

Figure IV.5 shows the dissipation rate, $\chi_\rho = 2/(Re_0 Pr)\left\langle(\partial\rho'/\partial x_i)^2\right\rangle$, of the density variance. This quantity is related to the rate at which the turbulent potential energy is lost. An inverse correlation between the spatial distribution of the χ_ρ and ε fields of the K-H rollers is observed when comparing figures IV.5(a,d) to figures IV.4(a,d) . The K-H roller at the far left in figure IV.5(a) has χ_ρ small in the core and large

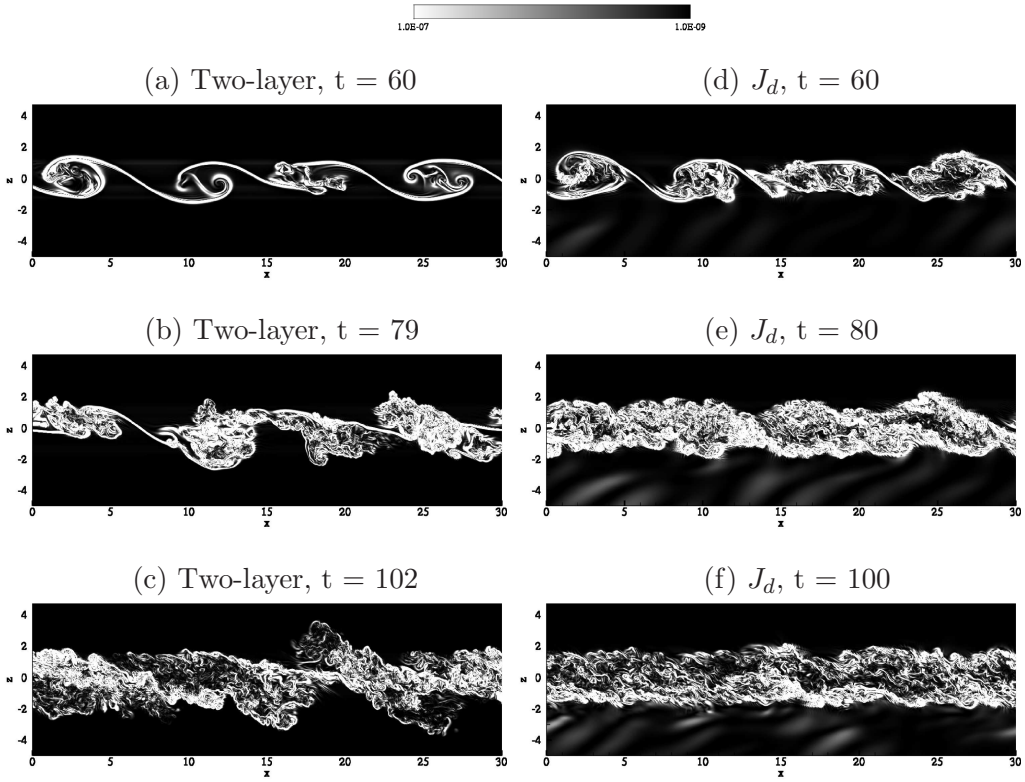

Figure IV.5: Density variance dissipation rate χ_ρ on a vertical xz plane at y = 3.9.

in the envelope. In contrast, figure IV.4(a) shows ε large in the core and small in the envelope. The observation is consistent with the fact that the envelope has larger instantaneous density gradient and thus larger χ_ρ. Similar behavior is observed when the shear layer becomes turbulent. While ε is usually not large at the edges, figures IV.4 (e,f), χ_ρ is large at the edges of the shear layer as in figures IV.5(e,f). Evidence of internal waves is seen in figures IV.5(d,e,f). The wave phase lines have mild χ_ρ, only a magnitude of order larger than the background value.

In addition to the primary K-H instability in the spanwise direction, we also observe the secondary instability in the streamwise direction that has been discussed previously by Caulfield & Peltier (2000). Figures IV.6(a,b) show the field of streamwise vorticity ω_1 on the yz cross-section at $x = 15.4$. The cross-section is a cut through the braid region shown in figure IV.3. In the two-layer case, shown in figure IV.6(a), the braid consists of vortex streaks. The secondary instability is observed at four different y locations on the braid. A pair of counter-rotating vortices pinches off the braid

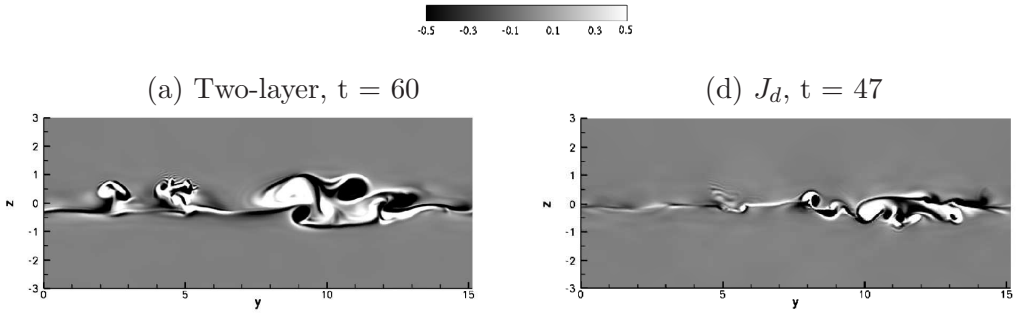

Figure IV.6: Streamwise vorticity ω_1 on a vertical transverse plane at x = 15.4.

at $y \approx 2.5$ while at $y \approx 5$ a group of smaller vortices are observed. At $y \approx 10$, a larger pair of counter-rotating vortices floats upward while a smaller pair cleaves off in the opposite direction. Another vortex pair is at $y \approx 12$.

In the J_d case, shown in figure IV.6(b), the instability is observed at $y \approx 8, 9$ and 10. The pair at $y \approx 8$ floats upward, the pair at $y \approx 9$ sinks downwards, and the pair at $y \approx 10$ is largest. A group of incoherent vortices are observed in the region $11 < y < 14$. The instability in the current study is not as coherent as shown in the study of Werne *et al.* (June 2005) because the initial fluctuations employed here have broadband spectrum in contrast to the flow initialization with primary K-H instability (Werne *et al.*, June 2005) which subsequently triggers the secondary instability. Caulfield & Peltier (2000) suggest that the secondary instability triggers three-dimensional perturbations which transition the flow from a two-dimensional quasi-laminar state to three-dimensional turbulence. In other words, turbulence is initiated from the braids of the K-H rollers, spreads toward the core and cause the breakdown of the rollers in the earlier low-Re DNS. In the current study, due to the high Re and broadband nature of the initial low-amplitude fluctuations, we observe that the generation of turbulence at the braid and at the core of the rollers is independent. Figure IV.4(b) shows the braid at $x \approx 7$ is still coherent while the cores of the rollers to the left and right of the braid already contain three-dimensional fluctuations.

The properties of the internal wave field generated by an unstable shear layer has been discussed at length by Pham *et al.* (2009). Here, we provide a short discussion of the internal wave field for completeness and also since Re is approximately four times

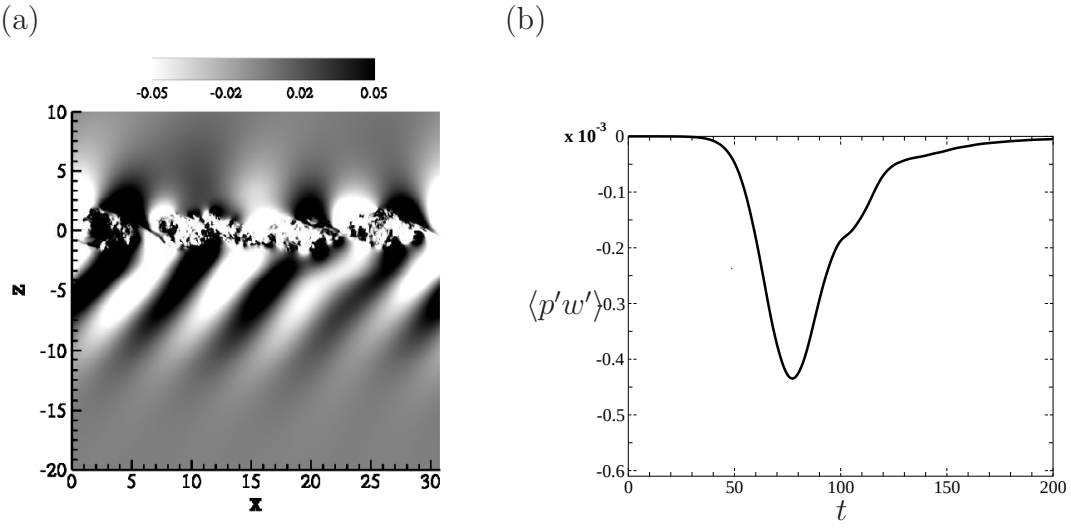

Figure IV.7: J_d cases: (a) Internal wave field shown in the xz cross section at y = 3.9 of the fluctuating vertical velocity w' field at t = 80; (b) Wave energy flux $\langle p'w' \rangle$ across the horizontal plane $z = -5$.

larger in the current simulations. Figure IV.7(a) shows the anatomy of the wave field with the cross section of the fluctuating vertical velocity w' field, while figure IV.7(b) shows the internal wave flux to be discussed later. The narrow-band waves are linear with the horizontal wavelength equal to the wavelength of the K-H rollers in the shear layer. The wave phase lines tilt downward and upstream at angle between $32 - 38°$ to the vertical. The direction of propagation can be explained using linear wave theory based on the Doppler-shifted frequency of the K-H mode (Pham *et al.*, 2009). With an increase in Reynolds number, we do not observe a change in the mechanism of wave excitation.

IV.D.2 Turbulence Budgets

The TKE budget for the simulated flows is described by the following equation,

$$\frac{dK}{dt} = P - \varepsilon + B - \frac{dT_3}{dz} \,, \tag{IV.5}$$

where, $K = 1/2 \langle u_i' u_i' \rangle$ is the TKE. P is the production rate, defined as

$$P = - \langle u'w' \rangle \frac{d \langle u \rangle}{dz} \,,$$

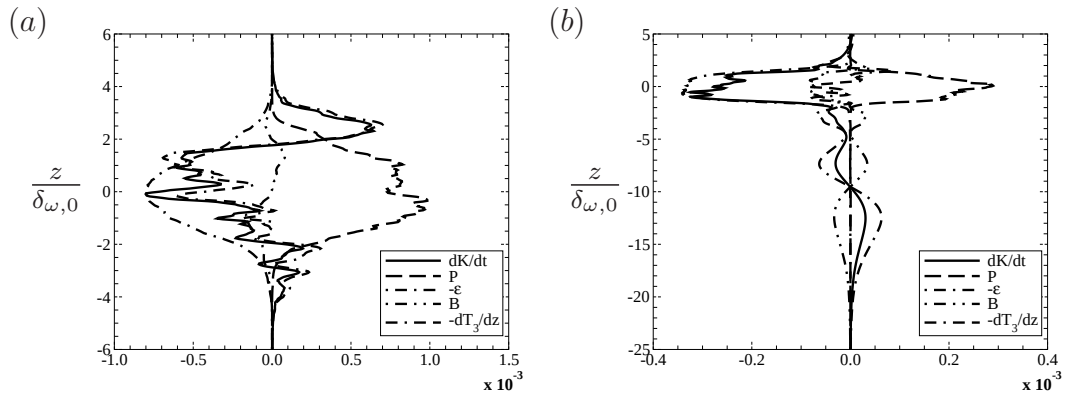

Figure IV.8: TKE budgets in the vertical direction z: (a) in the two-layer case at t = 102, and (b) in the J_d case at t = 100.

ε is the previously defined dissipation rate, and B is the buoyancy flux, defined as

$$B = -Ri_{b,0} \langle \rho' w' \rangle \ .$$

The transport term dT_3/dz is defined as

$$T_3 = \frac{1}{2} \left[\langle w'u'u' \rangle + \langle w'v'v' \rangle + \langle w'w'w' \rangle \right] + \frac{\langle p'w' \rangle}{\rho_0} - \frac{2}{Re_0} \left[\langle u's'_{31} \rangle + \langle v's'_{32} \rangle + \langle w's'_{33} \rangle \right].$$

Figures IV.8(a,b) show the budgets for the two-layer case at $t = 102$ and J_d case at $t = 100$, respectively. At this time, the shear layers are fully turbulent. In both cases, the budgets in the shear layer show the dominant balance between the dissipation ε and production P. In the two-layer case, the buoyancy flux is positive in the upper half of the shear layer and negative in the lower half indicating B can be both a source and a sink of energy. In the J_d case, B is the source of energy across the shear layer and the profiles of the buoyancy flux B, the transport $-dT_3/dz$ and the transient term dK/dt extend far into the region below the shear layer where internal waves are present. For the wave field, the production and dissipation are insignificant. Total energy transported by the wave fields is balanced by the rate of change of TKE in time and the rate at which TKE is converted to potential energy, i.e. buoyancy flux B.

The wave field in the current study is compared to one reported in Pham *et al.* (2009) in term of energetics. The wave energy flux $\langle p'w' \rangle$ across the horizontal plane $z = -5$ was shown earlier in figure IV.7(b). The peak energy flux at $t \approx 75$ is half of the value reported in the previous study. Integrating the energy budget, i.e. equation

IV.5, from $z = -5$ to the upper bound of the domain excluding the sponge region and also in time yields the bulk energy partitions in the balance of integrated TKE. The total wave energy flux is found to be approximately 9% of the integrated production, 17% of the integrated dissipation and 38% of the integrated buoyancy flux. Pham *et al.* (2009) reports values of 17%, 33%, and 75%, respectively. The wave field in the current study is weaker owing to the effects of high Reynolds number upon the source region of the waves. At high Re, the energy balance in the TKE budget is in favor of the dissipation over the transport. The energy at the large scale (K-H mode) cascades into the smaller scales at a faster rate. The K-H rollers at high Re lose more energy to small-scale motion and therefore the amount of energy available to excite internal waves is reduced.

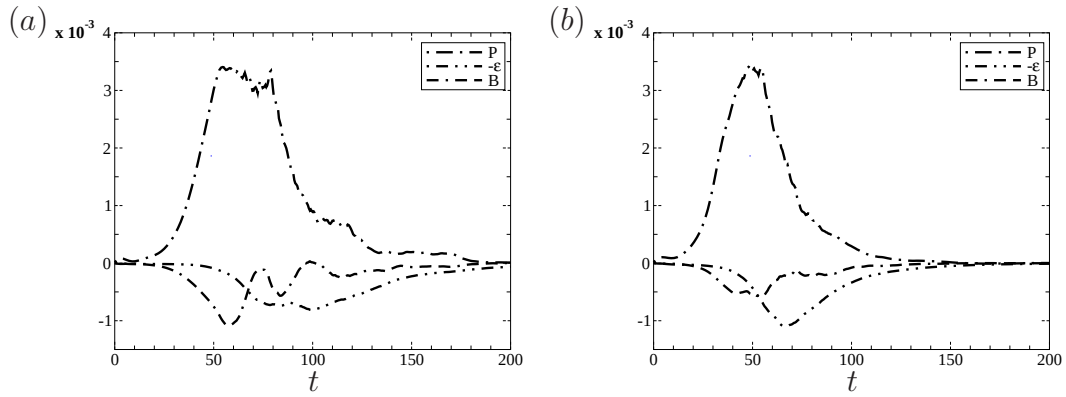

Figure IV.9: Evolution of TKE production, dissipation and buoyancy flux measured at center of the shear layer $z = 0$ in time: (a) in the two-layer case; (b) in the J_d case.

Figures IV.9(a,b) show the time evolution of the production, the dissipation and the buoyancy fluxes at the center of the shear layer $z = 0$ in the two-layer and J_d case, respectively. Overall, the evolution starts earlier and ends earlier in the J_d case while the evolution has a longer duration in the two-layer case. The production rate peaks earlier in the J_d case although the peak values are comparable between the two cases. Integrated over time, the net TKE production is larger in the two-layer case despite the initial gradient Richardson Ri_g being twice as large. Thus, the production and Ri_g do not have direct correlation; rather, the spatial transport of the Reynolds stress $\langle u'w' \rangle$

plays an important role in quantifying the rate at which TKE is generated. The peak buoyancy flux B has a larger value so that more TKE is transferred to potential energy in the two-layer case. At $t = 100$, B changes signs in figure IV.9(a) indicating available potential energy is converted back to TKE. Different from B, the peak dissipation rate ε is larger in the J_d case. In both cases, B is larger than ε during the rise of P but smaller during the decay of P. After approximately $t = 100$ in the two-layer case and $t = 80$ in the J_d case, the TKE budget shows a balance mainly between P and ε. The effect of the buoyancy flux is small suggesting the decaying turbulence at the center of the shear layer is in a homogeneous state.

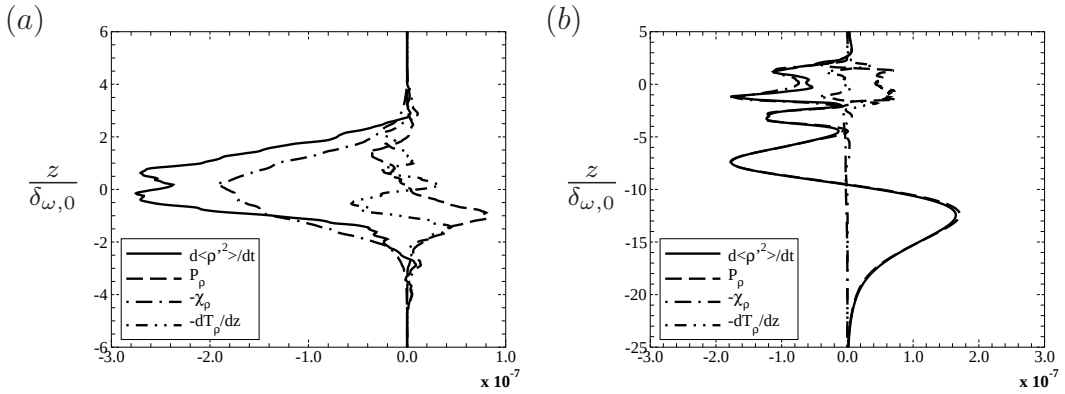

Figure IV.10: Density variance budgets in the vertical direction z (a) in the two-layer case at t = 102, and (b) in the J_d case at t = 100.

The equation for the budget of the density variance $\langle \rho'^2 \rangle$ is

$$\frac{d}{dt}\langle \rho'^2 \rangle = P_\rho - \chi_\rho - \frac{dT_\rho}{dz}, \tag{IV.6}$$

where the scalar production P_ρ is defined as

$$P_\rho = -2\langle \rho' w' \rangle \, d\langle \rho \rangle / dz \ ,$$

and the scalar dissipation χ_ρ is defined as

$$\chi_\rho = (2/PrRe_0)\left\langle (\partial \rho'/\partial x_i)^2 \right\rangle \ .$$

The transport term is

$$\frac{dT_\rho}{dz} = \frac{\partial \langle \rho'^2 w' \rangle}{\partial z} - \frac{1}{PrRe_0}\frac{\partial^2 \langle \rho'^2 \rangle}{\partial z^2}.$$

Figures IV.10(a,b) show the vertical profiles of the terms in the density variance budgets corresponding to the TKE budgets shown in figure IV.8. In both cases, the dissipation inside the shear layer is mainly balanced by the transient term indicating the shear layers are in a state of decaying stratified turbulence. In the two-layer case, all terms in the region $z < -3\delta_{\omega,0}$ are zero. In contrast, there is significant buoyancy flux up to $z = -15\delta_{\omega,0}$ in the J_d case, albeit without mixing ($\chi_\rho \simeq 0$). The sign of the production P_ρ and the sign of B shown in figure IV.8(a) are opposite; recall that $P_\rho = 2B/Ri_{b,0}d\left\langle\rho\right\rangle/dz$ and the stable density gradient has a negative sign. Therefore, B and P_ρ represent energy transfer between the TKE budget and the density variance budget. In the J_d case the production is balanced by the transient term in the region below the shear layer where internal waves propagate. The time evolution of P_ρ and

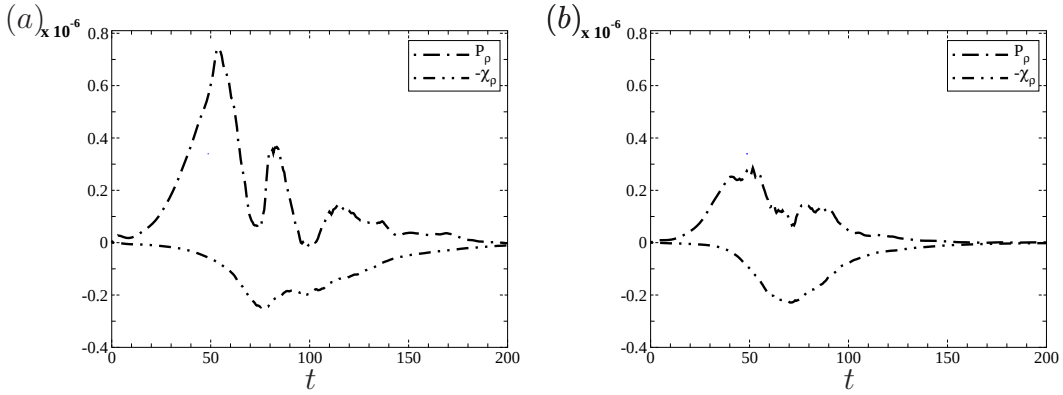

Figure IV.11: Evolution of production and dissipation of density variance measured at center of the shear layer $z = 0$ in time:(a) in the two-layer case; (b) in the J_d case.

χ_ρ at $z = 0$ for the two-layer and J_d cases are shown in figures IV.11(a,b), respectively. The peak value of P_ρ is significantly larger in the two-layer case while the peak value for χ_ρ is the same for the two cases.

IV.D.3 Length Scales

The growth of the following length scales: energy-containing scale L_{EN}, Ellison scale L_E, Ozmidov scale L_O and Kolmogorov scale L_K are now discussed. Their defi-

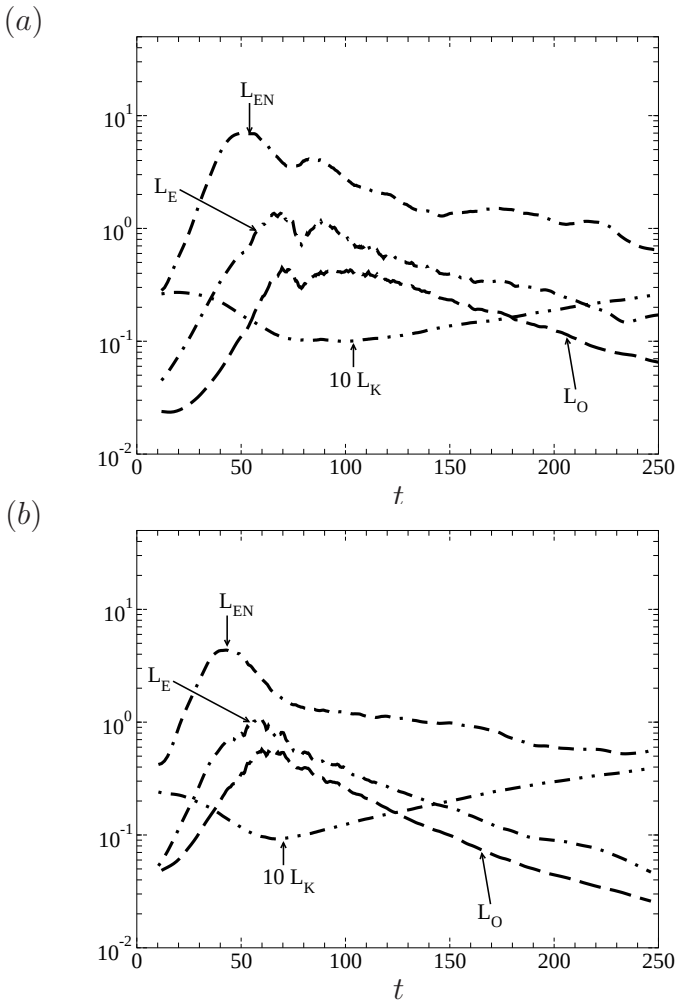

Figure IV.12: Evolution of length scales (a) in the two-layer case and (b) in the J_d case.

nitions (Smyth & Moum, 2000*b*,*a*; Smyth *et al.*, 2001) are given as follows,

$$L_{EN} = \frac{\left(\frac{2}{3}k\right)^{3/2}}{\varepsilon},$$
$$L_E = \frac{\rho_{rms}}{d\left\langle\rho\right\rangle/dz},$$
$$L_0 = \left(\frac{\varepsilon}{N^3}\right)^{1/2},$$
$$L_K = \left(\frac{\nu^3}{\varepsilon}\right)^{1/4}.$$

The evolution of these length scales is shown in figures IV.12(a,b) for the two-layer case and J_d case, respectively.

The energy-containing scale L_{EN} is calculated using the TKE and the dissipation

rate. In both cases, L_{EN} peaks early corresponding to the moment when the K-H rollers reach their largest size. At this time, the TKE reaches its peak while the dissipation has not yet evolved. The two-layer case has larger peak value of L_{EN} since the KH-rollers are larger. As rollers break and the shear layer turns turbulent, L_{EN} decreases corresponding to an increase in dissipation as shown in figure IV.9. At later time when turbulence decays L_{EN} is approximately equal to 1.

In both cases, the evolution of the Ellison scale L_E and Ozmidov scale L_O are similar despite a difference in the magnitude. The two length scales grow and decay similarly and also peak at the same time. The decay is exponential in time. The decay rate in the J_d case is larger than that in the two-layer case. The minimum value for the Kolmogorov scale L_K is nearly equal between the two cases. The value is approximately 0.01 which is a third of the grid spacing. The time at which L_O decreases to the value of 10η marks the buoyant-inertial-viscous (BIV) transition after which the inertial and buoyancy effects are damped out so that the fluctuations decay mainly due to viscosity. The transition occurs early in the J_d case at $t = 120$ and later in the two-layer case at $t = 180$. The time period of active turbulence indicated by $L_O > 10\,L_K$ is shorter in the J_d case, $35 < t < 120$, than that in the two-layer case, $55 < t < 180$.

IV.D.4 Non-dimensional Turbulent Parameters

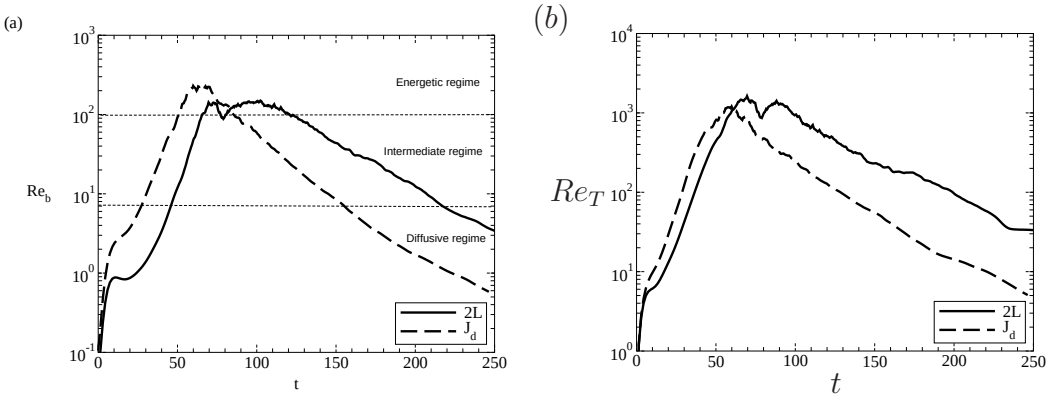

Figure IV.13: Evolution of (a) buoyancy Reynolds number, $Re_b = \epsilon/\nu N^2$, and (b) local turbulent Reynolds number $Re_T = qL_E/\nu$. Both are at the shear center.

The evolution of the buoyancy Reynolds number $Re_b = \epsilon/(\nu N^2)$, an indicator of

turbulent activity, at the center of the shear layer is shown in figure IV.13(a) for the two simulated cases. During the period of the formation of the K-H rollers, Re_b is larger in the J_d case although the growth rate of Re_b is the same between the cases. The peak value of Re_b in the J_d case is approximately twice that in the two-layer case. The larger Re_b is due to smaller value of the squared buoyancy frequency N^2, recalling the initial Ri_g at the center of the shear layer is twice smaller in the J_d case as shown in figure IV.1(b). According to the criterion by which Shih *et al.* (2005) differentiate the mixing regimes, both of our simulations span all three regimes. The time period during which energetic mixing occurs, $Re_b > 100$, is longer in the two-layer case. Note that since $Re_b = (L_O/L_K)^{\wedge}(4/3)$, the condition $Re_b > 100$ is equivalent to $L_0/L_K > 31$. The decay rate is the same for the intermediate mixing regime and the diffusive regime in both cases.

An alternative measure of turbulent activity is $Re_T = qL_E/\nu$ where $q = \sqrt{2k}$ (Shih *et al.*, 2005). Different from Re_b where information at the small scale, i.e. dissipation rate ε, is required, Re_T can be estimated using only information at the large scale, thus Re_T is more convenient to modelers. L_E is preferred to L_O despite their similar evolution because L_0 involves the dissipation rate in its definition. Figure IV.13(b) shows the evolution of Re_T qualitatively captures the shape of the evolution of Re_b in figure IV.13(a) in both cases. The magnitude and the decay rate show some differences. The peak value of Re_T is an order of magnitude larger than the peak value of Re_b. Also, the peak value of Re_T is larger in the two-layer case; the opposite is observed in Re_b. The decay rate of Re_T is smaller than that of Re_b. During the intermediate mixing regime, the exponential decay rate for Re_b is -0.027 in the two-layer case and -0.039 in the J_d case. For Re_T, the values in the two cases are -0.02 and -0.03, respectively. Following Shih *et al.* (2005), it is possible to relate Re_b to Re_T by the following argument: $Re_b \sim Re_T q^2/\left(L_E^2 N^2\right) \sim Re_T/Ri_g$ using the dimensional arguments of $\varepsilon \sim q^3/L_E$ and $q^2 \sim S^2 L_E^2$. In the next section, we will examine whether the ratio Re_T/Ri_g, which is defined only using large-scale information, can be used to parametrize the evolution of the eddy diffusivity in place of Re_b.

IV.E Eddy Diffusivity

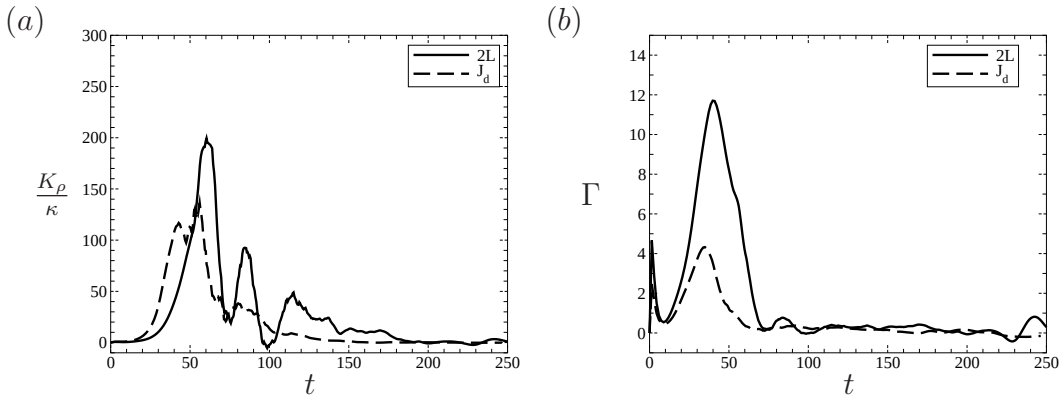

Figure IV.14: Evolution of (a) eddy diffusivity K_ρ and (b) mixing efficiency Γ at the center of the shear layer.

The eddy diffusivity is defined as

$$K_\rho = \frac{-\langle \rho' w' \rangle}{d\langle \rho \rangle / dz} = \frac{-B}{N^2}\,. \tag{IV.7}$$

K_ρ is a 'reversible' estimate since B can be both positive and negative in the evolution of the TKE budget. The evolution of K_ρ is shown in figure IV.14(a). Overall, K_ρ is significantly larger during the period of K-H roller formation compared to later time when there is broadband turbulence. The increase of K_ρ in the J_d case begins earlier but K_ρ has larger peak values in the two-layer case. K_ρ has negative value at $t = 100$ in the two-layer case. In the oceanic community, K_ρ is often inferred from the mixing efficiency defined as $\Gamma = -B/\varepsilon$ through the relationship: $K_\rho = \Gamma\varepsilon/N^2$. The value of $\Gamma = 0.2$ is typically used in combination with the measurements of the dissipation rate obtained by micro-structure profilers to deduce K_ρ. Figure IV.14 shows the evolution of Γ. In both cases, Γ is much larger than 0.2 when the rollers are forming but it reduces to the proximity of 0.2 during the turbulence decay.

We now examine how K_ρ varies with respect to Re_b. The variation is shown in figure IV.15(a), and the mixing regimes shown in the figure are determined by the criteria of Shih *et al.* (2005). The arrows indicate the time progression in which the simulations proceed. In both cases, there is not a direct one-to-one relationship as in decaying stratified homogeneous turbulence; rather, the evolution of K_ρ exhibits four

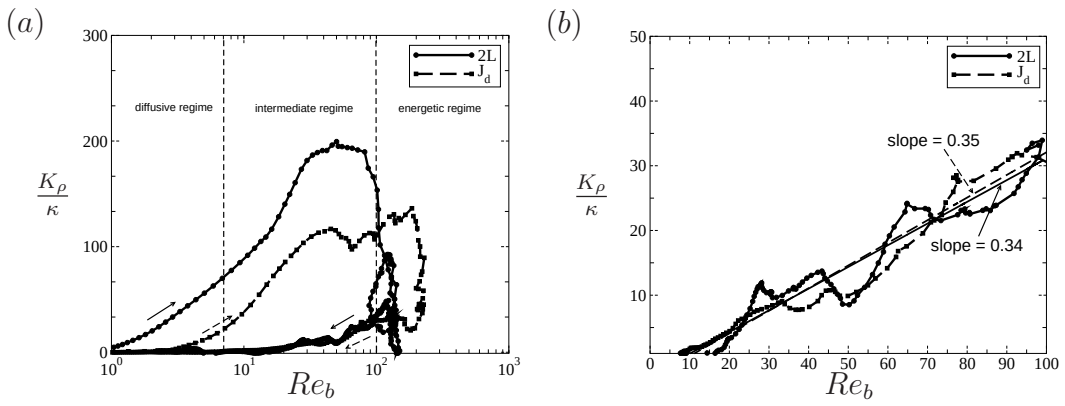

Figure IV.15: (a) $K_\rho \, vs \, Re_b$; (b) same as in (a) zoomed on to the intermediate mixing regime during the decay of the flow. Arrows indicate progress in time. Note the abscissa is given in logarithmic scale in (a) and linear scale in (b).

distinct stages. The first is the generation stage, $1 < Re_b < 50$ for both cases, during which K_ρ grows with an approximately linear dependence on Re_b corresponding to the formation of the K-H rollers. K_ρ is twice that in the two-layer case at the end of this stage. The second stage is the transition to turbulence, $50 < Re_b < 90$ in the two-layer case and $50 < Re_b < 200$ in the J_d case, during which K_ρ is approximately constant. The third is the collapse stage during which Re_b (equivalently turbulence dissipation rate) cannot grow further and K_ρ exhibits a sharp drop. The collapse is smoother in the J_d case in which K_ρ drops at constant Re_b. In the two-layer case K_ρ rises and falls many times within a small range of Re_b. Finally, the fourth stage corresponds to turbulence decay during which Re_b and K_ρ decreases simultaneously. The evolution of K_ρ in the two cases during this stage is similar suggesting the turbulence now independent of the initial and background flow conditions. The shear layer turbulence evolves as in the flows of homogeneous decaying stratified turbulence in which eddy diffusivity is directly related to Re_b (Shih *et al.*, 2005). Figure IV.15(b) shows a zoom on to the intermediate mixing regime. Even though K_ρ shows fluctuations, the best-fit lines are similar between the two cases. Recall that the ratio of K_ρ/κ and Re_b with $Pr = 1$ is the mixing efficiency Γ. The slopes of the best-fit lines indicate $\Gamma \approx 0.35$ which is higher than 0.2, the value typically used by the oceanic community.

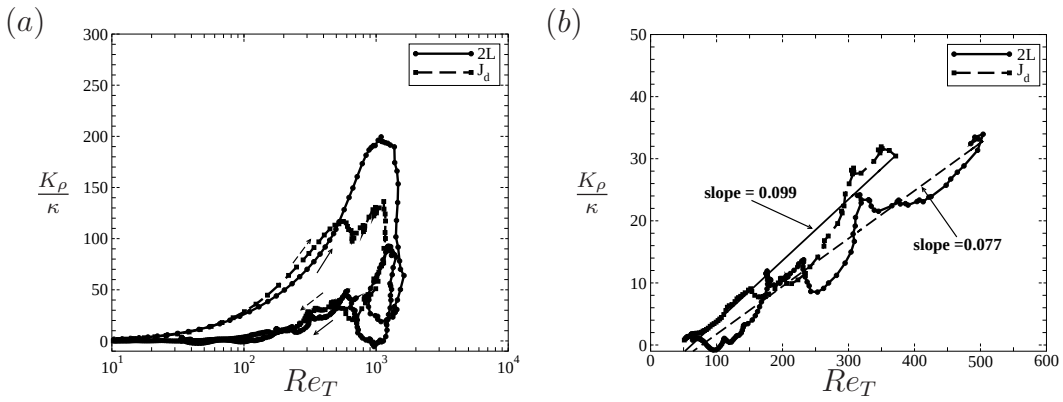

Figure IV.16: (a) $K_\rho \, vs \, Re_T$; (b) same as (a) zoomed on to the intermediate mixing regime during the decay of the flow. Arrows indicate progress in time. Note the abscissa is given in logarithmic scale in (a) and linear scale in (b).

The evolution of K_ρ with respect to Re_T is shown in figure IV.16(a). The evolution of K_ρ depicted by Re_T also consists of four stages similar to when Re_b is used. The general shapes of the evolution in figure IV.15(a) and IV.16 in both cases are considerably similar. Both Re_b and Re_T span two-order-of-magnitude range but Re_T is approximately an order of magnitude larger. Compared to figure IV.15, figure IV.16 shows a smaller difference during the generation stage between the two cases. The collapse stage in the J_d case occurs at larger Re_b but at smaller Re_T relative to the two-layer case. Figure IV.16(b), a surrogate to figure IV.15(b), indicates the slope during the intermediate mixing regime is 0.077 in the two-layer case and 0.099 in the J_d case when Re_T is used in place of Re_b. The normalized difference in the slopes between the two cases is larger than that computed using Re_b. Overall, Re_T can be used as a qualitative surrogate to Re_b only in terms of depicting the evolutionary processes but parametrizing K_ρ using Re_T is not promising since the dependence of K_ρ on Re_T is not universal, i.e. case dependent, even during the turbulence decay.

Different from Re_T, the evolution of K_ρ with respect to the ratio Re_T/Ri_g shown in figure IV.17(a) is not the same as one with respect to Re_b in figure IV.15(a). Re_T/Ri_g fails to depict the evolution of K_ρ during the generation, transition and collapse stage although it does well during the final turbulence decay stage. The expansion of the

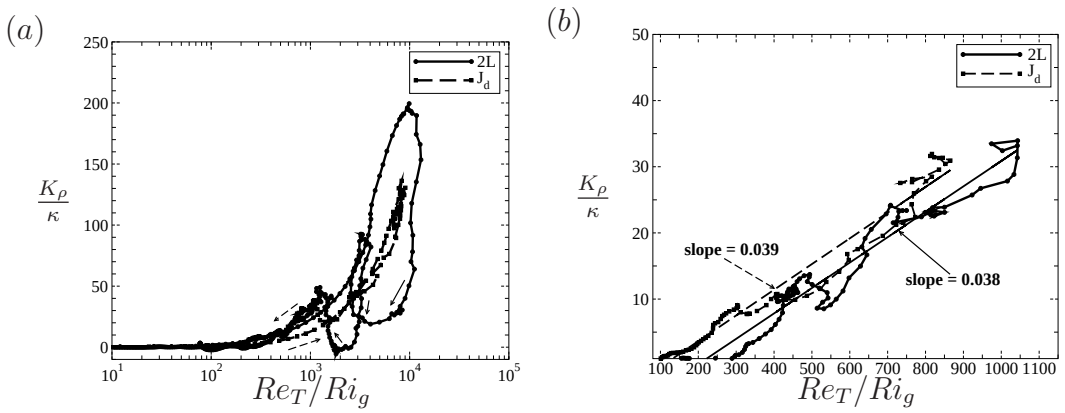

Figure IV.17: (a) $K_\rho \, vs \, Re_T/Ri_g$; (b) same as (a) zoomed on to the intermediate mixing regime during the decay of the flow. Arrows indicate progress in time. Note the abscissa is given in logarithmic scale in (a) and linear scale in (b).

decay stage in figure IV.17(a) is shown in figure IV.17(b). The best-fit lines show a slope of 0.038 in the two-layer case and a slope of 0.039 in the J_d case. The difference between the two values is significantly smaller than those computed based on Re_T alone. Consider Re_T/Ri_g is an order of magnitude larger than Re_b, the mixing efficiency computed using $10Re_T/Ri_g$ in place of Re_b is approximately $0.38-0.39$ which provides a close agreement with the value of 0.35 shown in figure IV.15(b).

IV.F Eddy Diffusivity Estimated Using Irreversible Mixing

When the transient and the transport terms in equation (IV.6) are negligible, the estimated eddy diffusivity can be defined in terms of χ_ρ, the dissipation rate of the density variance, as follows:

$$\tilde{K}_\rho = \frac{\chi_\rho}{2\left(d\left\langle\rho\right\rangle/dz\right)^2} \, .$$

The evolution of $\tilde{K}_\rho$ shown in figure IV.18(a) is similar between the two cases. $\tilde{K}_\rho$ grows exponentially during the K-H roller formation and decays exponentially after the shear layer becomes turbulent. Different from K_ρ whose peak value is larger in the two-layer case, the peak values of $\tilde{K}_\rho$ are comparable between the two cases. In the

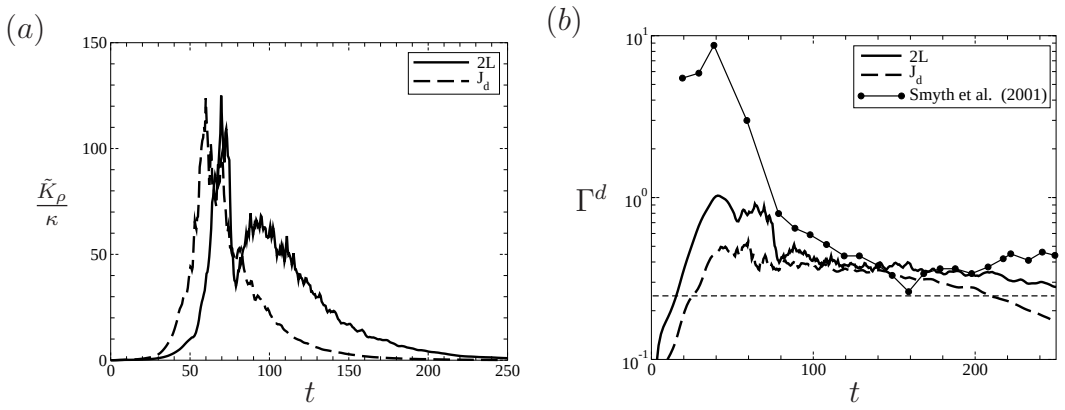

Figure IV.18: Evolution of (a) estimated eddy diffusivity $\tilde{K}_\rho$ and (b) irreversible mixing efficiency Γ^d (b). Arrow indicates progress in time. Note the abscissa is given in logarithmic scale in (a) and linear scale in (b).

two-layer case, $\tilde{K}_\rho$ increases to its peak value, momentarily decreases at $t = 70$, then increases again before the exponential decay. The secondary growth is absent in the J_d case resulting in smaller $\tilde{K}_\rho$ during the decay. When $\tilde{K}_\rho$ is used in place of K_ρ in the definition of the mixing efficiency $\Gamma = K_\rho \varepsilon / N^2$, the corresponding mixing efficiency is $\Gamma^d = 0.5N^2 / \left(d \left\langle \rho \right\rangle / dz\right)^2 (\chi_\rho / \varepsilon)$ and its evolution is plotted in figure IV.18(b). Overall, Γ^d is larger than the value 0.2 used in the oceanic community. During the time $80 < t < 160$, Γ^d is approximately 0.4 which agrees with the results from the DNS of the two-layer case of Smyth *et al.* (2001) and also with the results of decaying turbulence generated by Taylor-Green vortices of Riley & deBruynKops (2003).

Different from the evolution of K_ρ with respect to Re_b where four distinct stages are observed, the evolution of $\tilde{K}_\rho$ with respect to Re_b shown in figure IV.19(a) consists of only two stages: generation and decay. In the J_d case, the two stages lay on top of each other. In the two-layer case, there is an offset in Re_b between the two stages. The decay stage of the two-layer case also coincides with that of the J_d case. The difference in the generation stage between the two cases is due to the difference in the background N^2 value during this period. During the decay stage, with N^2 approximately equal between the two cases, the TKE dissipation ε and the scalar dissipation ε_ρ are directly related by the constant mixing efficiency Γ^d. Figure IV.19(b) shows the expansion of the intermediate regime in figure IV.19(a). The slopes of the best-fit lines indicate the

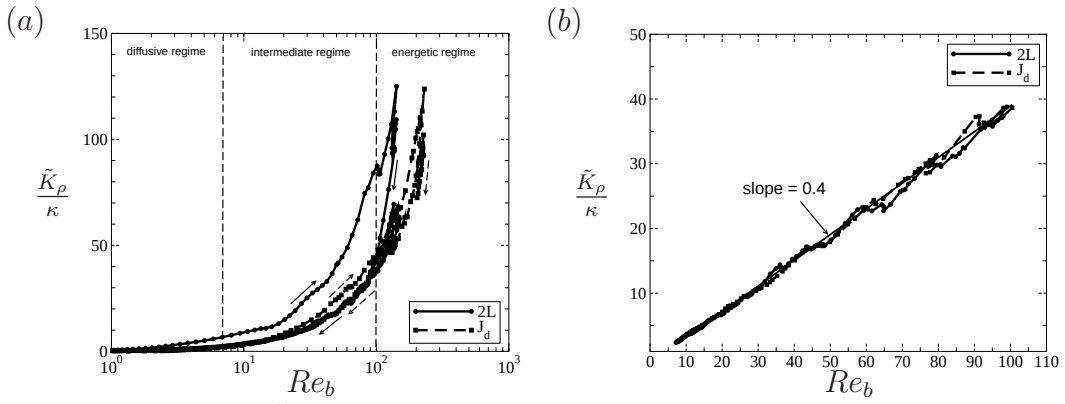

Figure IV.19: (a) $\tilde{K}_\rho \, vs \, Re_b$, (b) same as (a) zoomed on to the intermediate mixing regime during the decay of the flow. Arrows indicate progress in time. Note the abscissa is given in logarithmic scale in (a) and linear scale in (b).

mixing efficiency of $\Gamma^d = 0.4$ for both cases, slightly larger than the values of Γ shown in figure IV.15(b). Also, the standard deviations of the fits are considerably smaller for $\tilde{K}_\rho$ when compared to that for K_ρ.

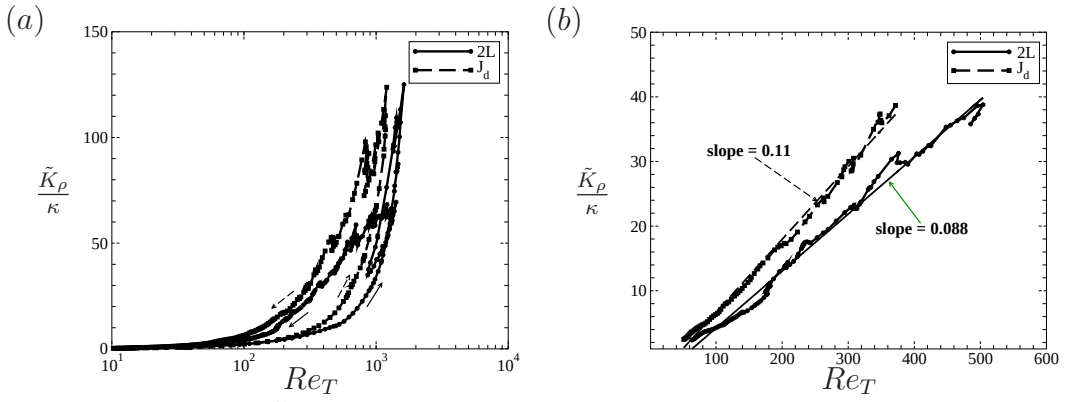

Figure IV.20: (a) $\tilde{K}_\rho \, vs \, Re_T$, (b) same as (a) zoomed on to the intermediate mixing regime during the decay of the flow. Arrows indicate progress in time. Note the abscissa is given in logarithmic scale in (a) and linear scale in (b).

The evolution of $\tilde{K}_\rho$ with respect to Re_T is shown in the figure IV.20(a). Figure IV.20(a) shows the generation and decay stages of $\tilde{K}_\rho$ similar to that in figure IV.19(a). In the J_d case, the generation and collapse stages do not fall on top of each other as when Re_b is used. Also, in figure IV.16(a), at a fixed value on the abscissa, K_ρ in both

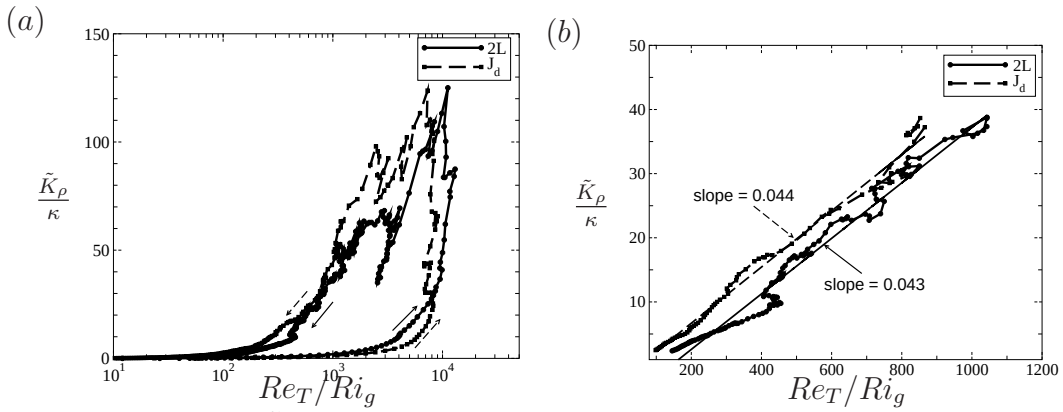

Figure IV.21: (a) $\tilde{K}_\rho \, vs \, Re_T/Ri_g$, (b) same as (a) zoomed on to the intermediate mixing regime during the decay of the flow. Arrows indicate progress in time. Note the abscissa is given in logarithmic scale in (a) and linear scale in (b).

cases is larger during the generation stage, but in figure IV.20(b), $\tilde{K}_\rho$ in both cases is larger during the decay stage. Figure IV.20(b) shows a zoom of figure IV.20(a) on to the decay stage of the flow. The collapse between the two cases shown in figure IV.19(b) is not observed here. The slopes of the best-fit lines in figure IV.20(b) are 0.088 in the two-layer case and 0.11 in the J_d case. When Re_T/Ri_g is used to depict the evolution of $\tilde{K}_\rho$ as shown in figure IV.21(a), the difference in the abscissa between the generation and decay stages is larger relative to that shown in figure IV.20(a). Shown in figure IV.21(b), the mixing efficiency Γ^d calculated using $10Re_T/Ri_g$ in place of Re_b is equal to 0.43 in the two-layer case and 0.44 in the J_d case, which are slightly larger than the value 0.4 calculated using Re_b.

IV.G Implications

We have used 3D-DNS to investigate the evolution of turbulent mixing in a stratified shear layer with a relatively high Reynolds number, initially $Re = 5,000$. Two cases with different background stratification are considered: (i) two layers of fluid with different density (two-layer case), and (ii) a continuously stratified background (J_d case). The latter has internal waves that propagate away from the mixing layer.

The evolution of the shear layer consists of shear instability, formation of Kelvin-Helmholtz rollers, transition to turbulence, establishment of fully-developed turbulence and, finally, decay towards a laminar state. In previous DNS, transition to turbulence occurs via secondary instability of the braids between the rollers (Peltier & Caulfield, 2003). At the higher Re of the present simulations, not only is there a braid instability but also the vortex core independently becomes turbulent.

When plotted against Re_b and the ratio Re_T/Rig, the evolution of the eddy diffusivity is different between the two cases during the early stages when turbulence is established. The eddy diffusivity and the mixing efficiency are the same between cases during the later turbulence decay stage. During this stage, the mixing efficiency defined by the ratio of $-B/\varepsilon$, is approximately 0.35 while the dissipation-based mixing efficiency defined using the scalar dissipation χ_ρ, is approximately 0.4. Parametrization of eddy diffusivity using Re_b and Re_T/Ri_g is shown to be a possibility during the decaying turbulence stage of the stratified shear layer.

Comparison of the current DNS at $Re = 5,000$ with the results of Pham *et al.* (2009) who performed the simulations at $Re = 1280$ indicates that an increase in Re does not alter the mechanism by which internal waves are excited. The direction at which the waves propagate agrees well with the previous study although the wave energy flux is reduced by approximately 50%. The weaker wave field observed in the current study is due to the earlier breakdown of the K-H rollers to turbulence in the shear layer owing to a high-Re effect.

The contents of this chapter have been published in the Journal of Turbulence: Pham, H. T., and Sarkar, S., "Transport and mixing of density in a continuously stratified shear layer", J. Turbulence, ***11****, No. 24, 1-23 (2010). The dissertation author is the primary researcher and the research advisor is the co-author of the paper.*

Chapter V

Internal Waves and Turbulence in a Stratified Jet

V.A Objectives

The excitation of shear instability, i.e. Kelvin-Helmholtz (KH) rollers, and its subsequent nonlinear evolution is one important source of turbulence and mixing in the stratified natural environment. Linear theory gives $Ri_g = N^2/S^2 < 0.25$, where Ri_g is the gradient Richardson number, N the buoyancy frequency and S the shear in the vertical direction, as a necessary condition for shear instability. The evolution of a unstable shear flow between two layers of homogeneous fluid with different density has been well studied using both laboratory experiments and numerical simulations, e.g. Thorpe (1973); Koop & Browand (1979); Smyth & Moum (2000*a*); Caulfield & Peltier (2000); Brucker & Sarkar (2007). If one of the layers has continuous stratification, it can support propagating internal waves and also influence the evolution of the shear layer instability as described in the studies of Sutherland & Linden (1998); Strang & Fernando (2001); Tse *et al.* (2003); Mahalov *et al.* (2007); Pham *et al.* (2009). For instance, Pham *et al.* (2009) in their three-dimensional direct numerical simulation (DNS) study find that the wave energy flux is a significant fraction of the turbulent production and dissipation rate suggesting that internal waves provide an important

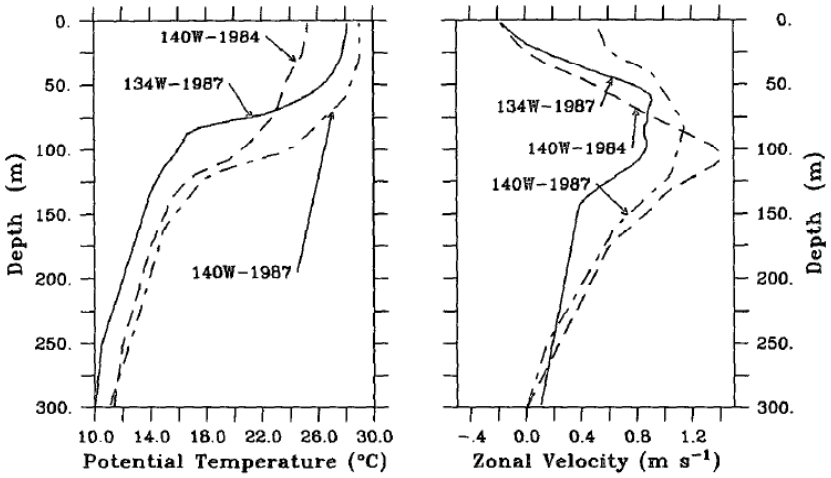

Figure V.1: Typical temperature profile and zonal currents in the EUC system (Skyllingstad & Denbo, 1994).

route of fluctuation energy from shear instabilities to the ocean interior. In the papers cited above, the waves are excited and propagate in stratified background with no shear. However, in geophysical flows, the unstable stratified region is often adjacent to a stratified background with shear that is stable ($Ri_g > 0.25$). The objective of the current work is to characterize and understand the internal wave field and turbulent mixing in a nominally stable sheared region by simulation of a simple model problem: a stable jet adjacent to an unstable shear layer.

Equatorial Undercurrents (EUC) provide an important example where internal waves and turbulence have been observed in a region of stable shear contiguous to a small region of unstable shear as described by Gregg *et al.* (1985); Peters *et al.* (1988); Moum *et al.* (1992); Lien *et al.* (1996). The EUC are eastward jet-like flows below wind-driven westward surface currents. Typical temperature and streamwise velocity profiles are shown in figure V.1. Internal waves are observed in the EUC and believed to be related to the enhanced deep-cycle turbulence in the upper-flank of the EUC jet. The peak night time dissipation rate of the turbulent kinetic energy (TKE) in the marginally-stable region exceeds the corresponding day time value by at least a factor of 10 (Moum *et al.*, 1992; Lien *et al.*, 1996). Hebert *et al.* (1992) capture a wave packet that is gravitationally unstable resulting in wave-breaking. The dissipation rate within

the patch of the overturning wave was found to be at least three orders of magnitude larger than outside the patch. Skyllingstad & Denbo (1994) used two-dimensional non-hydrostatic simulations with the background profiles shown in figure V.1 with forcing of wind stress and a heat flux at the surface. In the model, internal wave packets were observed to propagate downward and upstream relative to the jet velocity and the waves were shown to correlate with KH instabilities. Sun *et al.* (1998) performed linear stability analysis using the hourly-averaged current and stratification profiles and, from the computed positive growth rates in the regions with $Ri_g < 0.25$, inferred a connection between deep-cycle turbulence and shear instability.

Turbulence and internal waves in a stratified jet has been studied previously. Tse *et al.* (2003) use three-dimensional DNS to simulate a forced jet in quasi-equilibrium modeling of the tropopause jet. The buoyancy frequency in the upper-flank of the jet is taken to be twice that in the lower-flank. The jet is maintained at low Ri_g. Turbulence is observed in the jet core while patchy turbulence and nonlinear evanescent waves are seen at the edges. Mahalov *et al.* (2007) investigate a similar tropopause jet in a much larger domain than used by Tse *et al.* (2003) by using numerical viscosity for the unresolved scales. Internal waves propagating into region above the jet with stronger stratification are observed and characterized. Sutherland (2006) also models the tropopause jet but uses a piece-wise linear shear profile so that the upper flank of the jet is locally unstable while the lower flank is strongly stratified. Internal waves radiated from the upper-flank are found to carry significant momentum into the region above the jet. Waves also propagate downward into the lower-flank where they encounter a critical layer. Smyth & Moum (2002) employ linear stability analysis and two-dimensional DNS to study a Bickley jet that has a weak stratification in all of the upper-flank and a strong stratification in the lower flank. They find that internal waves, generated by the dynamic instability of the weakly stratified upper flank, propagate downward and break upon encountering the critical level present at the more strongly stratified lower flank. Turbulence due to interaction between propagating waves and mean shear at a critical layer where the wave phase speed and the mean velocity is equal has been studied by Winters & D'Asaro (1994). In our model problem, a critical layer is absent

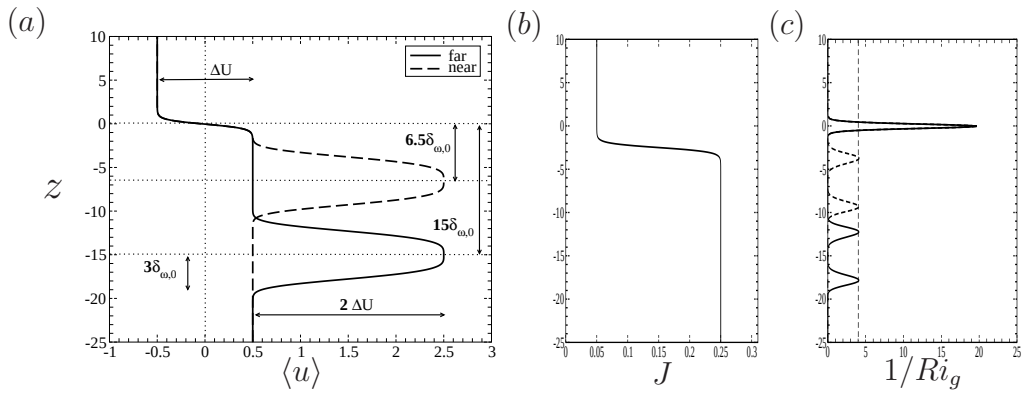

Figure V.2: (a) *Initial* mean profiles. The velocity profile corresponds to a shear layer on top of a jet. The jet center is at depth z = -15 $\delta_{\omega,0}$ in the *far jet* and at depth z = -6.5 $\delta_{\omega,0}$ in the *near jet*. (b) *Initial* stratification profiles J(z) used in both cases. (c) *Initial* $1/Ri_g(z)$ profiles.

by design.

Different from the three-dimensional simulations of Tse *et al.* (2003) and Mahalov *et al.* (2007) where the entire jet is unstable ($Ri_g < 0.25$) and the two-dimensional simulations of Smyth & Moum (2002) and Sutherland (2006) where a large portion of the jet is unstable, we use three-dimensional DNS to investigate internal waves and turbulence inside a stable jet ($Ri_g > 0.25$) located adjacent to an unstable shear layer. Our setup has the feature of a stratified stable jet contiguous to a unstable shear layer in common with the EUC but is simplified by the absence of wind forcing and diurnal cycle of heat flux. Our objectives are to provide a better understanding of some dynamical processes related to EUC mixing by answering the following questions in the model problem: (1) Can internal waves excited from an adjacent region of unstable shear propagate downward into a stably stratified jet? (2) Is there significant dissipation in the jet despite its stable stratification? (3) What is the connection between the propagating internal waves and turbulence in the jet?

V.B Problem Formulation

The flow corresponds to a weakly stratified shear layer situated on top of a strongly-stratified jet. A schematic is given in Fig. V.2. The shear layer has a hyperbolic tangent

profile with velocity difference ΔU,

$$\langle u_s \rangle = -\frac{\Delta U}{2} tanh\left(\frac{2z}{\delta_{\omega,0}}\right),$$

where the initial vorticity thickness is defined by $\delta_{\omega,0} = \Delta U/(d\langle u_s \rangle/dz)_{max}$. The angled brackets denote a x-y plane average.

A jet with peak velocity $2\Delta U$ and half-width $3\delta_{\omega,0}$ is added to the region below the shear layer and has the following profile:

$$\langle u_j \rangle = 2\Delta U exp\left[-\left(\frac{z - D_j}{3\delta_{\omega,0}}\right)^4\right],$$

where D_j is the distance between the shear layer center and the jet center. The complete velocity profile consists of the shear layer and the jet, $\langle u \rangle (z) = \langle u_s \rangle (z) + \langle u_j \rangle (z)$. Using the squared buoyancy frequency defined as $N^2(z) = -(g/\rho_0)\, d\langle \rho \rangle / dz$, the stratification is described with a non-dimensional Richardson number, $J(z) = N^2(z)\,\delta^2_{\omega,0}/\Delta U^2$. The initial stratification in the shear layer is $J_s = 0.05$ whereas at $z = -2.5\delta_{\omega,0}$ the stratification transitions to $J_j = 0.25$ in the deep jet region. The complete initial stratification profile is given by

$$J(z) = \frac{J_s + J_j}{2} + \frac{J_s - J_j}{2} tanh\left(\frac{z + 2.5\delta_{\omega,0}}{0.5\delta_{\omega,0}}\right).$$

The stratification is chosen such that the gradient Richardson number Ri_g shown in figure V.2 (c) corresponds to field measurement in the EUC system. Peters *et al.* (1988) reports three vertical regions of the EUC jet: (1) the upper shear zone, from 23 m to 100m below the ocean surface, has low Ri_g, average of 0.35; (2) the core, between 100 m and 130 m, has $Ri_g > 2$; (3) the lower shear zone, below 130 m, has $Ri_g \approx 0.5$. In our model, the jet has constant stratification such that the initial Ri_g in the upper shear region is approximately 0.25 slightly less than the value 0.35 reported in the field data. The smaller value is taken because Ri_g in this region approaches the field value, due to viscous effects, by the time that the unstable shear layer has fully-developed KH-rollers.

The initial shear layer vorticity thickness $\delta_{\omega,0}$, the density jump $\Delta\rho_0$ across twice the initial vorticity thickness, and the velocity difference ΔU are used for nondimension-

alization. We solve the Navier-Stokes equations under the Boussinesq approximation:

$$\frac{\partial u_k}{\partial x_k} = 0\,, \tag{V.1}$$

$$\frac{\partial u_i}{\partial t} + \frac{\partial\left(u_k u_i\right)}{\partial x_k} = -\frac{\partial p}{\partial x_i} + \frac{1}{Re_0}\frac{\partial^2 u_i}{\partial x_k \partial x_k} - Ri_{b,0}\rho'\delta_{i3}\,, \tag{V.2}$$

$$\frac{\partial \rho}{\partial t} + \frac{\partial\left(u_k \rho\right)}{\partial x_k} = \frac{1}{Re_0 Pr}\frac{\partial^2 \rho}{\partial x_k \partial x_k}, \tag{V.3}$$

The nondimensional parameters are Reynolds number $Re_0 = \Delta U \delta_{\omega,0}/\nu$, Prandtl number $Pr = \nu/\kappa$, and bulk Richardson number $Ri_{b,0} = \left(g\Delta\rho_0\delta_{\omega,0}\right)/\left(\rho_0\Delta U^2\right)$. Here, ν is the kinematic viscosity, and κ is the molecular diffusivity. Two simulations are performed with varying jet distance: $D_j = 6.5\delta_{\omega,0}$ (near jet) and $15\delta_{\omega,0}$ (far jet). Both simulations are run with $Re_0 = 1280$, $Pr = 1$ and $Ri_{b,0} = 0.1$. The near jet models the typical velocity profile of the EUC system while the far jet has a shear-free region with distinct internal wave propagation that help understand the more complex physics in the near jet.

The initial velocity perturbations (u', v', w') have an amplitude of 0.1% ΔU and a broadband spectrum given by

$$E\left(k\right) \propto k^4 exp\left[-2\left(\frac{k}{k_0}\right)^2\right],$$

where k_0 is set such that the spectrum peaks at $1.7\delta_{\omega,0}$.

Periodic boundary conditions are used in the streamwise (x) and spanwise (y) directions. Boundary conditions in the vertical direction (z) are set as follows:

$$\begin{aligned}
u\left(z_{min}\right) = \frac{1}{2}\,, \quad u\left(z_{max}\right) &= -\frac{1}{2}\,,\\
v\left(z_{min}\right) = v\left(z_{max}\right) &= 0\,,\\
p\left(z_{min}\right) = p\left(z_{max}\right) &= 0\,,\\
\frac{\partial w}{\partial z}\left(z_{min}\right) = \frac{\partial w}{\partial z}\left(z_{max}\right) &= 0\,,\\
\frac{\partial \rho}{\partial z}\left(z_{max}\right) &= -\frac{J_s}{g}\,,\\
\frac{\partial \rho}{\partial z}\left(z_{min}\right) &= -\frac{J_j}{g}\,.
\end{aligned}$$

The domain size is $50.4\delta_{\omega,0}$ x $16.8\delta_{\omega,0}$ x $55.0\delta_{\omega,0}$ and the grid has 384 x 128 x 512 points. The grid is uniform in the horizontal with spacing of $0.13125\delta_{\omega,0}$. The vertical grid size is $0.075\delta_{\omega,0}$ in the region $-19 < z < 3.5\delta_{\omega,0}$. Outside this region, the grid is mildly stretched at 2%. A second-order finite difference method on a staggered grid is used for spatial derivatives and a third-order low storage Runga-Kutta method is used for time advancement.

A sponge region is employed at the top ($z > 12\delta_{\omega,0}$) and the bottom ($z < -26\delta_{\omega,0}$) boundaries to eliminate wave reflections. The velocities and density in this sponge region are relaxed by adding to the right-hand-side of Eqs. (V.2) and (V.3) a term of the form

$$
\begin{aligned}
- \quad & \phi(z)\left[u_i(x_i,t) - \langle u\rangle_i(z,t=0)\right], \\
- \quad & \phi(z)\left[\rho(x_i,t) - \langle\rho\rangle(z,t=0)\right].
\end{aligned}
$$

The damping function, $\phi(z)$, increases quadratically from $\phi = 0$ to 1.0.

The evolution of the shear layer includes shear instability, formation of the KH rollers and their breakdown into small-scale three-dimensional turbulence. Simulations are continued until most of the fluctuations are dissipated, roughly at $t_f = 350$ time units ($\delta_{\omega,0}/\Delta U$). Details of the numerical methods can be found in Basak & Sarkar (2006), Brucker & Sarkar (2007), and Pham *et al.* (2009).

V.C Far Jet

As the shear layer evolves, KH rollers form and excite waves. The waves behave linearly similar to the ones analyzed in our previous work, Pham *et al.* (2009). Nonetheless, there are inherent differences due to the presence of the jet, a feature that was absent in Pham *et al.* (2009). In this section we examine the wave characteristics as well as their role in the TKE budget.

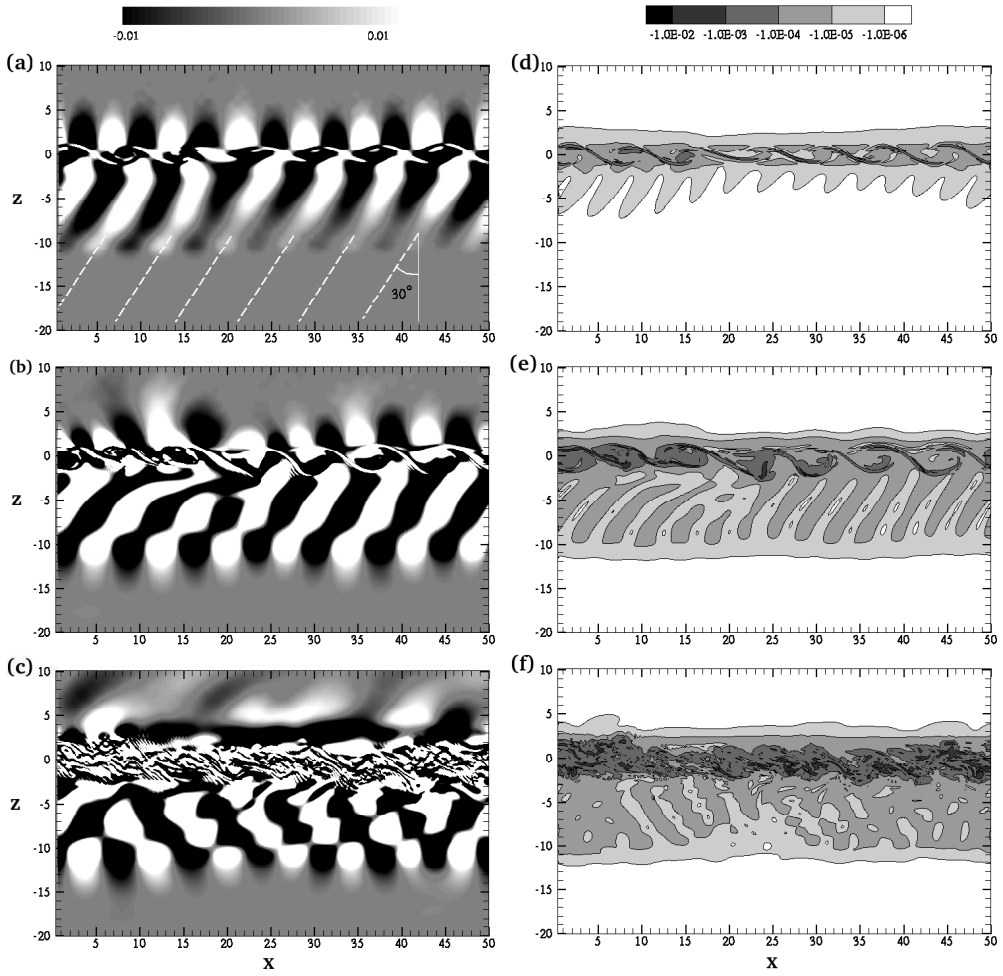

Figure V.3: Far jet. Instantaneous wave field in the x-z plane at $y = 8.4\delta_{\omega,0}$: (a) $\partial w'/\partial z$ at t = 100; (b) $\partial w'/\partial z$ at t = 150; (c) $\partial w'/\partial z$ at t = 200; (d) ε at t = 100; (e) ε at t = 150; (f) ε at t = 200. Dashed lines in (a) indicate propagation angle predicted by linear wave theory.

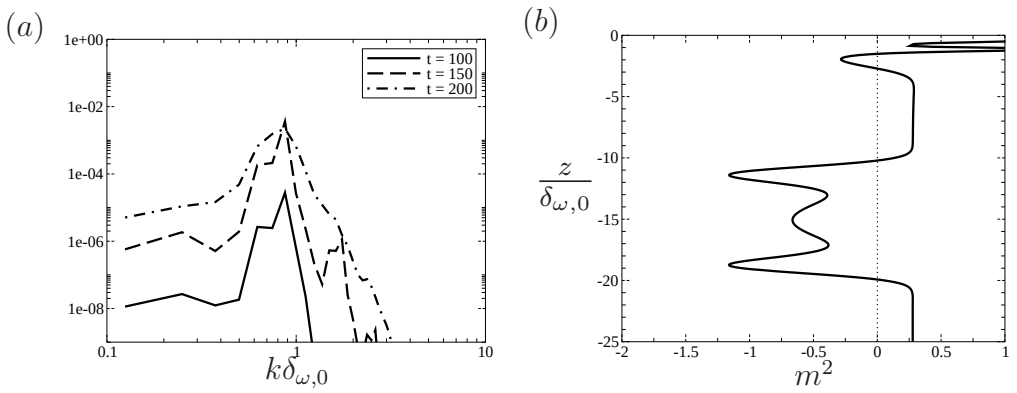

Figure V.4: Far jet. (a) Horizontally-averaged power spectra of the vertical velocity w on the horizontal plane $z = -10\delta_{\omega,0}$ at various times. (b) Squared vertical wavenumber m^2 at t = 100 computed using $k\delta_{\omega,0} = 0.87$ and $c_a = 0$.

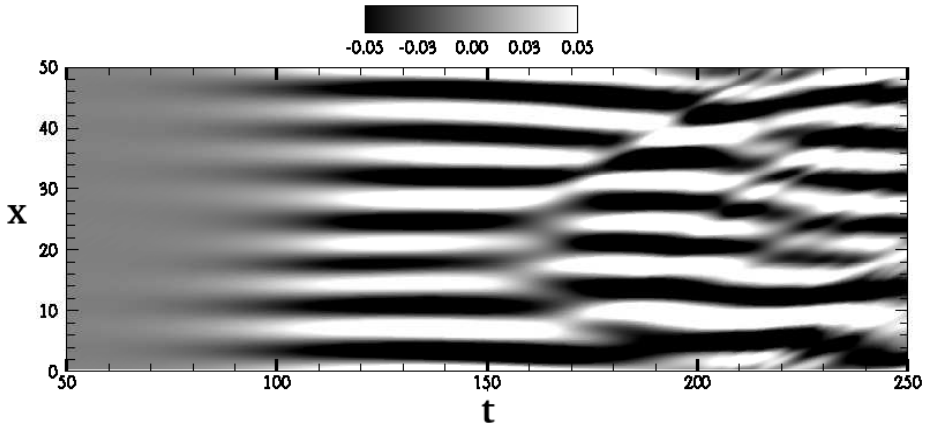

Figure V.5: Far jet. Instantaneous w field in the x-t plane at $y = 8.4\delta_{\omega,0}$ and $z = -6\delta_{\omega,0}$

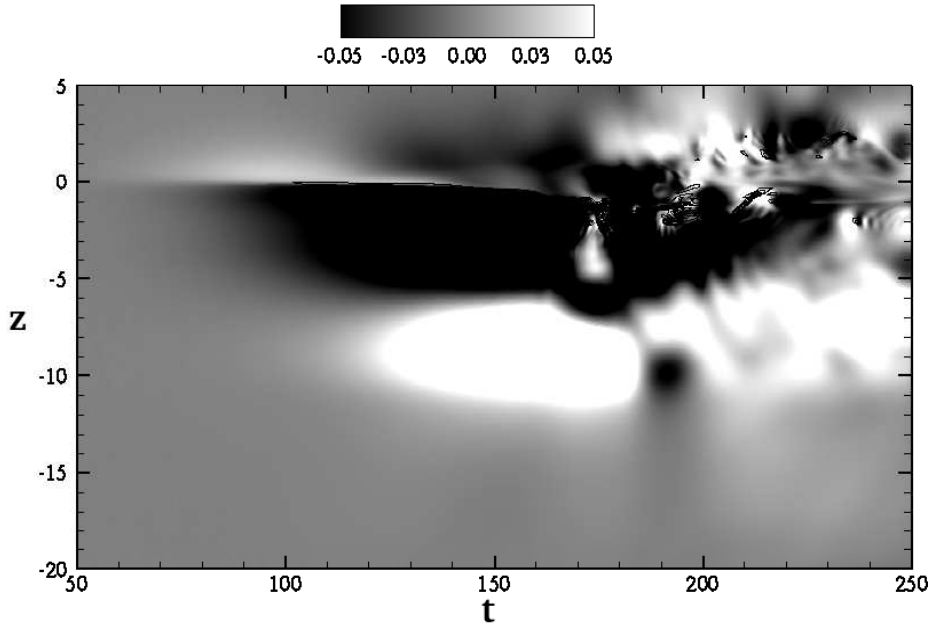

Figure V.6: Far jet. Instantaneous w field in the z-t plane at $x = 25.2\delta_{\omega,0}$ and $y = 8.4\delta_{\omega,0}$.

V.C.1 Internal Wave Field

Figures V.3(a-c) give the visualization of the wave field through the instantaneous fields of $\partial w'/\partial z$ at different times t = 100, 150 and 200. The coherent lines of constant phase in figure V.3(a) are parallel to the wave group velocity and are inclined at an angle of $28 - 34^\circ$ to the vertical. Later in time when the waves enter the jet region, approximately at $z = -10\delta_{\omega,0}$, they are restrained from penetrating the jet and are reflected back toward the shear layer as shown in figures V.3(b,c). The region between the shear layer and the jet has overlapping phase lines of the incident and reflected waves. Figures V.3(d-f) show the turbulent dissipation, ε, at corresponding times; their discussion is deferred until later.

The waves shown in figure V.3(a) are observed to lock on to the KH instability mode. They have horizontal wavenumber $k\delta_{\omega,0} = 0.87$ according to figure V.4 (a), corresponding to horizontal wavelength $\lambda_h = 7.2\delta_{\omega,0}$ which is equal to the wavelength of the most unstable mode, equivalently the spacing between KH rollers in the shear layer. The x-t diagram of the vertical velocity field w at $y = 8.4\delta_{\omega,0}$ and $z = -6\delta_{\omega,0}$ in

figure V.5 indicates the waves are stationary in the simulated frame during the time period between t = 75 and 150. Therefore, the apparent phase speed of the wave is $c_a = 0$. Between t = 150 and 200, the waves are still stationary but exhibit a phase shift. The positive wave crests (white) become negative troughs (black) and vice versa. Beyond t = 200, waves with shorter wavelength and non-zero phase speed are also present, being excited by smaller-scale turbulence in the shear layer.

The waves excited by the KH rollers exhibit linear behavior and, therefore, the propagating angle can be predicted by linear wave theory. In the simulation frame, the KH rollers have zero convective velocity $\langle u \rangle = 0$ while the convective velocity is $\langle u \rangle = 0.5\Delta U$ in the region between the shear layer and the jet. This setup resembles the problem of a flow of constant velocity over stationary surface corrugations which can be solved explicitly. Owing to a Doppler shift, the wave intrinsic speed in the region between the shear layer and the jet is $c_i = c_a + 0.5\Delta U = 0.5\Delta U$ giving the wave intrinsic frequency $\Omega = c_i k = 0.435\Delta U/\delta_{\omega,0}$. Linear wave theory predicts that Ω relates to the ambient stratification N by $\Omega = N cos\,\theta$ where θ is the angle between the wave phase line and the vertical. θ is computed to be 30° using $N = \sqrt{J_j} = 0.5$. The numerical value predicted by linear wave theory agrees well with the visualization shown in figure V.3(a).

Since the vertical direction is non-periodic in our simulation, we cannot directly compute the vertical wavenumber m using a Fourier transform. Nonetheless, we can estimate m using linear wave theory. The Taylor-Goldstein (TG) wave equation is

$$\frac{d^2 w}{dz^2} + m^2 w = 0, \tag{V.4}$$

where,

$$m^2 = \frac{N^2}{(c_a - \langle u \rangle)^2} + \frac{d^2 \langle u \rangle / dz^2}{(c_a - \langle u \rangle)} - k^2.$$

The squared vertical wavenumber m^2 is a key determinant of wave properties: when $m^2 > 0$, the solution consists of propagating modes and, in contrast, the waves are evanescent when $m^2 < 0$. The vertical profile of m^2, plotted in in figure V.4(b), shows that the region between the shear layer and the jet allows wave propagation since $m^2 > 0$. The vertical wavenumber is computed to be $m \approx 0.5\delta_{\omega,0}^{-1}$ giving a vertical

wavelength $\lambda_v \approx 12.6\delta_{\omega,0}$ which is longer than the distance between the shear layer and the top edge of the jet (the far jet starts at $z = -10\delta_{\omega,0}$). The z-t diagram of the vertical velocity field w at $x = 25.2\delta_{\omega,0}$ and $y = 8.4\delta_{\omega,0}$ in figure V.6 can be used to substantiate the vertical wavenumber m predicted by linear wave theory. Prior to t = 150, the waves are stationary with a distinct trough with negative (black) velocity and a positive (white) crest. The vertical extent of the wave trough is approximately $6\delta_{\omega,0}$ which is comparable to half of the vertical wavelength λ_v predicted by linear wave theory. It is noted that the vertical extent of the trough is longer than that of the crest below it since the propagating region $m^2 > 0$ between the shear layer and the jet is less than one complete wavelength as shown in figure V.4(b).

Figure V.4 (b) further shows that the jet region $-10 < z < -20\delta_{\omega,0}$ has $m^2 < 0$ and thus the waves in this region are evanescent with an amplitude that decays sharply with depth. This agrees well with the visualization in figures V.3(b,c) and V.6 suggesting the applicability of linear theory to characterize KH-excited internal waves in this problem.

V.C.2 Turbulent Kinetic Energy Budget

The evolution equation for the turbulent kinetic energy is

$$\frac{dK}{dt} = P - \varepsilon + B - \frac{\partial T_i}{\partial x_i} \; . \tag{V.5}$$

Here, K is the turbulent kinetic energy defined as $K = 1/2 \left\langle u_i' u_i' \right\rangle$, P is the production rate, defined as

$$P \equiv - \left\langle u_i' u_j' \right\rangle \frac{\partial \left\langle u_i \right\rangle}{\partial x_j} = - \left\langle u' w' \right\rangle \frac{d \left\langle u \right\rangle}{dz} \; ,$$

ε is the dissipation rate, defined as

$$\varepsilon \equiv \frac{2}{Re_0} \left\langle s_{ij}' s_{ij}' \right\rangle ; s_{ij}' = \frac{1}{2} \left(\frac{\partial u_i'}{\partial x_j} + \frac{\partial u_j'}{\partial x_i} \right) \; ,$$

B is the buoyancy flux, defined as

$$B \equiv - \frac{g}{\rho_0} \left\langle \rho' w' \right\rangle \; ,$$

$\partial T_i / \partial x_i$ is the transport of tke, defined as

$$T_i \equiv \frac{1}{2} \left\langle u_i' u_j' u_j' \right\rangle + \left\langle u_i' p' \right\rangle / \rho_0 - \frac{2}{Re_0} \left\langle u_j' s_{ij}' \right\rangle \; .$$

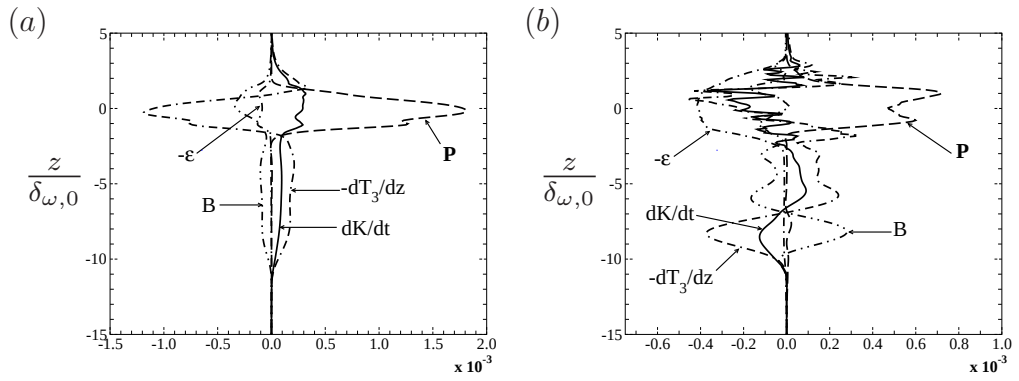

Figure V.7: Far jet. TKE budget at (a) t = 118 and (b) t = 183.

For the present flow, the transport term simplifies to $\partial T_3/\partial z$ with

$$T_3 = T_t + T_p + T_v, \tag{V.6}$$

where the turbulent transport T_t is defined as

$$T_t = \frac{1}{2}\left[\langle w'u'u'\rangle + \langle w'v'v'\rangle + \langle w'w'w'\rangle\right],$$

the pressure transport T_p is defined as

$$T_p = \frac{\langle p'w'\rangle}{\rho_0},$$

and the viscous transport T_v is

$$T_v = -\frac{2}{Re_0}\left[\langle u's'_{31}\rangle + \langle v's'_{32}\rangle + \langle w's'_{33}\rangle\right].$$

Since the current problem involves both internal waves and turbulence, TKE and K are understood to be 'fluctuating' kinetic energy comprised of energy due to both waves and turbulence.

We now examine the role of the internal waves in the evolution of TKE. The terms in the TKE budget are shown in figure V.7 (a) at $t = 118$. When the KH rollers are present in the shear layer, TKE is extracted from the mean velocity leading to the production P. The buoyancy flux B in the shear layer is significant because the rollers are large-scale, two-dimensional structures capable of entraining the heavier fluid from the bottom region into the shear layer. Owing to the lack of three-dimensional fine scales at this time, the turbulent dissipation, ε, in the shear layer is somewhat smaller

than B. While the production and the dissipation rate are limited in extent to the shear layer, the buoyancy flux, the transport dT_3/dz and the transient term dK/dt extend far into the bottom region reaching the top edge of the jet at $z \approx -10\delta_{\omega,0}$. Thus, the signature of internal waves propagating in a stratified shear-free background can be seen in the TKE budget through nonzero values of dK/dT, dT_3/dz and B. Since there is no background shear, internal waves do not lead to production of TKE and they are substantially less dissipative than the perturbations inside the shear layer. All terms in the TKE budget rapidly decrease to zero in the jet region below $z = -10\delta_{\omega,0}$ because the internal waves are evanescent in this region as discussed previously. Although the jet has background shear, there is neither jet instability nor shear production because the jet is strongly stratified ($Ri_g > 0.25$ in the jet). Linear inviscid wave theory states that internal waves exhibit energy equipartition, i.e. half of the energy carried by the waves is fluctuating kinetic energy TKE while the other half is in fluctuating potential energy TPE defined as $TPE = (g^2 \langle \rho'^2 \rangle) / (2\rho_0 N^2)$. The negative of the buoyancy flux, $-B$, is equal to the rate of change of TPE which, because of equipartition, is equal to the rate of change in turbulent kinetic energy, dK/dt, and inserting $B = -dK/dt$ in the TKE equation leads to the total rate of TKE transport, $-dT_3/dz = 2dK/dt$. The waves in the region $-3 < z < -10\delta_{\omega,0}$ in figure V.7 (a) approximately follow this property of linear inviscid waves in a shear-free background.

At $t = 183$, the shear layer is turbulent with the dissipation as the dominant term of the TKE budget as shown in figure V.7 (b). At this time, the region between the shear layer and jet has waves that propagate both upward and downward. Again, the production and the dissipation in this region outside the shear layer are significantly smaller than the other terms. The instantaneous dissipation field ε shown in figures V.3(d-f) further emphasizes that ε is large solely in the shear layer. The wave propagation region between the shear layer and the jet has substantially lower ε, at least three orders of magnitude less than the peak value in the shear layer.

We now discuss the transport term T_3 in equation (V.6) which redistributes fluctuation energy in physical space. Integration of equation (V.5) across the region of interest from depth $z^\star = -5\delta_{\omega,0}$ to z_{max}, the maximum vertical location in the test

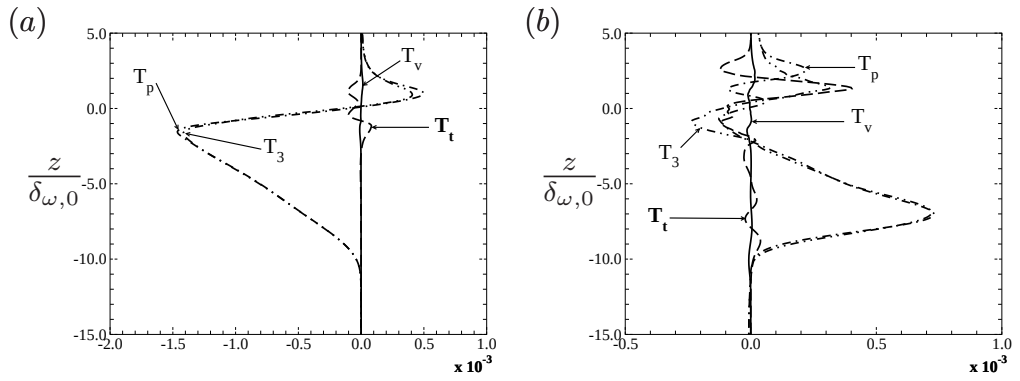

Figure V.8: Far jet. Components of transport T_3 at (a) t = 118 and (b) t = 183.

domain (excluding the sponge region), we obtain

$$\int_{z^\star}^{z_{max}} \frac{dK}{dt}\, dz = \int_{z^\star}^{z_{max}} P\, dz - \int_{z^\star}^{z_{max}} \varepsilon\, dz + \int_{z^\star}^{z_{max}} B\, dz \; + T_3\left(z^\star\right) . \tag{V.7}$$

Note that T_3 at z_{max} is found to be zero. Equation (V.7) indicates the rate of change of TKE in the region of interest is influenced by the rate of TKE transport, T_3, across the lower boundary $z = z^\star$. According to Equation (V.6), the total transport T_3 has three contributions: turbulent T_t, pressure T_p and viscous T_v. Figures V.8(a,b) shows profiles of T_3 and its components. At t = 118, when the KH rollers are dominant, T_p is the largest component of the total transport. T_v is substantially smaller while T_t is significant only in the shear layer. In the region $-10 < z < -3\delta_{\omega,0}$ all the TKE transport comes from pressure transport consistent with the picture that linear internal waves are responsible for the transport of fluctuation energy to the region external to the shear layer. Figure V.8(b), corresponding to a time when the shear layer is turbulent, shows that T_t extends down to $z = -10\delta_{\omega,0}$, a larger depth than at t = 118. T_t in the region $-10z < -3\delta_{\omega,0}$ has alternating signs inferring small-amplitude high-frequency internal waves excited by turbulent shear layer. Nevertheless, T_p dominates the total transport. Furthermore, T_p is positive, changing sign with respect to $t = 118$, showing that internal waves reflected from the jet transport energy upward towards the shear layer. Thus, it is feasible to spatially differentiate a turbulent region from a region with propagating linear waves in the flow using the turbulent transport term; a turbulent region has both T_p and T_t comparably contributing to T_3 while a wave region

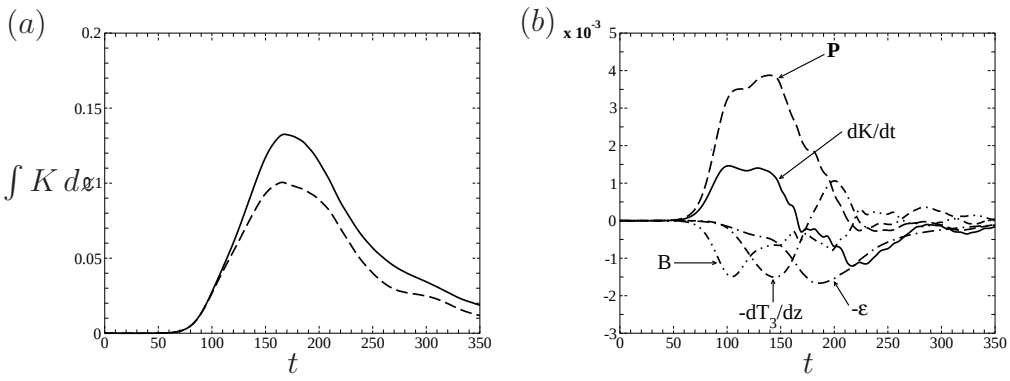

Figure V.9: Far jet. (a) Dashed line: Integrated TKE from $z^\star = -5\delta_{\omega,0}$ to z_{max}; solid line: Integrated TKE across the test domain. (b) Terms in the TKE budget integrated from $z^\star$ to z_{max}.

has a dominant contribution from T_p to T_3.

To illustrate the significance of the TKE carried by the wave field, we track the evolution of TKE in two separate regions: one from $z^\star$ to z_{max} and the other over the entire test domain. The result is shown in figure V.9 (a) where the solid line indicates integration of K over the test domain and the dashed line indicates integration from $z^\star$ to z_{max}. The location of $z^\star$ is chosen to be $-5\delta_{\omega,0}$ because T_t at this depth is relatively small over the duration of the simulation. The difference between the solid and dashed lines correspond to TKE in the region below the shear layer. Prior to t = 100, TKE is generated inside the shear layer and then transported into the region below $z^\star$ by internal waves. TKE is not transported into the region above the shear layer because this region do not support KH-excited waves and turbulence-excited waves are significantly weaker in term of energy transport (Pham *et al.*, 2009). At t = 170 when TKE inside the shear layer reaches its maximum value, TKE carried by internal waves can be as large as 30% of the maximum value inside the shear layer. TKE is transported back into the shear layer between t = 250 and 300 leading to a noticeable lessening of rate of TKE decay during that time interval.

The role of TKE transport by internal waves can be further quantified by tracking the time evolution of the terms indicated in equation (V.7) as shown in figure V.9 (b). The term dT_3/dz is spatially integrated instead of taking T_3 at $z^\star$ as in equation (V.7) although both provide the same results. In the figure, prior to t = 180 the transport

term is negative indicating TKE is carried outside the shear layer. After that, it changes sign so that TKE is transported upward into the domain of integration. The peak value of the transport is as large as the peak values of the buoyancy flux and the dissipation in the current study and somewhat larger that the peak value of the transport reported in Pham *et al.* (2009) which was about 33% of the peak dissipation and 75% of the peak buoyancy flux. The difference between the two studies is due to the constructive interference between incident and reflected waves in the current investigation. Although energy carried by the internal waves is large compared to other terms in the integrated TKE budget, the wave energy is lost only due to the viscous dissipation, ε, whose structure was shown earlier in figures V.3 (d-f). The value of ε in the jet is small relative to that in the shear layer. There is no signature of induced 'deep-cycle turbulence' in the stratified jet that has been observed in the EUC system.

V.D Near Jet

The evolution of the fluctuations in the near case is significantly different from that in the far case. First, internal waves are observed in and below the jet. Second, 'hot pockets' of fluid are observed to penetrate into the cold jet region and are precursors to coherent patches of *strong* induced dissipation, much larger than in the far jet. In the following text, we elaborate on these remarks.

V.D.1 Internal Wave Field

Instantaneous fields of $\partial w'/\partial z$ are shown in figures V.10(a,b) at time t = 125 and 150 to visualize the internal wave field. In figure V.10(a) the wave phase lines are not clear in the jet region $-2.5 < z < -10\delta_{\omega,0}$ but there are four ellipse-shaped lobes in the vicinity of $z = -10\delta_{\omega,0}$ with alternating signs implying two crests and two troughs. In figure V.10(b) phase lines which originate from the lobes are clear. The propagation angle θ is between $74 - 78^\circ$ to the vertical. Waves of horizontal wavelength larger than that observed in the *far* case are excited by larger-wavelength disturbances in the

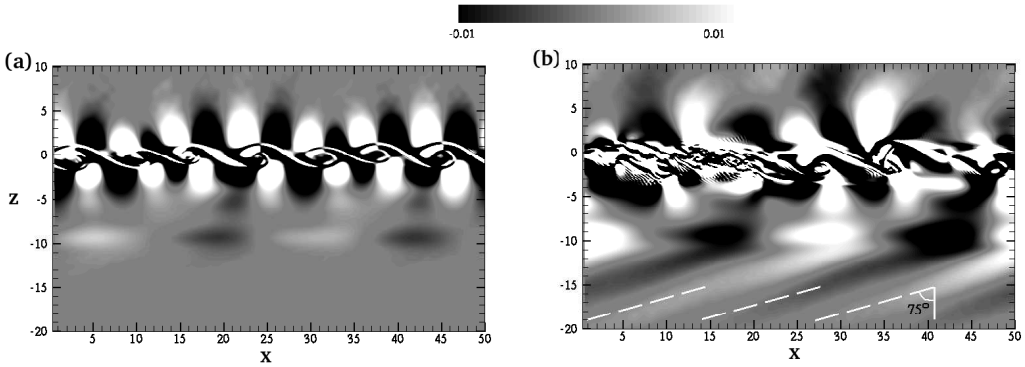

Figure V.10: Near jet. Internal wave field is visualized through a slice of $\partial w'/\partial z$ in the x-z plane at $y = 8.4\delta_{\omega,0}$ at time (a) t = 125 and (b) t = 150

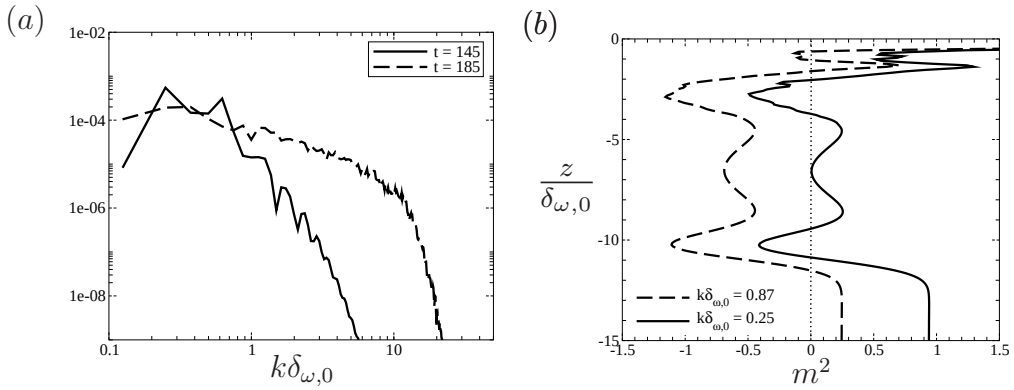

Figure V.11: Near jet. (a) Horizontally-averaged power spectra of the vertical velocity w on the horizontal plane $z = -4\delta_{\omega,0}$ at various times. (b) Squared vertical wavenumber m^2 at t = 150 computed using $c_a = 0$ and two values of horizontal wavenumber: $k\delta_{\omega,0} = 0.25$ based on the peak of energy spectrum at $t = 145$ in (a) and $k\delta_{\omega,0} = 0.87$ based on the KH mode.

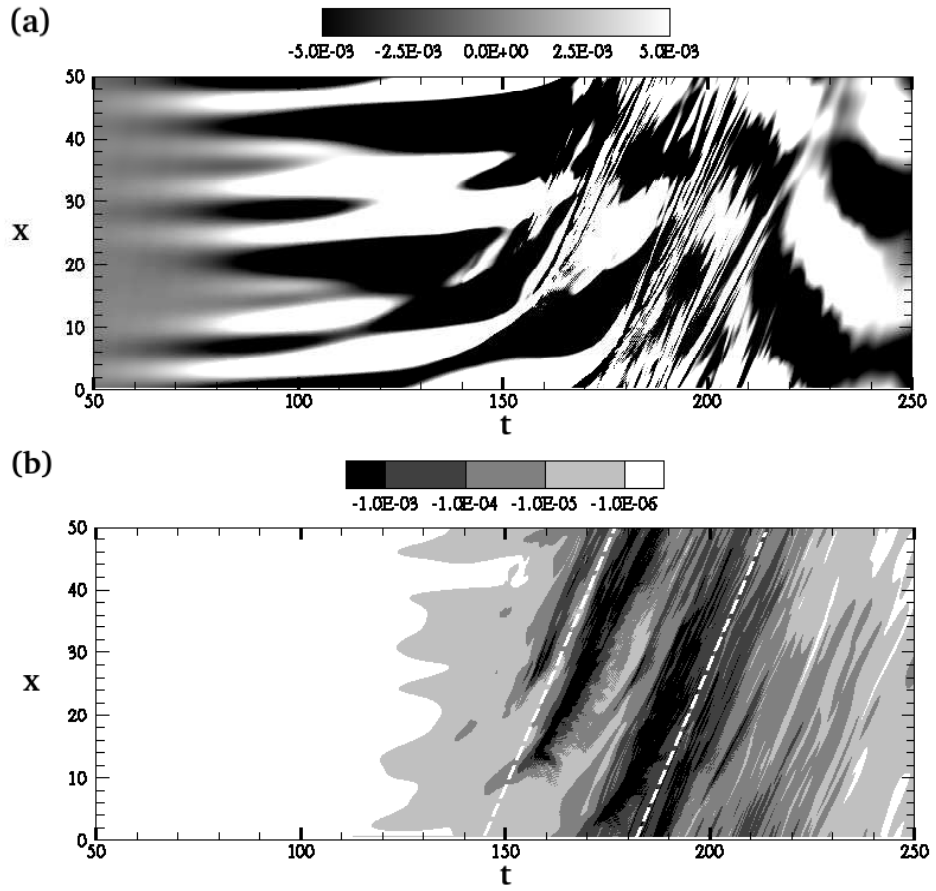

Figure V.12: Near jet. (a) Instantaneous vertical velocity field w in the x-t plane at $y = 8.4\delta_{\omega,0}$ and $z = -4\delta_{\omega,0}$. (b) Instantaneous dissipation field ε on the same plane. The white dashed lines denotes $\langle u \rangle = dx/dt \approx 1.7\Delta U$.

shear layer that occur owing to the nonlinear interaction, including pairing, of the KH rollers. It is noted that, in the present study, the jet is strongly stratified, well above the limit, $J(z) \approx 0.13$ (Sutherland & Peltier, 1992), for linear instability, suggesting that the fluctuations in the jet are not a result of jet instability.

The horizontally-averaged power spectra of the vertical velocity w measured at $z = -4\delta_{\omega,0}$, a location outside the shear layer, are shown in figure V.11(a). The spectrum at t = 145 shows a distinct peak at $k\delta_{\omega,0} = 0.25$ implying the waves are not excited by KH-rollers but rather by smaller-wavenumber disturbance in the shear layer. The contour plot of the vertical velocity w in the x-t plane at $y = 8.4\delta_{\omega,0}$ and $z = -4\delta_{\omega,0}$ shown in figure V.12 further characterizes the internal waves in the

jet. The x-wavelength increases from the KH value after t = 100 to a wavelength approximately equal to $25\delta_{\omega,0}$ yielding the wavenumber $k\delta_{\omega,0} = 0.25$ in good agreement with the spectral peak shown in figure V.11(a). Figure V.12(b) shows the dissipation field corresponding to the field shown in figure V.12(a) and will be discussed later.

Linear wave theory can be used to explain why the KH rollers cannot excite internal waves. Profiles of m^2, the term in square brackets in equation (V.4), are shown in figure V.11 (b) with two different values of horizontal wavenumber $k\delta_{\omega,0} = 0.25$ and 0.87. The former corresponds to the spectral peak in figure V.11(a) and the latter is the wavenumber for KH instability. Clearly, $m^2 < 0$ over the whole jet for $k\delta_{\omega,0} = 0.87$ and $m^2 > 0$ in the region $-4 > z > -9\delta_{\omega,0}$ of the jet for $k\delta_{\omega,0} = 0.25$. As the result, KH-excited waves cannot propagate inside the jet. The four distinct lobes observed at $z \simeq -10\delta_{\omega,0}$ in figures V.10(a,b) are consistent with the transition from $m^2 > 0$ to $m^2 < 0$ in the solid line of figure V.11(b) at $z \simeq -10\delta_{\omega,0}$. The observation of lobes here is analogous to the lobes in the far case shown in figure V.3(b) at $z = -10\delta_{\omega,0}$ where there is a similar change in the sign of m^2. However, different from the far case, freely propagating waves are observed in the near jet below the evanescent region with $m^2 < 0$ because they can tunnel through the evanescent region which is thinner relative to the far jet. Internal wave tunneling through a stratified shear region is possible, for example, see Brown & Sutherland (2007).

The internal waves propagating in the region below the jet are observed to be linear, similar to those in the far case. The propagation angle θ can be predicted as in the previous section. Taking the apparent phase speed $c_a = 0$ gives the intrinsic phase speed in this region as $c_i = 0.5\Delta U$. With the horizontal wavenumber $k = 0.25\delta_{\omega,0}$, linear theory yields the intrinsic frequency $\Omega = 0.13\Delta U/\delta_{\omega,0}$ and propagation angle $\theta = 75°$. This agrees well with the visualization given in figure V.10 (b). It is worth noting that, different from the studies of Smyth & Moum (2002) and Sutherland (2006), a critical layer does not exist in our simulated jet. The observed waves have phase speed in the opposite direction of the jet such that there is no location at which the wave phase speed is equal to the free-stream velocity. The value of m^2 is finite in the jet as shown in figure V.11 (b) in contrast to a critical layer which would have an infinite

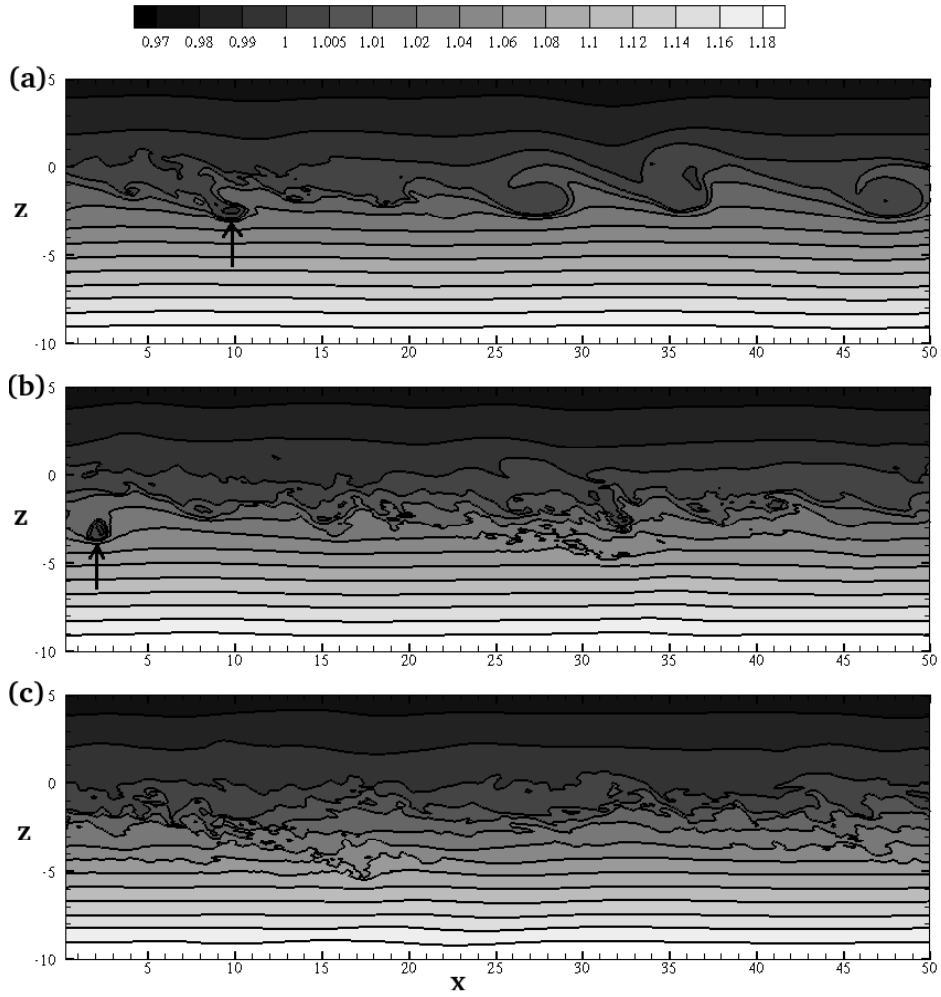

Figure V.13: Near jet. Isocontours in the density field in the x-z plane at $y = 8.4\delta_{\omega,0}$. (a-c) corresponds to t = 150, 170 and 185, respectively. Arrow indicates 'hot pocket'.

value of m^2.

V.D.2 'Hot Pockets'

During the time period between t = 140 and 200, we observe distinct events of a 'light', equivalently 'hot', pocket of fluid entrained into the cold jet region as shown in figures V.13 (a-c). The figures show the density isocontours in the vertical x-z plane at $y = 8.4\delta_{\omega,0}$ at various times. A 'hot pocket' is observed in the upper-flank of the cold jet region at $x \approx 10\delta_{\omega,0}$ in figure V.13(a). The pocket is swept downstream

and stretched by the background jet shear. The fluctuations in the vicinity of the pocket gain intensity and their spatial extent increases. Figure V.13(b) shows that, eventually, the region $-4 < z < -2\delta_{\omega,0}$ and $20 < x < 35\delta_{\omega,0}$ contains numerous small-scale structures indicating turbulence activity. At $x \approx 2\delta_{\omega,0}$ in figure V.13(b), there appears another 'hot pocket', which induces turbulence in the vicinity of $x \approx 15\delta_{\omega,0}$ later, as shown in figure V.13(c). The 'hot pocket' also leads to fluctuations which penetrate into the deeper region, down to $z = -5\delta_{\omega,0}$. The horizontal extent of the fluctuation regions left by the pockets are similar in both the events and comparable to half the wavelength of the internal waves observed in figures V.10(b).

Figure V.14(a) provides the three-dimensional structure of these 'hot pockets'. Two isopycnal surfaces at $t = 162$ are plotted: the darker isopyncal of $\rho = 1.0$ which is equal to the initial mean density at $z = 0$ and the lighter isopycnal of $\rho = 1.07$ which is equal to the initial mean density at $z = -4.7\delta_{\omega,0}$. The HS symbols denotes the horseshoe-like density structures, which appear as the 'hot pockets' in figures V.13(a-c). These structures originate from the shear layer where they are coherent and extends into the jet where they are mixed by the background shear. The structure at $x \approx 15\delta_{\omega,0}$ penetrates deep into the jet core, impinges the lighter isopyncnal causing localized region of intense fluctuation. The impingement of the density structures are carried by horseshoe vortices as shown in figure V.14(b). Here, vortex structure is defined using Δ criterion as in Jeong & Hussain (1995). The isosurface of $\Delta = 5$ distinctively identifies the horseshoe vortex which coincides with the density structure at $x \approx 15\delta_{\omega,0}$ shown in figure V.14(a). As the horseshoe vortex penetrates the jet, it gets elongated in the x direction by the background shear and finally diminishes after intense mixing.

V.D.3 Induced Dissipation

Figures V.15 (a-c) illustrate the instantaneous dissipation field ε corresponding to the density field shown in figures V.13 (a-c), respectively. Clearly, the 'hot pockets' in the former figures correlate with the coherent patches that have large dissipation in the later figures. The patch of turbulence that originates from the 'hot pocket' in

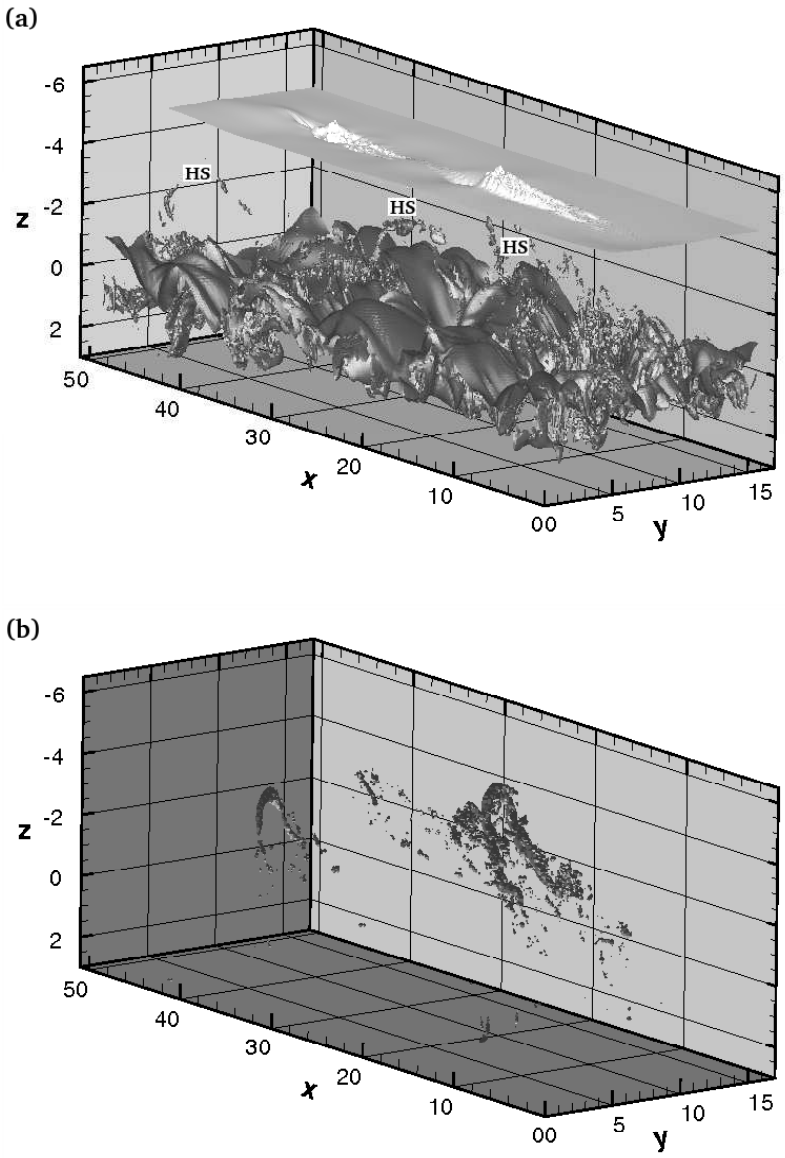

Figure V.14: Near jet. (a) Isopycnal surfaces at t = 162: the darker isopycnal is of $\rho = 1.0$ corresponding to the initial mean density at $z = 0$; the lighter isopycnal is of $\rho = 1.07$ corresponding to the initial mean density at $z = -4.7\delta_{\omega,0}$. HS indicates horseshoe-like density intrusions. The lighter isopycnal is blanked in the range $0 < y < 5\delta_{\omega,0}$. (b) Isosurface of $\Delta = 5$ at t = 162 shows the horseshoe vortices. In this figure, positive z direction points downward.

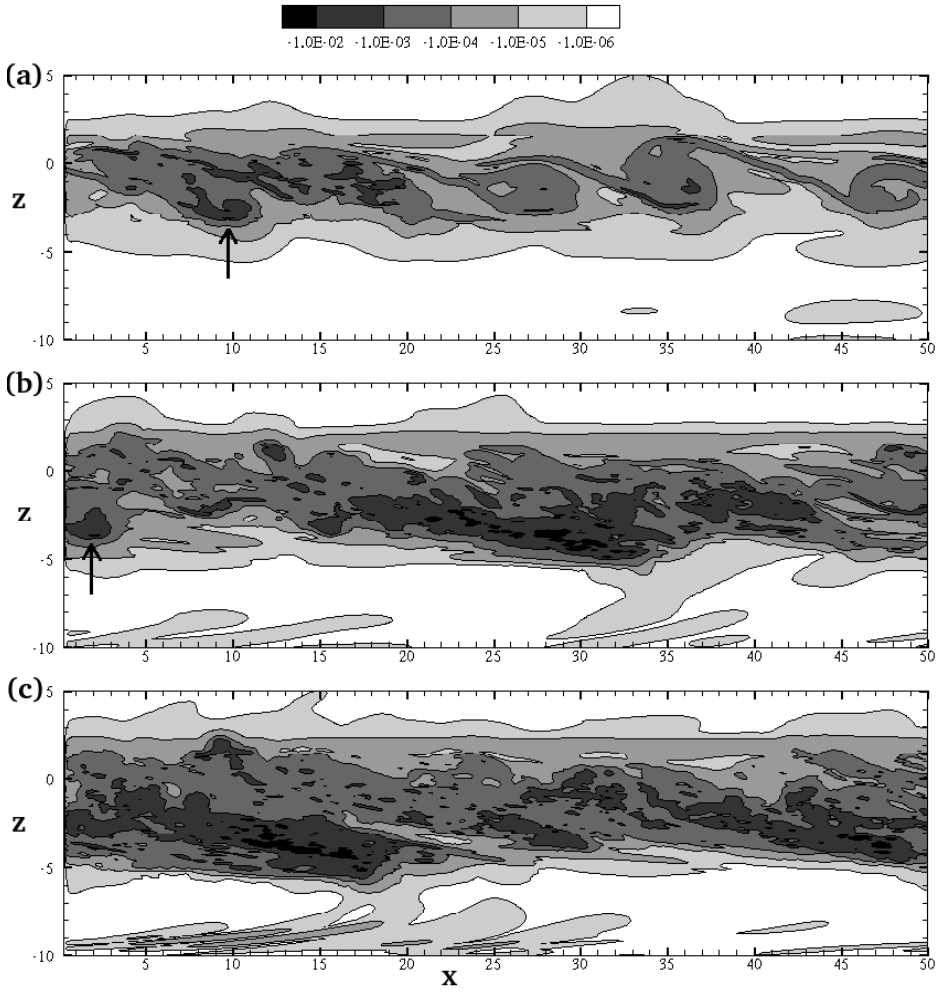

Figure V.15: Near jet. Isocontours in the dissipation field in the x-z plane at $y = 8.4\delta_{\omega,0}$. (a-c) corresponds to t = 150, 170 and 185, respectively. Arrow indicates 'hot pocket'.

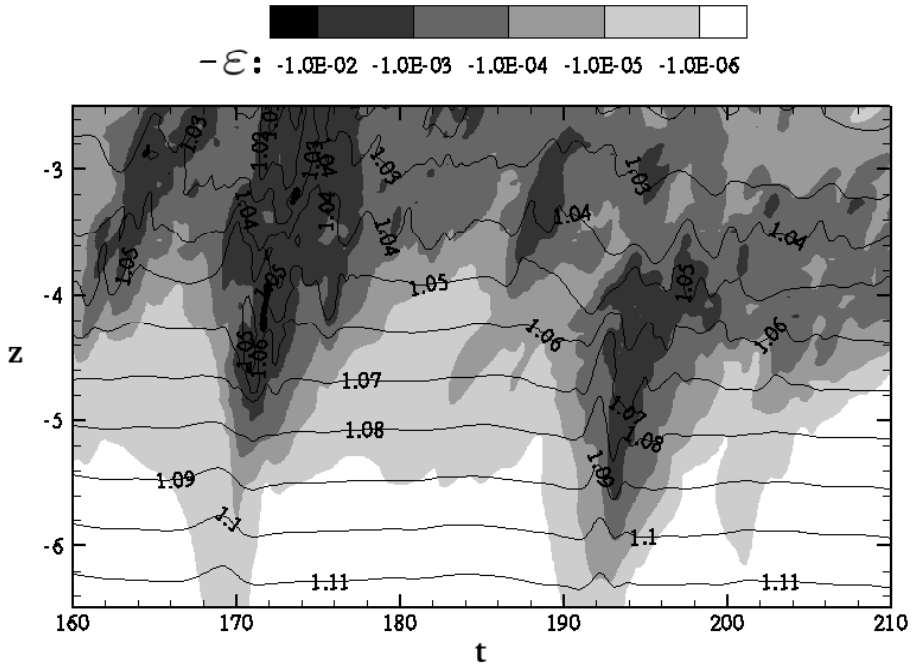

Figure V.16: Near jet. Instantaneous dissipation field ϵ field in the z-t plane at $x = 25.2\delta_{\omega,0}$ and $y = 8.4\delta_{\omega,0}$. Solid lines are isopycnals.

figure V.15(a) intensifies in figure V.15(b), which coincides with the strong fluctuation regions shown in figure V.13(b). At time t = 185, the dissipation in the upper-flank of the jet is *stronger* than in the shear layer. The value of ε in the near jet has values up to three orders of magnitude larger than the dissipation in wave propagation region in the far jet. These turbulence patches move with the free-stream velocity u as shown in x-t diagram of figure V.12(a). The patches with the strongest dissipation shown in black convect in the positive x direction with the slope dx/dt equal to the local value of $\langle u \rangle$. Therefore, these patches have the apparent phase speed $c_a = \langle u \rangle$ moving downstream and thus intrinsic phase speed $c_i = 0$, in contrast to the internal waves shown by the contour plot of w field during the time period t = 100 and 150 in figure V.12(b) that have $c_a = 0$ and $c_i = \langle u \rangle$ moving upstream. The dissipation in the internal wave field prior to t = 100 in figure V.12 (a) is substantially smaller than in the induced patches that occur at later time. The horizontally-averaged power spectrum at $z = -4\delta_{\omega,0}$ and at time t = 185 shown in figure V.11 indicates the jet is broadband turbulent with no

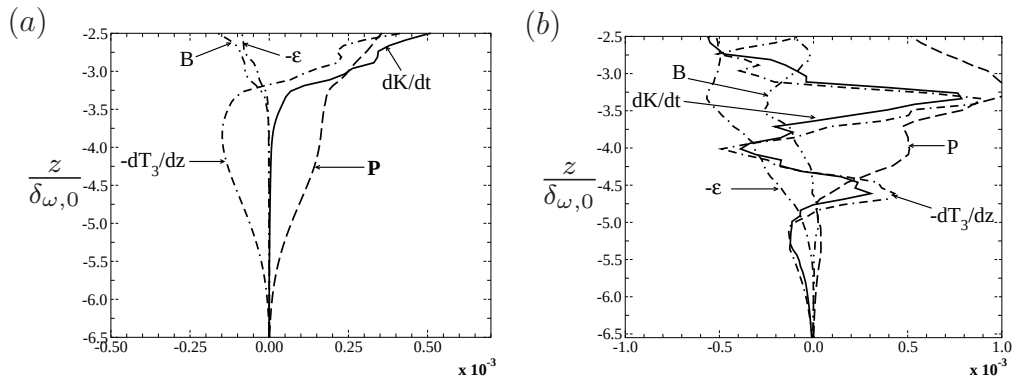

Figure V.17: Near Jet. TKE budget at (a) t = 143 and (b) t = 171.

distinct peaks. The peaks seen in the spectrum at earlier time t = 145 prior to the 'hot pocket' penetration have disappeared.

Figure V.16 shows a contour plot of the instantaneous dissipation field along with isopycnals in the z-t plane at $x = 25.2\delta_{\omega,0}$ and $y = 8.4\delta_{\omega,0}$. Two patches of induced turbulence are observed approximately at t = 170 and 191. The latter penetrates to greater depth compared to the former. Both patches are accompanied by fluctuations in the isopycnals. To the left of the regions with strongest dissipation ($\varepsilon > 10^{-3}$), high-amplitude low-frequency waves are observed while to the right are low-amplitude high-frequency fluctuations. Distinct wave packets are observed direct below the patches in the bottom three isopycnals. The packets occur at a time interval small compared to the buoyancy time period.

V.D.4 Turbulent Kinetic Energy Budget

As shown in the previous section, the penetration of the 'hot pockets' into the cold jet region starts the chain of events that culminates in patches of induced dissipation. The internal waves observed to propagate inside the jet disappear after the penetration. In this section, we analyze the TKE budget to elucidate the energy pathways that feed the dissipation patches. Figures V.17(a,b) present the TKE budgets at time t = 143 before the first 'hot pocket' begins to penetrate the jet and at t = 171 corresponding to figure V.13(b) and V.15(b) in which the induced dissipation in the jet is observed. When internal waves propagate in a quiescent background, the rate of energy transport

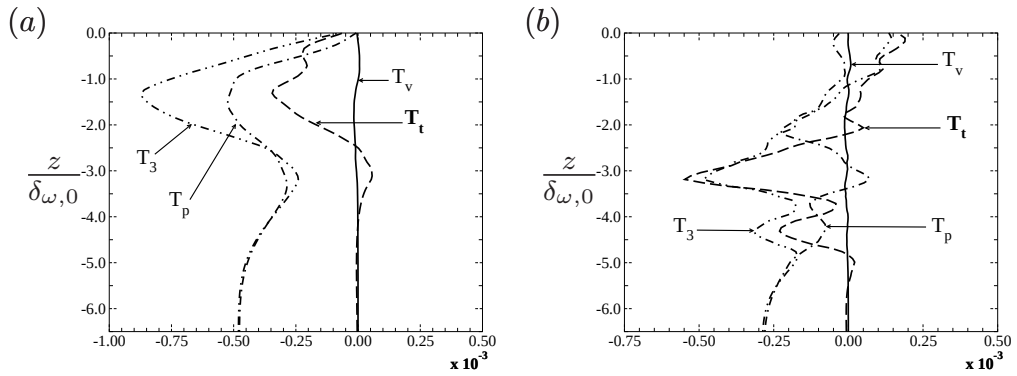

Figure V.18: Near Jet. Components of TKE transport T_3 at (a) t = 143 and (b) t = 171.

dT_3/dz is equipartitioned between the time rate of change in turbulent kinetic energy dK/dt and the buoyancy flux B as shown previously in the far case. Here, at time t = 143 the production P balances the transport dT_3/dz in the region between depth $z = -4\delta_{\omega,0}$ to the jet center. The production in this region is different from that observed in the shear layer. The latter is the result of energy extraction from the unstable mean shear, namely turbulent production, while the former originates from the interaction between the momentum flux carried by the internal waves and the background stable jet shear, namely wave production. The dissipation ε is insignificant at this time consistent with the low dissipation behavior of the propagating internal waves shown in figure V.12(b). The buoyancy flux B is relatively smaller than P and dT_3/dz because the effect of mean shear, that is involved in the definition of P and contributes to the source of the pressure equation and thereby the pressure transport component of T_3, is stronger on P and T_3 than on B. Here, the TPE carried by the waves is less than the TKE, which is different from the *far* jet where the TPE is equal to TKE. At time t = 171, in the region $-5.5 < z < -4.5\delta_{\omega,0}$, the buoyancy flux B changes sign and locally becomes a TKE source, a signature of counter-gradient heat flux. The available potential energy carried by the 'hot pockets' is released into kinetic form. Nonetheless, this energy source is significantly smaller than the energy lost to the induced dissipation.

To examine the role of the waves in the TKE budget of the jet, the contributions to the transport term T_3 are analyzed. As explained previously, the contributions are

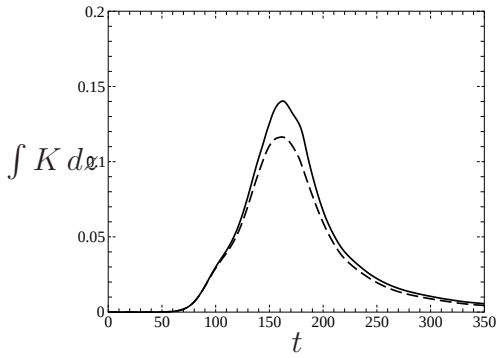

Figure V.19: Near Jet. Dashed line indicates integrated TKE in the region $-2.5 < z < z_{max}$. Solid line indicates integrated TKE over entire test domain. The difference between the two lines is the TKE outside the shear layer and in the jet.

viscous diffusion T_v, turbulent transport T_t and pressure transport T_p. Figures V.18 (a,b) show the contributions to the total transport at time t = 143 and 171, respectively. In figure V.18 (a), there are clearly two distinct regions: a wave-dominated region ($z < -4\delta_{\omega,0}$) with little turbulence and a region with stronger turbulence ($z > -4\delta_{\omega,0}$). T_p and T_3 are equal in the wave-dominated region, i.e. all the contribution to the transport is due to pressure. On the other hand, the transport in the turbulent region has significant contribution from T_t. The turbulent region $-3.5\delta_{\omega,0} < z < 0$ in figure V.18(a) thickens to $-5\delta_{\omega,0} < z < 0$ in figure V.18(b) as evidenced by the drop of T_p and the increase in T_t to become the dominant component of transport. In other words, part of the wave-dominated region in part (a) becomes turbulence-dominated in part (b) of the figure. The inference is that the internal wave field has evolved into turbulence.

How large is the wave energy contribution to the TKE that resides in the jet and external to the shear layer? Figure V.19 illustrates the time evolution of the integrated TKE over two spatial regions: one from $-2.5 < z < z_{max}$ shown by the dashed line and the other across the entire test domain shown by solid line. The evolution consists of three significant periods of time. The first period is between t = 100 and 150 when internal waves transport energy outside the shear layer. Figure V.17 (a) and V.18(a) indicate energy accumulation during this period is from wave production and wave

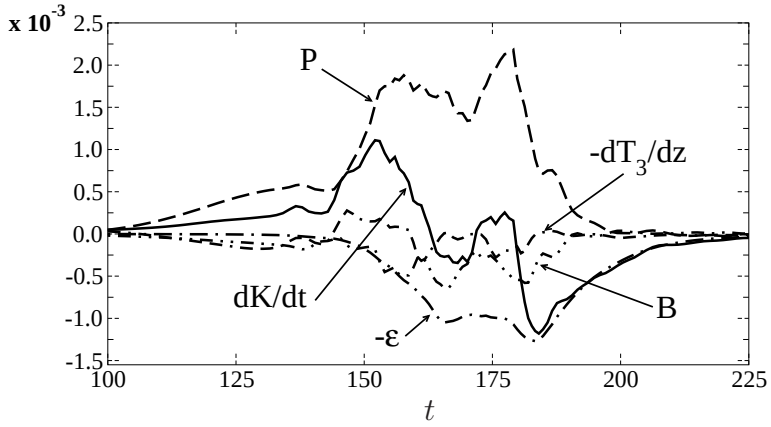

Figure V.20: Near Jet. Integrated TKE budget. The terms are spatially integrated in the jet upper-flank $-6.5 < z < -2.5\delta_{\omega,0}$.

transport. During the second period between t = 150 and 200, there are significant fluctuations outside the shear layer which, being quickly dissipated over the period, is indicative of turbulence. The amount of energy accumulated inside the jet during the first period is smaller than amount observed during the second period. Possible sources of energy accumulation in the jet are from the transport (both wave and turbulence), the production (both waves and turbulence) and counter-gradient buoyancy flux. As shown earlier, the counter-gradient heat flux is local and weak compared to other terms in the budget. The wave transport and wave production are too small to account for the larger TKE accumulation relative to that seen during the first period. This leaves turbulence transport and turbulent shear production as contributors to the large amount of energy observed during the time period $150 < t < 200$. It is worth noting that this is the time period in which the 'hot pockets' are active in the jet. In the third period, $t > 200$, there is a small difference between the two lines as in the first period. The time evolution of the spatially integrated TKE budget is given in figure V.20 to further elucidate the energy pathways leading to the enhanced TKE and dissipation in the near jet. The terms in the TKE budget are spatially integrated over the jet upper-flank $-6.5 < z < -2.5\delta_{\omega,0}$. Prior to the penetration of the first 'hot pocket' at $t \approx 145$, there is no dissipation in the region. The transport is mostly from the pressure transport, T_p. Positive dK/dt indicates an accumulation of TKE, mainly due to the positive wave production associated with wave momentum flux $\langle u'w' \rangle$

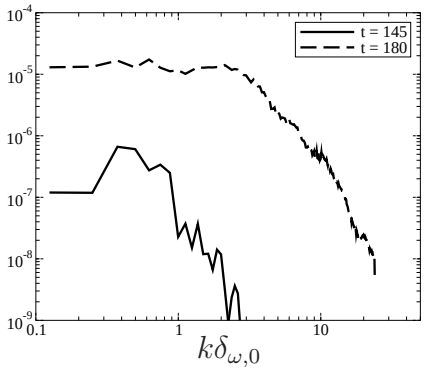

Figure V.21: Near Jet. Horizontally averaged power co-spectra of Reynolds stress $u'w'$ at $z = -4\delta_{\omega,0}$.

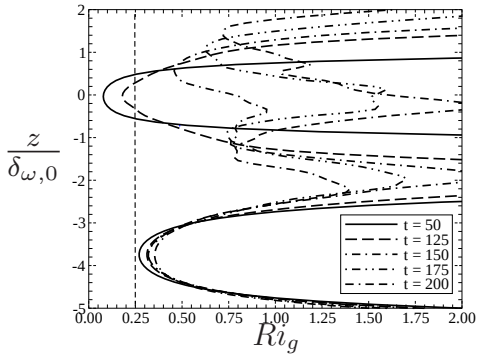

Figure V.22: Near Jet. Ri_g profiles.

interacting with the stable background shear. At $t \approx 145$, the 'hot pocket' penetrates the region causing the buoyancy flux to become less negative due to the positive effect of counter-gradient heat flux. The 'hot pocket' also arrives with turbulence transport T_t causing the transport term, $-dT_3/dz$, to become positive, i.e. a source of energy. Nonetheless, the largest source of TKE is the production. The production and the dissipation peaks twice corresponding to the two 'hot pocket' penetrations. The overall evolution of the budget indicates that most of the TKE accumulated in the region is due to shear production by interaction with both internal waves and turbulence. The counter-gradient heat flux resulting from the 'hot pockets' can be a source locally in space; however, overall the buoyancy flux is an energy sink. Integrating over time, the energy lost to the induced dissipation is mainly contributed by the production.

In the current study where both waves and turbulence are involved, it is not straightforward to identify during which time period $\langle u'w' \rangle$ represents wave momentum

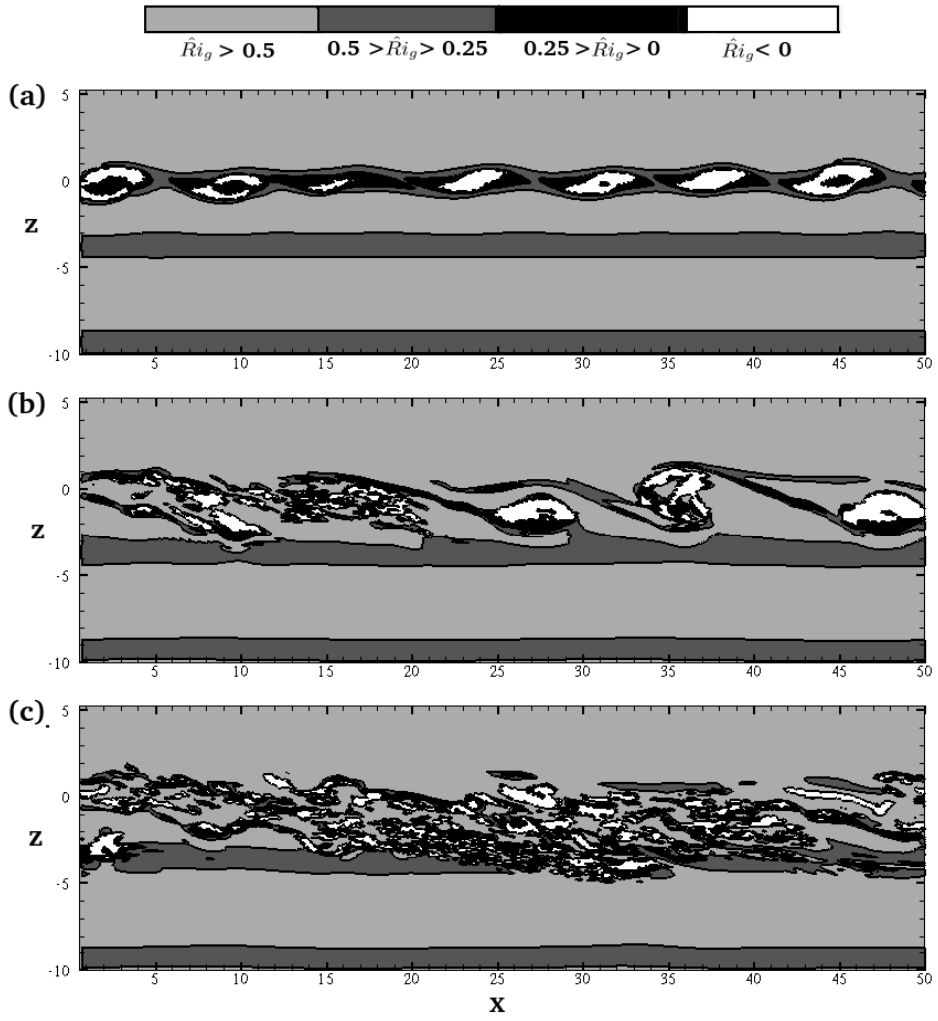

Figure V.23: Near jet. Local gradient Richardson number $\hat{Ri}_g$ field at y = $8.4\delta_{\omega,0}$ and t = 100, 145 and 175.

flux and when is it due to turbulent Reynolds shear stress. One way to differentiate between the two is to perform a spectral analysis of the $u'w'$ field. The horizontally-averaged co-spectrum measured at $z = -4\delta_{\omega,0}$ shown in figure V.21 indicates the peak value of the wave momentum flux (at t = 145) is an order of magnitude weaker than that of the Reynolds stress (at t = 180). The spectrum for the wave momentum flux clusters at low wavenumber while the turbulent Reynolds stress has broadband spectrum. Thus, the time evolution of the integrated production P shown in figure V.20 consists of two regimes: wave production prior to t = 145 and turbulence production during t = 145 and 200. The latter is significantly larger than the former.

The gradient Richardson profile $Ri_g(z)$, computed using horizontal averages of N and vertical shear S, that is plotted in figure V.22 indicates that linear shear instability in the jet is infeasible because $Ri_g(z) > 0.25$. At early time, the value of Ri_g is less than 0.25 only in the shear layer. The value of Ri_g at $z = -4\delta_{\omega,0}$ increases in time even during the time period when the 'hot pockets' are active. Nonetheless, the fields of local $\hat{Ri}_g$, computed on the x-z plane at $y = 8.4\delta_{\omega,0}$ and shown in figures V.23(a-c) at t = 100, 145 and 150, indicate the potential for local shear instability. Here, $\hat{Ri}_g$ is defined as

$$\hat{Ri}_g(x, y, z, t) = \frac{(-g/\rho_0)d\rho/dz}{du/dz},$$

where u and ρ are instantaneous values. In figure V.23(a), there are three visible bands with low $\hat{Ri}_g$ values: the shear layer, the upper- and lower-flank of the jet. The shear layer has $\hat{Ri}_g < 0$ shown in white and $\hat{Ri}_g < 0.25$ shown in black. The KH rollers have a black region surrounded by a white region while the braid is covered in black. At t = 100, the upper-flank of the jet has $0.25 < \hat{Ri}_g < 0.5$ shown in grey, not small enough to support linear instability. In figure V.23(b), at t = 145, the 'hot pocket' marked by a black region below a white region visible at $x = 10\delta_{\omega,0}$ right below the shear layer begins to penetrate the jet. In figure V.23(c), at t = 175, a large portion of the jet upper-flank is covered in black and white indicating that shear instability is now supported. Energy indeed can be extracted from the jet shear at this time.

From the discussion in this section, it is evident that the energy feeding into the induced dissipation originates from shear production of TKE. However, it is crucial

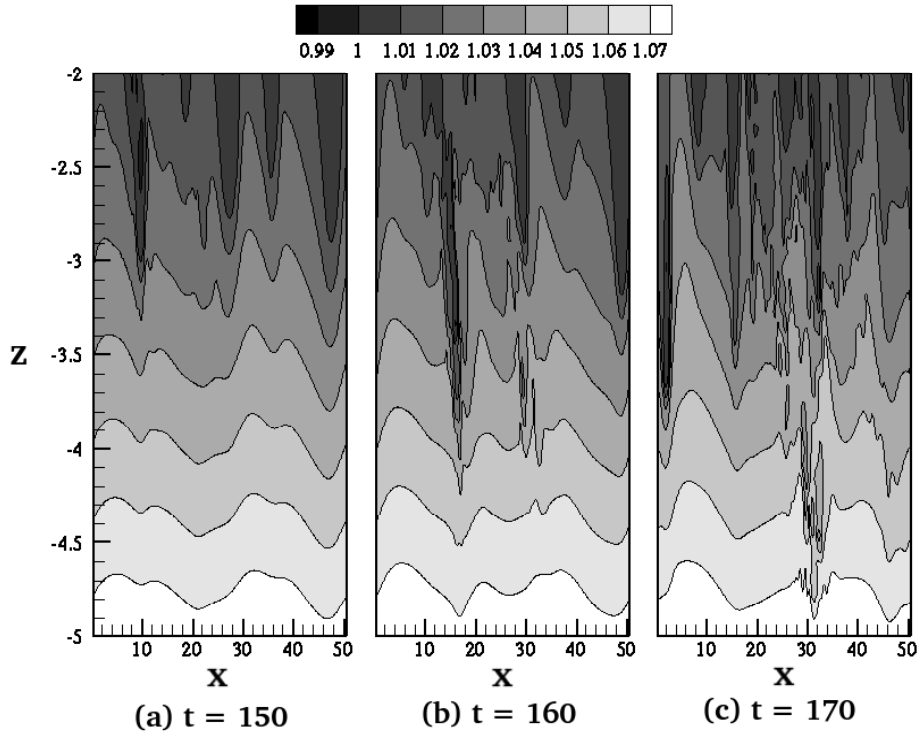

Figure V.24: Near jet. Expanded-view of the density fields with the aspect ratio L_z:L_x = 1:35.

to distinguish turbulent production from wave production. The time evolution of the integrated production shown in figure V.20 indicates the wave production is significant less than the turbulent production. Using t = 145 as a marker that separates the two types of production, over the entire simulation the wave production contributes 17% to the total production while the contribution of turbulent production is 83%.

It is of interest to visually illustrate how the internal waves contributes energy to the induced dissipation. The breakdown of the wave field is shown by the visualization in figure V.24 where the vertical scale is increased relative to the horizontal by a factor of 35 to amplify the wave amplitude. The lower four isopycnals in figure V.24(a) indicate that the internal waves present in the jet have an approximate wavelength of $25\delta_{\omega,0}$ with the strongest peak-to-trough amplitude of $0.4\delta_{\omega,0}$. The simulated domain contains two wavelengths starting with a crest at the far left and ending with a trough at the far right. The waves are coherent between depth $z = -3\delta_{\omega,0}$ and $z = -5\delta_{\omega,0}$.

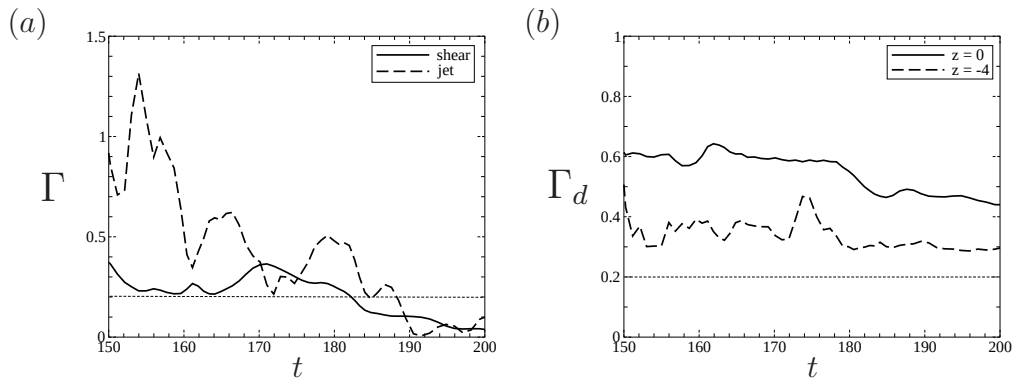

Figure V.25: Near Jet. Mixing efficiency. (a) Γ. (b) Γ_d. The dotted line shows the value $\Gamma = \Gamma_d = 0.2$.

The 'hot pocket' visible at x = 10 $\delta_{\omega,0}$ between $-3 < z < -2\delta_{\omega,0}$ causes a distortion of the left wave crest increasing its steepness. To assess the impact of $\partial\rho/\partial x$ caused by the penetration of the 'hot pocket', it is useful to write an evolution equation for the vertical density gradient. The background shear contributes a term as follows,

$$\frac{D}{Dt}\left(\frac{\partial\rho}{\partial z}\right) \sim -\frac{d\,\langle u\rangle}{dz}\frac{\partial\rho}{\partial x} \tag{V.8}$$

According to (V.8), since the background shear is negative, a positive value of $\partial\rho/\partial x$ causes a positive change to the background negative vertical density gradient. Therefore, the local magnitude of stable stratification is reduced and local shear instability is allowed. Figure V.24(b) shows the convection of the wave crest in part (a) by the jet velocity. The wave distortion, now at $x \approx 17\delta_{\omega,0}$, intensifies and is surrounded by steep features in the isopycnals. The wave crest is completely digested by strong small-scale fluctuations in figure V.24(c) confirming that the nonlinear breakdown of wave energy contributes to the observed dissipation.

It is useful to compare the mixing efficiency between the turbulent patches in the jet and the ones in the shear layer. One way to quantify the mixing efficiency is with the quantity Γ defined as

$$\Gamma\,(t) = \frac{-\int_V B\,dz}{\int_V \varepsilon\,dz},$$

where V is the region of interest. Figure V.25 (a) shows the evolution of Γ over the time period during which the turbulent patches in the jet are active. The solid line represents the value of Γ computed by integration over the shear layer with V from $z = -2.5\delta_{\omega,0}$

to z_{max}, while the dashed line corresponds to integration over the jet upper-flank, $-6.5 < z < -2.5\delta_{\omega,0}$. In many oceanic application, Γ is typically taken to be the constant value of 0.2 (Smyth *et al.*, 1996). In our simulation, Γ is close to this value only in turbulent shear layer. In the jet turbulence, Γ exhibits substantial fluctuations owing to the occasional penetration of the 'hot pockets' and is substantially larger than the value of 0.2 during $150 < t < 165$. Later in time, after turbulence develops and the dissipation rate increases, Γ becomes closer to 0.2. Another measure of mixing efficiency is the quantity $\Gamma_d(z,t) = \varepsilon/\varepsilon_\rho$ where

$$\epsilon_\rho(z,t) = \frac{1}{PrRe_0}\frac{g}{\rho_0|d\bar{\rho}/dz|}\overline{\frac{\partial\rho'}{\partial x_k}\frac{\partial\rho'}{\partial x_k}}.$$

Here, ε_ρ denotes the irreversible loss of available turbulent potential energy to the background density. The evolution of Γ_d is shown in figure V.25(b) in which the solid and dashed lines indicate the values at $z = 0$ and $z = -4\delta_{\omega,0}$, respectively. Γ_d in the shear layer, $z = 0$, has a value of approximately 0.6 during the time period $150 < t < 180$. This value is also observed by Smyth *et al.* (2001) who characterize mixing efficiency in turbulence patches formed by the breakdown of KH billows. Γ_d in the turbulent patches in the jet has a smaller value, about 0.4, over the same time period.

V.E Implications

We have investigated the interaction between an unstable shear layer and a stably stratified ($Ri_g > 0.25$) jet in two situations: a far jet where the distance between the jet and shear layer is large and a near jet where the distance is small relative to the shear layer thickness. Our focus is on the internal wave field and turbulence that ensues in the jet.

In the far case, internal waves with distinct phase lines are excited by KH rollers and broadband turbulence. The KH-excited waves follow linear wave theory so that the propagation angle observed in the simulations can be analytically predicted. These waves cannot penetrate the jet and are reflected because the squared vertical wavenum-

ber m^2 in the Taylor-Goldstein (TG) equation is negative in the jet. There is a buildup of fluctuation kinetic energy in the region between the shear layer and jet owing to the pressure transport or, equivalently, the internal wave flux. However there is little turbulence in this region and, consequently, the turbulent dissipation rate is small, three orders of magnitude below that in the shear layer.

In the near jet, internal waves are also observed but their excitation is not by KH rollers since the associated value of m^2 in the jet region adjacent to the shear layer is negative. Instead, as the KH rollers interact non-linearly and pair, internal waves with smaller wavenumber are excited and found to penetrate the jet since the corresponding $m^2 > 0$. These waves are found to follow linear wave theory as well. There is a region of $m^2 < 0$ in the lower flank of the jet, but the internal waves are able to tunnel through and propagate below the jet. 'Hot pockets' of fluid from the upper shear layer are entrained into the stably stratified jet. The pockets initiate turbulence and disrupt the wave field in the upper-flank of the jet. Coherent patches of small-scale turbulence in the stable jet that are convected by the local mean flow are observed. The dissipation in these patches is comparable to the value observed in the turbulent shear layer and up to three orders of magnitude larger than in the propagating wave field in the far jet case.

The fluctuation field in the stratified near jet consists initially of internal waves. There is a number of changes in the fluctuation field that occur later, immediately after the penetration of hot pockets, that signify turbulence: the spectrum of vertical velocity, w, and the co-spectrum of uw change from narrow-band with a discrete peak to broadband; the shear production of TKE and the dissipation rate increase sharply; the TKE transport is dominated by turbulent transport instead of the pressure transport (internal wave flux). The local gradient Richard Richardson number based on the local buoyancy frequency and shear becomes sub-critical, less than 0.25, showing the potential for shear instability. The terms contributing to the TKE integrated over the upper flank of the stratified jet are evaluated as a function of time. Most of the TKE accumulation in the jet is due to production by the interaction of jet shear with both internal waves and turbulence and not due to the transport term in the TKE equation.

Furthermore, the contribution of the wave momentum flux to the shear production of TKE is small (17 % of the net shear production) relative to that by turbulence. The counter-gradient heat flux is a source of TKE locally; however, overall, the buoyancy flux is an energy sink.

For the conditions of the model problem, we are able to answer the questions with which the introduction section ended. (1) Internal waves excited by an unstable shear layer propagate into a stable jet when the jet is near, not when it is far. The presence/absence of internal waves can be predicted by the sign of m^2 in the Taylor-Goldstein equation. (2) In the near jet, there are patches of significant dissipation with magnitude larger than in the unstable shear layer although the jet is linearly stable. (3) The turbulence in the jet is not primarily due to breakdown of the internal wave field.

The simulations suggest that the turbulence observed in our model jet is mainly contributed from local generation of TKE in the jet upper-flank where the background shear is marginally stable. Nonetheless, the role of internal waves should not be overlooked in the EUC. In our study, the waves excited by the pairing of the KH-rollers in the *near* jet are significantly weaker than the waves directly excited by the KH-rollers in the *far* jet. The observation of Hebert *et al.* (1992) show large-amplitude internal waves. With a modest variation in either background shear or stratification, the m^2 profile can be changed such that the jet can support KH-excited waves. Forcing by wind and diurnal heat flux can also force instabilities and energetic waves. Thus, there are situations where the internal wave energy flux can contribute more to the 'deep-cycle turbulence' than in the model jet considered here. A parametric study with systematic variation of background conditions and forcing is necessary to further decipher the complex dynamics of fine-scale fluctuations in the EUC system.

The contents of this chapter have been published in the Journal of Fluid Mechanics: Pham, H. T., and Sarkar, S., "Turbulence and internal waves in a stable stratified jet", J. Fluid Mech.*, **648**, 297-323 (2010). The dissertation author is the primary researcher and the research supervisor is the co-author of the paper.*

Chapter VI

Mixing events in a stratified jet subject to surface wind and buoyancy forcing

VI.A Objectives

Many environmental flows have jet-like velocity profiles such as the Equatorial Undercurrents (EUCs) and the Equatorial deep jets in the ocean, and the tropospheric jet in the atmosphere. These jets occur in a background with nonuniform continuous stratification. Observations (Gregg *et al.*, 1985; Moum *et al.*, 1992; Lien *et al.*, 1996), linear stability analysis (Sun *et al.*, 1998), two-dimensional simulations (Skyllingstad & Denbo, 1994; Sutherland, 2006; Smyth & Moum, 2002), and three-dimensional Large Eddy Simulations (Wang *et al.*, 1998; Wang & Muller, 2002) have been utilized to study aspects of these flows. However, there are only a handful of studies using three-dimensional (3D) Direct Numerical Simulation (DNS) (Tse *et al.*, 2003; Pham & Sarkar, 2010) in which all scales of motion are resolved. In the current study, 3D-DNS will be utilized to investigate the fine-scale response of a stratified jet subject to surface wind stress and buoyancy forcing.

The EUCs, jet-like eastward flows below westward surface currents, play an impor-

tant role in the balance of the equatorial heat budget. It is believed that variability in the EUCs can affect the surface temperature, modulate air/sea coupling, and thereby affect weather patterns (Philander, 1980). Therefore, it is important to understand and ultimately quantify the fine-scale processes in the EUCs. Observations in the Pacific EUC have shown nightly occurrences of intermittent highly-dissipative turbulence patches along with narrow-band high-frequency oscillations in the EUC upper-flank where the background gradient Richardson number is larger than the critical value of 0.25 for linear shear instability. However, the mechanism responsible for these dissipative patches remains unclear. One possible explanation is that, at night, the deepening of the surface layer allows formation of a shear-unstable region. Another possible explanation is that the high-frequency oscillations are gravity waves which overturn in the high shear region of the jet. Hebert *et al.* (1992) has recorded an overturning of a wave packet; nonetheless, in a recent study Smyth *et al.* (2010) apply linear stability analysis to the observed mean background velocity and density to infer that the oscillations could result from instabilities that are unrelated to gravity waves. In our previous work (Pham & Sarkar, 2010), we find that Kelvin-Helmholtz instabilities associated with an unstable shear region above a stable stratified jet lead to both internal waves and patches of turbulent dissipation. The patches are associated with horseshoe vortices originating from the unstable shear layer and not breaking internal waves.

A number of studies using 2D simulations have been used to investigate dynamical processes inside the EUC jets. The first 2D simulation performed by Skyllingstad & Denbo (1994) using field-observed velocity and density profiles, surface wind-stress and heat flux showed the presence of internal waves propagating downward and upstream. The waves are suggested to be related to Kelvin-Helmholtz instability; however, no patches of dissipation are observed and wave breaking is not discussed. Smyth & Moum (2002) perform simulations of a Bickley jet which has stratification in the upper flank weaker than that in the lower flank. With the low stratification, the shear instability in the upper flank is allowed resulting in formation of vortex structures. Internal waves are observed to propagate from the upper flank to the lower flank where they break after encountering a critical layer. Although not specifically targeting the EUCs,

the simulations of Sutherland (2006) also show that internal waves can be generated when a portion of a jet is linearly unstable such that vortex structures are formed. Nonetheless, the formation of vortex structures with vertical extent as large as the jet thickness in those simulations is not applicable to the observation of turbulence limited to the upper flank of the EUCs. Discussion of turbulence inside the jet is absent in the aforementioned 2D studies.

A 3D-DNS motivated by turbulence in the tropospheric jet was carried out by Tse *et al.* (2003). The jet is weakly stratified and the background shear is maintained by forcing. Turbulence is observed in the core of the jet while nonlinear waves are observed at the edges of the jet. In a subsequent study where numerical viscosity is used, Mahalov *et al.* (2007) finds propagating waves in the region above the jet when the stratification there is increased. Since Tse *et al.* (2003) and Mahalov *et al.* (2007) did not intend to study the EUCs, the background conditions of the simulations are different and the simulated turbulence in the jet deviates from EUC observations. Pham & Sarkar (2010) perform 3D-DNS to investigate a linearly-stable stratified jet adjacent to a linearly-unstable shear layer. The shear layer is subject to Kelvin-Helmholtz shear instability. Internal waves are observed to propagate upstream and downward from the the shear layer across the jet toward the region below. Intermittent highly-dissipative patches of turbulence are observed in the jet upper-flank where the gradient Richardson number is larger than 0.25. The turbulence patches are found to correlate to horseshoe-like vortex structures formed inside the Kelvin-Helmholtz rollers that extend downward deep inside the jet.

All the studies targeting the EUCs mentioned above have been helpful to decipher the small-scale dynamical process in the EUCs and related stratified shear flows but at the same time important questions remain unanswered. For example, (1) previous studies have shown that internal waves are strongly related to large-scale vortex structures that result from shear instability in a small region of the jet. Can internal waves be found inside the jet in the absence of such large-scale vortex structures ? (2) Pham & Sarkar (2010) have indicated that the turbulence inside the jet is driven by the formation of horseshoe vortices which originate from a spanwise instability of

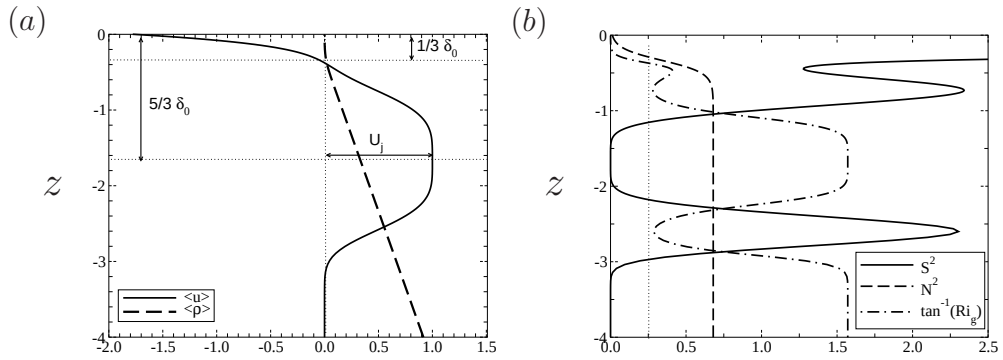

Figure VI.1: (a) *Initial* mean profiles. The velocity profile consists of a stratified jet below a wind-driven mixed layer. The jet center is at depth z = -5/3 δ_0. (b) *Initial* squared shear profile S^2, squared buoyancy frequency profile N^2 normalized by U_j^2/δ_0^2, and gradient Richardson number profile Ri_g. The vertical dotted line indicates the critical value $Ri_g = 0.25$ for shear instability. Thus, only the thin surface region, $-0.33 < z < 0$, has linearly unstable shear.

Kelvin-Helmholtz rollers. Can similar vortex structures be formed in the absence of the large-scale Kelvin-Helmholtz rollers ? (3) Except in Skyllingstad & Denbo (1994), most studies have assumed some form of shear instability inside the jet neglecting the turbulent mixed layer. What role does surface forcing of the mixed layer play relative to shear instability inside the jet ? In the current study, we will address these issues by using 3D-DNS to investigate the interaction of a surface layer driven by a constant wind stress and surface cooling with a linearly-stable stratified jet.

VI.B Problem Formulation

Consider a subsurface jet with peak velocity U_j and thickness δ_0 centered at $z = -5/3\delta_0$:

$$\langle u_j \rangle (z) = U_j exp \left[- \left(\frac{z + 5/3\delta_0}{\delta_0} \right)^4 \right],$$

where the brackets $\langle \cdot \rangle$ indicates horizontal x-y average. A free surface shear layer of thickness $\delta_m = \delta_0/3$ driven by a constant wind stress of $\tau_w = -6.67 \times 10^{-4}\, \rho_0 U_j^2$ with

the following profile:

$$\langle u_w \rangle (z) = -1.76 U_j \left\{ \left(1 + 2 \left(\frac{z}{\delta_m} \right)^2 \right) erfc \left(\frac{z}{\delta_m} \right) - \frac{2}{\pi} \frac{z}{\delta_m} exp \left[- \left(\frac{z}{\delta_m} \right)^2 \right] \right\} ,$$

is added to the jet velocity. Here, ρ_0 is a reference density. The negative sign of the wind stress indicates that the wind blows opposite to the jet. The exerted wind stress corresponds to the frictional velocity $u_\tau = \sqrt{(\tau_w/\rho_0)} = 0.026 U_j$. The complete initial velocity profile $\langle u \rangle = \langle u_j \rangle + \langle u_w \rangle$ is shown in figure VI.1(a).

The vertical density profile consists of a well-mixed surface layer that transitions to a linearly stratified jet region and the region below. The corresponding non-dimensional stratification profile, $J(z) = N^2 \delta_0^2 / U_j^2$, is given by

$$J(z) = \frac{J_j}{2} - \frac{J_j}{2} tanh \left(\frac{z + \delta_m}{0.5 \delta_m} \right) ,$$

where $N^2 = -g/\rho_0 d \langle \rho \rangle / dz$ is the squared buoyancy frequency, g is gravity, J_j is a measure of stratification in the jet layer that is set to 0.68. The initial mean profiles of S^2, J and Ri_g are shown in figure VI.1(b). $Ri_g < 0.25$ only in a thin surface region $-0.33 < z < 0$ and $Ri_g > 0.25$ everywhere in the jet and the region below. A constant surface cooling of $Q_s = 3.87 \times 10^{-5} U_j^3 / \delta_0$ is imposed at $z = 0$.

Using δ_0, U_j and $\delta_0 d \langle \rho \rangle / dz|_{-\infty}$ as the characteristic length, velocity and density, the non-dimensional, non-hydrostatic governing equations with the Boussinesq approximation are:

$$\frac{\partial u_k}{\partial x_k} = 0 , \tag{VI.1}$$

$$\frac{\partial u_i}{\partial t} + \frac{\partial (u_k u_i)}{\partial x_k} = - \frac{\partial p}{\partial x_i} + \frac{1}{Re} \frac{\partial^2 u_i}{\partial x_k \partial x_k} - J_j \rho' \delta_{i3} , \tag{VI.2}$$

$$\frac{\partial \rho}{\partial t} + \frac{\partial (u_k \rho)}{\partial x_k} = \frac{1}{Re\, Pr} \frac{\partial^2 \rho}{\partial x_k \partial x_k}, \tag{VI.3}$$

The non-dimensional parameters are Reynolds number $Re = U_j \delta_0 / \nu$ and Prandtl number $Pr = \nu / \kappa$. It should be noted that p is the dynamic pressure and ρ does not include the reference density ρ_0 as shown in figure VI.1. Hereafter, all parameters are discussed in non-dimensional units. In the current study, $Re = 18,000$ while $Pr = 1$. The Reynolds number, $Re_\tau = u_\tau \delta_m / \nu$, based on the wind stress is 156. Table VI.1

compares the imposed parameters to those observed in the fields. Although the shape of the velocity and the stratification profiles are similar resulting in similar values of Ri_g, the jet Reynolds numbers and non-dimensional heat flux are significantly smaller in the DNS.

The initial velocity perturbations have a broadband spectrum given by

$$E\left(k\right) \propto \left(\frac{k}{k_0}\right)^4 exp\left[-2\left(\frac{k}{k_0}\right)^2\right],$$

where wavenumber k_0 is set such that the spectrum peaks at $5.1\delta_0$. The fluctuations introduced only in the surface layer have $r.m.s$ values that peak at the surface at (u', v', w') of 7% U_j and rapidly decrease with depth.

Periodic boundary conditions are used in the streamwise (x) and spanwise (y) directions. Boundary conditions in the vertical direction (z) are set as follows:

$$\begin{aligned}
\frac{\partial u}{\partial z}\left(z=0\right) = Re\tau_w\,, \quad u\left(z_{min}\right) &= 0\,,\\
\frac{\partial v}{\partial z}\left(z=0\right) = \frac{\partial v}{\partial z}\left(z_{min}\right) &= 0\,,\\
\frac{\partial p}{\partial z}\left(z=0\right) = \frac{\partial p}{\partial z}\left(z_{min}\right) &= 0\,,\\
w\left(z=0\right) = w\left(z_{min}\right) &= 0\,,\\
J\left(z=0\right) &= RePrQ_s\,,\\
J\left(z_{min}\right) &= J_j\,.
\end{aligned}$$

The domain size is $8/3\pi$ x $2/3\pi$ x 10 and the grid has 768 x 256 x 320 points. The grid is uniform in the horizontal with spacing of 0.011 in the x-direction and 0.008 in the y-direction. The vertical grid size is stretched from a value of 0.002 at the surface to a value of 0.011 at depth $z = -0.33$. In the region $-1.5 < z < -0.33$ the grid is uniform with spacing of 0.011. Below this region, the grid is mildly stretched at 3%. Corresponding to the wall unit $\delta^+ = \nu/u^* = 0.0022$, the grid spacing is $5.5\delta^+$ and $4\delta^+$ in the x- and y-direction, respectively. The minimum vertical grid spacing is $1\delta^+$ at the surface and $5.5\delta^+$ in the jet upper-flank.

A second-order finite difference method on a staggered grid is used for spatial derivatives and a third-order low storage Runga-Kutta method is used for time advancement except for the viscous term which is advanced by a Crank-Nicolson scheme.

A sponge region is employed at the bottom boundary ($z < -8.6$) to eliminate spurious wave reflections. The velocities and density in this sponge region are relaxed by adding to the right-hand-side of Eqs. (VI.2) and ($VI.3$) a term of the form

$$\begin{aligned} - \quad & \phi(z)\left[u_i(x_i,t) - \langle u\rangle_i(z,t=0)\right], \\ - \quad & \phi(z)\left[\rho(x_i,t) - \langle\rho\rangle(z,t=0)\right]. \end{aligned}$$

The damping function, $\phi(z)$, increases quadratically from $\phi = 0$ to 1.0. Further details of the numerical method can be found in Basak & Sarkar (2006) and Brucker & Sarkar (2007).

In subsequent sections, the evolution equation for turbulent kinetic energy is used extensively for discussion; therefore, it is convenient to introduce the notation here. The equation is:

$$\frac{dK}{dt} = P - \varepsilon + B - \frac{\partial T_3}{\partial z}. \tag{VI.4}$$

Here, K is the turbulent kinetic energy defined as $K = 1/2\,\langle u_i' u_i'\rangle$. The prime indicates deviation from the horizontally averaged quantity as in $u_i' = u - \langle u\rangle$. P is the production rate, defined as

$$P \equiv -\left\langle u_i' u_j'\right\rangle \frac{\partial\langle u_i\rangle}{\partial x_j} = -\langle u'w'\rangle \frac{d\langle u\rangle}{dz},$$

ε is the dissipation rate, defined as

$$\varepsilon \equiv \frac{2}{Re}\left\langle s_{ij}' s_{ij}'\right\rangle \text{ where } s_{ij}' = \frac{1}{2}\left(\frac{\partial u_i'}{\partial x_j} + \frac{\partial u_j'}{\partial x_i}\right),$$

B is the buoyancy flux, defined as

$$B \equiv -J_j\langle\rho'w'\rangle,$$

$\partial T_3/\partial z$ is the transport of tke, defined as

$$T_3 = T_t + T_p + T_v, \tag{VI.5}$$

where the turbulent transport T_t is defined as

$$T_t = \frac{1}{2}\left[\langle w'u'u'\rangle + \langle w'v'v'\rangle + \langle w'w'w'\rangle\right],$$

Table VI.1: Comparison of parameters between simulations and observations. Observational data in the first column is taken from Moum *et al.* (1992) in which the jet center velocity is U_j, the jet thickness is δ_0 and mixed layer depth is δ_m. Values of N^2, S^2, and Ri_g are measured at depth $z = 28\,m$ in the observational data while they are computed at $z = -0.5$ in the current study.

Parameters	Observation	Current study
U_j	$1\,m\,s^{-1}$	1
δ_0	$80\,m$	1
δ_m	$20\,m$	0.33
N^2	$1.3 \times 10^{-4}\,s^{-2}$	0.6
S^2	$4.2 \times 10^{-4}\,s^{-2}$	1.4
Ri_g	0.31	0.43
τ_w	$-0.02\,N\,m^{-2}$	-6.7×10^{-4}
u_τ	$0.0045\,m\,s^{-1}$	0.026
Q_s	$6.4 \times 10^{-8}\,W\,kg^{-1}$	3.9×10^{-5}
Pr	7	1
Re	8×10^7	1.8×10^4
Re_τ	8.9×10^4	156
$Q_s\delta_m/u_\tau^3$	14.0	0.75

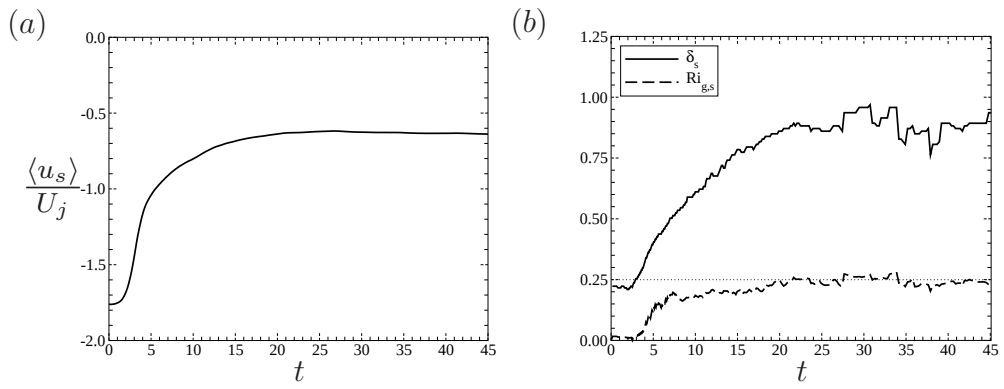

Figure VI.2: Time evolution of (a) surface velocity $\langle u_s \rangle$ at $z = 0$, and (b) stirring depth δ_s and the corresponding $Ri_{g,s}$. The dotted lines indicate the critical value of $Ri_g = 0.25$

the pressure transport T_p is defined as

$$T_p = \frac{\langle p'w' \rangle}{\rho_0},$$

and the viscous transport T_v is

$$T_v = -\frac{2}{Re} \left[\langle u's'_{31} \rangle + \langle v's'_{32} \rangle + \langle w's'_{33} \rangle \right].$$

VI.C Evolution of the mean flow

As the wind stress and the buoyancy flux are applied at the surface, the mixed layer deepens and turbulence penetrates the jet. Significant changes in profiles of the mean quantities such as velocity and density are observed and discussed in this section. Although the wind exerts a constant momentum flux at the surface at $z = 0$, the surface velocity $\langle u_s \rangle$ rapidly decreases owing to mixing of momentum as shown in figure VI.2(a). From the beginning of the simulation to $t = 20$, $\langle u_s \rangle$ decelerates by more than 50%. The decrease in $\langle u \rangle$ is similar to the results of Tsai *et al.* (2005). It will be demonstrated later that the rapid initial deceleration is due to the drag caused by the extraction of Reynolds turbulent stress from the mean shear provided in the initial velocity profile $\langle u \rangle$ in the surface layer. Figure VI.2(b) shows the deepening of the surface mixed layer as the simulation progresses. In this figure, δ_s is the stirring depth measured by the distance between $z = 0$ and the stirring boundary defined by the

location at which the maximum $r.m.s$ value of the density fluctuation ρ' is recorded. The initial stirring boundary is located at $z = -0.22$ at the transition between the surface mixed layer and the linearly stratified region below. The simulation is initialized with velocity fluctuations peaking at the surface and decaying with depth. However, stronger velocity fluctuations near the surface do not stir the density field because the background condition is well-mixed. Rather, the peak density fluctuation is observed in the transition region where the density stratification is present despite the weaker velocity fluctuations relative to the region above. After the initial adjustment period $0 < t < 2$, δ_s increases approximately from 0.22 to $0.9\delta_0$ at $t = 20$ and then fluctuates about this value after that. The increase in δ_s signifies the deepening of the turbulence-active mixed layer into the quiescent linearly stratified jet region. The increase of δ_s up to $0.9\delta_0$ also indicates that the turbulence is active in most of the jet upper-flank ($-1.67 < z < 0$) for $0 < t < 20$. After $t = 20$, stirring, weaker with respect to earlier, continues to occur at the location $z = -\delta_s$ but the turbulence in the region above this location decays except in the thin surface region driven by the wind stress and the surface heat flux. As discussed in a later section, the turbulence generated by the surface forcing is relatively weak compared to that extracted from the mean background velocity. Figure VI.2(b) also shows the values of the gradient Richardson number $Ri_{g,s}$ measured at the stirring boundary $z = -\delta_s$. As δ_s increases, $Ri_{g,s}$ also increases. At $t = 20$ when δ_s ceases to increase, $Ri_{g,s}$ asymptotes at the critical value of 0.25. This suggests that no further stirring can be achieved when the gradient Richardson number exceeds the critical value, which agrees with the prediction of linear stability theory of parallel shear flows.

The profiles of the mean streamwise velocity $\langle u \rangle$ and mean shear S in the surface layer and the jet upper-flank at different times are shown in figures VI.3(a,b), respectively. The surface velocity at $z = 0$ decreases initially as discussed above. As the surface layer deepens, the wind stress exerts drag on the layer causing the region with negative velocity to widen. The positive velocity in the upper-flank of the jet also decreases in time indicating significant amount of momentum is lost from the mean flow. The momentum lost is observed in the jet region as deep as $z = -1.1\delta_0$ where

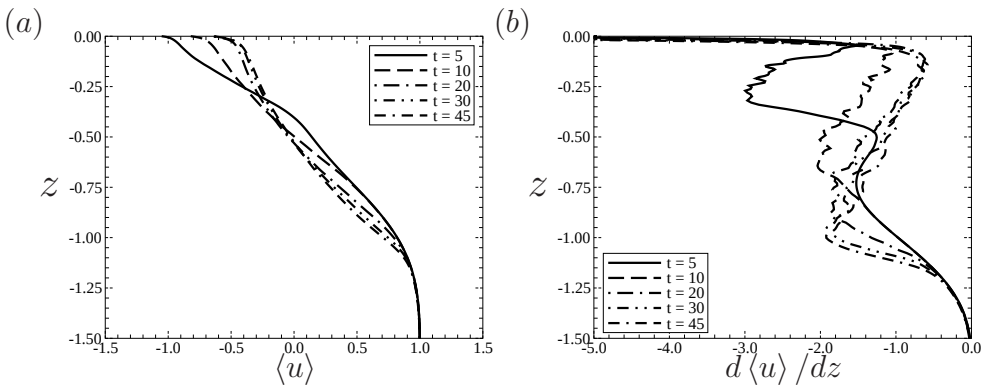

Figure VI.3: Vertical mean profiles at various time: (a) streamwise velocity $\langle u \rangle$, (b) shear rate $d\langle u \rangle / dz$.

there is insignificant background shear. The profiles of shear S in figure VI.3(b) show significant variations in time except in the thin viscous layer, $-0.1 < z < 0$, at the surface. The initial shear in the surface layer, $-0.33 < z < 0$, is reduced rapidly. From t = 5 to t = 10, the magnitude of S is reduced by nearly half and continues to decrease after that. In contrast, the shear in the region, $-1.2 < z < -0.75$, of the jet upper-flank increases in time although the velocity in this region is reduced as shown in figure VI.3(a). From t = 5 to 45 the magnitude of S approximately doubles at depth $z = -1$. The S profile at t = 5 consists of two distinct regions of strong shear in addition to the surface shear that are denoted by two local maxima in the profile: one with relatively larger magnitude of S at z = -0.25 in the surface layer and one at z = -0.75 in the jet upper-flank. At the end of the simulation at t = 45, the former region disappears while the latter persists with stronger magnitude. The dynamic transformation of the mean velocity and mean shear suggests that the mean background condition has an important role in the momentum and the energy budgets of the flow.

The evolution of the mean density $\langle \rho \rangle$ and the squared buoyancy frequency N^2 are shown in figures VI.4(a,b), respectively. Except in the thin region near the surface where the density profile is gravitationally unstable due to the positive surface buoyancy flux, the profiles at all time show that the mean density increases with depth. Over time, the surface layer gets heavier and the jet upper-flank gets lighter. The stirring of the background density, although co-gradient with the molecular diffusion, is active since the corresponding background shear changes significantly. Neglecting

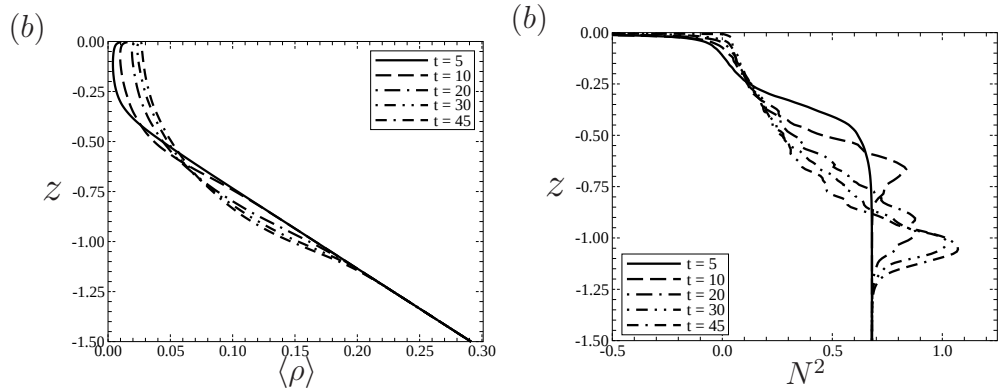

Figure VI.4: Vertical mean profiles at various time: (a) density $\langle\rho\rangle$ and (b) squared buoyancy frequency N^2.

the molecular diffusion effects, the surface layer get heavier due to two sources: the surface flux injects heavier fluid downward and from the jet where heavier fluid is lifted upward. The time variation of shear profiles suggest that the latter dynamical process is related to shear instability. The profiles of N^2 in figure VI.4(b) indicate that the effect of the surface flux is limited to a region as thin as $0.1\delta_0$ near the surface. It should be noted that, by definition, a negative N^2 corresponds to a positive unstable density gradient. The variation among the N^2 profiles is more significant in the region below the surface layer than at the surface. In the surface layer, $-0.33 < z < 0$, the stratification increases in time suggesting that the initial mixed state cannot be maintained despite the surface forcing. In other words, re-stratification inside the surface layer, even at early time, implies that uplifting of heavier fluid from the jet upper-flank is more important than the downward injection of the positive buoyancy flux at the surface. As the surface layer deepens, the fluid in the region below is stirred resulting in a significant decrease in stratification. For example, from t = 5 to 45, the stratification at z = -0.5 is reduced by a factor of approximately six. Below the stirring region, N^2 increases sharply to values larger than the ambient value J_j before dropping down toward J_j similar to the observations of the ocean pycnocline capping the surface mixed layer. The overshooting value of N^2 at z = -1 and t = 45 can be more than 50% larger than J_j. The formation of a pycnocline adjacent to a region of active stirring has been observed in other studies such as mixing in a turbulent boundary layer (Taylor

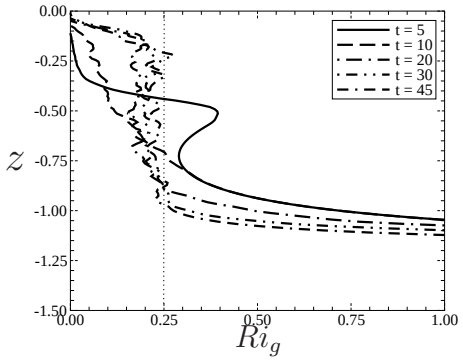

Figure VI.5: Vertical profiles of the vertical gradient Richardson number Ri_g at various time.

& Sarkar, 2008; Gayen *et al.*, 2010) and mixing via shear instability (Sutherland & Linden, 1998; Pham *et al.*, 2009).

It is remarkable that, despite significant variations in the shear and squared buoyancy profiles both in time and in space, the values of the gradient Richardson profiles Ri_g after $t = 5$ tend to converge toward the critical value 0.25 in the region where stirring occurs as shown in figure VI.5. The Ri_g profile at $t = 5$ shows that the region with $Ri_g < 0.25$ extends from the surface down to $z = -0.4$. The local minimum at $z = -0.75$ results from the maximum in the jet shear at that location as shown in figure VI.3(b). Stirring causes the entire surface layer and part of the jet upper-flank to become linearly unstable, i.e. $Ri_g < 0.25$ as observed at t = 20. The t = 20 profile indicates three distinct regions: the thin viscous region, $-0.1 < z < 0$, in which Ri_g increases monotonically from the surface value, the stirring region, $-0.9 < z < -0.1$, in which Ri_g is maintained in a narrow band, $0.175 < Ri_g < 0.25$, of near-critical values and the quiescent region, $z < -0.9$, where Ri_g becomes larger than 0.25 and sharply increases toward infinity (due to zero shear at the center of the jet). At t = 30 and 45, the stirring region deepens and the Ri_g values in this region moves closer to the critical value of $Ri_g = 0.25$ as stirring subsides. Recall the shear and squared buoyancy frequency profiles in figure VI.3(b) and VI.4(b), respectively. Locally, i.e. at different depths, the shear S can increase or decrease in time; nonetheless, mixing alters the squared buoyancy frequency accordingly such that Ri_g converges toward the critical value. The convergence of Ri_g toward the critical value along with the even-

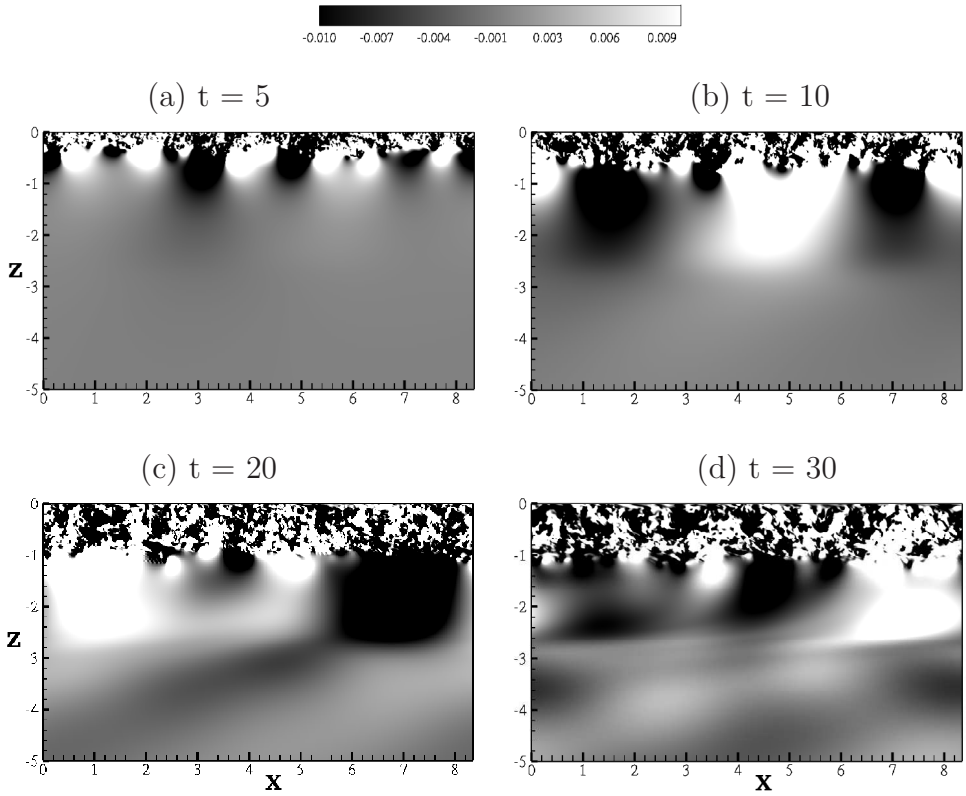

Figure VI.6: Internal wave fields are shown with the vertical fluctuating velocity field w' in the x-z plane at $y = 1.1$.

tual decay of stirring suggests the core dynamical process in the current study is shear instability according to linear stability theory. The convergence to $Ri_g \approx 0.25$ after $t = 20$ substantiates the typical use of $Ri_g > 0.25$ as a cutoff for turbulent mixing in many environmental models. However, the significant mixing between $t = 5$ and $t = 10$ would be missed by such a simple mixing model.

VI.D Internal Waves

In the previous section, we have shown that mean background conditions have changed throughout the simulation indicating significant transfer between mean and fluctuating fields. In the current investigation, the fluctuating quantities can signify the presence of either internal gravity waves or turbulence or both. In this section, we present observations of the internal waves field, excited by the wind-driven surface

layer, that propagates across the region with background jet shear.

Figure VI.6(a-d) show snapshots of the instantaneous fluctuating vertical velocity fields w' in the x-z plane at $y = 1.1$ at various times. In all figures, two distinct regions are observed: the turbulence region above and the wave region below. The region with turbulence shows small-scale fluctuations corresponding to high wavenumber while the wave region exhibits more coherent fluctuations which are at significantly larger wavelength. The wave regions have alternate black and white lobes in the horizontal direction corresponding to the negative wave troughs and the positive wave crests. As the simulation progresses, the turbulence layer penetrates to greater depth. The internal wave region changes noticeably in time. The wave field in figure VI.6(a) has smaller wavelength than those in other figures. The waves in figures VI.6(b-d) extend across the jet with the phase lines oriented in the vertical direction. Recall that the jet spans the region $-3 < z < -0.33$; the wave field in the region below the jet has phase lines that tilt upstream as shown in figures VI.6(b,d). The change in the propagating direction of the wave phase lines is due to the change in the background shear. Similar to observations in the study of Pham & Sarkar (2010) in which the vertical wavenumber m of the internal waves is governed by the Taylor-Goldstein equation, m is dependent on the horizontal wavenumber k, the background shear S and stratification N^2. In the region below $z = -1.25$ where N^2 is constant but the jet shear S varies with depth, the vertical wavenumber m also varies with depth resulting in the change in the wave phase lines.

In a previous study, Pham *et al.* (2009) reported that the internal waves excited by Kelvin-Helmholtz rollers have wavelength equal to that of the rollers. Pham & Sarkar (2010) further showed that, in the presence of a stratified jet with EUC-type shear and stratification, the rollers cannot excite internal waves since the background shear and stratification do not allow propagating waves with positive values of m. Nevertheless, internal waves with larger horizontal wavelength were observed inside and below the jet because the smaller wavenumber k has positive m such that waves propagate. In both studies, the excited waves were found to be closely related to the coherent structures in the unstable shear layer. The waves were nearly two-dimensional

(a) t = 5

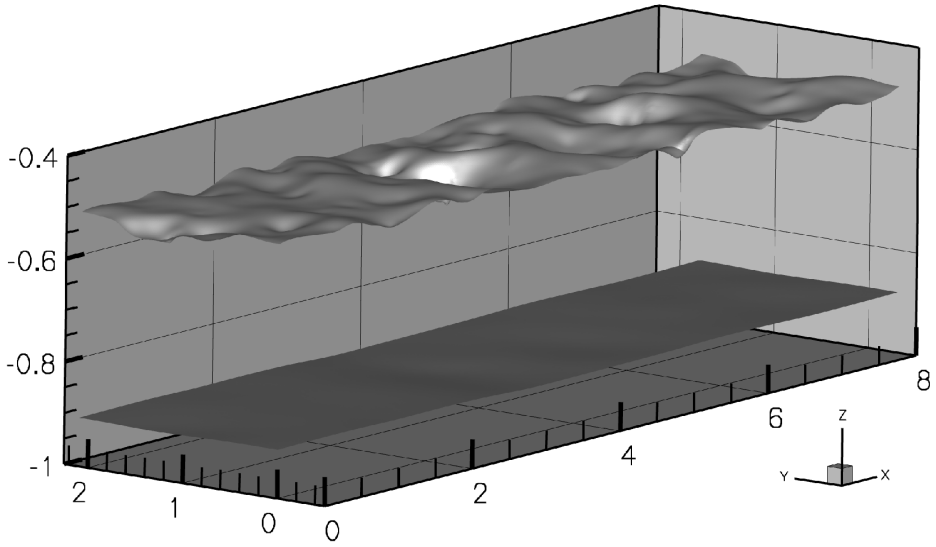

(b) t = 10

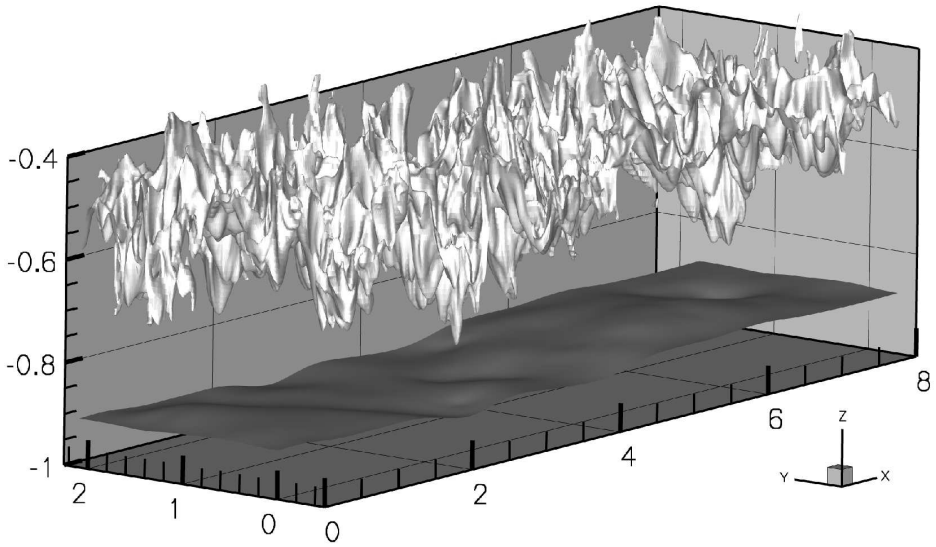

Figure VI.7: Internal waves are shown with 3D isocontours in the density field at (a) $t = 5$ and (b) $t = 10$. The lighter isosurface denotes $\rho = 0.048$ while the darker denotes $\rho = 0.144$.

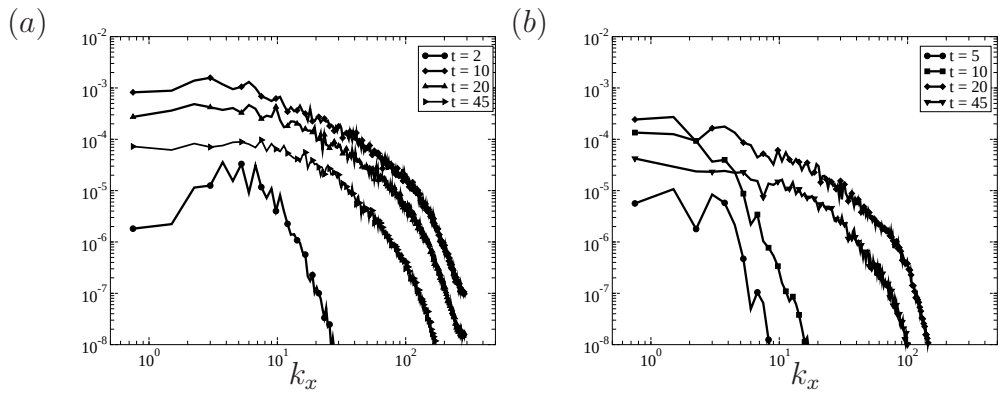

Figure VI.8: Horizontally-averaged k_x spectra of the vertical fluctuating velocity field w' at various time: (a) at $z = -0.33$ and (b) at $z = -1$.

and could be described by linear wave theory. In the current study, while there is a stratified jet as was in Pham & Sarkar (2010), the coherent rollers are absent and replaced by broadband turbulence in the upper mixed layer. Nonetheless, the wave excitation mechanism has similarities. Although the turbulence in the surface layer is broadband, there exist fluctuations at low wavenumber k which in combination with appropriate background conditions results in positive m for propagating internal waves. Figure VI.7(a) shows the internal waves through the density isocontour surfaces of $\rho = 0.048$ and 0.144 at t = 5. Unlike in previous studies where the internal waves are two-dimensional, i.e. x-z plane waves, the wave field shown in the isocontour of $\rho = 0.048$ at $t = 5$ is highly three dimensional with distinct crater-like structures rather than lines of wave crests and troughs. The three-dimensional features of the wave field suggest that these waves are correlated with the low wavenumber fluctuation of the broadband turbulence in the region above. The isocontour of $\rho = 0.144$ shows no wave signature at early time. Figure VI.7(b) shows the same isocontours but at later time when the waves propagate toward greater depth. The waves shown in the isocontours of $\rho = 0.144$ have larger wavelength and smaller amplitude with less three-dimensional structures than those in the isocontour of $\rho = 0.048$ in figure VI.7(a). At t = 10, the isocontour of $\rho = 0.048$ shows the distinct features of turbulence especially in terms of larger amplitude and broader wavenumber spectrum than in the waves observed at $t = 5$.

The horizontally-averaged k_x spectra at z = -0.33 and -1 at various time are shown in figures VI.8(a,b), respectively. In figure VI.8(a), the spectrum at t = 2 is narrow-band at low wavenumber and sharply drops off at wavenumber $k_x > 10$. At t = 10, the spectrum becomes broadband with a energy containing range, inertial subrange and dissipation range indicative of turbulence. The difference in amplitude between the energy containing range and the dissipation range is 4 orders in magnitude. The peak magnitude in the spectrum at t = 2 is small suggesting that the internal waves present at this time are significantly weaker than the low-wavenumber fluctuations present during later time when there is broadband turbulence . Figure VI.8(b) shows similar evolution of the spectra at depth z = -1 inside the jet upper-flank. The narrow-band spectra at t = 5 and 10 are indicative of internal waves arriving from the surface layer above. At later time t = 20 and 45 the spectra become broadband and the turbulence is relatively weaker than that observed at similar time at z = -0.33.

While figure VI.8 shows that the peaks in the internal wave spectra are relatively smaller than those of the turbulence spectra, figures VI.9(a-f) further compare the magnitudes of the wave fluctuations with that of the turbulence fluctuations in terms of the $r.m.s$ values of streamwise velocity u', spanwise velocity v', vertical velocity w', density ρ', cross-correlation $\langle u'w' \rangle$ and pressure-velocity correlation $\langle p'w' \rangle$ at different time in the simulation. In these figures, there are two distinct regions: the turbulent region with larger fluctuations above (approximately $-1.25 < z < 0$) and the wave region with smaller fluctuations below (approximately $z < -1.25$). The peak velocity fluctuations in figure VI.9(a-c) in the wave region is an order of magnitude less than those in the turbulent region. Thus, the fluctuating kinetic energy carried by the waves is significantly smaller compared to the turbulent kinetic energy present in the surface layer and upper portion of the jet. The wave fluctuations have larger u' and w' components than the v' components. The ρ' field shows a smaller difference between the wave and the turbulence region. It is noted that the location of the upper peak in ρ' indicate the approximate bottom boundary of turbulence and, thus, the stirring depth δ_s as discussed in previous section. The lower peak in ρ' occurs at the jet center where there is internal wave reflection. The cross-correlation $\langle u'w' \rangle$ in the wave region

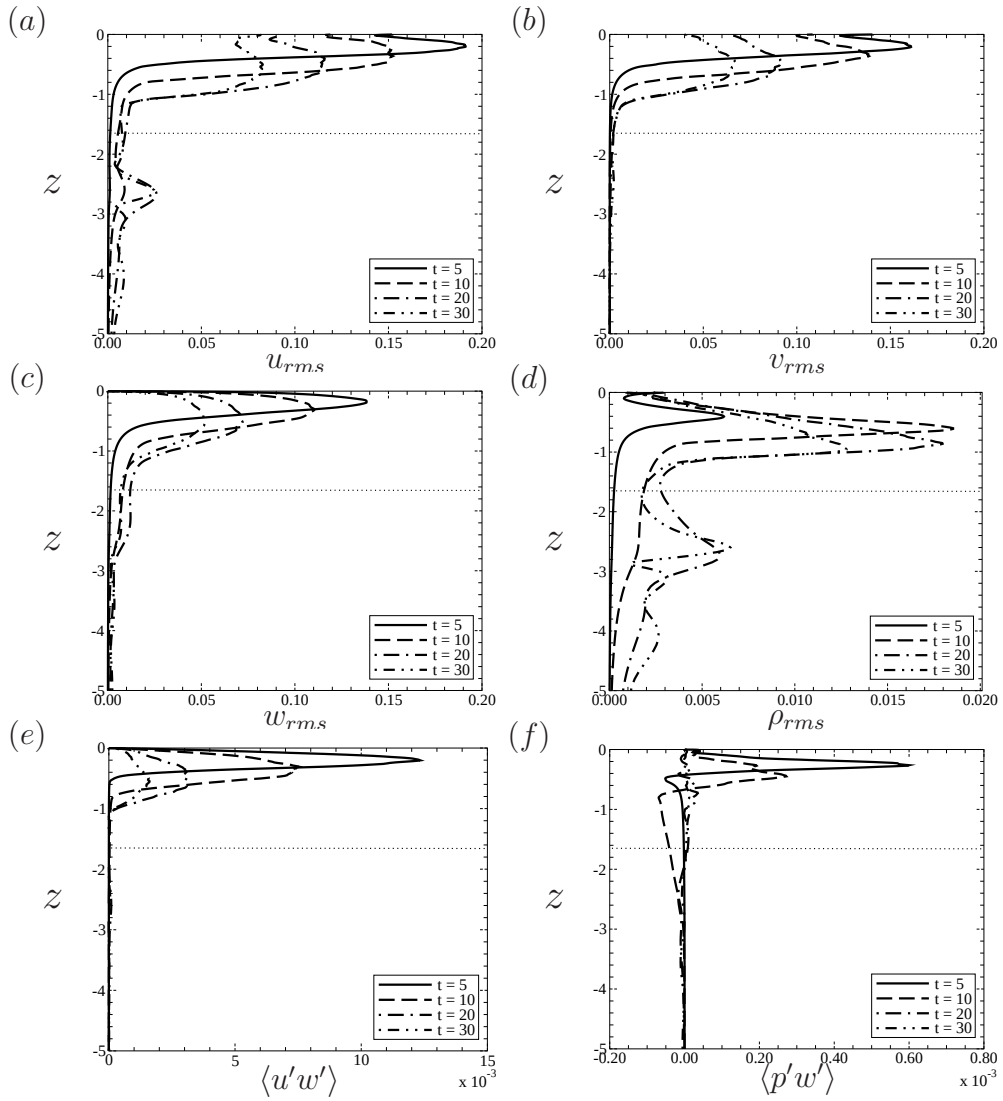

Figure VI.9: Horizontally-averaged profiles of the fluctuating fields at various time: (a) streamwise velocity u_{rms}, (b) spanwise velocity v_{rms}, (c) vertical velocity w_{rms}, (d) density ρ_{rms}, (e) Reynolds stress $\langle u'w' \rangle$ and (f) wave energy flux $\langle p'w' \rangle$. The horizontal dotted lines indicates the center of the jet. The upper zero-velocity point of the jet is at approximately $z = -0.4$ after t $= 10$.

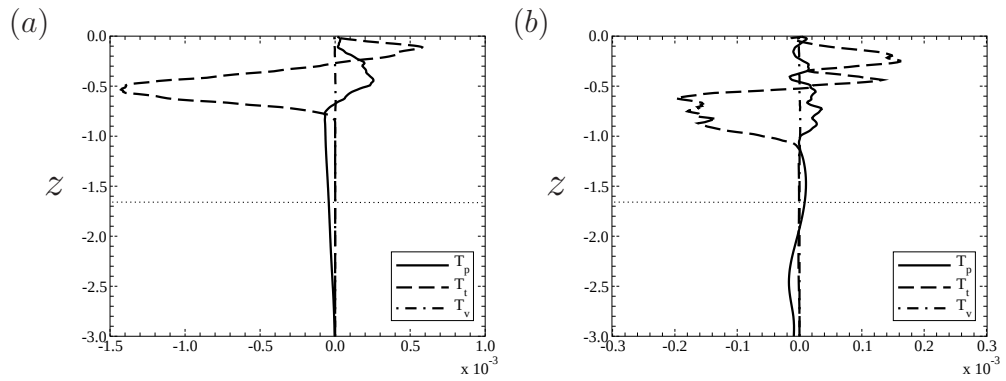

Figure VI.10: Contributions to the transport at (a) t = 10 and (b) t = 20. The dotted lines indicate center of the jet.

is substantially smaller than that in the turbulent region and thus the momentum flux carried by the waves is insignificant compared to the turbulent Reynolds stress. The pressure-velocity correlation $\langle p'w' \rangle$, representative of the amount of fluctuating energy carried by waves, shows stronger downward energy transport at t = 10 compared to later time.

It is important to emphasize that the wave energy flux, T_p, in the current study is significantly weaker than turbulence transport, T_t, defined in Eq.(VI.5). The vertical profiles of the three components of the transport term at $t = 10$ and $t = 20$ are plotted in figure VI.10(a,b), respectively. In figure VI.10(a), the domain consists of two regions: turbulence region above $z = -0.75$ in which T_t dominates the total transport and the wave region below $z = -0.75$ in which T_p, i.e. wave energy flux, dominates. In the turbulence region, T_t is positive in the surface layer indicating *upward* transport while T_t is negative in the jet upper-flank denoting *downward* transport. In the wave region, the negative T_p indicates downward wave energy flux which is significant smaller than the T_t values in the turbulence region. At later time, the turbulence region deepens to depth $z = -1.1$ as shown in figure VI.10(b). Both T_t and T_p are smaller than the values at earlier time indicating weaker turbulent diffusion and weaker wave flux. T_p changes signs across the center of jet showing upward wave flux for the wave region above. The reason is that some of the internal waves cannot penetrate past the center of the jet and thus reflect upward. Internal wave reflection due to changes in the ambient velocity has been observed by Brown & Sutherland (2007); Pham & Sarkar (2010).

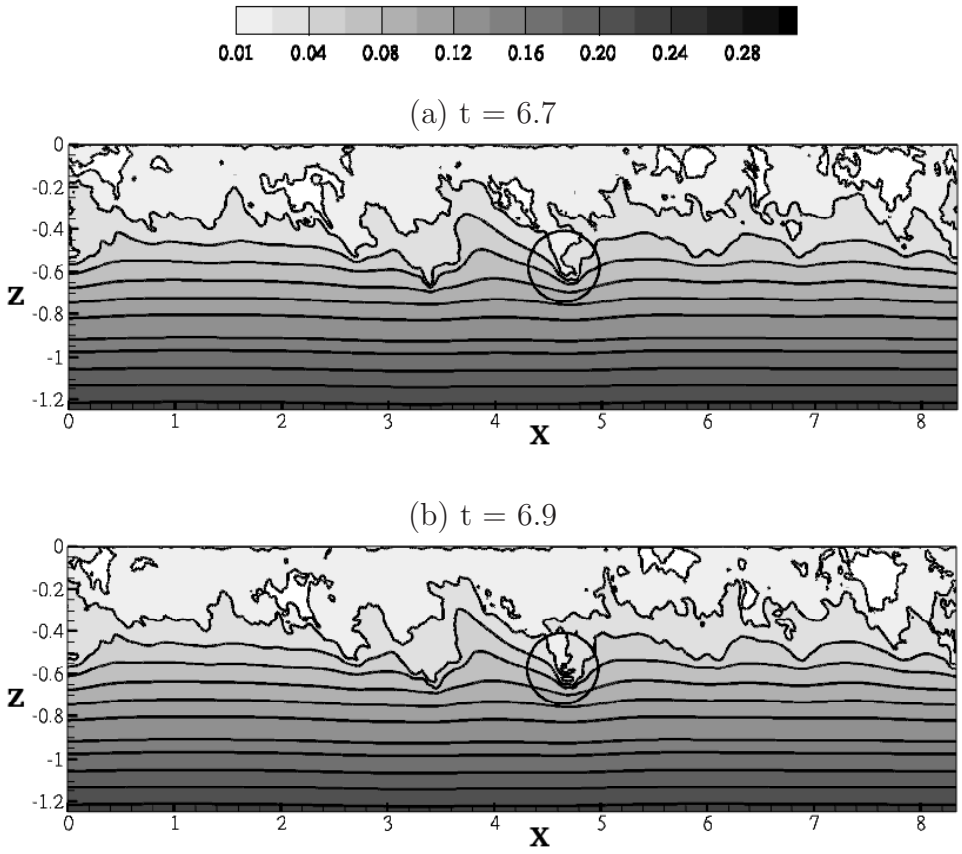

Figure VI.11: Downward ejection in the circled region is shown in the vertical x-z slices of the density field at $y = 1.1$.

VI.E Mixing and generation of intermittent turbulence

As the surface layer deepens, we observe intermittent patches of turbulence in the upper flank of the jet where the background gradient Richardson number is larger than 0.25. In this section we examine the density field to elucidate the mixing mechanisms leading to turbulence in the jet. The patches of turbulence are correlated with the formation of gravitationally unstable density 'pockets'. The formation is due to downward ejections in which lighter fluid is ejected downward into the quiescent region with heavier fluid, upward ejections in which heavier fluid from the quiescent region is ejected upward into the region with lighter fluids, and finally isopycnal overturns. Evidence of these mechanisms is presented in the following text.

Downward ejections are evident in figure VI.11 which shows snapshots of the instantaneous density field in the x-z plane at y = 1.1 at t = 6.7. In figure VI.11(a), as the surface layer deepens the isopycnals in the interface region lying between the turbulence region above and quiescent region below are distorted. The distortions mainly consist of large-scale undulations. When the distortion has large amplitude as in the region $3 < x < 5$, lighter fluid in the turbulence region extends deep into the the quiescent region with significantly heavier fluid. The isopycnals at the tip of the distortion at x = 4.7 and z = -0.6 in the circled region are compressed against each other denoting stronger density gradients in both horizontal and vertical directions compared to the ambient gradient. Figure VI.11(b) shows the subsequent evolution of figure VI.11(a) at later time t = 6.9. The tip of the distortion shown in figure VI.11(a) detaches from the isopycnal to evolve into individual 'pockets' of light fluid surrounded by heavier fluid in figure VI.11(b). The 'pockets' are swept downstream by the jet, i.e. the relative velocity is directed toward the positive x direction as they are ejected downward.

Figure VI.12 illustrates upward ejections. As shown in the circled region in figure VI.12(a), the fifth and sixth isopycnals from the bottom indicate the upward ejection of heavier fluid in the region $1 < x < 1.5$. The ejections resemble finger-like structures pointing upstream, i.e. in the negative x direction. The ejections occur at depth z = -0.9 which is more than half of the total depth of the jet upper-flank. In figure VI.12(b) which shows the subsequent evolution, the ejections are swept downstream by the jet velocity. The ejection in the sixth isopycnal from the bottom has disappeared; the ejection in the fifth isopycnal has evolved to become a separate 'pocket' surrounded by lighter fluid. The 'pocket' here is relatively smaller than those observed in the downward ejections, and it moves in the opposite direction. The orientation of the upward ejections is governed by the direction of mean spanwise vorticity ω_2. Since the background shear is negative and the positive y axis direct into the page in figure VI.12, the negative ω_2 rotates fluid counter-clockwise and so do the upward ejections.

Figure VI.12 also presents evidence of isopycnal overturns in the rectangular region $7 < x < 8$. The fourth and fifth isopycnals from the bottom in figure VI.12(a) indicates two adjacent distortions which are about to overturn. The distortion to the right is

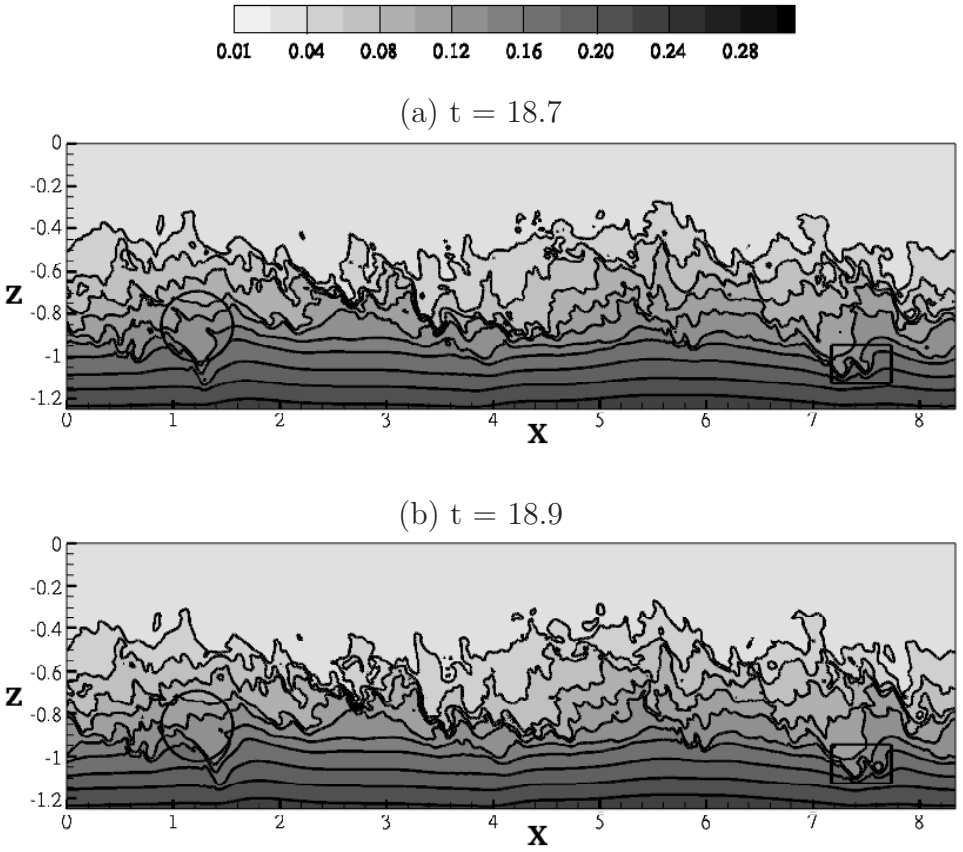

Figure VI.12: Upward ejection in the circled region and isopycnal overturn in the rectanglular region are shown in the vertical x-z slices of the density field at $y = 1.1$.

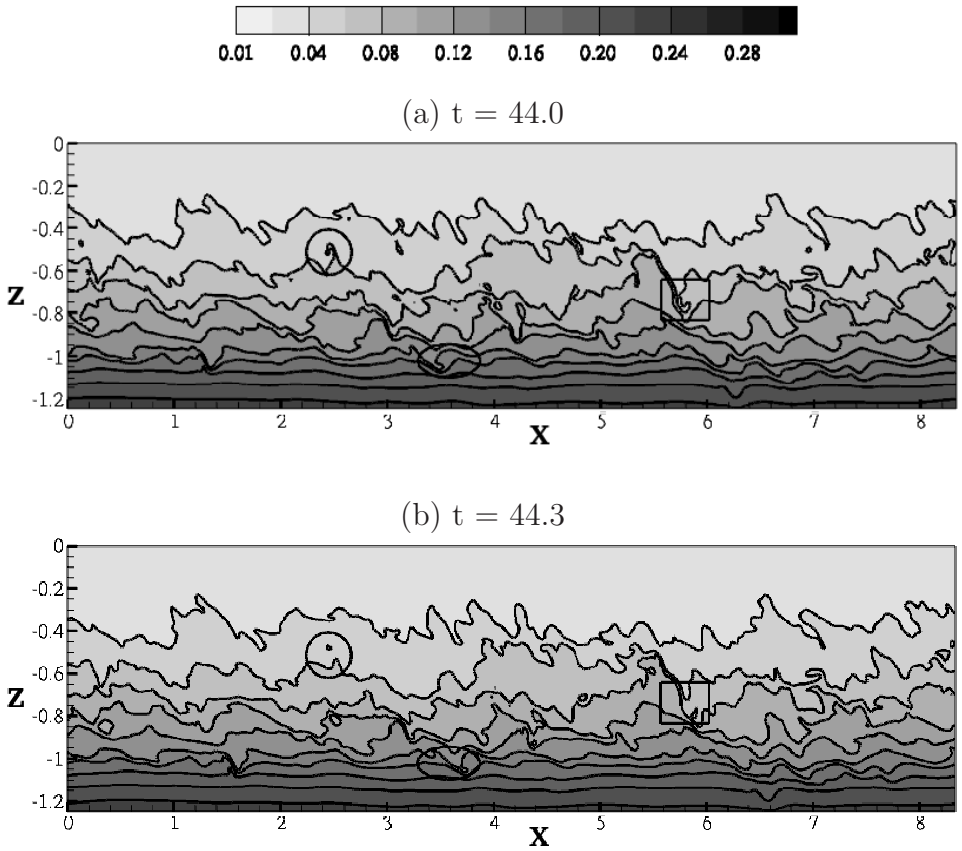

Figure VI.13: Upward ejection in the circled region, downward ejection in the rectangular region, and isopycnal overturning in the oval region are observed in the vertical x-z slices of the density field at $y = 1.1$.

of larger scale and the overturn direction is counter-clockwise. In figure VI.12(b), the distortions have been swept downstream and the one to the right has already overturned resulting a 'pocket' of light fluid surrounded by heavier fluid. The 'pocket' here is relatively larger than the one resulting from upward ejections.

The three mechanisms are presented again through snapshots at different time in figure VI.13 to emphasize their frequent occurrence in the jet upper-flank. Figures VI.13(a,b) show density contour plots near the end of the simulation at t = 44.0 and 44.3, respectively. Signatures of upward ejections are the abundant finger-like structures with counter-clockwise rotation in the isopycnals in the region $-0.8 < z < -0.4$. For example, the finger-like structure in the circled region in figure VI.13(a) at $x = 2.4$ and $z = -0.5$ is in process of ejecting heavier fluid upward; the ejection is

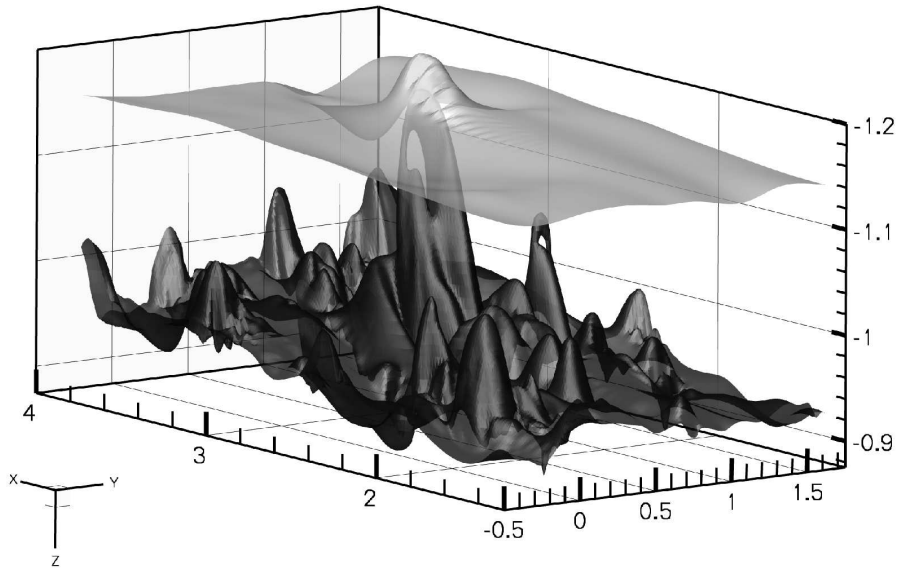

Figure VI.14: Ejections of light fluid are shown with 3D isocontours in the density field. Up in this figure corresponds to down in physical space. Horseshoe-like vortex tube ejecting fluid from the stirring surface downward in physical space at $t = 18$. The darker isosurface denotes $\rho = 0.144$ while the lighter one corresponds to $\rho = 0.197$. The negative z direction points upward in this figure.

completed in figure VI.13(b) in which a 'pocket' can be seen. The downward ejection is observed in the rectangular region at $x = 5.7$ and $z = -0.8$. The second isopycnal from the top is distorted over a large vertical extent, $-0.8 < z < -0.5$, in figure VI.13(a). In figure VI.13(b), the bottom tip of the distortion detaches to become a separate 'pocket' which is advected further downward in the positive x direction. Finally, isopycnal overturn is evident as shown in the fifth isopycnal from the bottom in the oval region at $x = 3.5$. Figure VI.13(a) shows the distortion ready to overturn while figure VI.13(b) shows the completed overturn with a detached 'pocket'. Out of the three mechanisms, the downward ejections generate turbulence over larger spatial extent as well as longer duration in time compared to the other two mechanisms.

The drivers of the observed ejections are vortex tubes as shown in figures VI.14 and VI.15. In figure VI.14, three-dimensional isopycnal surfaces are used to visualize the downward ejection observed at $t = 18$. It is noted that the vertical axis has been

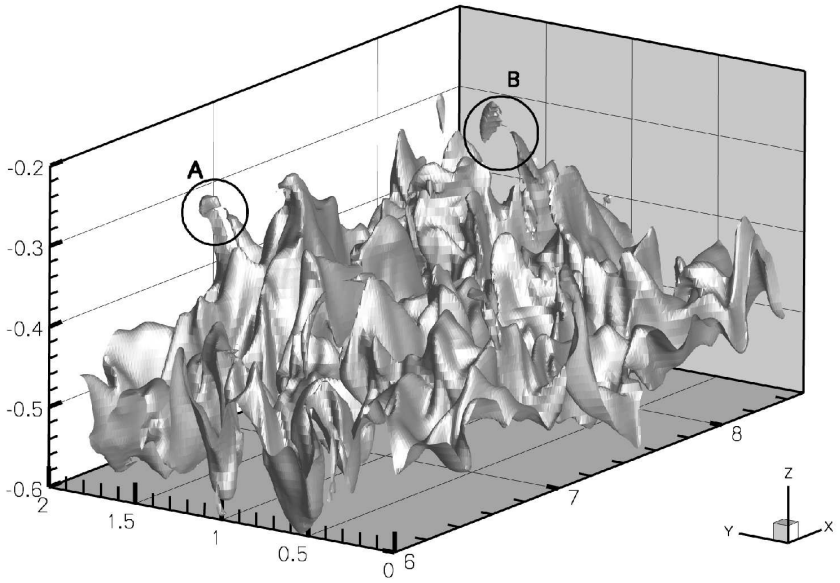

Figure VI.15: Ejections of heavy fluid are shown with 3D isocontours in the density field. Breaking horseshoe-like vortex tube denoted by circle A and single vortex tube denoted by circle B show ejections from the stirring surface upward toward the free surface at $t = 45$. The isosurface corresponds to $\rho = 0.048$.

flipped for visualization, i.e. up in physical space is directed downward in the figure so that the surface layer is at the bottom of the figure. Two isopycnal surfaces are shown: the darker corresponds to $\rho = 0.144$ while the lighter corresponds to $\rho = 0.197$. The ejection in the middle of the figure shows a horseshoe-like vortex originating from the darker surface extending toward the lighter surface. The vortex is slightly swept in the positive x direction as it penetrates upward in the figure (downward in physical space). A horseshoe-like vortex tube has been reported in Pham & Sarkar (2010); however, there the vortex tube was a result of a secondary instability of a Kelvin-Helmholtz rollers that interacted with the mean shear of a laminar jet. In figure VI.15, the three-dimensional feature of the upward ejections is shown with the isopycnal surface of $\rho = 0.048$ at $t = 45$. The positive z axis is directed upward in this figure consistent with physical space. A horseshoe-like vortex tube is observed in the circle A. Unlike the one shown in figure VI.14, the vortex tube extends upward and leans toward the negative x direction and it is in the process of breaking into two smaller tubes. A completed upward ejection of heavy fluid by a single vortex tube is shown in circle B. Again, the ejection is upward and toward negative x direction. The separated portion of the tube which looks like a 'pocket' in the x-z plane shows the rotational feature of a vortex.

Figure VI.16(a) shows the deepening of turbulence through a z-t diagram of density, analogous to a record taken by a density profiler, at fixed horizontal location, $x = 1.3$ and $y = 1.1$. The deepening occurs prior to $t = 20$ and penetrates to depth $z = -1$ which is well inside the jet upper-flank. During the deepening, two downward ejections are observed: one at $t = 15$ and $z = -0.75$, and the other at $t = 18$ and $z = -1.1$. The ejections cause isolated short-lived dips in the density associated with fluid that is ejected downward. The second ejection penetrates to greater depth relative to the first. The dip due to the first ejection is seen in two consecutive isopycnals while the second ejections affects three consecutive isopycnals. After $t = 20$, the density shows continuous high-frequency fluctuations in region $-1 < z < -0.75$ in contrast to region $-1.25 < z < -1$ where the density exhibits intermittent dips corresponding to downward ejections of fluid, for example, at $t = 28$, 33 and 38. The ejections that

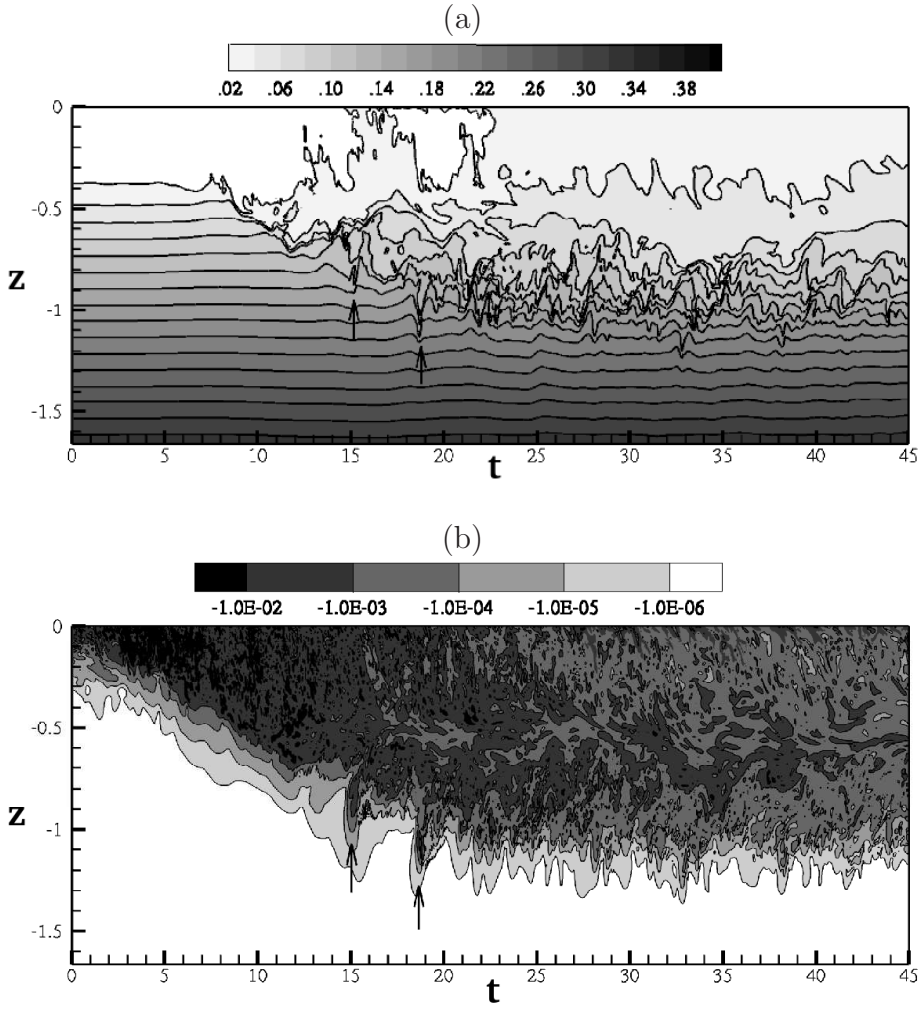

Figure VI.16: z-t diagrams of (a) the density field and (b) dissipation field measured at $x = 1.3$ and $y = 1.1$. Arrows indicate the effect of downward ejections.

occur after $t = 20$ are weaker than those that occur prior with respect to the vertical penetration. The corresponding z-t diagram of the dissipation at the same profiler is presented in figure VI.16(b). As the surface layer deepens, the turbulence region can penetrate as deep as $z = -1$ below which the dissipation rate sharply drops at least three orders of magnitude in a short vertical extent. The ejections in figure VI.16(a) are correlated with strong bursts of dissipation in figure VI.16(b). The bursts at $t = 15$ and 18 have dissipation at least three orders of magnitude larger than the surrounding values. The former burst causes strong dissipation, on the order of 10^{-2}, in the region $-1.2 < z < -1$ in which the gradient Richardson number Ri_g based on the mean profiles is significantly larger than 0.25 as shown in figure VI.5. It is evident that the dissipation observed in this region is *not initiated* by 'local' shear instability. Rather, the dissipation is initiated by the density ejections from the region above that then interact with the background shear.

VI.F Momentum budget

In section VI.C we have shown that the mean streamwise velocity $\langle u \rangle$ changes considerably throughout the simulations suggesting that the momentum budget of the jet has changed in time. In this section, we analyze the momentum budget to show that the momentum loss inside the jet is due to the drag of the applied wind stress τ_w as well as the drag from the Reynolds stress $\langle u'w' \rangle$ extracted from the imposed mean shear in the surface layer with the latter providing the dominant contribution.

Consider the horizontally-averaged x-momentum equation after Reynolds decomposition:

$$\frac{\partial \langle u \rangle}{\partial t} = \frac{1}{Re} \frac{\partial^2 \langle u \rangle}{\partial z^2} - \frac{\partial \langle u'w' \rangle}{\partial z} \,. \tag{VI.6}$$

Integrating the above equation from z_1 to z_2 yields:

$$\underbrace{\frac{\partial}{\partial t} \int_{z_1}^{z_2} \langle u \rangle \, dz}_{M_1} = \underbrace{\frac{S(z_2)}{Re}}_{M_2} \underbrace{- \frac{S(z_1)}{Re}}_{M_3} \underbrace{- \langle u'w' \rangle (z_2)}_{M_4} \underbrace{+ \langle u'w' \rangle (z_1)}_{M_5} , \tag{VI.7}$$

where S is used in place of $d \langle u \rangle / dz$. Eq.(VI.7) indicates the time rate of change of

Table VI.2: Momentum budget: Equation VI.7 integrated over the time of simulation.

Domain	M_1	M_2	M_3	M_4	M_5
$-0.33 \leqslant z \leqslant 0$	0.098	-0.030	0.003	0.0	0.126
$-1.67 \leqslant z \leqslant -0.33$	-0.127	-0.003	0.0	-0.126	0.001

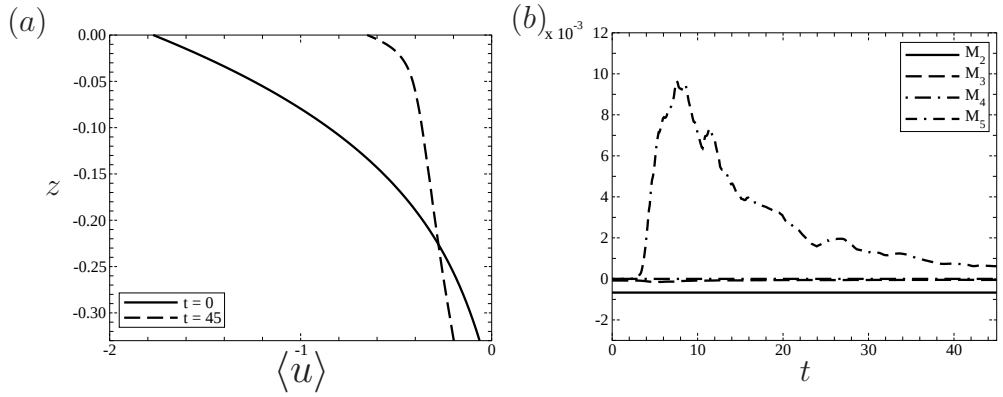

Figure VI.17: In the surface layer $-0.33 < z < 0$: (a) the initial and final mean streamwise velocity $\langle u \rangle$; (b) Viscous drag, M_2 at z = 0 and M_3 at z = -0.33, and turbulence/wave drag, M_4 at z = 0 and M_5 at z = -0.33, as a function of time.

momentum inside a domain M_1 is equal to the net effect of viscous stresses, M_2 and M_3, and Reynolds stresses, M_4 and M_5.

Lets apply Eq.(VI.7) to the surface layer with $z_1 = -0.33$ and $z_2 = 0$. Figure VI.17(a) shows the mean streamwise velocity $\langle u \rangle$ in the region at initial time $t = 0$ and at final time $t = 45$. In the region $-0.22 < z < 0$ the velocity magnitude decreases considerably while it increases slightly in region $-0.33 < z < -0.22$ so that the surface layers exhibits a net loss of its initial (negative) momentum. The time evolution of the terms on the right-hand-side of the Eq.(VI.7) is plotted in figure VI.17(b). At the surface $z_2 = 0$, M_2 is the applied wind stress τ_w taken to be constant in time. M_4 is equal to zero since no vertical velocity is allowed at the surface and M_3 is insignificant due to weak shear at z_1 as well as the large value of Re. The dominant term is M_5, the drag due to the Reynolds turbulent stress at z_1. M_5 increases sharply to its peak value during the early time when the background shear in the region is large. As the

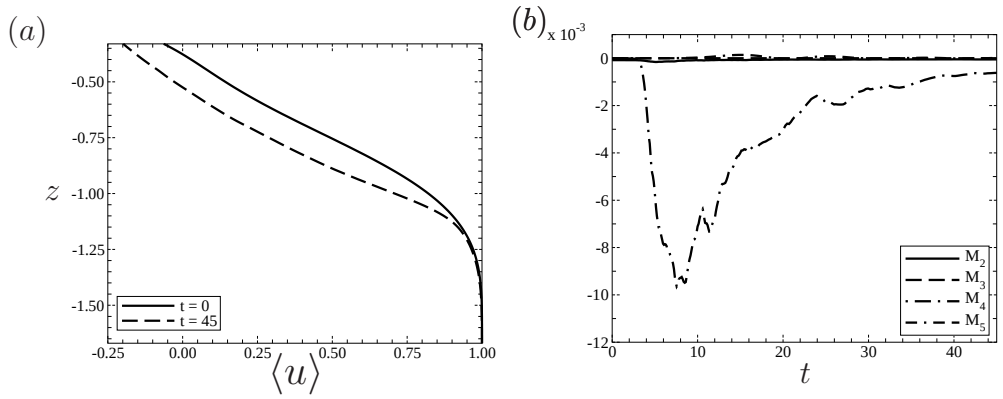

Figure VI.18: In the jet upper-flank $-1.67 < z < -0.33$: (a) the initial and final mean streamwise velocity $\langle u \rangle$; (b) Viscous drag, M_2 at z = -0.33 and M_3 at z = -1.67, and turbulence/wave drag, M_4 at z = -0.33 and M_5 at z = -1.67, as a function of time.

mean shear in the region decreases, M_5 also decreases. At the end of the simulation, the magnitude of M_5 is as small as that of the applied wind stress M_2. Integrating Eq.(VI.7) over the time of simulation yields the bulk evolution of the momentum budget, and results are tabulated in table VI.2. Overall, the momentum loss in the background velocity M_1 is balanced by the wind drag M_2 at the surface and the turbulent drag M_5 at the bottom of the surface layer. Furthermore, M_5 is the largest term in the budget and it is the cumulative effect of both M_1 and M_2. In other words, the net turbulent drag at the base of the surface layer is the sum of the wind drag and the momentum extracted from the background velocity. The former is approximately 30% of the latter as shown in table VI.2. Therefore, the background velocity provides a significantly larger contribution to the total drag than the wind stress.

Similar analysis is performed for the jet upper-flank with $z_1 = -1.67$ and $z_2 = -0.33$. Figure VI.18(a) presents two profiles of the background velocity $\langle u \rangle$ at time $t = 0$ and 45. The difference between the two profiles indicates the momentum loss. Significant drag is observed in the top half of the jet upper-flank; for example, the velocity at $z = -0.75$ is reduced by nearly half over the simulation. Figure VI.18(b) shows the time evolution of the terms on the right-hand-side of Eq.(VI.7). The viscous drag M_2 and M_3 are relatively small due to weak shear and large Reynolds number

effect. The wave drag M_5, i.e. $\langle u'w' \rangle$, at the bottom of the region is small as discussed in section VI.D. The only noticeable term is M_4 which is the drag due to the turbulent stress at the top of the jet. The results of integrating Eq.(VI.7) in time are included on table VI.2 which indicates a direct balance between M_1 and M_4. The jet upper-flank loses significant amount of momentum due to the turbulent drag at the upper surface, $z_2 = -0.33$. The net momentum loss in the jet upper-flank is 25% larger than that in the surface layer. Combining the two analyses above yields the net effect of the wind stress and the initially imposed shear in the surface layer upon the jet. In bulk numbers, the wind stress contributes approximately 25% of the total drag on the jet; the other 75% is contributed by the background shear in the surface layer via turbulent extraction.

VI.G Kinetic Energy Budgets

Analysis of the momentum budget, given in the preceding section, indicates that the wind stress plays a smaller role in terms of momentum drag upon the jet when compared to turbulent momentum fluxes in the subsurface sheared region. In this section, the budgets of the mean kinetic energy, mke, and the turbulent kinetic enery, tke, are examined to show that the mean energy input by the wind stress τ_w is also smaller than the amount of energy extracted from background shear. Also, the energy input by surface cooling is minuscule relative to the dominant terms in the tke budget. Most of the energy lost to dissipation in the jet upper-flank is localized to the region. The turbulent energy flux from the surface layer above provides a smaller net contribution but serves as an essential catalyst for mixing in the jet.

When Eq.(VI.6) is multiplied by $\langle u \rangle$, the evolution equation for the mke is obtained:

$$\frac{\partial\, mke}{\partial t} = \frac{\partial}{\partial z}\left[\langle u \rangle \left(\frac{S}{Re} - \langle u'w' \rangle\right)\right] - V - P\,, \tag{VI.8}$$

where $mke = 1/2\,\langle u \rangle^2$, S is the shear rate, $V = S^2/Re$ is the viscous dissipation of the mean flow, and $P = -\langle u'w' \rangle\, S$ is the amount of mke feeding into the turbulence. Integrating the above equation from the center of jet $z_j = -1.67$ to the surface $z = 0$

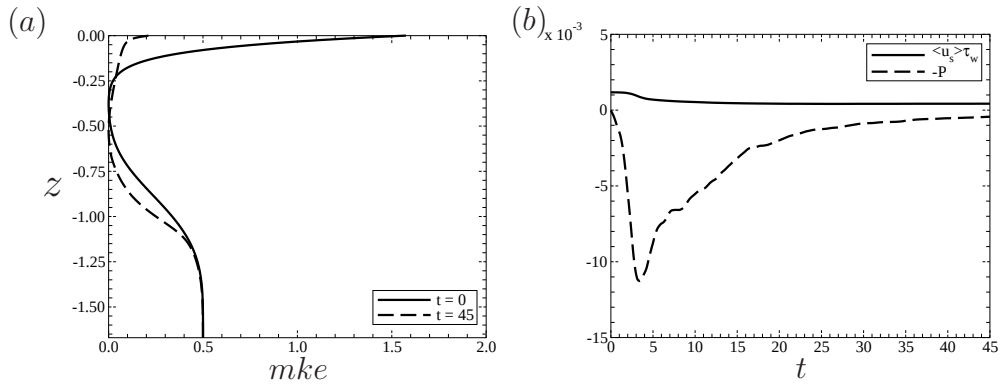

Figure VI.19: (a) Mean kinetic energy at $t = 0$ and 45; (b) Energy input by the wind stress, $\langle u_s \rangle \tau_w$, and energy converted to turbulent kinetic energy P integrated over the region $-1.67 < z < 0$.

yields:

$$\frac{\partial}{\partial t} \int_{z_j}^{0} mke \, dz = \langle u_s \rangle \tau_w - \int_{z_j}^{0} V \, dz - \int_{z_j}^{0} P \, dz \,, \tag{VI.9}$$

where the shear rate S at z_j and the Reynolds stresses $\langle u'w' \rangle$ at z_j and 0 are neglected. Eq.(VI.9) indicates two sources and two sinks for mke during the simulation. The two sources are the energy available in the mean velocity at initial time and the energy input by the wind stress. The two sinks are the viscous dissipation and the energy conversion to the turbulent kinetic energy.

Figure VI.19(a) plots the vertical profiles of the mke at the initial time $t = 0$ and the final time $t = 45$. The substantial difference between the two profiles indicates a significant amount of the mke is lost over the simulation especially in the surface layer. At the surface $z = 0$, despite continuous supply of energy by the wind, the mke at the final time is 8 times smaller than that at initial time. The jet upper-flank also loses a considerable amount of mke. Figure VI.19(b) contrasts the time evolution of the wind stress term and the production term on the right-hand-side of Eq.(VI.9). While the wind stress exerts a constant momentum drag over time upon the surface as discussed in the previous section, its energy input varies in time due to the decreasing surface velocity $\langle u_s \rangle$. The maximum energy input is at $t = 0$ and drops toward a constant at later time. The turbulence production term P is insignificant at time $t = 0$ but rises quickly to its peak followed by a decrease as the background shear decreases. The

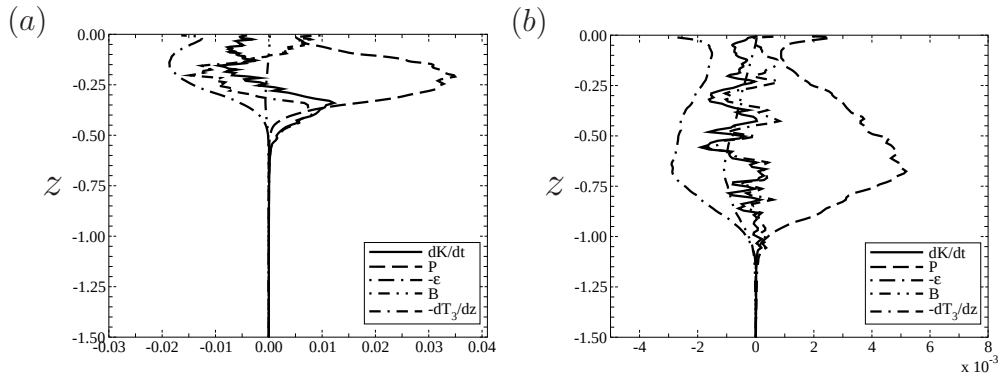

Figure VI.20: TKE budgets at (a) t = 5 and (b) t = 20.

peak value of P is nearly 10 times larger than the peak energy input by the wind. At the end of the simulation, the two terms are approximately equal. Integrating the terms of the right-hand-side of Eq.(VI.9) over the time of the simulation gives the total energy input by the wind equal to 0.023 and the total energy converted to the *tke* equal to -0.144. The left-hand-side yields the total lost of *mke* from the initially imposed background velocity equal to -0.13. Thus, the total amount of energy converted to the *tke* is the sum of the energy input by the wind and the *mke* lost from the mean velocity subtracting the relatively small viscous dissipation. The wind energy input only contributes 16% of the energy converted to the *tke*, and the reservoir of mean kinetic energy in the surface layer and the jet makes the major contribution.

Figures VI.20(a,b) plot the *tke* budgets at $t = 5$ when the surface layer is deepening and at $t = 20$ when the deepening ceases, respectively. At $t = 5$ the dominant terms in the budget are the production P and the dissipation ε; the buoyancy flux B is small relative to other terms. The transport term consisting of both positive and negative values indicates that *tke* is transported both upward and downwards. It is noted that it is the negative of dT_3/dz that is plotted in figure VI.20. At the surface, *tke* generated by the wind stress is transported downward. From $-0.35 < z < -0.1$, *tke* is transported upward since large amount of *tke* is generated in the region of peak production. The peak production and dissipation occurs inside the sheared region, not at the surface, suggesting that more *tke* is extracted from the mean shear than that input by the wind stress. At the base of the surface layer, positive dK/dt indicates *tke* accumulation due

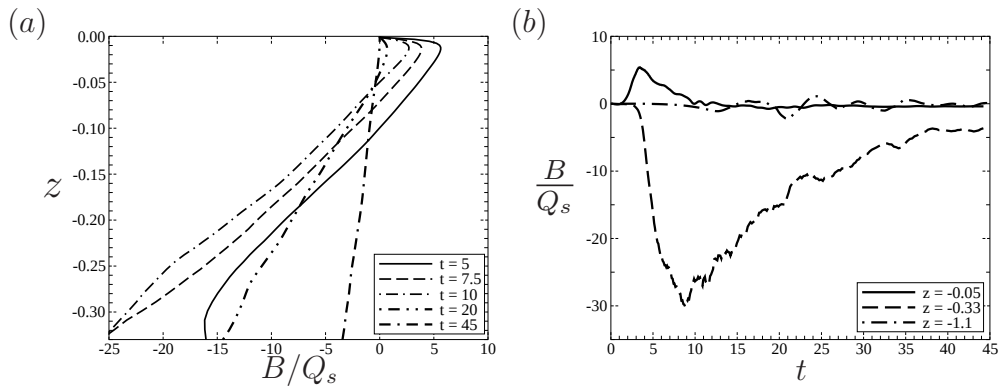

Figure VI.21: (a) Vertical profiles of the buoyancy flux B at various time; (b) The time evolution of B at different depth.

to the downward negative energy transport. The production and dissipation at $t = 20$ in figure VI.20(b) are approximately an order of magnitude smaller than those at earlier time in figure VI.20(a). Over the surface layer and the jet upper-flank, the production is balanced by the dissipation and the buoyancy flux. The peaks of the production and dissipation at $t = 20$ are further away from the surface when compared to those at $t = 5$ in figure VI.20(a). At the surface, the production locally peaks but the peak value is less than half of the peak value in the jet upper-flank. Thus, even when the surface layer ceases to deepen, the larger energy input to the *tke* budget is from the background shear in the jet, *not* from the wind stress.

Although the buoyancy flux B in figures VI.20(a,b) is smaller than the production and the dissipation, its magnitude is substantially larger than the surface cooling Q_s. Figure VI.21(a) shows vertical profiles of B normalized by Q_s at different time in the simulations in the surface layers. Near the surface $z = 0$, B carries positive sign denoting generation of *tke* from potential energy. At the bottom portion of the layer, B changes to negative sign consistent with loss of *tke* in stirring the background density. The magnitude of the negative B is significantly larger than that of the positive B at any time. Figure VI.21(b) illustrates the time evolution of B normalized by Q_s at different depths: $z = -0.05$ just outside the thin viscous layer, $z = -0.33$ at the base of the surface layer and $z = -1.1$ inside the jet upper-flank. At $z = -0.05$, B has positive value over the period $0 < t < 15$ with magnitude significantly larger than later values. The peak value of B occurs at $t = 3$ and is approximately 5 times

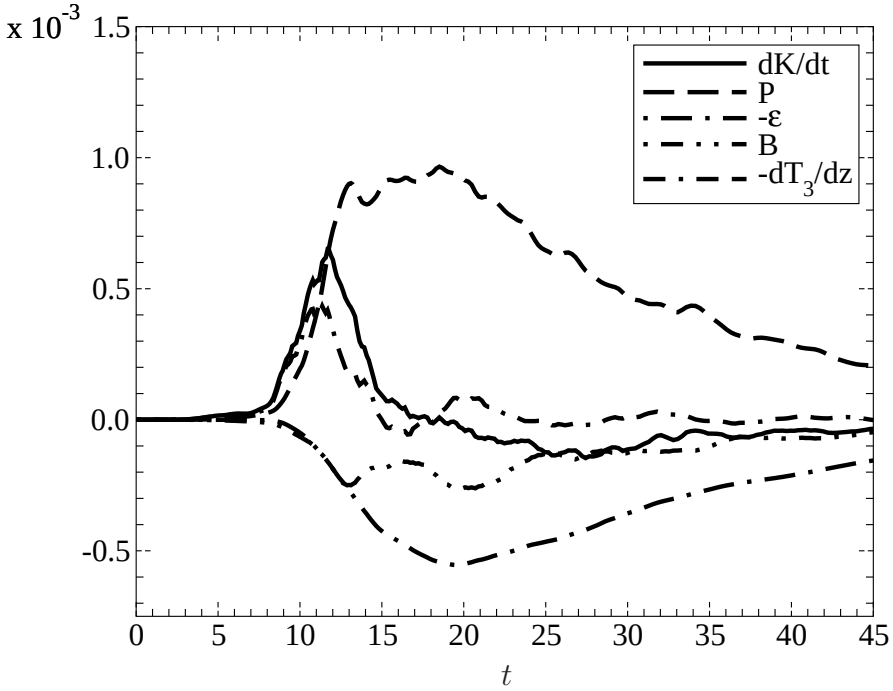

Figure VI.22: Integrated TKE budget over the upper-flank of the jet $-1.67 \leqslant z \leqslant -0.33$.

larger than Q_s. At $z = -0.33$, B is negative over the entire simulation with the peak magnitude substantially larger than the value recorded at depth $z = -0.05$. Also, B at $z = -0.33$ is greater than Q_s at all time after $t = 3$. At $z = -1.1$, B has alternating signs with amplitude of order Q_s suggesting the presence of weak internal waves. The temporal and spatial evolution of B in figures VI.21(a,b) supports the notion that the energy input by surface cooling is minimal compared to the energy lost to stirring the background density, B, which in turn is significant smaller than the turbulent production and dissipation.

To track the energy pathway to the turbulence observed in the jet upper-flank, we integrate Eq.(VI.4) across the region $-1.67 < z < -0.33$ to give the time evolution of the *tke* budget, which is shown in figure VI.22. The evolution begins at $t = 7$ prior to which turbulence is contained in the surface layer. At $t = 7$, the dK/dt and transport terms rise followed later by a rise in the production. Therefore, at the beginning of the evolution, *tke* is transported from the surface layer into the jet upper-flank, only subsequently is energy extracted from the mean background jet shear. The peak

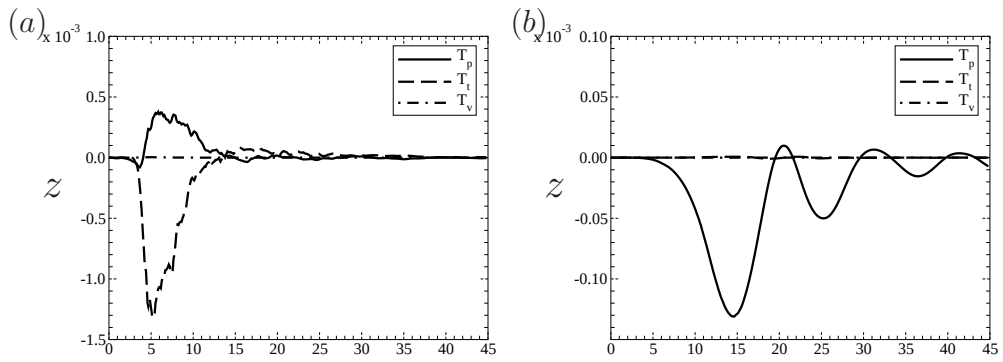

Figure VI.23: Amount of turbulent kinetic energy carried by the pressure transport T_p, turbulent transport T_t and viscous transport T_v across depth: (a) $z = -0.33$ and (b) $z = -1.67$.

downward transport that occurs at $t = 12$ is as large as 40% of the peak production as $t = 19$. The downward transport continues until $t = 15$ after which for a period of time the transport direction is reversed, i.e. *tke* is pumped from the jet back to the surface layer. During this period, the surface layer ceases to deepen and the production in the surface layer decreases to values smaller than the production in the jet as was shown in figure VI.20(b). Overall, the evolution shows that two sources of *tke* are the production and transport while two sinks are the dissipation and buoyancy flux. Integrating the evolution over time gives the following values: net production of 0.02, transport of 0.0016, dissipation of -0.012, and buoyancy flux of -0.0049 and a surplus *tke* of 0.0024 inside the jet upper-flank at the end of the simulation. The production is more than 12 times larger than the transport indicating the major source of *tke* is local.

Although the net transport integrated over time is substantially smaller that the integrated production, the two term are comparable during the deepening of the surface layer $5 < t < 20$ as shown in figure VI.22. Therefore, it is important to identify which component of transports, i.e. T_p or T_t or T_v, is responsible for the energy delivery during deepening. The amount of energy transported by each component across the top boundary $z = -0.33$ and the bottom boundary $z = -1.67$ of the jet upper-flank is plotted in figures VI.23(a,b), respectively. In figure (a), the viscous transport T_v is substantially smaller than the other components throughout the simulation. The

pressure transport T_p begins to pump energy downward first via internal waves but quickly reverses direction at the same time that downward turbulent transport T_t commences. The peak downward T_t is more than three times larger than the peak upward T_p. Over the simulation, T_t is the largest component of transport, and therefore, tke transported downward from the surface layer by turbulent diffusion is larger than that by internal waves. In figure VI.23(b), T_t is significantly smaller than T_p because there is no turbulence activity at the center of the jet. Weak internal waves propagate across this depth toward the region below the jet. The peak value of T_p is approximately 10 times smaller than the peak of T_t in figure VI.23(a). The net result of the transport over the region $-1.67 < z < -0.33$ is an accumulation of tke as discussed above. Even though the accumulation through the transport term is small compared to the production, it is the catalyst for turbulence extraction from the background shear. It should be emphasized that while wave energy enters the jet before turbulent transport by vortex structures, turbulence is not generated at that time, i.e. there is no evidence of internal wave breaking. As soon as a small amount of turbulence arrives through turbulent transport, it triggers energy extraction from the background shear even though the nominal gradient Richardson number is larger than 0.25.

VI.H Implications

In the current study, we have examined internal waves and turbulence in a linearly-stable stratified jet subject to the forcing of wind stress and surface cooling. The simulation begins with a symmetric jet situated below a surface shear layer driven by a constant wind stress. The surface layer is well mixed while the jet is stably stratified such that the gradient Richardson number inside the jet is larger than the critical value for linear shear instability.

Turbulence initiated by finite-amplitude broadband fluctuations is generated in the surface layer and deepens into the jet upper-flank. Internal waves generated by the turbulent surface layer are observed to propagate downward across the jet. The wave momentum flux is significantly smaller than the Reynolds turbulent stress extracted

from the background velocity. Similarly, the wave energy flux is insignificant compared to other terms in the balance of turbulent kinetic energy.

Intermittent patches of intense dissipation are observed inside the jet upper-flank where the background gradient Richardson number is larger than 0.25. The dissipation in the patches is at least three orders of magnitude stronger than the ambient value. The patches are the result of ejections of fluid parcels. The ejections are observed to be directed both upward and downward and driven by the formation of horseshoe vortices and vortex tubes.

Mixing leads to strong variation in both space and time of the mean shear, S, and the mean buoyancy frequency, N. Remarkably, the associated gradient Richardson number, $Ri_g = N^2/S^2$, evolves from both large and small values towards the critical value of $Ri_g = 0.25$ so that the region spanning the upper flank of the jet and the lower part of the surface layer is characterized by $Ri_g \sim 0.25$. The turbulent buoyancy flux, B, takes large negative values with magnitude as as large as 30 times the surface buoyancy flux and to significant turbulent dissipation rate, ε, in the jet that is 3 orders of magnitude larger than the surface buoyancy flux. The subsurface mixing events lead to values of ε at locations deep in the upper flank of the jet that are comparable to the peak surface value at that time.

The momentum budget shows significant drag on the jet. The drag due to the wind stress is approximately 3 times smaller than the drag caused by turbulent stress inside the surface layer. The total energy input by the surface stress is 16% of the net amount lost in mean kinetic energy over the simulation. The constant energy input by surface cooling is insignificant compared to the turbulent production and dissipation in the surface layer at any time during the simulation.

The analysis of the *tke* budget over the jet upper-flank indicates that the major sources of turbulence in the region are the energy extraction from local mean shear and the downward turbulent transport from the surface layer. Turbulent transport occurs prior to turbulent production but is significantly smaller. Therefore, the role of surface forcing is to provide the finite-amplitude fluctuations that then draw energy from the background shear resulting in turbulence generation and intermittent patches

of dissipation in the stratified jet.

The contents of this chapter are under review for publication in the Journal of Fluid Mechanics: Pham, H. T., and Sarkar, S., "Mixing events in a stratified jet subject to surface wind and buoyancy forcing", J. Fluid Mech.*, submitted (2010). The dissertation author is the primary researcher and the research supervisor is the co-author of the paper.*

Chapter VII

Conclusions

A series of Direct Numerical Simulations have been used to investigate turbulence and internal waves in the simplified EUC models. Some important results are summarized here.

The simulations of a weakly stratified shear layer in the presence of a strongly stratified region beneath it are considered in Chapter III. Both, coherent Kevin-Helmholtz (KH) rollers and small-scale turbulence, are observed during the evolution of the shear layer. The deep stratification measured by the Richardson number, J_d, is varied to study its effect on the dynamics. In all cases, a pycnocline is found to develop at the edges of the shear layer. The region of maximum shear shifts downward with increasing time. Internal waves are excited, initially by KH rollers, and later by small-scale turbulence. The wave field generated by the KH rollers is narrow-band and of stronger amplitude than that of the broad-band wave field generated by turbulence. Linear theory based on Doppler-shifted frequency of the KH mode is able to predict the angle of the internal wave phase lines during the direct generation of internal waves by KH rollers. Waves generated by turbulence are relatively weaker with a broader range of excitation angles which, in the deep region, tend towards a narrower band. The linear theory that works for the internal waves excited by KH rollers does not work for the turbulence generated waves. The momentum transported by the internal waves into the interior can be large, about 10% of the initial momentum in the shear layer, when $J_d \simeq 0.25$. Integration of the turbulent kinetic energy budget in time and over the

shear layer thickness shows that the energy flux can be up to 17% of the turbulent production, 33% of the turbulent dissipation rate and 75% of the buoyancy flux. These numbers quantify the dynamical importance of internal waves. In contrast to linear theory where the effect of deep stratification on the shear layer instabilities has been found to be weak, the present nonlinear simulations show that the evolution of the shear layer is significantly altered because of the significant momentum and energy carried away by the internal waves.

Scalar transport and mixing by active turbulence in high-Reynolds-number time-dependent inhomogeneous stratified shear flows are investigated in Chapter IV. Two density profiles are considered: two layers of homogeneous fluid with different density, namely two-layer case, and a continuously stratified background ambient, namely the J_d case. The evolution of the mixing layer includes shear instability, formation of Kelvin-Helmholtz rollers, and transition to turbulence followed by its decay. In the J_d case, internal gravity waves carrying momentum and energy are observed to propagate away from the shear layer. The turbulent kinetic energy budgets indicate a larger peak value of the buoyancy flux at the shear center in the two-layer case and therefore a larger production in the budget of the density variance. The peak values of outer length scales such as the momentum thickness, the energy-containing scale and the Ellison scale are larger in the two-layer case while those of Ozmidov and Kolmogorov scale are similar. The eddy diffusivity and mixing efficiency take similar values between the two cases during the turbulence decay. In both cases, the mixing efficiency computed based on the buoyancy flux is approximately 0.35 while the mixing efficiency estimated from the scalar dissipation is approximately 0.4.

The interaction between a stably stratified jet and internal gravity waves from an adjacent shear layer with mild stratification is considered in Chapter V. Results from two simulations are presented: one with the jet located far from the shear layer (far jet) and the other with the shear layer right on top of the jet (near jet). The near jet is more representative of EUC conditions. In the far jet, internal waves excited by the Kelvin-Helmholtz rollers do not penetrate the jet. They are reflected and trapped in the region between the shear layer and the jet and lead to little dissipation. In the near

jet, internal waves with wavelength larger than that of the KH rollers are found in and below the jet. Pockets of hot fluid that originate from the shear layer penetrate into the jet region, initiate turbulence and disrupt the internal wave field. Coherent patches of enhanced dissipation moving with the mean velocity are observed. The dissipation in the stably stratified near jet is large, up to three orders of magnitude stronger than that in the propagating wave field or the jet of the far case.

Finally, the fine-scale response of a subsurface stable stratified jet subject to the forcing of surface wind stress and surface cooling is investigated in Chapter VI. A linearly-stable symmetric jet situated below a well-mixed surface layer driven by a constant wind stress is considered. The gradient Richardson number inside the jet is larger than the critical value for linear shear instability. Broadband finite-amplitude fluctuations are introduced into the surface layer to initiate the simulation. Turbulence is generated in the surface layer and deepens into the jet upper-flank. Internal waves generated by the turbulent surface layer are observed to propagate downward across the jet. The momentum flux carried by the waves is significantly smaller than the Reynolds shear stress extracted from the background velocity. The wave energy flux is also smaller than the turbulence production. Fluid ejections by vortex tubes cause intermittent patches of intense dissipation inside the jet upper-flank where the background gradient Richardson number is larger than 0.25. The momentum budget shows significant drag on the jet. The drag due to the wind stress is smaller than the drag caused by turbulent stress inside the surface layer. The energy input by the surface forcing is also smaller than the energy extracted from the initially imposed background shear in the surface layer.

The model problems leads us to the following conclusions regarding internal waves and 'deep-cycle turbulence' in the EUC:

1. Large-amplitude internal waves can be excited by shear instability and its subsequent formation of Kelvin-Helmholtz rollers. Internal waves generated by the broadband turbulence in the mixed layer are significantly weaker.

2. The interaction between internal waves and the EUC jets depend strongly on the

length scale of the waves and the background velocity and stratification. In our model problems, internal waves are observed inside the jets but the breaking of internal waves due to the wave/mean interaction is *not* observed.

3. Intermittent patches of strong dissipation in a nominally stable stratified jet are observed in the simulations similar to observations of 'deep-cycle turbulence' inside the EUC jet. The patches result from vortex tubes originating from the mixed layer penetrating into the jet.

4. Ejections of fluids driven by vortex tubes inside the jet upward toward the mixed layer and isopycnal overturning are observed to also cause mixing and turbulence in regions of EUC jet where the nominal gradient Richardson number is marginally stable. The events are possibly related to local shear instability and subject to further investigation.

The assertions above are in line with the recent studies by Moum *et al.* (2010) and Smyth *et al.* (2010). Their analysis on the new observation data of the Pacific EUC suggests that the narrow-band oscillations are *not* internal waves. They suggest the near-N oscillations are the indication of random shear instability. In our models, the oscillations in the isopycnals due to the ejection of fluids have significantly shorter wavelength and higher frequency than that of propagating internal waves. Although the vortex tubes discussed in chapter VI are yet affirmed to be related to shear instability, those discussed in chapter V are correlated to a secondary instability of Kelvin-Helmholtz rollers. While formation of vortex tubes are yet to be confirmed in the field observations, full-scale simulations using Large Eddy Simulation with realistic input data will be an useful step in confirming the presence of vortex tubes. Such simulations are also important in making precise role of gravity waves in vertical mixing since our simplified model problems have weaker surface forcing than potential scenarios in the EUC.

Bibliography

Andrew, D. & McIntyre, M. 1978 An exact theory of nonlinear waves on a lagrangian mean flow. *J. Fluid Mech.* **89**, 609–646.

Basak, S. 2005 Dynamics of stratified shear layers with horizontal shear. PhD thesis, University of California San Diego, San Diego USA.

Basak, S. & Sarkar, S. 2006 Dynamics of a stratified shear layer with horizontal shear. *J. Fluid Mech.* **568**, 19–54.

Booker, J. & Bretherton, F. 1967 The critical layer for internal gravity waves in a shear flow. *J. Fluid Mech.* **27**, 513–539.

Brown, G. L. & Sutherland, B. R. 2007 Internal wave tunnelling through non-uniformly stratified shear flow. *Atmosphere-Ocean* **45**, 47–56.

Brucker, K. & Sarkar, S. 2007 Evolution of an initially turbulent stratified shear layer. *Phys. Fluids* **19**, 101105.

Brucker, K. A. 2009 Numerical investigation of momentumless wakes in stratified fluids. PhD thesis, University of California San Diego, San Diego USA.

Caulfield, C. P. & Peltier, W. R. 1994 Three dimensionalization of the stratified mixing layer. *Phys. Fluids* **6**, 3803–3805.

Caulfield, C. P. & Peltier, W. R. 2000 The anatomy of the mixing transition in homogeneous and stratified free shear layers. *J. Fluid Mech.* **413**, 1–47.

D'Asaro, E., Eriksen, C., Levine, M., Niiler, P., C., P. & Meurs, P. 1995 Upper ocean inertial currents forced by a strong storm. part i: Data and comparisons with linear theory. *J. Phys. Oceanogr.* **25**, 2909–2936.

Deloncle, A., Chomaz, J. & Billant, P. 2007 Three-dimensional stability of a horizontally sheared flow in a stably stratified fluid. *J. Fluid Mech.* **570**, 297–305.

Diamessis, P. J. & Nomura, K. K. 2004 The structure and dynamics of overturns in stably stratified homogeneous turbulence. *J. Fluid Mech.* **499**, 197–229.

Dohan, K. & Sutherland, B. 2003 Internal waves generated from a turbulent mixed region. *Physics of Fluids* **15** (2), 488–498.

Drazin, P., Zaturska, M. & Banks, W. 1979 On the normal modes of parallel flow of inviscid stratified fluid. part 2. unbound flow with propagation at infinity. *J. Fluid Mech.* **95**, 681–705.

E, X. & Hopfinger, E. J. 1986 On mixing across an interface in stably stratified fluid. *J. Fluid Mech.* **166**, 227–244.

Einaudi, F., Lalas, D. & Perona, G. 1978/79 The role of gravity waves in tropospheric processes. *Pure Appl. Geophys.* **117**, 627–663.

Eliassen, A. & Palm, E. 1960 On the transfer of energy in stationary mountain waves. *Geofys. Publ. (Geophys. Norv.)* **22**, 1–23.

Eriksen, C. 1982 Geostrophic equatorial deep jets. *J. Mar. Res.* **40**, 143–157.

Fernando., H. J. S. 1991 Turbulent mixing in stratified fluids. *Annu. Rev. Fluid Mech.* **23**, 455–493.

Firing, E. 1987 Deep zonal currents in the central equatorial pacific. *J. Mar. Res.* **45**, 791–812.

Fritts, D. 1982 Shear excitation of atmospheric gravity waves. *J. Atmos. Sci.* **39**, 1936–1952.

Gayen, B., Sarkar, S. & Taylor, J. R. 2010 Large eddy simulation of a stratified boundary layer under an oscillatory current. *J. Fluid Mech.* **643**, 233–266.

Gerz, T., Schumann, U. & Elghobashi, S. E. 1989 Direct numerical simulation of stratified homogeneous turbulent shear flows. *J. Fluid Mech.* **200**, 563–594.

Gregg, M. C., Peters, H., Wesson, J. C., Oakey, N. S. & Shay, T. J. 1985 Intensive measurements of turbulence and shear in the equatorial undercurrent. *Nature* **314** (14), 140–144.

Hazel, P. 1972 Numerical studies of the stability of inviscid stratified shear flows. *J. Fluid Mech.* **51**, 39–61.

Hebert, D., Moum, J., Paulson, C. & Caldwell, D. 1992 Turbulence and internal waves at the equator. part ii: Details of a single event. *J. Phys. Oceanogr.* **22**, 1346–1356.

Holt, S. E., Koseff, J. R. & Ferziger, J. H. 1992 A numerical study of the evolution and structure of homogeneous stably stratified sheared turbulence. *J. Fluid Mech.* **237**, 499–539.

Holton, J., Haynes, P., McIntyre, M., Douglass, A., Rood, R. & Pfister, L. 1995 Stratosphere-troposphere exchange. *Rev. Geophys.* **33**, 403–439.

Ivey, G. N., Winters, K. B. & Koseff., J. R. 2008 Density stratification, turbulence, but how much mixing? *Annu. Rev. Fluid Mech.* **40**, 169–184.

Jacobitz, F. G. & Sarkar, S. 1999 On the shear number effect in stratified shear flow. *Theoret. Comput. Fluid Dyn.* **13**, 171–188.

Jacobitz, F. G. & Sarkar, S. 2000 A direct numerical study of transport and anisotropy in a stably stratified turbulent flow with uniform horizontal shear. *Flow Turbul. Combust.* **63**, 343–360.

Jacobitz, F. G., Sarkar, S. & VanAtta, C. W. 1997 Direct numerical simulations of the turbulence evolution in a uniformly sheared and stably stratified flow. *J. Fluid Mech.* **342**, 231–261.

Jeong, J. & Hussain, F. 1995 On the identification of a vortex. *J. Fluid Mech.* **285**, 64–94.

Johnston, T. & Rudnick, D. 2009 Observations of the transition layer. *J. Phys. Oceanogr.* **39**, 780–797.

Kaltenbach, H. J., Gerz, T. & Schumann, U. 1994 Large-eddy simulation of homogeneous turbulence and diffusion in stably stratified shear flow. *J. Fluid Mech.* **280**, 1–40.

Koop, C. G. & Browand, F. K. 1979 Instability and turbulence in a stratified fluid with shear. *J. Fluid Mech.* **93**, 135–159.

Lien, R.-C., D'Asaro, E. & McPhaden, M. 2002 Internal waves and turbulence in the upper central equatorial pacific: Lagrangian and eularian observations. *J. Phys. Oceanogr.* **32**, 2619–2639.

Lien, R.-C., McPhaden, M. & Gregg, M. 1996 High-frequency internal waves at 0°, 140° w and their possible relationship to deep-cycle turbulence. *J. Phys. Oceanogr.* **26**, 581–600.

Linden, P. 1975 The deepening of a mixed layer in a stratified fluid. *J. Fluid Mech.* **71**, 385–405.

Luyten, J. & Swallow, J. 1976 Equatorial undercurrents. *Deep Sea Res.* **23**, 499–524.

Mahalov, A., Moustaoui, M., Nicolaenko, B. & Tse, K. L. 2007 Computational studies of inertia-gravity waves radiated from upper tropospheric jets. *Theoret. Comput. Fluid Dyn.* **21**, 399–422.

McPhaden, M. & Peters, H. 1992 Diurnal cycle of internal wave variability in the equatorial pacific ocean: Results from moored observations. *J. Phys. Oceanogr.* **22**, 1317–1329.

Moeng, C. 1984 A large-eddy-simulation model for the study of planetary boundary-layer turbulence. *J. Atmos. Sci.* **41**, 2052–2062.

Monkewitz, P. & Huerre, P. 1982 Influence of the velocity ratio on the spatial instability of mixing layers. *Phys. Fluids* **25**, 1137–1143.

Moum, J., Caldwell, D. & Paulson, C. 1989 Mixing in the equatorial surface layer and thermocline. *J. Geophys. Res.* **94** (C2), 2005–2021.

Moum, J., Hebert, D., Paulson, C. & Caldwell, D. 1992 Turbulence and internal waves at the equator. part i: Statistics from towed thermistors and a microstructure profiler. *J. Phys. Oceanogr.* **22**, 1330–1345.

Moum, J. N., Nash, J. D. & W., S. 2010 Narrowband, high-frequency oscillations at the equator. part I: Intepretaion as shear instability? *J. Phys. Oceanogr.* **submitted**.

Munk, W. 1981 Internal waves and small-scale processes. *Evolution of Physical Oceanography* **B.A. Warren and C. Wunsch, Eds.**, 264–291.

Nappo, C. J. 2002 *An Introduction to Atmospheric Gravity Waves*. San Diego: Elsevier Science.

Oakey, N. 1985 Statistics of mixing parameters in the upper ocean during jasin phase 2. *J. Phys. Oceanogr.* **15**, 1662–1675.

Osborn, T. 1980 Estimates of the local rate of vertical diffusion from dissipation measurements. *J. Phys. Oceanogr.* **10**, 80–89.

Pedlosky, J. 2003 *Waves in the Ocean and Atmosphere*. New York: Springer.

Peltier, W. R. & Caulfield, C. P. 2003 Mixing efficiency in stratified shear flows. *Annu. Rev. Fluid Mech.* **35**, 135–167.

Peters, H., Gregg, M. & Sanford, T. 1994 The diurnal cycle of the upper equatorial ocean: Turbulence, fine-scale shear, and mean shear. *J. Geophys. Res.* **99** (C4), 7707–7723.

Peters, H., Gregg, M. & Toole, J. 1988 On the parameterization of equatorial turbulence. *J. Geophys. Res.* **93** (C2), 1199–1218.

Pham, H. T. & Sarkar, S. 2010 Internal waves and turbulence in a stable stratified jet. *J. Fluid Mech.* **648**, 297–324.

Pham, H. T., Sarkar, S. & Brucker, K. A. 2009 Dynamics of a stratified shear layer above a region of uniform stratification. *J. Fluid Mech.* **630**, 191–223.

Philander, S. 1980 The equatorial undercurrent revisited. *Ann. Rev. Earth Planet. Sci.* **8**, 191–204.

Piccirillo, P. & VanAtta, C. W. 1997 The evolution of a uniformly sheared thermally stratified turbulent flow. *J. Fluid Mech.* **334**, 61–86.

Riley, J. J. & deBruynKops, S. M. 2003 Dynamics of turbulence strongly influenced by buoyancy. *Phys. Fluids* **15**, 2047–2059.

Rohr, J. J., Itsweire, E. C., Helland, K. N. & VanAtta, C. W. 1988 Growth and decay of turbulence in a stably stratified shear flow. *J. Fluid Mech.* **195**, 77–111.

Rosenlof, K. 1996 Summer hemisphere differences in temperature and transport in the lower stratosphere. *J. Geophys. Res.* **101**, 19129–19136.

Shih, L. H., R., K. J., Ivey, G. N. & Ferziger, J. H. 2005 Parameterization of turbulent fluxes and scales using homogeneous sheared stably stratified turbulence simulations. *J. Fluid Mech.* **525**, 193–214.

Skyllingstad, E. & Denbo, D. 1994 The role of internal gravity waves in the equatorial current system. *J. Phys. Oceanogr.* **24**, 2093–2110.

Smyth, W. & Moum, J. 2002 Shear instability and gravity wave saturation in an asymmetrically stratified jet. *Dyn. Atmos. Oceans* **35**, 265–294.

Smyth, W. D., Hebert, D. & Moum, J. N. 1996 Local ocean response to a multiphase westerly wind burst. part 2: Thermal and fresh water responses. *J. Geophys. Res.* **101** (C10), 22513–22533.

Smyth, W. D. & Moum, J. N. 2000*a* Anisotropy of turbulence in stably stratified mixing layers. *Phys. Fluids* **12** (6), 1343–1362.

Smyth, W. D. & Moum, J. N. 2000*b* Length scales of turbulence in stably stratified mixing layers. *Phys. Fluids* **12** (6), 1327–1342.

Smyth, W. D., Moum, J. N. & Caldwell, D. R. 2001 The efficiency of mixing in turbulent patches: Inferences from direct simulations and microstrucure observations. *J. Phys. Oceanogr.* **31**, 1969–1992.

Smyth, W. D., Moum, J. N. & Nash, J. D. 2010 Narrowband, high-frequency oscillations at the equator. part II: Properties of shear instabilities. *J. Phys. Oceanogr.* **submitted**.

Staquet, C. 2000 Mixing in a stably stratified shear layer: two- and three-dimensional numerical experiments. *Fluid. Dyn. Res.* **27**, 367–404.

Staquet, C. & Riley, J. J. 1989 A numerical study of a stably-stratified mixing layer. In *Turbulent Shear Flows 6*, pp. 381–397. Springer-Verlag, Berlin.

Stewart, R. H. 2004 *Introduction to Physical Oceanography*. Texas A & M University.

Strang, E. J. & Fernando, H. J. S. 2001 Entrainment and mixing in stratified shear flows. *J. Fluid Mech.* **428**, 349–386.

Sullivan, P., McWilliams, J. & Moeng, C. 1996 A grid nesting method for large-eddy simulation of planetary boundary-layer flows. *Bound.-Layer Meteor.* **80**, 167–202.

Sun, C., Smyth, W. & Moum, J. 1998 Dynamic instability of stratified shear flow in the upper equatorial pacfic. *J. Geophys. Res.* **103**, 10323–10337.

Sutherland, B. & Linden, P. 1998 Internal wave excitation from stratified flow over thin barrier. *J. Fluid Mech.* **377**, 223–252.

Sutherland, B. R. 1996 Dynamic excitation of internal gravity waves in the equatorial ocean. *J. Phys. Oceanogr.* **26**, 2398–2419.

Sutherland, B. R. 2006 Rayleigh wave-internal wave coupling and internal wave generation above a model jet stream. *J. Atmos. Sci.* **63**, 1042–1055.

Sutherland, B. R. & Peltier, W. 1992 The stability of stratified jets. *Geophys. Astrophys. Fluid Dyn.* **66**, 101–131.

Taylor, J. R. & Sarkar, S. 2007 Internal gravity waves generated by a turbulent bottom ekman layer. *J. Fluid Mech.* **590**, 331–354.

Taylor, J. R. & Sarkar, S. 2008 Stratification effects in a bottom ekman layer. *J. Phys. Oceanogr.* **38**, 2535–2555.

Thorpe, S. 1978 On the shape and breaking of finite amplitude internal gravity waves in a shear flow. *J. Fluid Mech.* **138**, 185–196.

Thorpe, S. A. 1973 Experiments on instability and turbulence in a stratified shear flow. *J. Fluid Mech.* **61**, 731–751.

Tsai, W., Chen, S. & Moeng, C. 2005 A numerical study on the evolution and structure of a stress-driven free-surface turbulent shear flow. *J. Fluid Mech.* **545**, 163–192.

Tse, K. L., Mahalov, A., Nicolaenko, B. & Fernando, H. J. S. 2003 Quasi-equilibrium dynamics of shear-stratified turbulence in a model tropospheric jet. *J. Fluid Mech.* **496**, 73–103.

Wang, D., McWiliams, J. & Large, W. 1998 Large-eddy simulation of the diurnal cycle of deep equatorial turbulence. *J. Phys. Oceanogr.* **28**, 129–148.

Wang, D. & Muller, P. 2002 Effects of equatorial undercurrent shear on upper-ocean mixing and internal waves. *J. Phys. Oceanogr.* **32**, 1041–1057.

Weller, R. & Plueddemann, A. 1996 Observations of the vertical structure of the oceanic boundary layer. *J. Geophys. Res.* **101**, 8789–8806.

Werne, J., Lund, T., Pattersson-Reif, B. A., Sullivan, P. & Fritts, D. C. June 2005 Cap phase ii simulation for the air force hel-jto project: Atmospheric turbulence simulations on navo's 3000-processor ibm p4+ and arl's 2000-processor intel xeon em64t cluster. *15th DoD HPC User Group Conference* .

Wijesekera, H. & Dillon, T. 1991 Internal waves and mixing in the upper equatorial pacific ocean. *J. Geophys. Res.* **96** (C4), 7115–7125.

Winters, K., Lombard, P., Riley, J. & D'Asaro, E. A. 1995 Available potential energy and mixing in density-stratified fluids. *J. Fluid Mech.* **289**, 115–128.

Winters, K. B. & D'Asaro, E. A. 1994 Three-dimensional wave instability near a critical layer. *J. Fluid Mech.* **272**, 255–284.